IDENTIFYING E-TYPE AND N-TYPE MORB PICRITES FROM PAALLAVVIK ISLAND, BAFFIN ISLAND, CANADA.

Ryan Mooney

Submitted in fulfilment of the requirements of the

Degree of Master of Science (Research)

School of Geographical and Earth Sciences,

College of Science and Engineering

University of Glasgow

Abstract

A new suite of 27 igneous rocks were collected during a 2021 expedition to Paallavvik Island, funded by Red Bull. Picrites from Baffin Island have been previously investigated due to their high MgO of up to 22 wt.%, high $^{3}He/^{4}He$ ratio of $49.5R_a$ and the two geochemical distinct types of N-type and E-type MORB (Francis, 1985; Robillard et al., 1992; Fitton et al.; 1997; Mahoney et al., 2002; Stuart et al., 2003; Yaxley et al., 2004; Starkey, 2009; Maisonneuve, 2012). Within this study, the geochemistry and mineralogy of the new suite of igneous rocks were investigated and compared to previously published data.

Using XRF and LA-ICP-MS, the samples were analysed and then split into the two groups, N-type and E-type MORB. The conditions of separation used were K/Ti </> 0.2 and $(La/Sm)_N$ </> 0.8, where less than for both conditions meant N-type MORB and more than meant E-type MORB (Robillard et al., 1992; Mahoney et al, 2002; Stuart et al., 2003; Starkey, 2009; Starkey et al., 2009; Maisonneuve, 2012). Using SEM, EMPA and LA-ICP-MS, the mineralogy and geochemistry of the minerals were investigated.

The major and trace element relationships against MgO were found to agree with previously published results (Francis, 1985; Robillard et al., 1992; Holm et al., 1993; Larsen and Pedersen, 2000; Yaxley et al., 2004; Starkey, 2009; Starkey et al., 2009). Using the conditions of separation, samples were split into 3 categories – N-type MORB, E-type MORB and those that failed one condition but not the other. N-type MORB samples were found to be 1, 4, 6, 7, 9, 13, 15, 16, 24 and 25. E-type MORB samples were 3, 5, 10, 12, 14, 20, 21, 23 and 26.

Contamination by mantle metasomatism was investigated after it was found that the Na_2O/TiO_2 ratio agrees with other studies at ~1.48 ($\sigma = 0.31$) for these samples, meaning that the lavas erupted through thick lithosphere and so have the potential to be contaminated (Su, 2003; Jackson and Dasgupta, 2008; Starkey, 2009). However, the investigation was inconclusive due to poor quality of data.

The olivine minerals analysed had a forsterite range of Fo_{34} to Fo_{79}. In comparison to previously published studies, this is around 10% less, which may have been down to the standards used (Francis, 1985; Larsen and Pedersen, 2000; Starkey, 2009; Maisonneuve, 2012). Continuous trends of CaO, NiO and Fo% against Cr_2O_3, as well as no difference in Fo% for different sizes of olivines showed that the olivines are all sampling the same source (Starkey, 2009; Starkey et al., 2012).

Further work is advised for the study of the samples. By measuring $^{3}He/^{4}He$ of the melt inclusions and comparing it with previously published studies – e.g. Stuart et. al. , 2003. This will show whether the samples have a relationship with a primitive undegassed mantle reservoir. Furthermore, SIMS should also be used to investigate hydrogen and nitrogen isotopes within the melt inclusions and surrounding minerals. Hydrogen and nitrogen isotopes can help determine how the Earth became rich in volatiles and offer more information about the geochemistry of the deep mantle.

Acknowledgements

First, I would like to thank my supervisor Lydia Hallis. Thank you for all your help and guidance! It's really much appreciated and I wouldn't be completing this without you. To Iain Neill, thank you for providing insight early on as to keep me focussed throughout.

I would like to thank Connor Brolly, for helping to create the thin sections and all the numerous trial and error ideas we came up with. During my trip to Zurich, I would like to thank Lydia Zehender at ETH for the guidance on how to crush the samples and explanation of how XRF works. Thank you to Mark Wildman for all your help and assistance on how to use LA-ICP-MS at Glasgow. Also, thank you Iris Buisman at Cambridge University for conducting SEM and EMPA when I was unable to.

A special mention to Connor Brolly, Annemarie Pickersgill and Áine O'Brien for assisting during an eventful lab incident, thank you so much!

I would also like to thank Rede Bull for funding the expedition that collected the samples.

Finally, I would like to thank my family and friends for their support during my masters.

Authors Declaration

I declare that, except where explicit reference is made to the contribution of others, that this dissertation is the result of my own work and has not been submitted for any other degree at the University of Glasgow or any other institution.

Name: **Ryan Mooney** Signature:

All data is presented in appendices at the end of this dissertation or is available in electronic form on request from the author.

Table of Contents

List of Figures and Tables

Chapter 1: Introduction

Over the past five decades, expeditions have been undertaken to Baffin Island and Western Greenland to investigate the geochemistry of the lavas found there (Clark and Upton, 1971, Francis 1985, Larsen and Pedersen, 2000). A further expedition was conducted through the funding of Red Bull by Dr. Lydia Hallis in 2021 to Paallavvik Island, Baffin Island. This expedition created a new suite of 27 igneous samples which are the focus of this study.

The proto-Icelandic plume has been an area of geochemistry that's a topic of much debate. Picrites obtained from Baffin Island have been noted to have a very high bulk rock MgO of up to 22 wt.%, and a forsterite range of up to Fo_{93} for olivines (Francis, 1985; Starkey 2009). The highest $^{3}He/^{4}He$ ratio recorded from magmatic origins, $49.5R_a$, was also measured from these picrites (Stuart et al., 2003). Further analysis of trace elements and isotopic data has led to the discovery that the picrites on Baffin Island can be separated into two geochemically distinct types, N-type MORB and E-type MORB, which are interbedded. This has led to discussions around the origins of the source and the possibility of an undegassed primitive mantle existing (Robillard et al., 1992; Fitton et al.; 1997; Mahoney et al., 2002; Yaxley et al., 2004; Starkey, 2009; Maisonneuve, 2012).

Within this study, the geochemistry and mineralogy of the new suite of igneous rocks were investigated and compared to previously published data. This study was conducted so as to determine which samples would be best for further analysis to gain insights into the origins of the source and the undegassed primitive mantle.

1.1 Background Geology

The geological setting of Baffin Island is composed of a mixture of Precambrian metamorphic basement rock, which forms part of the Canadian Shield, and Tertiary volcanics and sediments – which form part of the North Atlantic Igneous Province (Clarke and Upton, 1971; Francis, 1985; Saunder et al., 1997). *Fig 1.1* shows the regional area of the North Atlantic Igenous Province, with the study area highlighted.

1.1.1 Regional Geology

The regional area encompasses Baffin Island, Baffin Bay, Davis Strait and Western Greenland. The geology of the east coast of Baffin Island and the west coast of Greenland share similarities. Studies taking samples from Cape Dyer to Cape Searle – on Baffin Island - and Syartenhuk peninsula to Disko Island - on Greenland – show that they erupted at the

same time; and are also mineralogically and geochemically similar (Clarke and Upton, 1971; Francis, 1985).

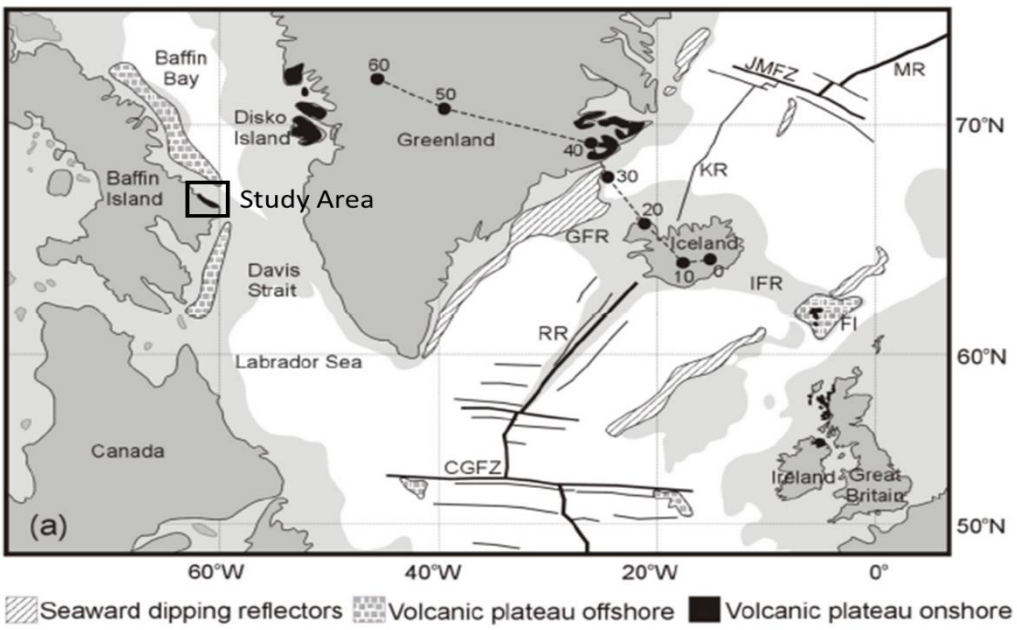

Figure 1.1: Map of North Atlantic Igneous Province. *Map taken from Starkey et al. (2009) and modified to show the study area.*

Canadian Shield

The Canadian Shield is a Precambrian metamorphic province, of which the basement rock on Baffin Island is a part of. The Canadian Shield is formed of 5 individual sub-provinces, with Baffin Island located on the eastern part of Churchill Province. Churchill Province contains Archean and Proterozoic aged rocks (4 – 0.541Ga), thus the basement rock of Baffin Island is amongst the oldest known. The basement geology of Baffin Island is made of Precambrian gneisses and migmatites, which form part of the Canadian Shield. The common mineral assemblage is quartz, feldspar and biotite, frequently containing secondary minerals garnet, pyroxene and/or muscovite and accessory minerals of apatite, zircon and magnetite. The metamorphic grade is generally of an amphibolite facies, however there are localised areas of granulite facies. Due to the high Ni content of ~900ppm, it is suggested that the protolith rock is ultrabasic rather than metamorphosed marly sediments. Rb-Sr and K-Ar dating place the basement to be pre-Cambrian at ~1.7Ga (Clarke and Upton, 1971).

North Atlantic Igneous Province (NAIP)

The North Atlantic Igneous Province (NAIP) stretches from the Canadian coast to Northern Britain, with a total magmatic volume of at least 6 x 10^6 km^3. The NAIP occurred in two main phases, with the first phase occurring between 62Ma and 58Ma, and the second phase – break-up phase - starting at 56Ma and still ongoing today (Saunders et al., 1997). It is during the first phase of magmatism that the lavas on Baffin Island erupted (Storey et al., 1998).

1.1.2 Local Geology

The samples analysed within this study are from Paallavvik Island. *Fig 1.2* shows the areas where the samples were collected on Paallavvik Island -formerly Padloping Island. Paallavvik Island is on the Eastern Coast of Baffin Island and situated between Cape Dryer and Cape Searle. The basement rock of Paallavvik Island is the same as that found on the rest of the east coast of Baffin Island – Precambrian metamorphic gneisses (Clarke and Upton, 1971).

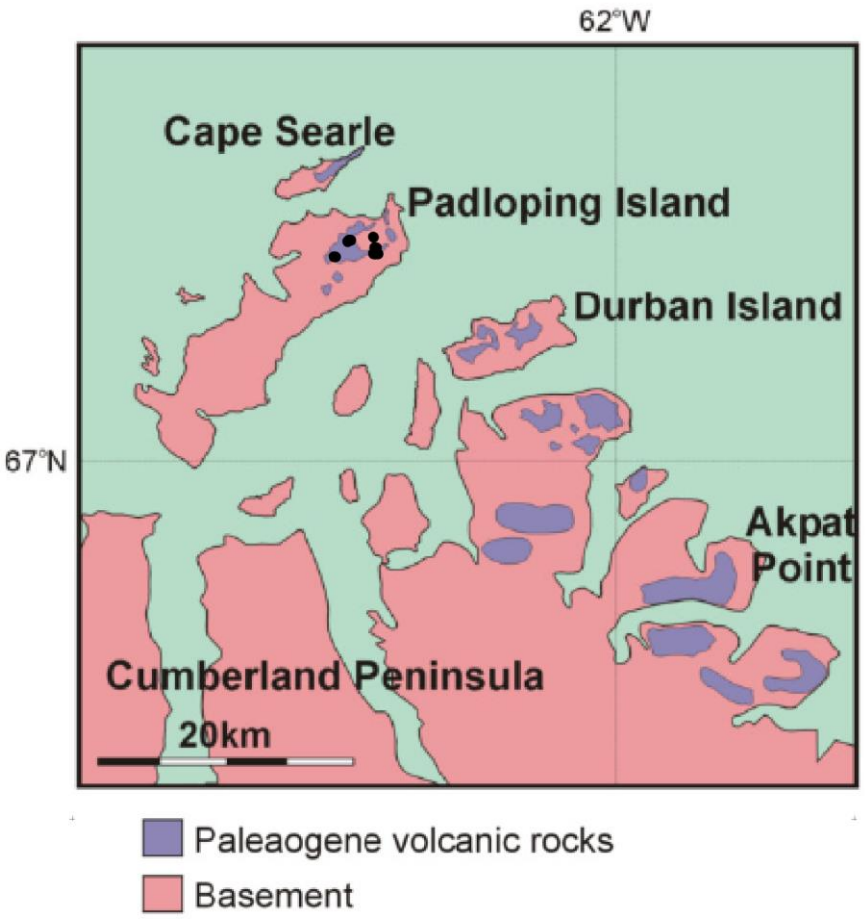

Figure 1.2: Map of local area. *Map taken from Starkey et al. (2009) and modified to show the sample locations which are denoted by black dots.*

In conjunction with the North Atlantic Igneous Province, in 61Ma the Baffin Island and West Greenland margin lavas erupted (Storey et al., 1998). This suite of igneous rocks, along with Tertiary sediments, lay unconformably upon the metamorphic Precambrian basement. The Tertiary sediments occur in a cyclical delta pattern of sandstone, mudstone, coal and conglomerate. The majority of the sediments are unconsolidated sandstones containing current cross beds, with minor beds of coal, mudstone and fluvial conglomerates. On Baffin Island, the sediments thicken from Cape Dyer to Cape Searle and contain no marine fossils. However, on Western Greenland the same sediments contain both marine and non-marine Palaeocene fossils. The common fossils found are *Metasequoia occidentalis* and *Crednaria spectabilis*, which are from the Palaeocene and so coincide with the 61Ma from Storey et al. (1998) (Clarke and Upton, 1971; Francis, 1985).

The igneous suite lays either unconformably upon the basement gneiss or conformably on the sediments. On Baffin Island, the lavas are of picritic composition, whereas in West Greenland the lavas grade from picritic to basaltic plagioclase lavas. Picrites are found along the Eastern Coast of Baffin Island, between Cape Searle to Cape Dyer, and on the Western coast of Greenland - between Syartenhuk peninsula and Disko Island (Franics, 1985).

The igneous suite consists of breccias, lava flows and dykes. The breccias are either orange or black in colour. Both coloured breccias contain hyaloclastites, basaltic fragments and massive basaltic blocks. However, black breccias contain non-brecciated pahoehoe, whereas the orange breccias have smaller crystalline block varieties. As both breccias are identical in mineralogy, the difference in colour is thought to be due to greater hydration of the glass and oxidation of iron in the orange breccias (Clarke and Upton, 1971; Francis, 1985).

Lava flows are picritic and olivine rich basalts. As they weather, they become light grey and crumbly, although as the olivine content decreases the basalts become darker. Each lava flow has the same 4 sections within them. The first section is the lower basal chilled margin which is a few centimetres in thickness and characterised by vesicles and tachylyte. The second section is the lower massive zone. This comprises of about 60% of the lava flow and is mainly featureless apart from occasional vesicles and flow banding. The third section is the upper vesicular zone, which is about 40% of the lava flow. The upper vesicular zone contains subspherical to ellipsoidal vesicles with many filled with zeolites. The fourth section of the lava flows are a few centimetres in thickness containing glass with a pahoehoe texture. On the late flows, hematite and alteration of olivines creates a red colour to the flow tops. Prolonged weather of some flows during periods of no volcanism have developed a layer of red bole a few cm thick, which is then subsequently baked by the next flow. As there are no post volcanic deposits, it is unknown if the lava successions are complete. However, the lack of glacial striation and erratics suggests that no erosion took place during the Pleistocene (Clarke and Upton, 1971; Francis, 1985).

The lava flows on Baffin Island thin rapidly and are concentrated along the coast, with none extending more than 10km inland. The rapid thinning is thought to be due to short lived volcanism flowing from the NE as the Davis Strait opened. The causation of the volcanism is known, however the source is contentious. The lavas fill depressions in the basement and

are between 1-35m thick, however only a minority of flows exceed 10m in thickness (Clarke and Upton, 1971; Francis, 1985).

Dykes are geochemically and mineralogically indistinguishable from the lava flows, however they cut through sediments and volcanics only in local areas, such as Cape Searle and Paallavvik Island (Clarke and Upton, 1971; Francis, 1985).

1.2 Background Work

The picrites on Baffin Island have long been a topic of continued debate around their source. Initial investigations found that the bulk rock of these picrites have a composition up to 22 MgO *wt.%*. Olivines within the picrites were also found to be highly forsteritic of up to Fo_{93}. The high Mg content of these rocks led to the question of what the parental source is (Francis, 1985).

Robillard et al. (1992) analysed the trace element and isotopic geochemistry of the picrites. The picrites were found to be geochemically comparable to E-MORB and N-MORB, despite being interbedded – emplaced at the same time. E-MORB stands for 'enriched' mid ocean ridge basalt, and N-MORB stands for 'normal' mid ocean ridge basalt. Both types have similar major and trace elements, however the N- type MORB's were found in picrites that have a higher MgO wt.% and are depleted in LREE's - $(La/Sm)_N$ ~ 0.6-0.7, K/Ti < 0.05 and $^{87}Sr/^{86}Sr$ < 0.7032. Whereas E-type MORB's were found mainly in picrites that have a lower MgO wt.% and are enriched in LREE's - $(La/Sm)_N$ ~ 1.1-1.2, K/Ti > 0.05 and 0.7032 < $^{87}Sr/^{86}Sr$ < 0.7039. As both types are geochemically distinct, different mantle source regions are need. Robillard et al. (1992) proposes that this would occur by material from an enriched plume mixing with depleted mantle prior to emplacement of the picrites.

Independently, Kent et al. (1998) investigated glass inclusions within olivine phenocrysts of the Baffin Island picrites. Using an electron microprobe and an ion microprobe, it was found that N- and E-type MORB can be separated by $^{87}Sr/^{86}Sr$ and $^{143}Nd/^{144}Nd$. For N-type MORB, $^{87}Sr/^{86}Sr$ < 0.7030 and $^{143}Nd/^{144}Nd$ > 0.51300, and $^{87}Sr/^{86}Sr$ > 0.7030 and $^{143}Nd/^{144}Nd$ < 0.51300 for E-type MORB. These results were compared to those by Robillard et al. (1992) and found to be similar. Likewise, the proposed model is similar to that proposed by Robillard et al. (1992). N-type MORB picrites are derived from an incompatible element depleted source, and E-type MORB picrites are derived from a mixture of melts made of the incompatible element depleted source as well as an incompatible element enriched source (Kent et al., 1998).

Maisonneuve (2012) used a ratio of K/Ti to probe the mantle source of E- and N-type MORB picrites - as both elements are incompatible in plagioclase and olivine so unaffected by crystal fractionation. The N-type were defined as K/Ti <0.2, and E-type were defined as >0.2 – higher than the values set out but Robillard et al. (1992). E-type were found to be less magnesian than N-type, and both types were low in volatiles so both magmas degassed on eruption – although higher Cl and F in E-type suggests there was less degassing than compared to N-type. The sampled melt inclusions are thought to be entrapped before

eruption due to compositional similarities in the inclusions and bulk rock. Both E- and N-type MORB compositions were found within the one sampled inclusion suggesting that E- and N- type magmas were distinct in the mantle but with partial mixing present.

Stuart et al. (2003) measured the $^{3}He/^{4}He$ isotope ratio within olivine phenocrysts of Baffin Island. The olivine phenocrysts were crushed so as to release He. The released amount was measured to be up to $49.5R_a$, which is the highest ever recorded. The unit R_a is in reference to the atmospheric ratio $^{3}He/^{4}He$ at 1.39×10^{-6}. Due to the high $^{3}He/^{4}He$, it is reasoned that the picrites are sourced from a mantle plume that has a relationship with a primitive undegassed mantle reservoir. The picrites themselves was argued to be the result of melted depleted upper mantle which is then recharged in He – and other volatiles – via a mantle plume fed from the primitive undegassed mantle reservoir.

Building on the evidence of there being a primitive mantle reservoir, Jackson et al. (2010) looked at Pb isotopes to date via geochron models. Plotting $^{207}Pb/^{204}Pb$ against $^{206}Pb/^{204}Pb$, the sampled picrites from Baffin Island and Western Greenland were clustered between 4.45-4.55Ga reference lines. The $^{143}Nd/^{144}Nd$ ratio of samples was also found to be similar to the $^{143}Nd/^{144}Nd$ ratio found in a 4.5Ga terrestrial mantle reservoir. Therefore, the source of the samples was argued to be a primitive mantle reservoir which may be between 4.45-4.55Ga.

Starkey et al. (2012) investigated major and trace elements within olivine melt inclusions. There was no evidence of enriched or depleted inclusions, and the REE's were the same as the bulk rock composition. Therefore, the high $^{3}He/^{4}He$ ratio is within a large range of mantle source compositions, and the primordial He is from an independent enriched reservoir that creates the high $^{3}He/^{4}He$ ratio in the depleted and enriched picrite sources. Starkey et al. (2012) conclude that either there is a high concentration ^{3}He primordial reservoir that has been preserved – by avoiding convective mantle mixing – and imposes a high He ratio through mixing or diffusive equilibration, or primordial He has diffused from the core into the lower mantle thermal boundary which fed the Iceland plume.

Riso et al. (2016) present an analysis of ^{182}Hf - ^{182}W, and $^{182}W/^{184}W$ ratios in high-MgO picrite samples on Paallavvik Island, as well as samples from Ontong Java Plateau, to reinforce the argument of the preservation of a primitive mantle. Results showed that mantle reservoirs formed by early Earth differentiation events remain in the mantle to the present time. These primitive reservoirs may be preserved due to their temperature, composition and density differences with the surrounding mantle allowing them to not mix and be isolated.

To help understand the preservation of a primordial high $^{3}He/^{4}He$ ratio reservoir, Jackson et al. (2017) looked at the distribution of mantle plumes. Some plumes result in lavas which have both high and low $^{3}He/^{4}He$ ratios – e.g. those in Baffin Island - whilst others only result in low $^{3}He/^{4}He$ ratios. It was found that those with both high and low $^{3}He/^{4}He$ overlie seismic low-velocity anomalies in the upper mantle and have a high hotspot buoyancy flux in comparison to low $^{3}He/^{4}He$ ratio fed hotspots. This comparison was capped at a depth of

200km though as relationship between maximum $^{3}He/^{4}He$ values and seismic anomalies are only understood in the upper mantle. This shows preservation as if high $^{3}He/^{4}He$ ratios only come from the deep mantle and are only delivered from the hottest most buoyant plumes, then the high $^{3}He/^{4}He$ reservoir is very dense allowing it to remain isolated from the convecting mantle within the eddies.

More recently, Horton et al., (2021) vacuum crushed olivine separates to further investigate the $^{3}He/^{4}He$ ratio and $^{20}Ne/^{22}Ne$ ratio and then compared them against each other. They found that the $^{3}He/^{4}He$ ratio overlaps with that found by Stuart et al., (2003), at a range of 36.2 ± 0.6 to 48.6 ± 1.3 R_a. They also found that the $^{20}Ne/^{22}Ne$ ratio fell on a mixing line between atmosphere and a high $^{20}Ne/^{22}Ne$ mantle endmember – the maximum $^{20}Ne/^{22}Ne$ ratio was 12.2. The mixing line was found to be similar to that of subglacial Holocene glass from Iceland and distinct from other hotspots and MORB. Hence suggesting that they have a common high $^{3}He/^{4}He$ mantle component. They also conclude that high $^{3}He/^{4}He$ mantle reservoirs have a $^{3}He/^{22}Ne$ variability that may further support the argument of helium addition in the upper or lower mantle, or reflects primitive mantle heterogeneity (Horton et al., 2021).

1.3 Aim and Objectives

The aim of this thesis is to classify rock samples into N- and E-type MORB based on their bulk rock chemistry. Melt inclusions and olivine composition will also be investigated to determine parental source.

Objective 1: Classifying Rocks

Using Wavelength Dispersive X-Ray Fluorescence (WD-XRF) and Laser Ablation - Inductively Coupled Plasma - Mass Spectrometry (LA-ICP-MS), the major and trace elements of each sample will be determined. Knowing the bulk rock composition will allow for classification of samples into N- or E-Type MORB.

Objective 2: Finding and Mapping Melt Inclusions

Thin sections of each sample will be created and then imaged in reflective, plane polarised and cross polarised light. Thin sections will also be imaged via scanning electron microscopy (SEM) to create a back-scatter electron image. The images will allow for determination of minerology and mapping of melt inclusions.

Objective 3: Composition of Olivine's and Melt Inclusions

Using Electron Micro-probe Analysis (EMPA) and Laser Ablation - Inductively Coupled Plasma - Mass Spectrometry (LA-ICP-MS), olivines and glassy melt inclusions will have their major and trace elements investigated. This will show the composition of the parental melt – from the melt inclusions - as well as whether there is more than one type of olivine population.

Chapter 2: Methodology

An expedition to Paallavvik Island off the east coast of Baffin Island, Canada, was undertaken by Dr Lydia Hallis with Red Bull in August 2021. During the expedition, 27 samples were collected from different areas and lava outcrops. These 27 samples are the subject of this thesis. The methods of Wavelength Dispersive X-Ray Florescence, Laser Ablation - Inductively Coupled Plasma - Mass Spectrometry, Scanning Electron Microscopy and Electron Microprobe Analysis were used to investigate the geochemistry and properties of the samples.

2.1 Bulk Composition Analysis Methods

Bulk composition of each sample was determined by creating glass beads to be analysed by Wavelength Dispersive X-Ray Florescence (WD-XRF) and Laser Ablation - Inductively Coupled Plasma - Mass Spectrometry (LA-ICP-MS). WD-XRF was used to obtain the major and trace elements, with LA-ICP-MS used to investigate the Rare Earth Elements.

2.1.1 Creating Glass Beads

To create the glass beads for analysis, the samples must first be powdered. As such, 15-30g fragments of each sample were collected using a Logitech CS 10 thin section cut-off saw and cleaned in a water bath for 20 minutes. The saw was cleaned between each use with water as a contamination prevention measure.

The sample fragments were taken to ETH Zurich for the creation of the glass beads as set out by PANalytical (Willis, 2010). All work was carried out under the supervision of Lydia Zehnder. Sample fragments were placed in a steel beaker and crushed to less than 4mm using a hydraulic press. To combat against contamination, the steel beaker and hydraulic press were cleaned using steel wire brushes (on a drill) and ethanol between each use.

An agate ball mill was used to powder the samples. Agate was chosen as there is less contamination risk when compared to a steel or tungsten ball mill (Thompson & Bankston, 1970). Although only 1.5g of powder is needed to create the glass beads, 15-30g of each sample was ground for 4 minutes - anything less than 15g would cause high wear and tear on the ball mill. The ball mill was cleaned between each use by powdering sand to ensure no previous sample was left as residue and then cleaning with water and finally ethanol.

Once powdered, samples were stored in individual sterile glass bottles and placed in an oven for at least 6 hours at 105°C to remove any humidity. Upon being removed from the oven, samples were placed in a desiccator to stop dust from mixing with the powder. 1.5g of powder was measured into a ceramic crucible and placed into a furnace at 1050°C for 2 hours. After being left to cool for 10 minutes, the ceramic and powder were remeasured to

determine the Loss On Ignition (LOI) – ceramic was measured prior to powder being placed inside it. The LOI is the evaporated volatiles - including sulphur and water/hydrogen - and the added oxidation from the furnace. This gives the additional benefit of just Fe_2O_3 being measured rather than a mix between Fe_2O_3 and FeO.

For the powdered sample to become a glass bead the next time it's in a furnace, a flux must be added. The ratio of sample to flux is 1:5, so the powdered sample must be remeasured. Powdered sample was transferred into a glass beaker wrapped in aluminium foil, so as to prevent electrostatic charge and having powder stick to the sides. Noting the sample weight, the added flux was 6 times the sample weight so as to get a 1:5 ratio.

The flux used was 66% Lithium tetraborate and 34% Lithium metaborate. The powdered sample and flux were then homogenised in an agate pestle and mortar before being melted and mixed to create a glass bead at 1080°C. An ammonium iodine tablet was inserted into the furnace to act as a catalyst. A crucible of 95% platinum and 5% gold was used to hold the mixture and the resulting glass bead. The crucible was cleaned using 25% citric acid in an ultrasonic water bath for 10 minutes. Agate pestle and mortar was cleaned using water, deionised water and ethanol – same procedure was used to clean the measuring beakers.

2.1.2 Wavelength Dispersive X-ray Fluorescence (WD-XRF)

Wavelength Dispersive X-Ray Fluorescence (WD-XRF) is a non-destructive analytical method. Like a standard XRF, WD-XRF uses X-rays to excite the atoms and cause an emission of characteristic X-rays. However, in WD-XRF these characteristic X-rays are dispersed by a diffraction grating into individual wavelengths. The wavelengths are then used to identify and quantify the element based on the angle of diffraction of the wavelength. WD-XRF is more beneficial than a standard XRF as it's able to measure light elements and has a higher spectral resolution and sensitivity. However, like all XRF's, the REE's are hard to separate out due to close atomic numbers and similar characteristics (Reed, 2005). As such, to measure the REE's another type of method is needed – e.g. LA-ICP-MS.

The glass beads were analysed at ETH Zurich by Lydia Zehnder using a PANalytical Axios X-Ray Fluorescence Spectrometer. The internal standard used during analysis was USGS BCR-2. The resulting data was analysed in Microsoft Excel.

2.1.3 Laser Ablation – Inductively Coupled Plasma – Mass Spectrometry (LA-ICP-MS)

Laser ablation inductively coupled plasma mass spectrometry (LA-ICP-MS) is a partially destructive analytical method that combines both laser ablation and ICP-MS. This allows for the measuring of trace elements. The laser ablates a portion of the sample creating an ionized plume of particles. These particles are then delivered to the ICP-MS via argon gas where they are further excited by high temperature plasma. The mass spectrometer then separates out the particles based on their mass-to-charge ratio and the signal this produces

quantifies the concentration of the elements (Longerich and Jackson, 1996; Koch and Gunther, 2017).

The glass beads were ablated to measure the REE content for the whole rock of each sample. The ablation was conducted at the University of Glasgow under the supervision of Dr Mark Wildman. The laser is a RESOlution laser made by Australian Scientific Instruments and the mass spectrometer is the iCAPRQ model by Thermoscientifica. Geostar software was used to operate the laser and Iolite 4 software to process the resulting data. The processed data was analysed in Microsoft excel.

The beads were first broken into smaller pieces so as to fit into a 1 inch round resin mould. The resin mixture was of a 2:1 ratio of epoxy thin and epoxy hardener, respectively. Once the resin had set overnight, the samples were then polished. Initially on a lapping machine at 20µm, which used an Al_2O_3 solution, and then silicon carbide paper with a FEPA of grade P1200. The final polish was performed with a 6-, 3- and 1µm monocrystalline diamond suspension at 12 minutes per stage.

The laser setup was a spot size of 50µm, beam energy of 3.5J/cm^3, a frequency of 5Hz and an ablation time of 45s per spot. Each sample was ablated 3 times so as to give an average. Between ablating each sample, standards were also ablated to ensure that results remained consistent throughout use. The standards used were synthetic glasses NIST612 and NIST610, and natural standards KL2 and ML3B.

The Iolite software package was used to process the laser data. Within the processing, the laser had to be calibrated to an internal standard, so Si-29 was chosen. Si-29 had less variation across the samples, hence a better internal standard than other known elements, based on the XRF data. When running the data through the data reduction scheme (DRS) for trace elements, the reference material used was KL2. In comparison to the other standards, KL2 had less variation of Si-29 when the quality assurance/quality check (QA/QC) processed the data.

When exporting the data to an excel file for analysis, the limits of detection were calculated using the methods from Longerich et al. (1996), Howell et al. (2013) and Pettke et al. (2012).

2.2 Thin Section Analysis Methods

Thin sections were required to analyse the minerals within the rocks. Using the thin sections, general mineralogy was determined with SEM QESCAN. The elemental composition of the minerals was then investigated through EMPA and LA-ICP-MS.

2.2.1 Creating thin sections

Following the supervision of Dr. Connor Brolly, rock samples were cut to a cube of 1cm x 1cm x 1cm using a Logitech CS 10 thin section cut-off saw. The cubes were covered with a thin layer of resin on the side that was to be mounted, so as to fill any pores and prevent plucking of inclusions by adding an extra adhesive layer. Previous attempts at polishing without the resin had resulted in melt inclusions being plucked out. The excess resin was removed using P800 carbide paper, on a Buehler Beta Grinder-Polisher, lubricated with water. Once the surface was flat and excess resin removed, then the stages of polishing with carbide paper were moved down from P1200, P2500 and finally P4000 – using the FEPA Europe standard. The polished side of the blocks were attached to a 1-inch round glass slide using resin. The resin mixture was of a 2:1 ratio of epoxy thin and epoxy hardener. The 1-inch rounds were frosted using a 12µm grinding solution of Al_2O_3, creating a uniform flat surface for the sample to be mounted on. The reasoning for the 1-inch round slides was so that samples could be loaded into the LA-ICP-MS holder more easily.

In order to get the samples to a thickness of 60µm, the 1-inch rounds were attached to a standard rectangular glass section with wax, as the Buehler petro-thin saw only fits rectangular slides. Wax was used as it created a flatter layer than glue and was a stronger bonding agent than crystal bonding, which often broke when the sample made contact with the petro-thin blade. The samples were then grinded down to 100µm using the petro-thin before applying a thin layer of resin on top. Similarly to the polishing on the mounted side, the excess resin was removed with P800 carbide paper, before being polished through the grades of P1200, P2500 and P4000. For the final finish, a water based Monocrystalline diamond suspension of 6µm, 3µm and 1µm was used for a period of 12 minutes at each stage on a Kemet 300 series polisher at 80 rpm.

The desired thickness for the samples was 60µm, however a repolish was carried out. The reason for the repolish was due to poor polishing by not changing the carbide papers regularly enough and using a 12, 20 and 30µm Al_2O_3 solution initially. The Al_2O_3 solution is a rolling abrasive which can promote plucking (Craig and Vaughan, 1995). Therefore, the final thickness for the samples was between 20-30µm. Images were taken of each sample in XPL, PPL and reflected light. The images showed how well each sample was polished, as well as the thickness of each sample by adjusting the z-axis on the microscope to focus from the top of the sample to the bottom and noting the difference.

2.2.2 Scanning Electron Microscopy Imaging (SEM)

A scanning electron microscope (SEM) images the surface of a sample using a high-energy electron beam. The beam interacting with the surface creates a backscatter electron (BSE) map of the sample surface. A secondary electron (SE) map can also be created. However, SEM does have limitations, such as charging. Charging is a build-up of electrons on the sample surface that causes distortion, resulting in poor image quality. To reduce the risk of charging, samples should be coated in a conductive coating such as gold or carbon (Goldstein et al., 2018).

Samples were sent to the University of Cambridge for use on their SEM, this was carried out by Dr. Iris Bussiman. Prior to being sent down however, all samples were carbon coated to a thickness of 25-30nm. The carbon coating was done at the University of Glasgow**.** All 27 samples were imaged by the SEM and an electron backscatter image was produced. These images were then used to identify 5 samples for further analysis. Only 5 samples were chosen for further analysis due to financial and time constraints. Samples were chosen according to the size of their olivine minerals, structures within the olivine crystals (i.e. kink bands) and the size of glassy melt inclusions.

As well as a backscatter image from the SEM, a QEMSCAN was carried out to identify the minerals present in each sample. This was carried out on the 5 samples that were chosen for further analysis. The QEMSCAN measured the Mg, Ca and Fe content of each mineral, giving an indication whether the mineral was an olivine, plagioclase feldspar or a pyroxene. As Fe and Mg was measured, Fo.% was computed for each olivine allowing for further narrowing down on where to analyse with the EMPA.

2.2.3 Electron Microprobe Analysis (EMPA)

Electron Microprobe Analysis (EMPA) is a non-destructive analytical method. EMPA uses an electron beam to excite electrons and generate characteristic X-rays. The X-rays are analysed by their wavelengths to identify and determine the concentration of the elements within the sample (Reed, 2005).

EMPA was carried out at the University of Cambridge by Dr Iris Buissman on the 5 chosen samples - 2, 10, 14, 16 and 19. On each sample, spot analysis was performed on plagioclase feldspars, pyroxenes, melt inclusions and olivines of different sizes. On the largest olivines of each sample, at least 2 olivines per sample, a transect was taken from the rim to the core.

Having EMPA data meant that when using the LA-ICP-MS on the thin sections, an independent data set could be used to select an internal standard.

2.2.4 Olivine LA-ICP-MS

Measuring the REE's of the olivines followed a similar setup to the bulk rock analysis (Section 2.1.3). The laser settings were the same, however 3 short pulses per spot was initially needed to remove the carbon coating. Each olivine was ablated 3 times, with one spot on the rim, one on the core and one between the core and rim – this is denoted as being the middle. The reference materials used were GOR-128 and NIST 610 glass. The reference materials were analysed between each thin section so as to ensure consistent results. For the DRS trace element processing of the data, GOR-128 was used as there was less variation in the QA/QC compared to NIST 610.

Using an initial spot size of 50µm and ablation time of 45s meant that REE'S were below detection limits. Hence, ablation time was increased to 60s and spot size to 100µm. With the increased spot size, only one spot per olivine could be undertaken. The samples were

thin at 20-30µm, so the laser would only ablate some olivines for less than 20s before hitting the mounting resin. For future work, thin sections need to be 100µm, as they were in Masiounne (2012) to allow for more depth when ablating.

Melt inclusions found on the samples were meant to be ablated, however the MI's were less than 50µm with a depth of 20-30µm. Hence the collected data would have been below detection limits or with a large error resulting in poor results. Therefore, MI's were not investigated.

Chapter 3: Results

3.1 Rocks

27 samples were collected from across Paallavvik Island. *Table 1* below outlines the field data and mass collected of each sample.

Table 3.1: **Hand specimen information table.**

Sample Number	Northing	Easting	Altitude (m)	Notes	Weight (Kg)
1			300	Dark grey, fine groundmass	0.45
2	745083	-52356	400	Grey, fine groundmass, olivines up to 0.5mm	1.01
3	7448512.202	-523899.875	478	Grey, vesicular, olivines up to 2mm	1.54
4	7448882.267	-523766.617	571	Grey, very fine groundmass, olivines up to 0.5mm	1.57
5				Light grey, small vesicles, olivines up to 2mm, crumbles easily	0.57
6	7449681.5	-521913.623	439	Dark grey, olivines up to 1mm	0.43
7	745075	-52348	450	Dark grey, fine groundmass, vesicular, olivines up to 2mm	1.30
8	7449689.257	-521907.929	440	Dark grey, fine groundmass, olivines up to 1mm	0.35
9	7450319.183	-519291.336	496	Dark grey, very fine groundmass, no olivines visible	0.9
10	7441509.012	-523917.235	478	Grey, fine groundmass, vesicular, olivines up to 1mm	2.62
11	7448506.268	-523606.144	542	Grey, fine groundmass, vesicular, olivines up to 1mm	0.3
12				Grey, fine groundmass, vesicular, olivines up to 1mm	0.54
13	7449689.257	-521907.929	436	Dark grey, very fine groundmass, no olivines visible	0.34
14				Dark grey, very fine groundmass, contains vesicles, olivines up to 0.5mm	2.59
15	7449577.338	-521716.53	367	Dark grey, fine groundmass, olivines up to 0.5mm	0.58

16	7449715.435	-521836.687	474	Dark grey, very fine groundmass, no olivines visible	0.51
17	745083	-52355	400	Grey, fine groundmass , olivines up to 0.5mm	2.22
18	7445777.694	-523663.433		Grey, fine groundmass, vesicular, olivines up to 1mm	2.87
19	745073	-52345	460	Dark grey, very fine groundmass, vesicular, olivines up to 1.5mm	0.98
20	7448554.043	-520596.922	625	Dark grey, very fine groundmass, no olivines visible	0.76
21	7448517.659	523633.776	520	Grey, very fine groundmass, olivines up to 1mm	0.52
22	7448924.014	-523823.003	540	Grey, fine groundmass, contains small vesicles, olivine up to 0.5mm	1.57
23	7450333.353	-519246.203	484	Dark grey, very fine groundmass, no olivines visible	0.75
24	7450354.921	-519300.173	466	Dark grey, very fine groundmass, no olivines visible	0.88
25	7448474.16	-523631.558	510	Grey, fine groundmass, olivines up to 0.5mm	0.61
26	7448512.202	-523899.875	476	Grey, fine groundmass, small vesicles, olivines up to 0.5mm	2.22
27	7448523.471	-520535.195	604	Dark grey, very fine groundmass, olivines up to 1mm	0.32

3.2 Hand Specimen Bulk Rock

3.2.1 Bulk Rock Chemistry

The bulk rock geochemistry of each sample was determined using data collected by XRF – the full suite of geochemical data can be found in Appendix I. Samples were classified as picro-/basalts by the TAS Diagram in *Fig. 3.1*, based on Le Matire's classification scheme (Le Matire, 2005). In *Fig. 3.2*, samples were further classified as being Mg- rich Tholeiitic basalts, with the

exception of samples 1 and 22 which plot as Tholeiitic basalts, based on the classification scheme of Jensen (1976) and Jenson and Pyke (1982).

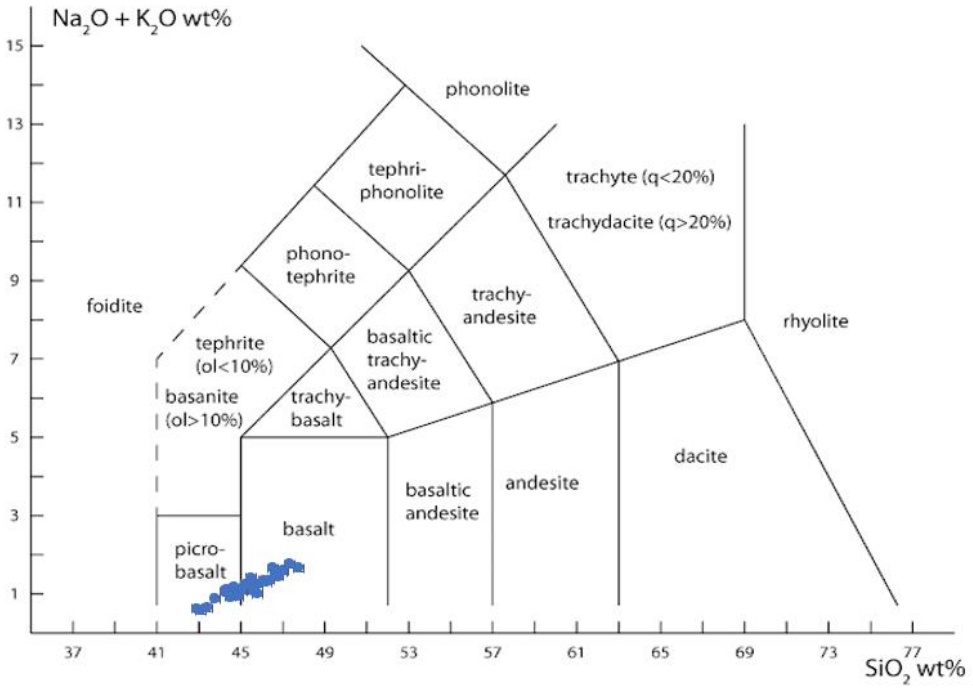

Figure 3.1: **TAS classification diagram of samples**. *Samples plot within the picro-basalt and basalt sections of the diagram, as shown by blue circles. The associated error bars may be obscured by the blue circles. TAS diagram from* Le Maitre (2005).

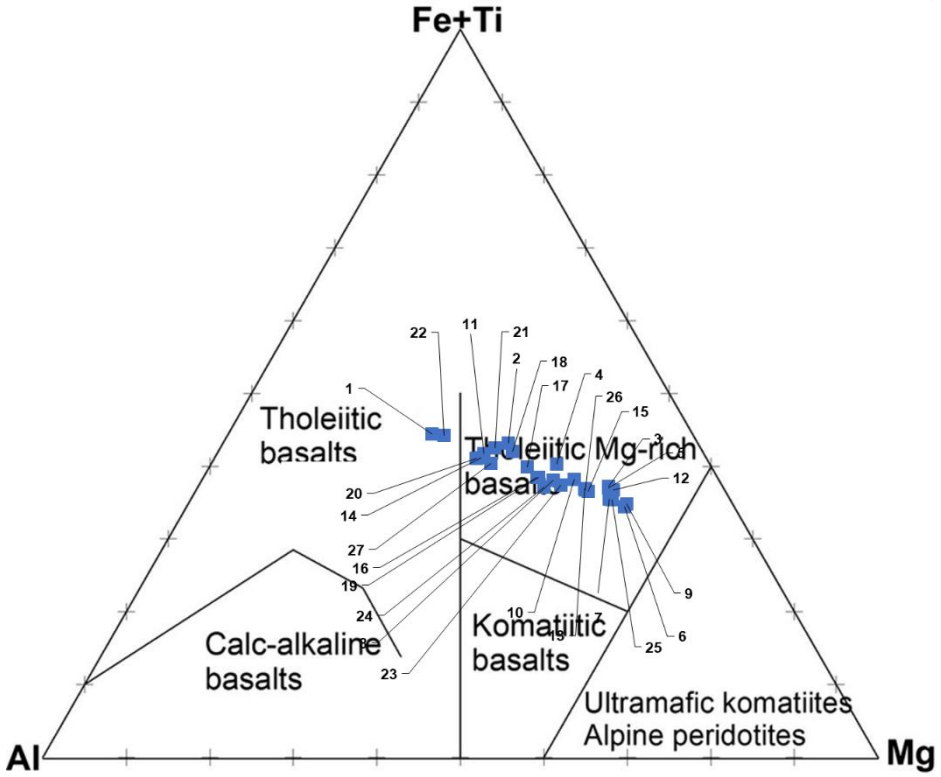

Figure 3.2: Basalt Classification Triangular plot by Al, Mg and Fe+Ti. *All samples plot as Tholeiitic Mg-rich basalts apart from sample 1 and 22 which are Tholeiitic basalts.*

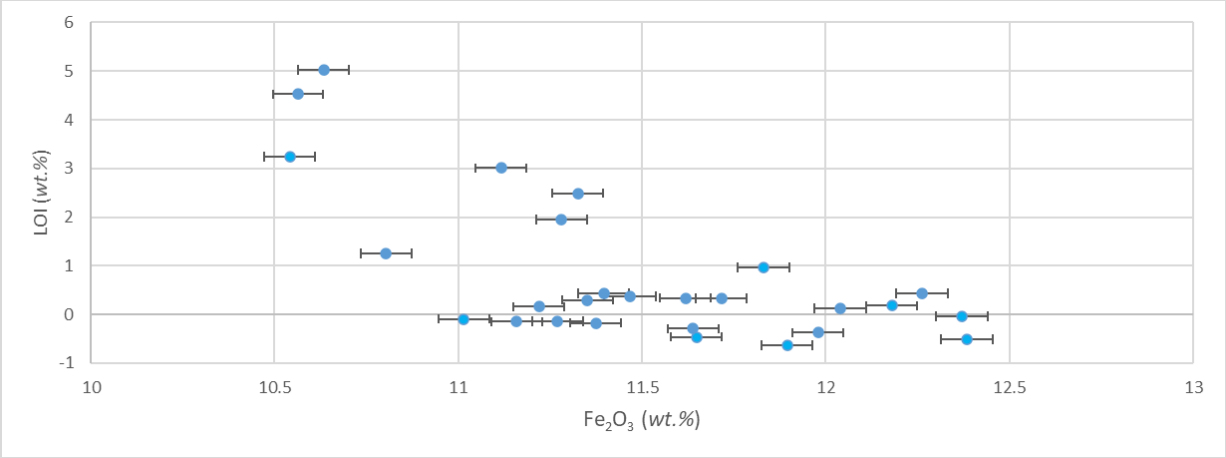

Figure 3.3: Plot of LOI (wt.%) against Fe_2O_3 (wt.%). *LOI is Loss On Ignition during sample preparation and ranges from -0.63 – 5.03 wt.%.*

The total weight % (wt. %) of each sample was not corrected to 100%, hence the total weight % of the samples ranges from 99.33 – 100.53 wt. %. The total weight is not exactly 100% due to the associated errors and the potential for alteration. It must also be stated that there are no associated errors recoded for LOI. LOI is a result of the sample preparation process and as such there is no standard against which it can be related to in order to determine the error. LOI has a range between -0.63 to 5.03 wt.% . LOI can be negative or positive due to either adding mass by oxidation or removal of mass by evaporating volatiles. Due to oxidation in sample preparation, Fe_2O_3 was measured rather than FeO. This gives a better representation of iron content within the rock as there is no mixture between FeO and Fe_2O_3. Plotting LOI against Fe_2O_3 in *Fig 3.3*, there is a greater variability in LOI for lower Fe_2O_3 which then stabilises at 11.5 Fe_2O_3 wt. %.

Bivariate Harker plots of the major oxides can be found in *Fig. 3.4*. The samples are rich in MgO, ranging from 9.26 - 27.28 wt.%. In relation to MgO, there is a negative linear regression with SiO_2 (42.88 - 47.75 wt.%), CaO (6.40 - 12.55 wt.%), Al_2O_3 (8.19 - 14.60 wt.%), Na_2O (0.51 - 1.64 wt.%), TiO_2 (0.52 - 1.16 wt.%) and P_2O_5 (0.047 - 0.176 wt.%). MnO (0.166 - 0.183 wt.%), Fe_2O_3 (10.54 - 12.38 wt.%) and K_2O (0.018 - 0.190 wt.%) have a random scatter pattern with MgO. All elements measured do have their associated error bars being displayed, however the errors on certain elements are smaller than the data points, such as for MgO, making them harder to see on the plots in *Fig 3.4*. If presenting the error ranges as a ±%, the errors are less than ±2% for most of the major elements – SiO_2 (0.52 - 0.56), MgO (0.43 - 0.89), TiO_2 (0.91 – 1.92), MnO (1.72 – 1.91), CaO (0.45 – 0.75), Al_2O_3 (0.68 – 1.10) and Fe_2O_3 (0.56 – 0.65). K_2O has the highest error range of 11.43 - 120.92±%. Na_2O and P_2O_5 also have a large variable error range of 3.35 - 10.83±% and 4.36 – 15.93±%, respectively. Sample 8 has an anomalously high P_2O_5 at 0.176 wt.% in comparison to the others that are all below 0.12 wt.%. Samples 1, 27, 13, 7 and 6 (in order of increasing MgO wt.%) do follow the negative linear trends for SiO_2 and Na_2O, however they are lower than the main trend cluster. They do not appear to be any higher or lower in the other major elements.

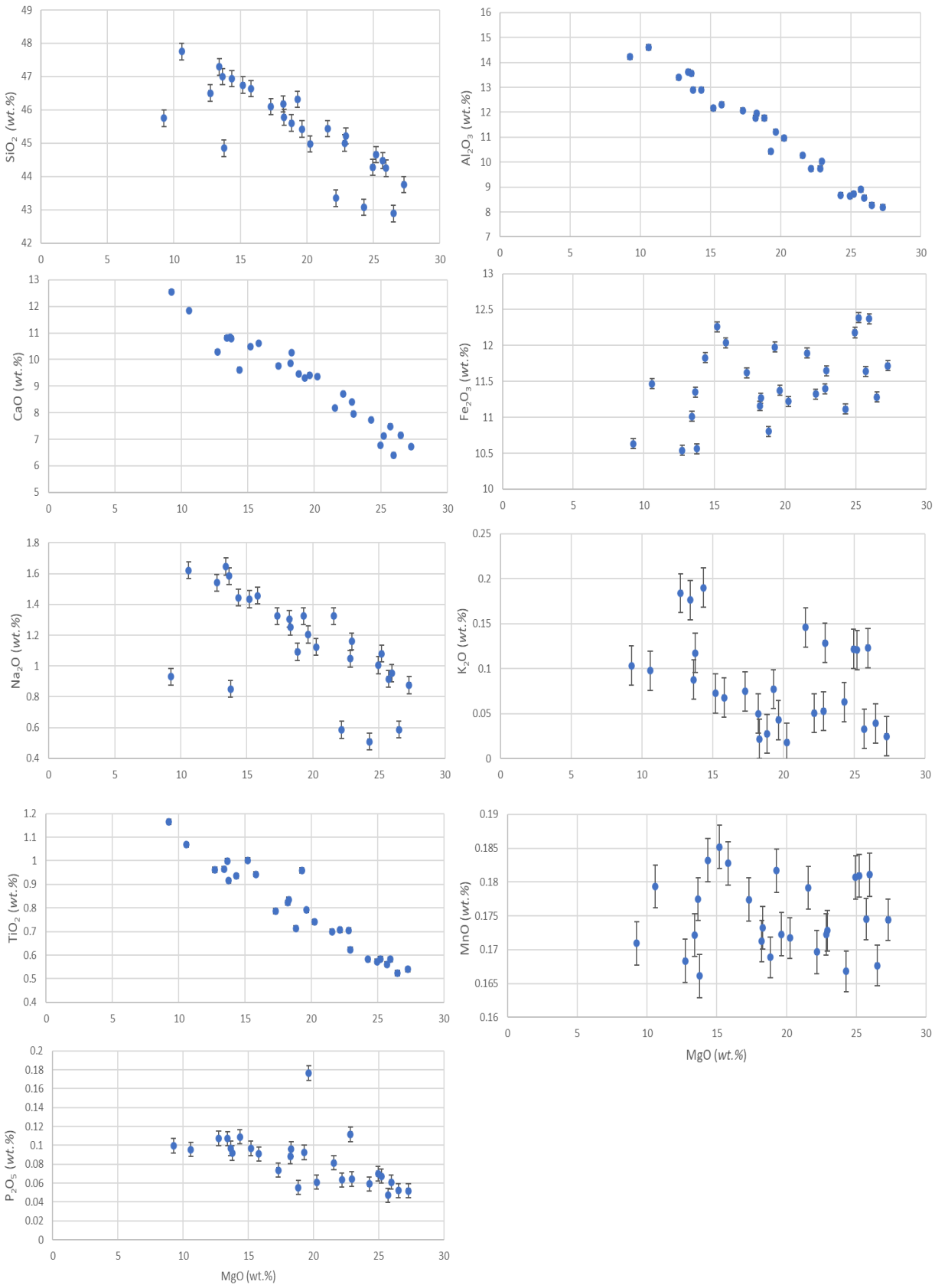

Figure 3.4: Bivariate Harker plots of major elements against MgO. *All x-axes are on the same scale, however all y-axes are on different scales for each element.*

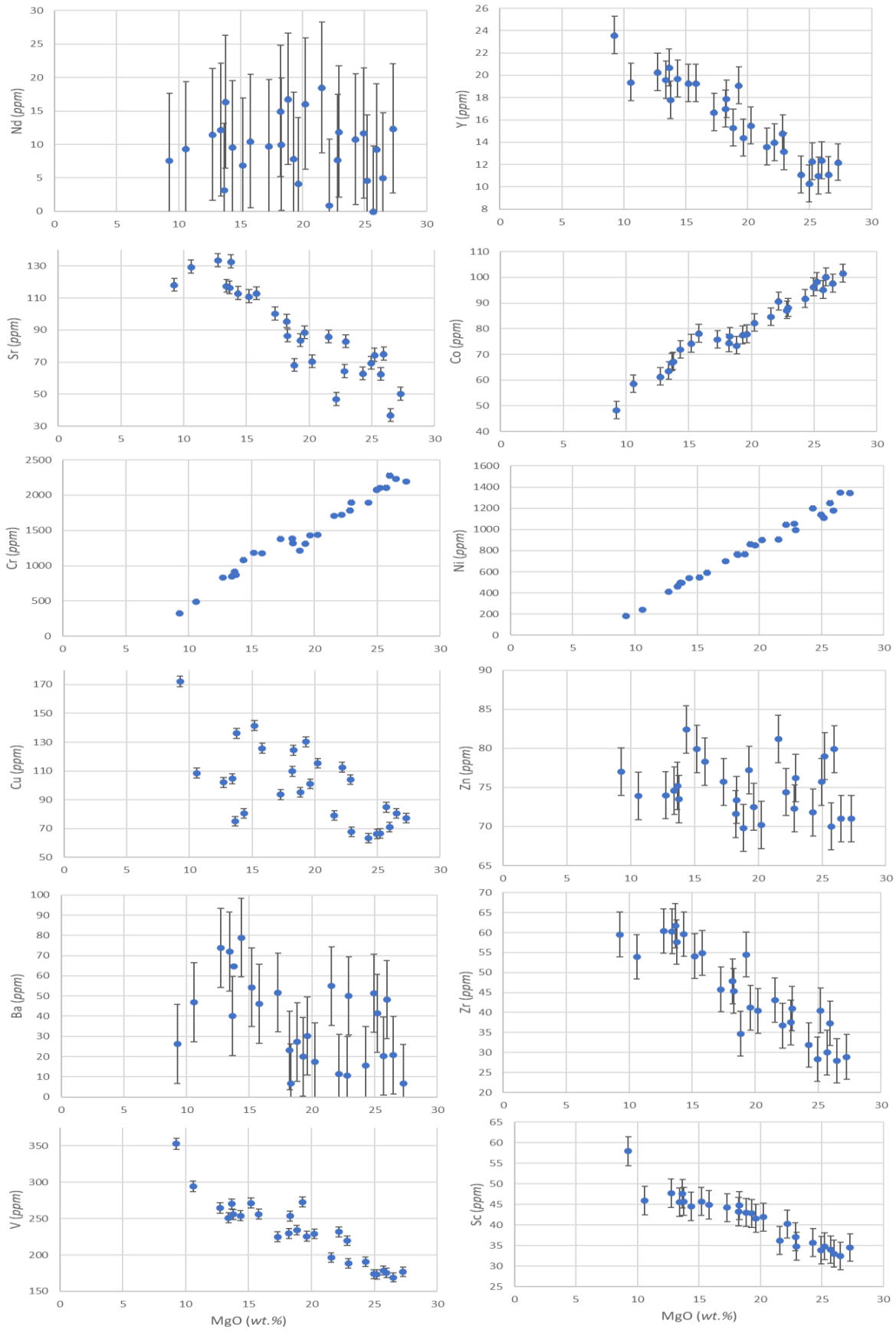

Figure 3.5: Bivariate Harker plots of trace elements against MgO. *All x-axes are on the same scale, however all y-axes are on different scales for each element.*

Plotting the trace elements against MgO wt.% (*Fig. 3.5*), Co (48.4 – 101.7 ppm), Ni (188.6 - 1351.4 ppm) and Cr (330.5 - 2285 ppm) follow a positive linear relationship. Whereas Y (10.3 – 23.6 ppm), Zr (27.9 – 61.7 ppm), V (173 - 353 ppm), Sr (36.9 – 133.6 ppm), Cu (63.3 – 172 ppm) and Sc (32.4 - 57.9 ppm) follow a negative relationship with MgO. Ba (6.7 - 78.9 ppm) and Nd (0 – 16.8 ppm) seem to have a scatter with Zn (69.8 - 82.4 ppm) remaining stable across increasing MgO values. The errors on Ba and Nd are high, sometimes greater than the recorded value such as in sample 15 where Ba and Nd are 10.6 ppm and 7.7 ppm, with respective errors of ±19.36 ppm and ±9.80 ppm. Sample 1 has an anomalously high Cu (172 ppm), V (353 ppm) Y (23.6ppm) and Sc (57.9 ppm).

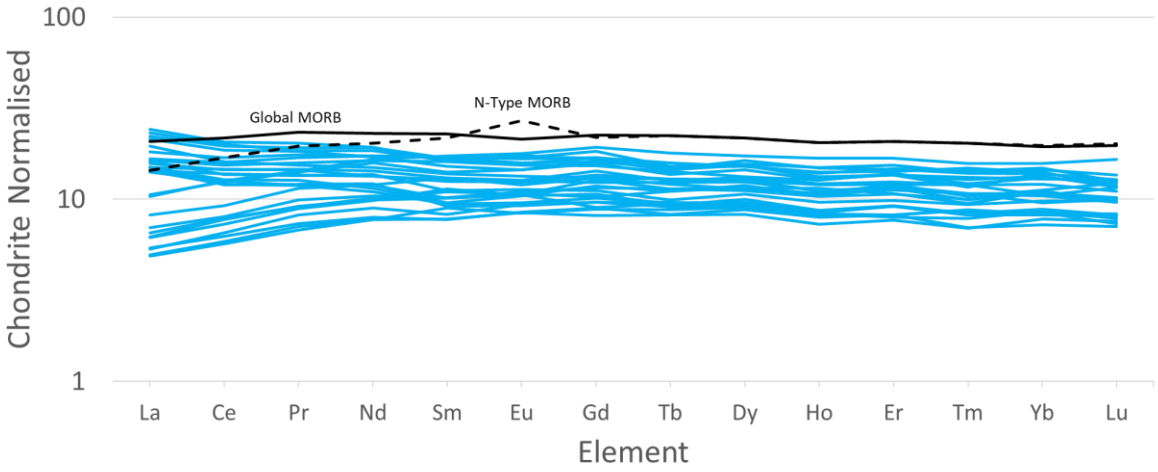

Figure 3.6: REE profile for the whole rock of samples. *The blue lines are the REE profiles of the samples, the solid black line is the Global MORB mean REE profile (White and Klein, 2014) and the dashed black line is the N-Type MORB mean REE profile (White and Klein, 2014). All REE data were normalised to the values of Anders and Grevesse (1989).*

From the REE profiles in *Fig. 3.6*, there are two types of REE profiles apparent - those that increase in LREE's and those that decrease in LREE's. However, as the profiles move into the HREE's no such distinction can be made and the profiles remain stable. It must be noted that the REE profiles are all below the mean Global MORB and mean N-Type MORB for the heavier REE's (White and Klein, 2014).

3.2.2 Classifying E- and N-Type MORB Samples

Previous studies have established N- and E-type MORB's using at least one of three conditions. Using laser ablation, the required data to separate out the samples based on these conditions was obtained. The first condition uses a ratio of K/Ti. If K/Ti is < 0.2 then the sample is considered to be N-Type. If K/Ti > 0.2 then E-Type (Robillard et al., 1992; Maisonneuve, 2012). From *Fig. 3.7*, samples 3, 5, 10, 12, 14, 20, 21 and 26 plot above the 0.2 boundary line, suggesting that they are E-type MORB.

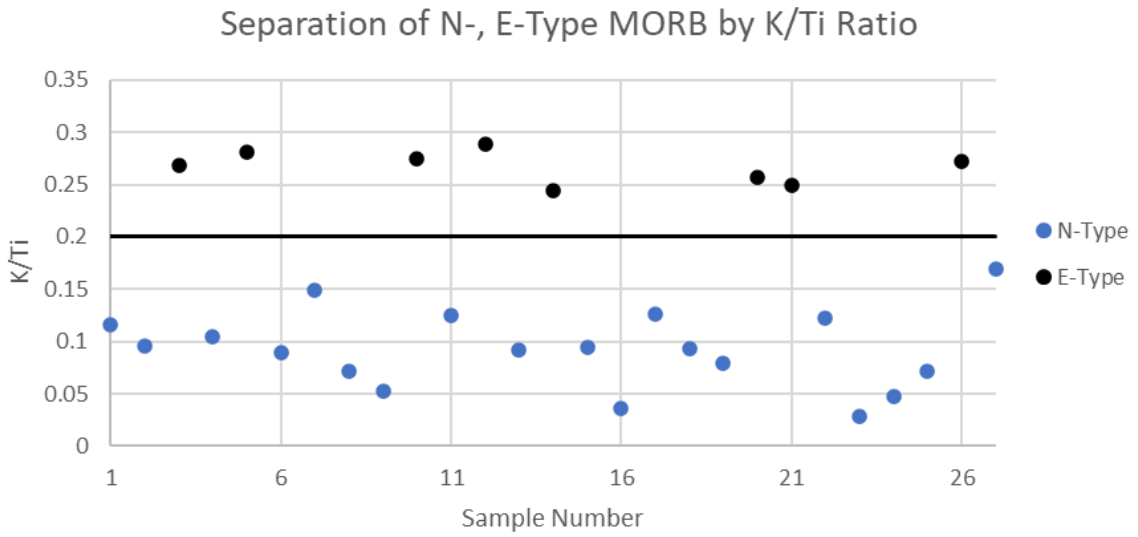

Figure 3.7: Samples separated into N- and E-Type MORB by their K/Ti ratio. *The black line denotes the 0.2 K/Ti boundary where the samples that plot above are E-type (black dots) and the samples below are N-type MORB (blue dots).*

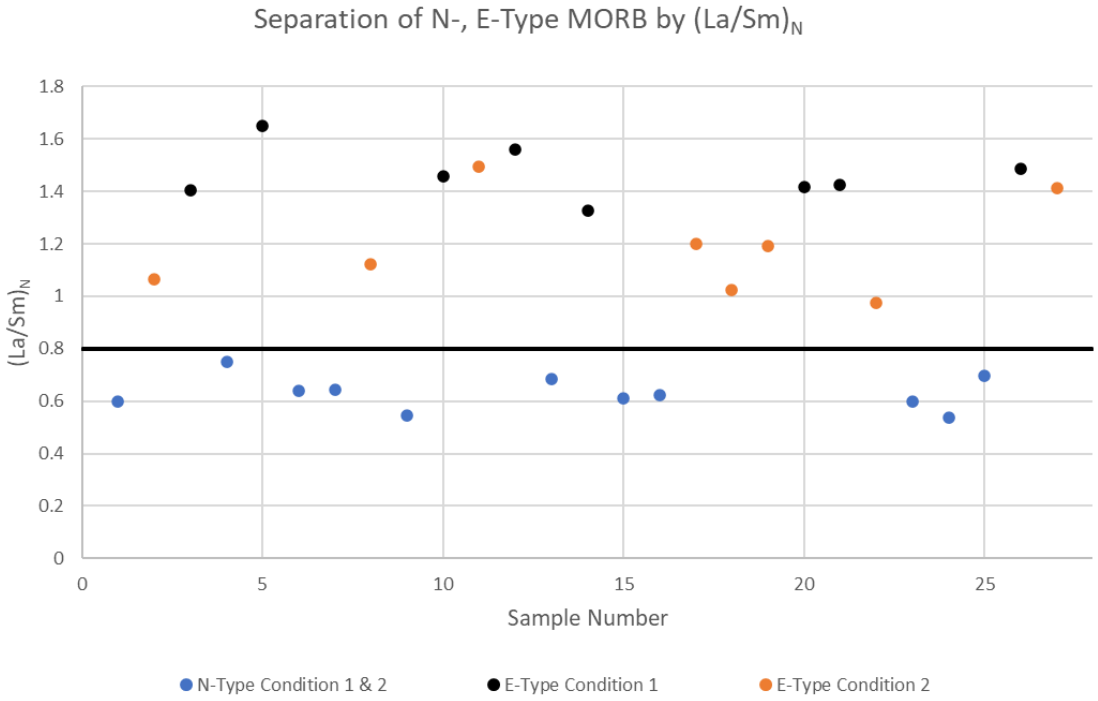

Figure 3.8: Separation of N-, E-Type MORB by $(La/Sm)_N$. *Where blue dots denote samples that are classified as N-type under both conditions, black dots are samples that are E-type in both conditions and the orange dots are samples that are E-type by condition 2. The black line shows the boundary of $(La/Sm)_N$ = 0.8.*

The second condition separates samples along a $(La/Sm)_N$ = 0.8 boundary line. This is to separate samples out based on the enrichment of LREE's (Mahoney et al, 2002; Stuart et al., 2003; Starkey, 2009; Starkey et al., 2009). If a sample was <0.8 then it was considered to be N-type, and if >0.8 then E-Type. From *Fig. 3.8*, the E-Type samples from condition 1 still plot as E-Type. Samples 2, 8, 11, 17, 18, 19, 22, and 27 also plot above the boundary line. Hence suggesting that they may also be E-type MORB. Samples 1, 4, 6, 7, 9, 13, 15, 16, 23, 24 and 25 remain below the boundary line suggesting that they are N-type MORB.

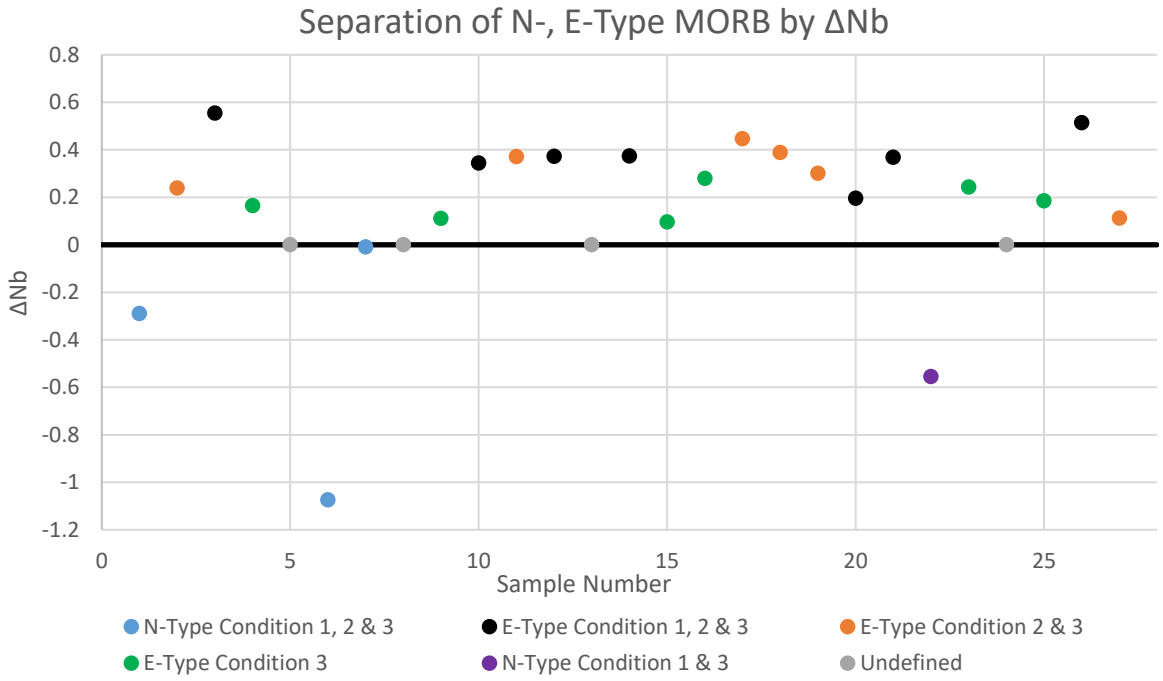

Figure 3.9: Separation of N-, E-Type MORB by ΔNb. *Where blue dots denote samples that are classified as N-type under all conditions, black dots are samples that are E-type in all conditions, the orange dots are samples that are E-type by conditions 2 and 3, the green dots are E-type by condition 3 only, the purple dots are N-type by condition 1 and 3, and the grey dots are samples that have missing data. The black line shows the boundary of ΔNb = 0.*

The third condition of separation trialled was based on ΔNb, where ΔNb=1.74+log(Nb/Y)-1.92[log(Zr/Y)]. If ΔNb>0 then E-Type and if ΔNb<0 then N-Type. This condition was trialled as ΔNb is unperturbed by the effects of variable degrees of mantle melting, source depletion through melt extraction, crustal contamination or alteration from weathering (Fitton et al., 1997; Starkey, 2009). From *Fig 3.*9, samples 1, 6 and 7 remain below the separation line of ΔNb < 0, hence are N-type MORB. Samples 5, 8, 13 and 24 had no Nb data measured by XRF, therefore they are undefined.

3.2.3 Contamination of Samples

Contamination of the samples by mantle metasomatism was looked into. To determine if any sample underwent metasomatism, the conditions set out by Willhite et al. (2019) were followed. Samples were separated out by Nb/Th > 13, Ce/Pb > 20 and MgO > 10 wt.%. Anything below this was considered to have been altered by mantle metasomatism. In *Fig. 3.10*, every sample fails at least one of these conditions, suggesting all samples may have been altered.

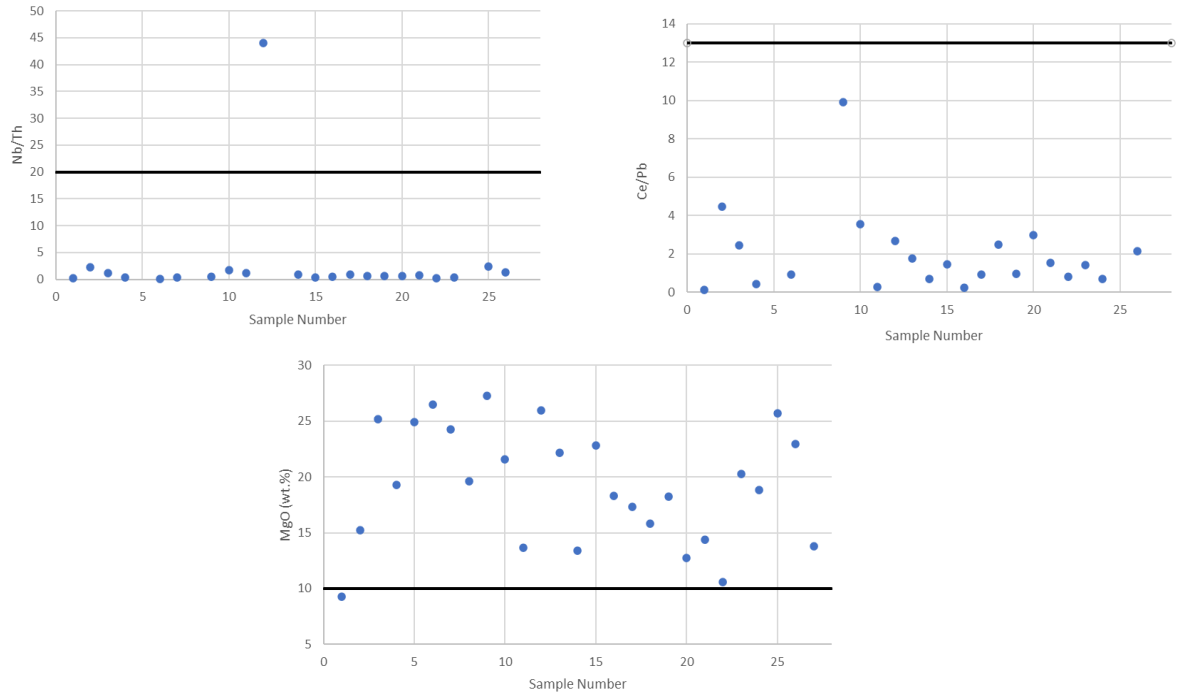

Figure 3.10: Conditions of metasomatism as set out by Whillhite et al. (2019). *The black lines are the boundary lines of Nb/Th = 13, Ce/Pb = 20 and MgO = 10 wt.%, anything below these lines is considered to have been contaminated by metasomatism.*

3.3 Thin Sections

3.3.1 Mineralogy

Using an SEM and optical microscope, images of each sample were taken so as to determine and investigate their mineralogy – a full catalogue of these images can be seen in Appendices IV, V, VI and VII. In *Fig 3.11*, a cross polarised image of samples 10 (*Fig. 3.11A*) and 16 (*Fig. 3.11B*) can be seen. These samples have been picked out as in hand specimen 16 looked like a pillow lava and 10 looked sub-aerial. In these images, there are large phenocrysts of olivine that are ≥1mm in diameter, as well as smaller plagioclase feldspars and clinopyroxenes. The groundmass in sample 10 is larger than that in sample 16. This is suggestive of a faster cooling period for sample 16 in comparison to sample 10.

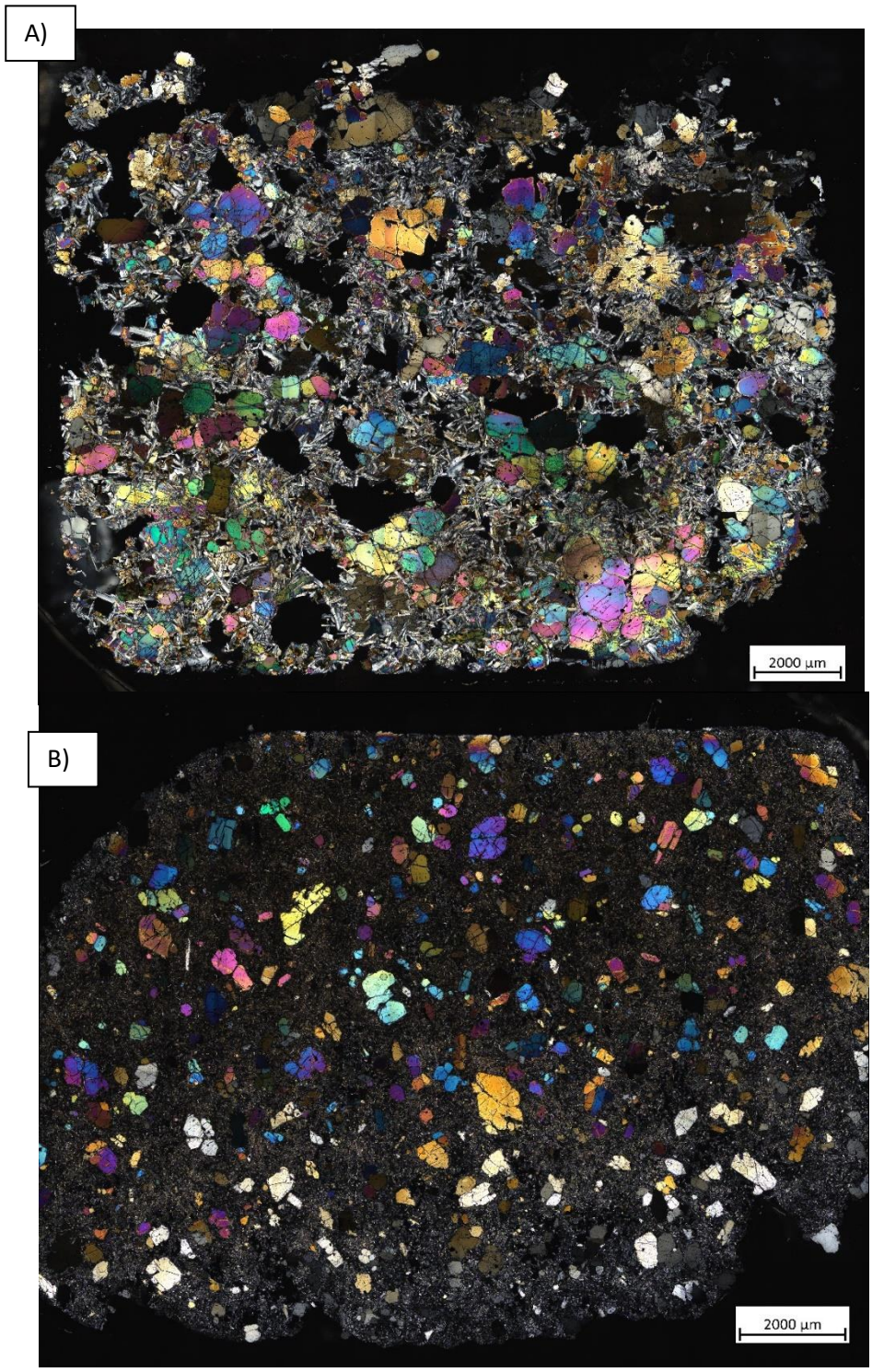

Figure 3.11: Cross polarised light images of samples 10 and 16. *Where A) is sample 10 and B) is sample 16.*

Using QESCAM, the individual minerals are able to be picked out more clearly and can be used to determine the mineral percentage of the sample. Only samples 2, 10, 14, 16 and 19 were chosen for QESCAM and subsequent EMPA and LA-ICP-MS – all QESCAM images can be found in Appendix III. These samples were chosen according to the size of their olivine minerals,

structures within the olivine crystals (i.e. kink bands) and the size of glassy melt inclusions. From the QESCAM in *Fig 3.12A*, sample 10 is approximately 38% olivine, 36% plagioclase feldspar, 18% pyroxene and 7% glass. Whereas sample 16 (*Fig 3.12B*) is 28% olivine, 26% plagioclase feldspar, 18% pyroxene and 27% glass. Trace elements ilmenite, apatite and chromium-spinel made up the rest of the 1% in both samples.

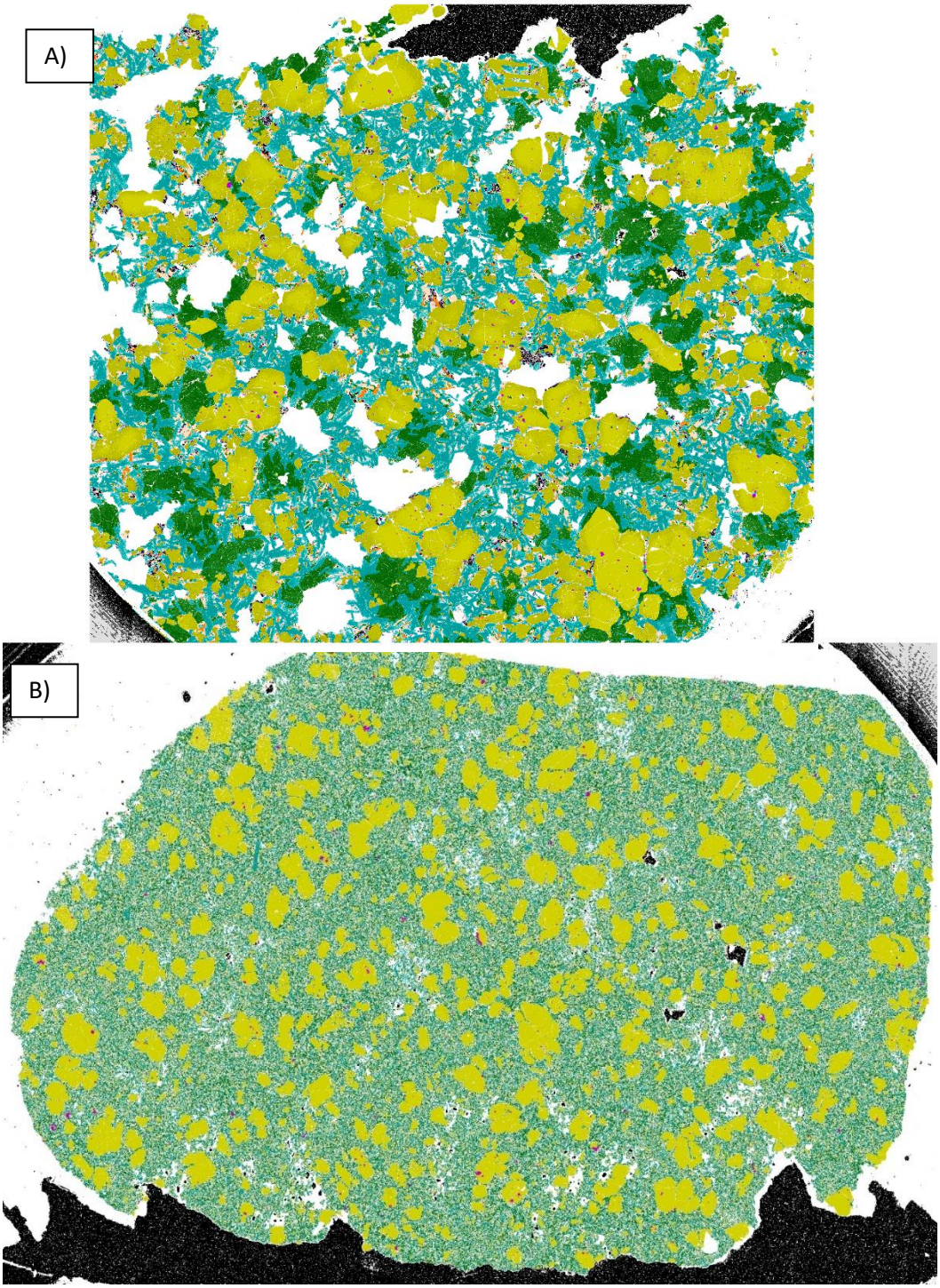

Figure 3.12: QEMSCAN of samples 10 and 16. *Where sample 10 is A) and sample 16 is B). The yellow-green colours denote olivines, dark green denotes pyroxenes, blue denotes plagioclase and beige is glass.*

3.3.2 Plagioclase Feldspar Classification

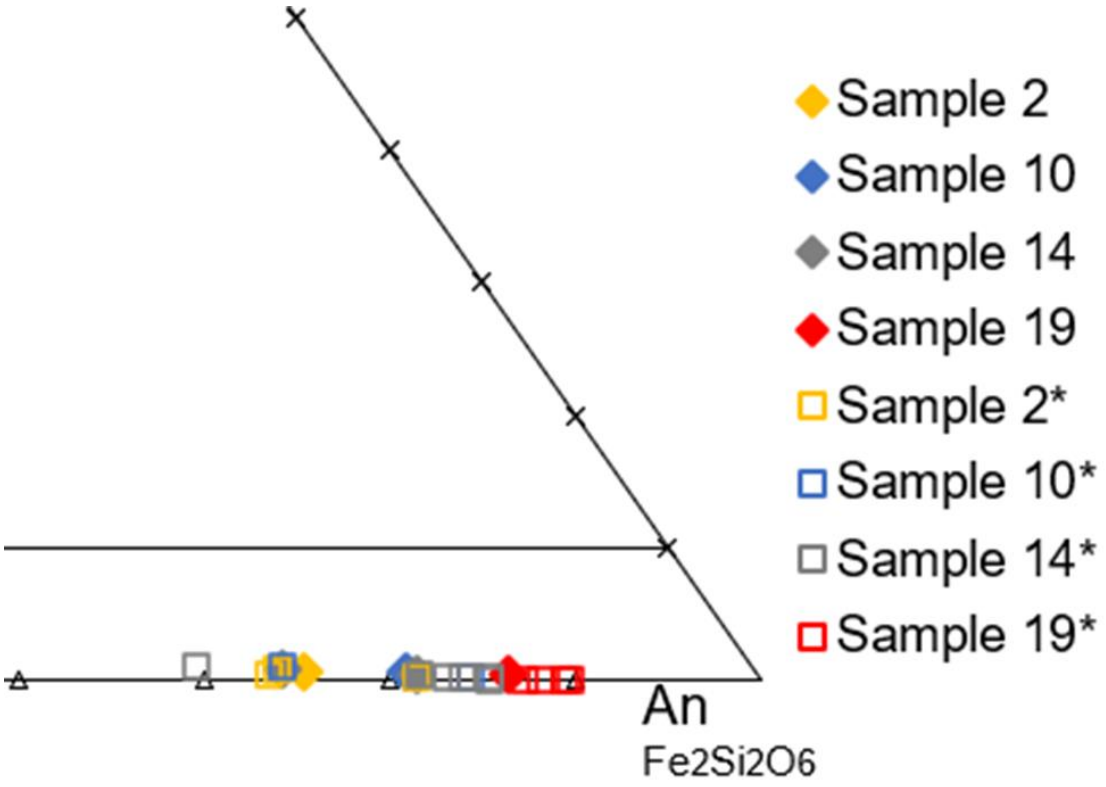

Figure 3.13: Plagioclase Feldspar classification. *Plot of plagioclase feldspars analysed where the quadrangles are feldspars that have a total wt.% between 98.5-101.5% and the open squares are feldspars that are 97.5-102.5 wt.%.*

In *Fig 3.13*, the plagioclase feldspars in sample 2 and one from sample 14 plot within the Labradorite classification. The plagioclase in sample 10, 19 and the other from sample 14 plot within the Bytownite classification. Only 5 plagioclase samples have a total wt.% between 98.5-101.5%. Data out with this range would have been excluded because low or high data may indicate a mixed mineralogical signal, or that a crack or surface topography was hit during analysis. However, to get a greater population size the accepted total wt.% range was increased to 97.5%-102.5% - this can be seen from the asterixed sample names in the legend of *Fig 3.13*. These plot similarly to the 98.5-101.5% plagioclase samples. Plagioclase feldspars were analysed in sample 16, however these fell out with both the accepted and extended wt.% ranges.

3.3.3 Pyroxene classification

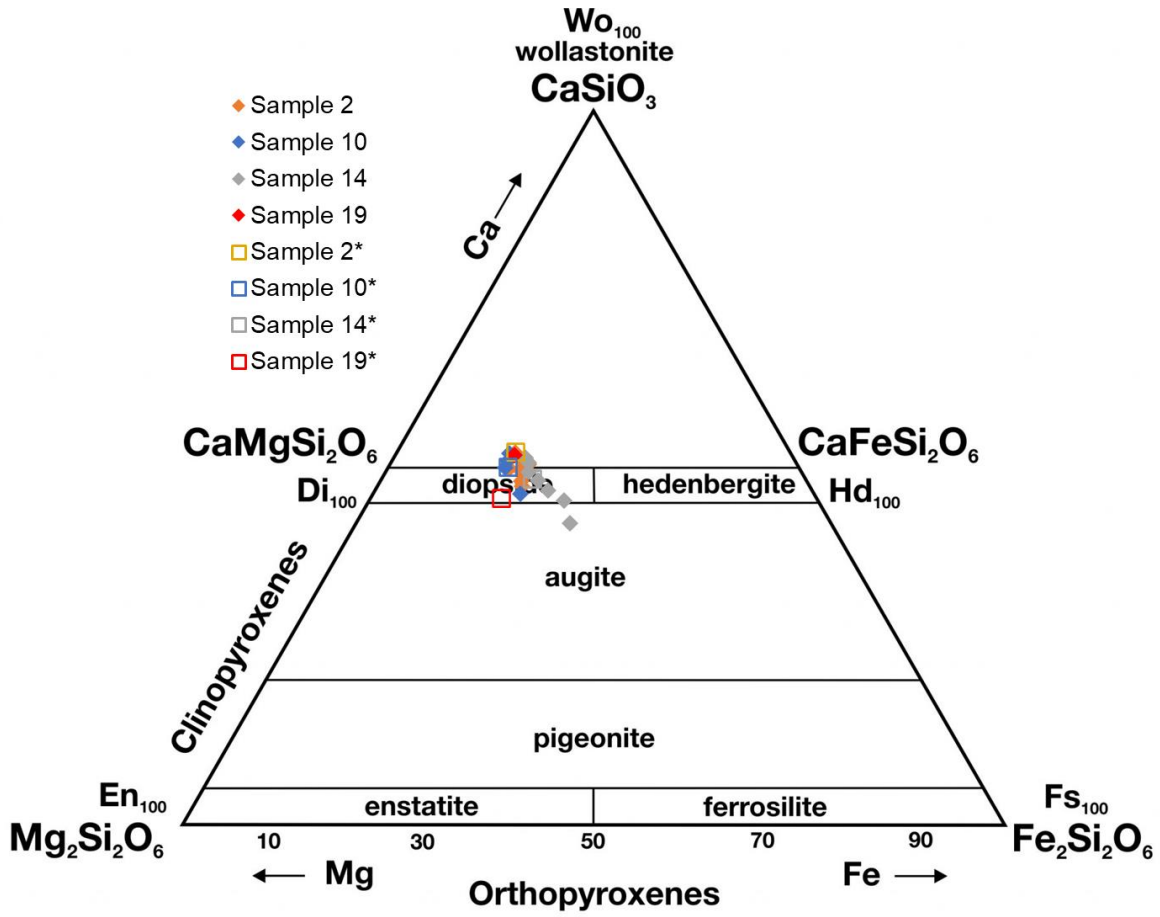

Figure 3.14: Pyroxene classification. *Plot of pyroxenes analysed where the quadrangles are pyroxenes that have a total wt.% between 98.5-101.5% and the open squares are pyroxenes that are 97.5-102.5 wt.%.*

From *Fig. 3.14*, pyroxenes plot towards the higher end of the clinopyroxene Ca spectrum. All pyroxenes appear to be classified as diopside, with the exception of one in sample 14 which is augite. Some pyroxenes have a Ca >50%, which is unable to happen. This may be due to the associated errors, or a non-optimal standard was used for Ca during EMPA analysis which has increased the Ca content for all pyroxenes. Similarly with the plagioclase feldspars, in order to create a larger population size, the wt.% range was increased from 98.5-101.5% to 97.5-102.5%. The added pyroxenes show no difference in comparison and are also classified as diopside pyroxenes.

3.3.4 Olivines

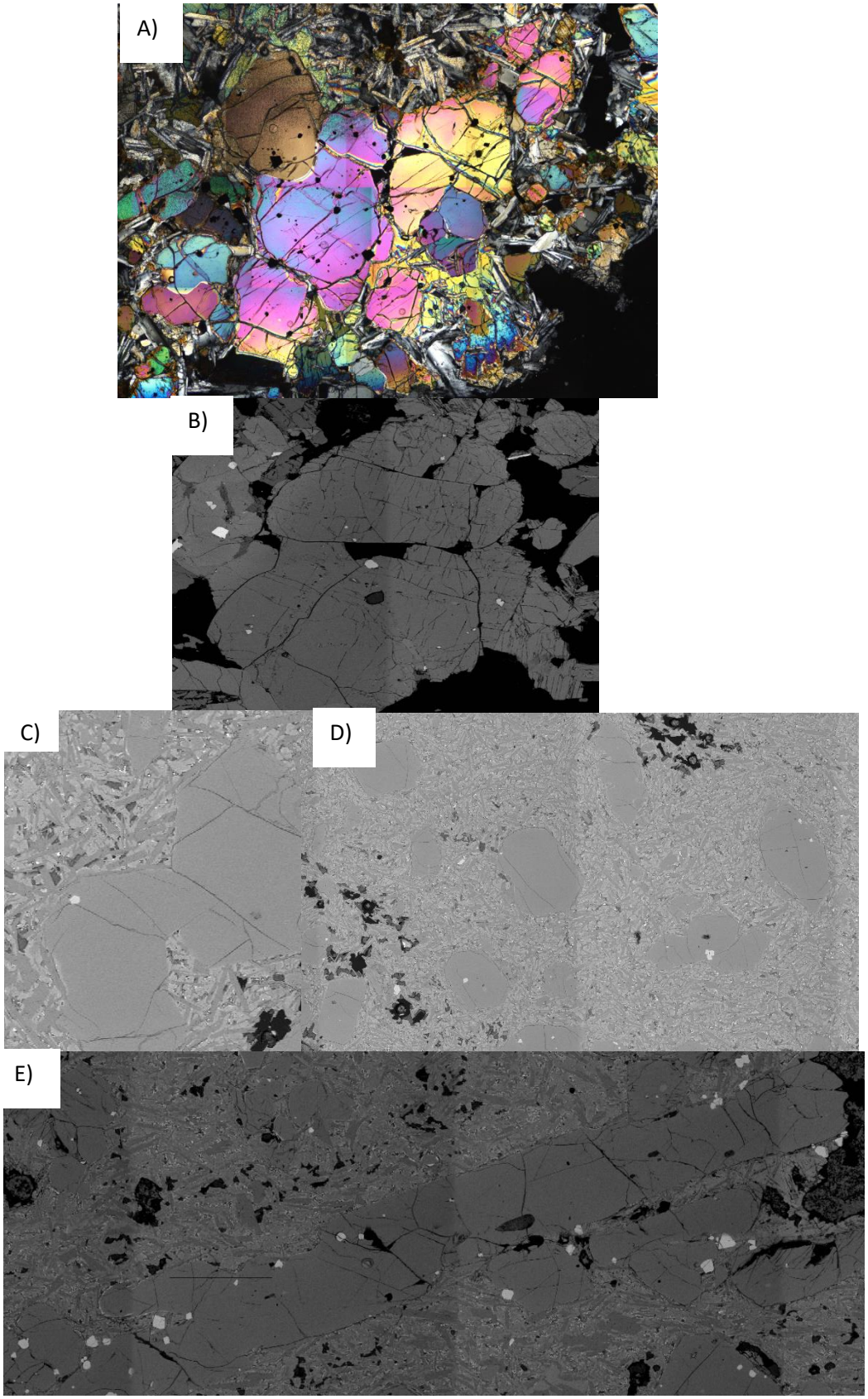

Figure 3.15: Morphology of olivines in analysed samples. *A is an olivine glomerocryst, B is an olivine that exhibits kink banding, C is an embayed olivine, D shows the equant and euhedral*

to sub-euhedral olivines that were common in sample 16 and E is a needle like olivine which were common in sample 19.

Fig 3.15, shows the range of morphologies and textures that were found within the olivines of the analysed samples. Olivines are commonly equant and sub-euhedral to euhedral, however needle like olivines were also common in some samples, e.g. 19. Embayed olivines were also common, as too were glomerocrysts. Olivines varied in size from 0.1mm to >2mm. For EMPA, the largest olivines in the analysed samples were chosen for transects and the smaller ones for spot analysis. It can be seen across all olivines in *Fig 3.15*, that chromites are very common and are in a variety of shapes from rounded to squares. Where possible, these chromites were avoided when conducting transects.

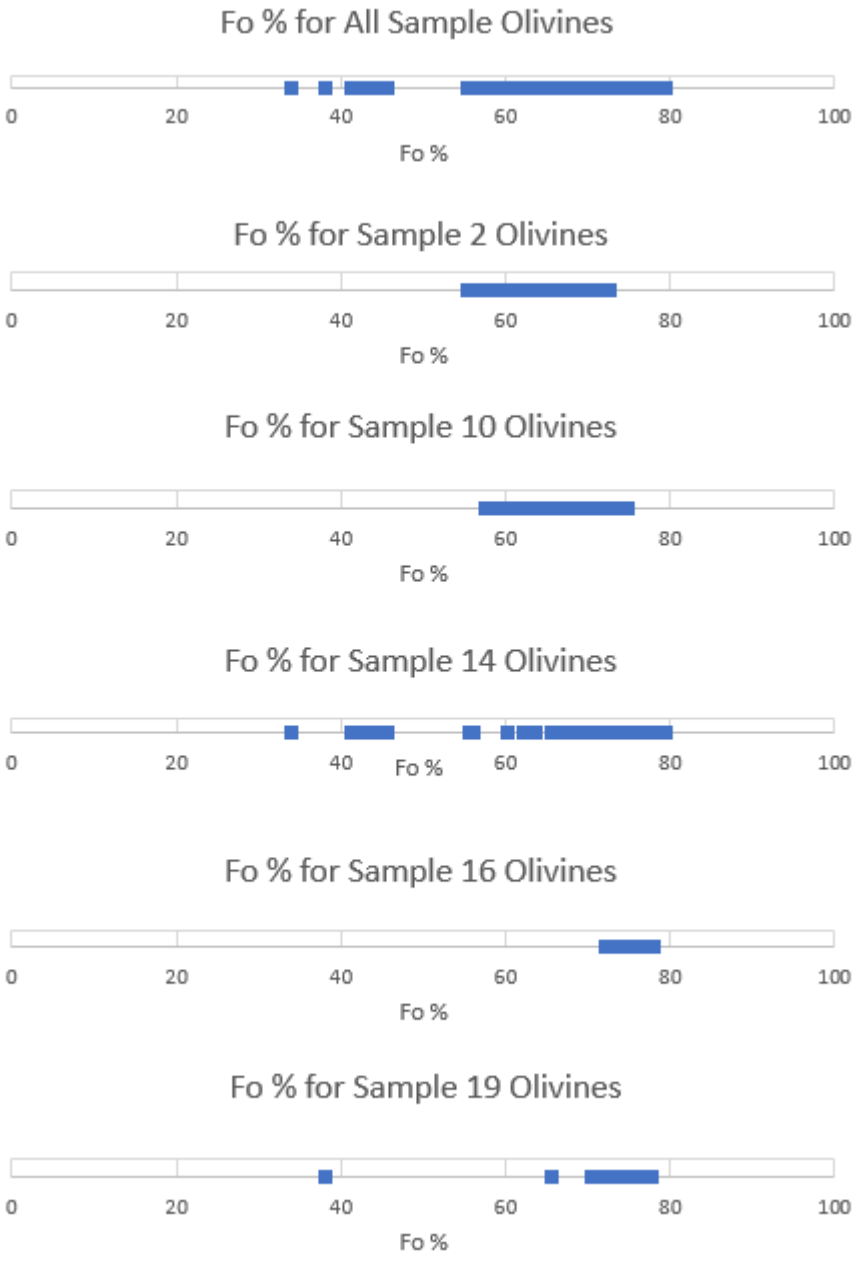

Figure 3.16: Forsterite % of olivines by sample. *The first graph shows the collated Fo% of all olivines from the 5 samples, with the subsequent graphs being the Fo% of the olivines in that*

sample. Graphs are a combination of both transects and spot analysis – spot analysis was done on the cores and rims of olivines.

From *Fig 3.16*, the full range of Fo% on the analysed samples is Fo_{34} to Fo_{79}. The cores of samples 2 and 10 have a higher Fo% by ~20% in comparison to the rims at Fo_{75} compared to Fo_{55}. In samples 16 and 19, the cores and rim are only ~10 Fo% different, Fo_{72} to Fo_{78}. However, in sample 19, the rim spot analysis gives outliers of Fo_{38} and Fo_{67}. In sample 14, the largest range of Fo % can be seen at Fo_{34} to Fo_{79}. The average Fo% is Fo_{71}, with a standard deviation of 5.78 and standard error of 0.25. Overall, the cores of the samples are all of a similar range with none being more forsteritic than the others.

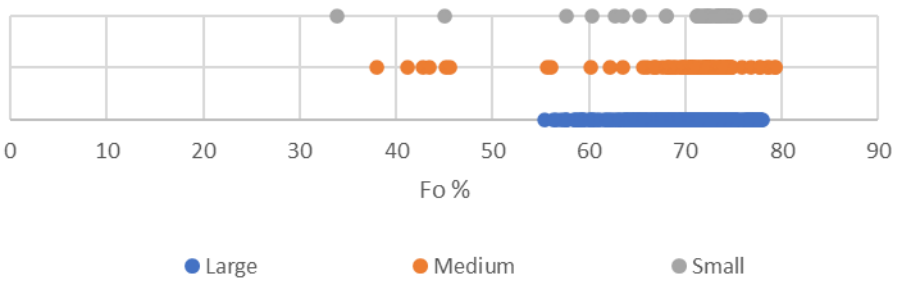

Figure 3.17: Forsterite % of Olivine with the separation based on their size. *Small olivines are <0.25mm, medium are 0.25-1mm and large olivines are >1mm.*

Olivines were split into different population sizes, where the olivines are considered large if greater than 1mm; medium if between 0.25 - 1mm and small of less than 0.25mm. Size separation values were arbitrarily chosen. This was done to investigate whether later formed olivines (smaller olivines) are any different to earlier formed olivines (larger olivines). From *Fig 3.17*, there is no difference between Fo% based on size. The cores of the olivines tend to be between 70-80%, and the rims generally start at 55%, although the small and medium sized olivines have the outlier rims ranging from 34-45%.

From *Fig. 3.18*, there is a positive relationship between Fo% and NiO in all samples. Whilst there is also a positive relationship between Cr_2O_3 and NiO, this relationship is weaker than Fo% and NiO. The low cluster of NiO, Cr_2O_3 and Fo% relates to these analysed points being on the rims of low magnesium olivines rather than being attributed to only sample 14. CaO against Cr_2O_3 remains stable and constant, but with there being more spread and scatter for samples 2 and 10. All the analysed olivines, regardless of sample, follow the same continuous trends, suggesting that they may be linked in some way. The Cr_2O_3 outlier at 0.246 wt.% may be due to hitting a chromite inclusion during the transect.

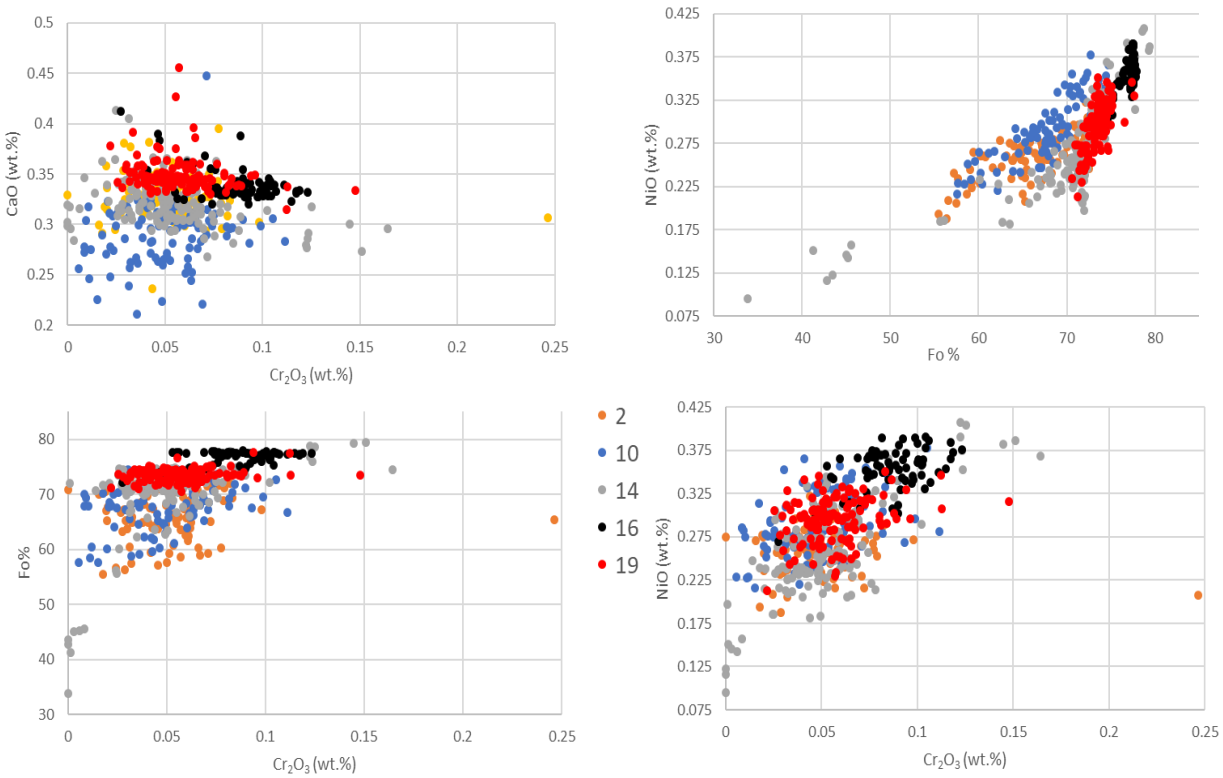

Figure 3.18: Comparison of oxides based on samples. *Where the orange dots are sample 2, blue are sample 10, grey are sample 14, black are sample 16 and red are sample 19.*

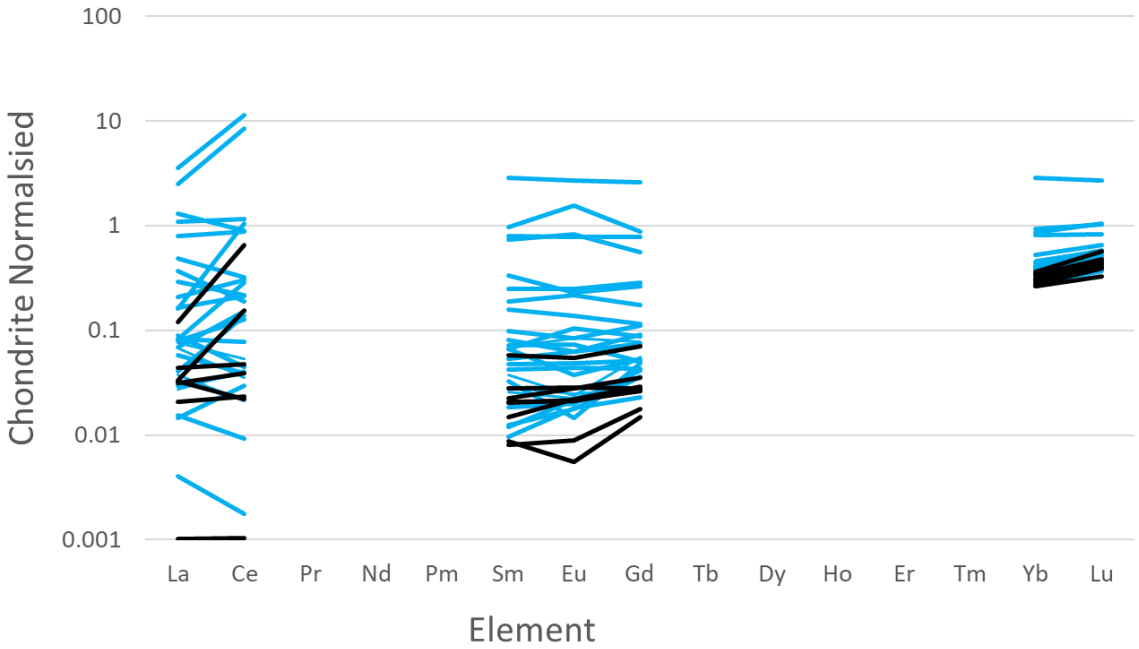

Figure 3.19: REE profiles of olivine cores from a 100µm laser spot size. *The blue lines are olivines from the E-type MORB samples 2, 10, 14 and 19. The black lines are olivines from the N-type MORB sample 16. REE's were normalised to the values of Anders and Grevesse (1989).*

In *Fig. 3.19*, the olivines from sample 16 – an N-type MORB sample – generally have a lower REE profile of MREE's (middle rare earth elements) in comparison to the other olivines. However, for LREE's and HREE's there is no distinct difference. One could argue that there is a difference for HREE's, however the REE profile lines for sample 16 olivines overprint the ones for olivines from E-type MORB samples. Overall, no discernible pattern can be made in relation to LREE's and MREE's. However, for HREE's olivines either have an increasing trend or remain stable.

The full geochemical suite of data for the analysed olivines (cores only), plagioclase feldspars and pyroxenes can be found in Appendix II.

Table 3.2: Summary classification of the minerals in analysed samples. *The E- and N-type classification comes from their bulk rock chemistry.*

Sample	Fo. % range of Olivines	Plagioclase Classification	Pyroxene Classification	N- or E- Type MORB
2	Fo_{55-73}	Labradorite	Diopside	**N**
10	Fo_{58-75}	Bytownite	Diopside	**E**
14	Fo_{34-79}	Labradorite - Bytownite	Augite - Diopside	**E**
16	Fo_{72-78}	Bytownite	Diopside	**N**
19	Fo_{38-78}	Bytownite	Diopside	**E**

Chapter 4: Discussion and Conclusions

4.1 Bulk Rock Geochemistry

The incompatible behaviour of SiO_2, CaO, Al_2O_3 and Na_2O against MgO in *Fig 3.4* is expected. As the highly magnesian olivines fractionate out of the melt first, you would then expect higher levels of SiO_2, CaO, Al_2O_3 and Na_2O with associated lower levels of MgO before pyroxene and plagioclase feldspar fractionate out of the melt. You would also expect Fe_2O_3 to be incompatible rather than a scatter pattern as the olivines become less MgO rich and more Fe_2O_3 rich. However, the bulk rock geochemistry follows that found within other studies. The negative linear regression, in relation to MgO, with SiO_2, CaO, Al_2O_3 and Na_2O follows the same trend as previously published data. Similarly, the scatter pattern in MnO and K_2O, as observed in *Fig 3.4*, was also seen in previously published data (Francis, 1985; Robillard et al., 1992; Holm et al., 1993; Larsen and Pedersen, 2000; Yaxley et al., 2004; Starkey, 2009; Starkey et al., 2009).
These bulk rock trends have been associated with a liquid line of descent due to olivine phenocrysts driving the bulk composition along or near to an olivine control line. It's been proposed that should the lavas have accumulated olivine, and the linear trends represent olivine addition lines, then they can be projected back to the cumulus olivine composition (Krishnamurthy and Cox, 1977). Starkey (2009) believes this to be meaningless to find though. This is due to the lavas coming from different locations, so are likely to have their own local plumbing systems which may have slightly different compositions. However, the expected olivine cumulus composition will be highly forsteritic due to the high magnesium content.
In regard to trace elements, Ni and Cr have a positive linear relationship with MgO in this study as it does in other studies. This compatible behaviour is expected, as similarly to MgO, Cr and Ni fractionate out of the melt early and thus become depleted in the melt. The negative relationship of V, Sc, Y, Cu, Sr and Zr with MgO concurs with that found in previous studies (Holm et al., 1993; Yaxley et al., 2004; Starkey, 2009).

The REE profiles of the samples analysed in this study follow a similar trend as those in previous studies – *Fig. 3.6* (Robillard et al., 1992; Yaxley et al., 2004; Starkey, 2009). These REE profiles have two distinct groups in the LREE's – which can be shown by splitting the samples into E- type MORB and N- type MORB. Furthermore, the HREE concentrations are considered depleted when compared to the global MORB (White and Klein, 2014). Starkey (2009) proposes that this could be due to deep melting of the picrites under thick lithosphere.

To determine the relative pressure of melting for different tectonic settings, Jackson and Dasgupta (2008) used the Na_2O/TiO_2 ratio. They showed that Iceland has a ratio of ~1.56 and Hawaii a ratio of ~0.96. These ratios represent a higher pressure of melting under thick lithosphere compared to MORB, which ranges from ~1.82 to 1.87 (Su, 2003). Starkey (2009) showed that when accounting for all published data on samples from Baffin Island and West Greenland, they have a Na_2O/TiO_2 ratio of ~1.45 and ~1.17, with a standard deviation of σ = 0.33 and σ = 0.22, respectively. For the samples in this study, the Na_2O/TiO_2 ratio is ~1.48 (σ

= 0.31), which is similar to the previously published data for Baffin Island. Therefore, as Starkey (2009) concluded, Baffin Island and West Greenland have higher average pressures of melting in comparison to Iceland and MORB, which shows the magmas erupted through thick lithosphere.

As the lavas erupted through thick lithosphere, there is the potential for crustal contamination to occur. If crustal contamination were to occur, it may account for the enriched nature of LREE's in some of the samples. However, crustal contamination has been ruled out by various studies (Robillard et al., 1992; Kent et al., 2004; Starkey et al., 2009; Starkey, 2009; Maisonneuve, 2012). Kent et al. (2004) argue that the lavas are the product of mixing from at least two different components. They showed that $\delta^{18}O$ of olivine phenocrysts in E-type lavas are lower than those in N-type lavas, which is conflicting with crustal contamination. Furthermore, Maisonneuve (2012), modelled a granitic contaminant to N-type bulk rock composition to simulate E-type melt inclusion K/Ti ratios. They found that 10% assimilation of granite and 5% crystallisation can produce K/Ti ratios in only the least enriched E-type melt inclusions but not the majority of E-type inclusions. Also, the Al content was unrealistically high, hence concluded that crustal contamination by granitic crust was not a source of enrichment.

In this study, metasomatism was looked at by following the method set out by Willhite et al. (2019). In this method, samples are separated out by Ce/Pb > 20, Th/Nb > 13 and MgO > 10 wt.%, where anything below these thresholds was considered to have been altered by mantle metasomatism. In *Fig. 3.10*, it was shown that all samples failed at least one of these conditions, hence all samples are considered to have been contaminated by mantle metasomatism. However, only one sample measured greater than it's associated error for Ce, likewise for Pb on a different sample and only three samples for Th. Furthermore, some samples are missing data either by it being below detection limits or non-existent – for example samples 5 and 8 have no Nb, Th and Pb measured and sample 27 has no data for Ce, Pb and Th. Therefore, due to the high uncertainty in errors associated with these elements from the collected XRF data, as well as missing data for some samples, the conclusion that all samples experienced mantle metasomatism should be rejected in this particular case. To fully investigate contamination by mantle metasomatism, it's suggested that more accurate and precise data collection should be undertaken – for example by LA-ICP-MS.

4.2 N- and E- Type MORB Classification

Table 4.1: E- and N-Type MORB separation for bulk rock of each sample based on the conditions of K/Ti > 0.2 and $(La/Sm)_N$ > 0.8.

Sample	K/Ti > 0.2	$(La/Sm)_N$ > 0.8	Final Classification
1	**N**	**N**	**N**
2	**N**	**E**	**N/E**

3	**E**	**E**	**E**
4	**N**	**N**	**N**
5	**E**	**E**	**E**
6	**N**	**N**	**N**
7	**N**	**N**	**N**
8	**N**	**E**	**N/E**
9	**N**	**N**	**N**
10	**E**	**E**	**E**
11	**N**	**E**	**N/E**
12	**E**	**E**	**E**
13	**N**	**N**	**N**
14	**E**	**E**	**E**
15	**N**	**N**	**N**
16	**N**	**N**	**N**
17	**N**	**E**	**N/E**
18	**N**	**E**	**N/E**
19	**N**	**E**	**N/E**
20	**E**	**E**	**E**
21	**E**	**E**	**E**
22	**N**	**E**	**N/E**
23	**N**	**N**	**E**
24	**N**	**N**	**N**
25	**N**	**N**	**N**
26	**E**	**E**	**E**
27	**N**	**E**	**N/E**

For the final classification of samples into E- and N-type MORB, the third condition, ΔNb, was discounted due to missing Nb data for some of the samples. Also, the error on Nb was larger than the Nb value recorded for some samples - e.g. for sample 1 and 4, Nb is 1.3ppm and 3.8ppm, however both have an error of 4.1ppm. For future reference, Nb should be measured via LA-ICP-MS for more precision and accuracy rather than XRF.

Using the conditions of K/Ti and $(La/Sm)_N$ from *Table 4.1*, samples 1, 4, 6, 7, 9, 13, 15, 16, 24 and 25 are N-type MORB's. Also from *Table* 41, samples 3, 5, 10, 12, 14, 20, 21, 23 and 26 are E-type MORB's. The other samples (2, 8, 11, 17, 18, 19, 22 and 27) fail one of the two conditions. *Fig. 4.1* shows the variation of the sample suite where there are clear separations about $(La/Sm)_N = 0.8$ and K/Ti = 0.2.

The N-type MORB samples are the most interesting ones as it is likely that they sampled a depleted primitive mantle reservoir as part of their source (Stuart et al., 2003; Starkey, 2009; Starkey et al., 2009; Riso et al., 2016; Jackson et al., 2017). Therefore, it is these samples that should be investigated further.

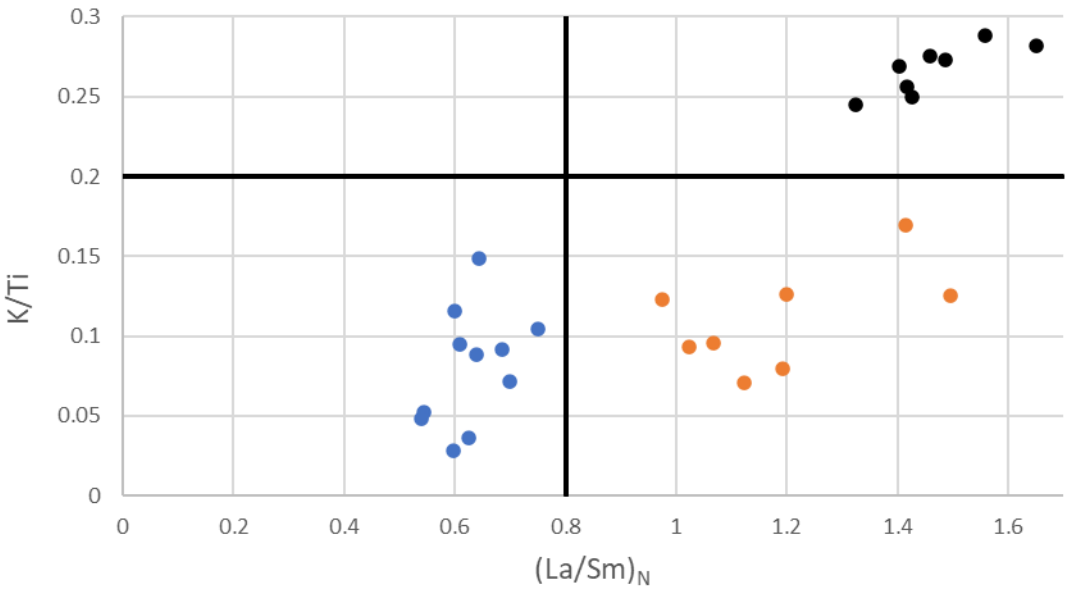

Figure 4.1: Variation of sample suite based on the two accepted conditions K/Ti and $(La/Sm)_N$. *Samples that satisfy both K/Ti and $(La/Sm)_N$ are in blue for N-type MORB's and black for E-type MORBS. The orange dots are the samples that satisfy only one of the conditions. The solid black lines are K/Ti = 0.2 and $(La/Sm)_N$ = 0.8.*

4.3 Olivine Geochemistry

In previous studies, the highest recorded forsterite was Fo_{93}, with a typical range of Fo_{74} to Fo_{93} (Francis, 1985; Larsen and Pedersen, 2000; Starkey, 2009; Maisonneuve, 2012). However, the olivines analysed in this study have a high of only Fo_{79}, with a range of Fo_{34} to Fo_{79}. There are a number of plausible reasons as to the different ranges. It could be that the most magnesian rich olivines weren't analysed, or that the EMPA calibration was off and the incorrect standards were used. A further reason could be that the olives themselves were altered from weathering, even though during sample preparation the thin section was chosen from the freshest and most internal part of the rock specimen to combat against this. Another reason could be due to analysing a 2D surface from a 3D shape, wherein the supposed analysed 'cores' are actually the core of the rim and not the very centre of the olivines themselves. Possible ways to check these reasons would be to re-do the EMPA using different standard materials and also analyse the olivines as separates – i.e. grain mount the individual olivines.

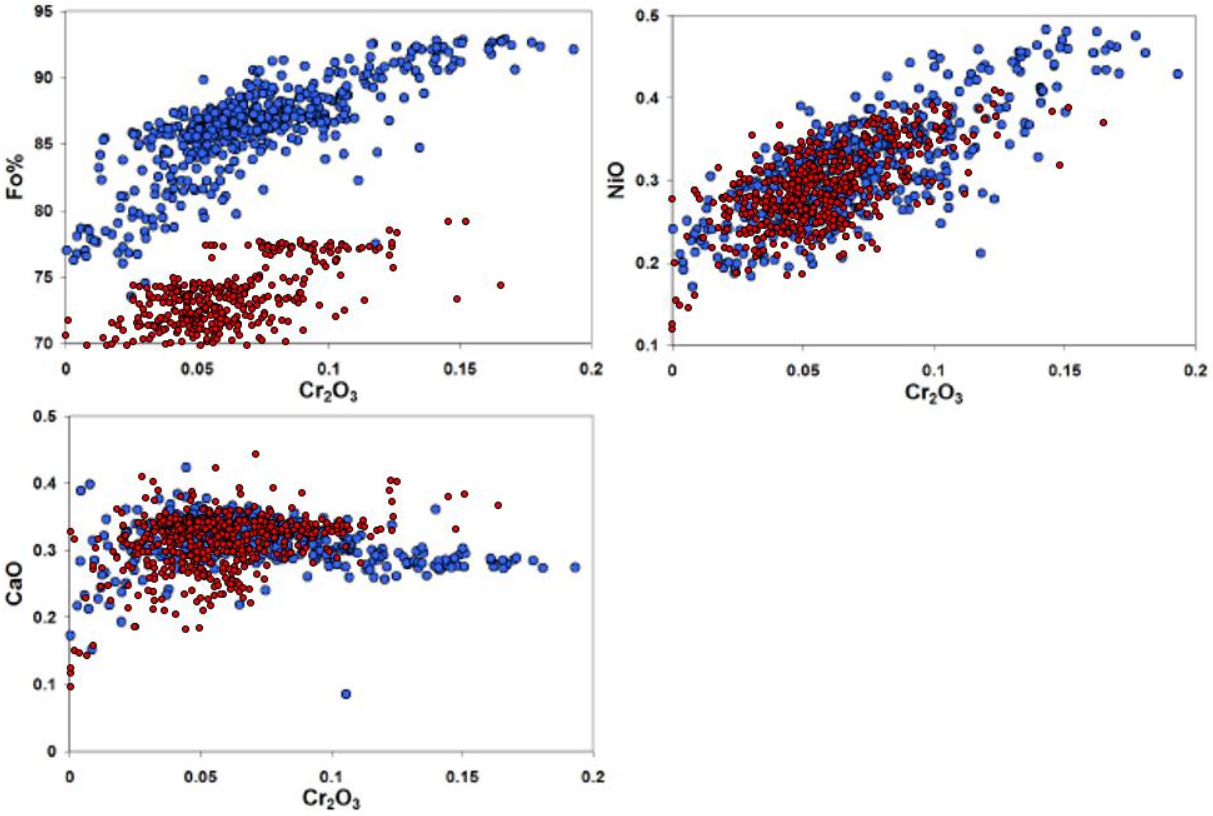

Figure 4.2: Comparison of previously published data against data in this study. *Data from this study is in red, with previously published data in blue (Starkey, 2009).*

From *Fig 4.2*, it's clear that for the comparison of CaO and NiO, against Cr_2O_3, both datasets are similar. Both datasets have a continuous positive relationship for NiO in relation to Cr_2O_3 and have a continuous relationship for CaO. Note that the outlier of high Cr_2O_3 (*Fig 3.17)* has been omitted so as to have the same scale as Starkey (2009). Similarly, only Fo_{70} or higher was plotted so as to keep the same scale. The olivines analysed in this study have a forsterite value at least 10% lower than Starkey (2009) – previously mentioned as to why this could be. However, there is a positive relationship of Fo% against Cr_2O_3 in both datasets. Starkey et al. (2012) showed that as the trends are continuous, the olivines are not xenocrysts that were picked up along the way but are instead antecrysts where their origin and relationship to the erupted lavas are unknown.

Furthermore, Starkey et al. (2012), showed that there is an overlap between small and large olivines – as also seen in *Fig. 3.16*. They propose that the smaller olivines started to grow at the time when the larger olivines' rims were growing. The larger olivines would have continuously grown during the entire phase of magma evolution so as to achieve normal zoning from high forsterite cores to low forsterite rims (Starkey et al., 2012). Hence, olivines are all from a source that is similar, regardless of their size.

Conclusions

- The bulk rock geochemistry of the samples analysed in this study concur with the trends of previous studies *(*Francis, 1985; Robillard et al., 1992; Holm et al., 1993; Larsen and Pedersen, 2000; Yaxley et al., 2004*;* Starkey, 2009; Starkey et al., 2009).

- The Na_2O/TiO_2 ratio agrees with other studies at ~1.48 (σ = 0.31), meaning that the lavas erupted through thick lithosphere and so have the potential to be contaminated (Su, 2003; Jackson and Dasgupta, 2008; Starkey, 2009). The investigation of mantle metasomatism was inconclusive due to poor quality of data, when following the method set out by Willhite et al. (2014).

- Based on the two conditions of separation K/Ti and $(La/Sm)_N$, samples 1, 4, 6, 7, 9, 13, 15, 16, 24 and 25 are classed as being N-type MORB (Robillard et al., 1992; Mahoney et al, 2002; Stuart et al., 2003; Starkey, 2009; Starkey et al., 2009; Maisonneuve, 2012).

- Forsterite % of sampled olivines are about 10% less than those sampled in other studies (Francis, 1985; Larsen and Pedersen, 2000; Starkey, 2009; Maisonneuve, 2012).

- Continuous trends of CaO, NiO and Fo% against Cr_2O_3, as well as no difference in Fo% for different sizes of olivines shows that they are all sampling the same source (Starkey, 2009; Starkey et al., 2012).

Future Work

The following recommendations for future work are given based on what went wrong, what could have been done better and further questions to investigate:

- The thin sections created were too thin for LA-ICP-MS analysis to be conducted on the melt inclusions. Therefore, create thin sections that are 100 microns thick so that more data can be gathered due to more depth - for both the melt inclusions and mineral grains.

- Change the standards used for EMPA to high Fe and Mg olivines so as to be better suited to measuring Fe and Mg in the olivines.

- Target the smaller olivine population with EMPA so as to get the full history of olivine crystallisation and cooling periods – only the larger olivine phenocryst population was sampled in this investigation.

- Collect more EMPA data of plagioclase feldspars, pyroxenes and the groundmass so as to give a greater representation and population size.

- Fluid inclusions, which were observed, should be investigated by Raman spectroscopy. Fluid inclusions will give an insight into the gasses preserved within the melt. Particular attention should be paid to fluid inclusions within N-type MORB samples, as this may give an indication of the volatile content of the early Earth/primitive mantle.

- Measure $^{3}He/^{4}He$ of the melt inclusions and compare it with previously published studies – e.g. Stuart et. al. , 2003. This will show whether the samples have a relationship with a primitive undegassed mantle reservoir.

- SIMS should also be used to investigate hydrogen and nitrogen isotopes within the melt inclusions and surrounding minerals. Hydrogen and nitrogen isotopes can help determine how the Earth became rich in volatiles and more information about the deep mantle.

References

Anders, E., & Grevesse, N., (1989). Abundances of the elements: Meteoritic and solar. *Geochimica et Cosmochimica Acta*, **53(1)**: 197–214.

Clarke, D.B. & Upton, B.G.J., 1971. Tertiary basalts of Baffin Island — field relations and tectonic setting. *Canadian Journal of Earth Sciences*, **8**: 248–258.

Craig, J.R., and Vaughan, D.J., 1995. Ore Microscopy and Ore Petrography. (2nd), *John Wiley and Sons LTD*, **Ch2**: 17-34.

Fitton, J. G., Saunders, A. D., Norry, M. J., Hardarson, B. S. and Taylor, R. N., 1997. Thermal and chemical structure of the Iceland plume. *Earth and Planetary Science Letters,* **153**: 197-208.

Francis, D., 1985. The Baffin Bay lavas and the value of picrites as analogues of primary magmas. *Contributions to Mineralogy and Petrology*, **89**: 144-155.

Goldstein, J.I., Newbury, D.E., Michael, J.R., Ritchie, N.W.M., Scott, J.H.J. & Joy, D.C., 2018. Scanning electron microscopy and X-ray microanalysis. *Springer*, **Ch 9**, *pg. 139-142*

Holm, P. M., Gill, R. C. O., Pedersen, A. K., Larsen, J. G., Hald, N., Nielsen, T. F. D., and Thirlwall, M. F., 1993. The Tertiary picrites of West Greenland: contributions from Icelandic and other sources. *Earth and Planetary Science Letters*, **115**: 227-244.

Horton, F., Curtice, J., Farley, K.A., Kurz, M.D., Asimow, P.D., Treffkron, J. & Boyes, X.M., 2021. Primordial neon in high -^{3}He/^{4}He Baffin Island olivines. *Earth and Planetary Science Letters*, **558**: 116762.

Howell, D., Griffin, W.L., Pearson, N.J., Powell, W., Wieland, P., and O'Reilly, S.Y., 2013. Trace element partitioning in mixed-habit diamonds. *Chemical Geology*, **355**: 134–143.

Jackson, M. G. and Dasgupta, R., 2008. Compositions of HIMU, EM1, and EM2 from global trends between radiogenic isotopes and major elements in ocean island basalts. *Earth and Planetary Science Letters*, **276**: 175-186.

Jackson, M.G., Carlson, R.W., Kurz, M.D., Kempton, P.D., Francis, D. & Blusztajn, J., 2010. Evidence for the survival of the oldest terrestrial mantle reservoir. *Nature*, **466**: 853-856.

Jackson, M.G., Konter, J.G., Becker, T.W., 2017. Primordial helium entrained by the hottest mantle plumes. *Nature*, **542**: 340.
Jensen, L.S., (1976). A New Cation Plot for Classifying Subalkalic Volcanic Rocks. *Ontario Division Mines, Miscellaneous Paper,* 66: 22 p.

Jensen, L. S., and Pyke, D. R., (1982). Komatiites in the Ontario portion of the Abitibi belt, in Arndt, N. T, and Nisbet, E. G. (eds), *Komatiites: London, George Alien and Unwin*, p. 147-158.

Kent, A.J.R., Stolper, E.M., Francis, D., Woodhead, J., Frei, R. & Eiler, J., 2004. Mantle heterogeneity during the formation of the North Atlantic Igneous Province: constraints from trace element and Sr-Nd-Os-O isotope systematics of Baffin Island picrites. *Geochemistry, Geophysics, Geosystems*: **5**, Q11004, doi:10.1029/2004GC000743.

Kent, A.J.R., Stolper, E.M., Woodhead, J., Huctcheon, I.D. & Francis, D., 1998. Using glass inclusions to investigate a heterogenous mantle: An example from N- EMORB-like lavas from Baffin Island. *Goldschmidt Conference, Toulouse 1998.*

Koch, J. & Gunther, D., 2017. Laser Ablation Inductively Coupled Plasma Mass Spectrometry. *Encyclopaedia of Spectroscopy and Spectrometry (Third Edition)*, 526-532.

Krishnamurthy, P. and Cox, K. G., 1977. Picrite basalts and related lavas from Deccan Traps of Western India. *Contributions to Mineralogy and Petrology*, **62**: 53-75.

Larsen, L. M. and Pedersen, A. K., 2000. Processes in high-mg, high-T magmas: Evidence from olivine, chromite and glass in Palaeogene picrites from West Greenland. *Journal of Petrology*, **41**: 1071-1098.

Le Maitre, RW., Streckeisen, A., Zanettin, B., Le Bas, MJ., Bonin, B., and Bateman, P., 2002. Igneous Rocks: A Classification and Glossary of Terms: Recommendations of the International Union of Geological Sciences Subcommission on the Systematics of Igneous Rocks. *Cambridge University Press (second edition).*

Longerich, H., and Jackson, S., 1996. Laser Ablation Inductively Coupled Plasma Mass Spectrometric Transient Signal Data Acquisition and Analyte Concentration Calculation. *Journal of Analytical Atomic Spectrometry - J ANAL ATOM SPECTROM*, 11.

Mahoney, J. J., Graham, D. W., Christie, D. M., Johnson, K. T. M., Hall, L. S. and Vonderhaar, D. L., 2002. Between a Hotspot and a Cold Spot: Isotopic Variation in the Southeast Indian Ridge Asthenosphere, 86°E-118°E. *Journal of Petrology*, **43**: 1155-1176.

Maisonneuve, M., 2012, Constraining the nature of E- and N-type components in the Baffin Island picrites using olivine-hosted melt inclusions. MSc Thesis, Department of Earth & Planetary Sciences McGill University, Montréal, Québec, Canada.

Pettke, T., Oberli, F., Audétat, A., Guillong, M., Simon, A.C., Hanley, J.J., and Klemm, L.M., 2012. Recent developments in element concentration and isotope ratio analysis of individual fluid inclusions by laser ablation single and multiple collector ICP-MS*. Ore Geology Reviews*, **44**: 10–38.

Reed, S.J.B., 2005. Electron Microprobe Analysis and Scanning Electron Microscopy in Geology. *University of Cambridge Press (Second edition).*

Rizo, H., Walker, R.J., Carlson, R.W., Horan, M.F., Mukhopadhyay, S., Manthos, V., Francis, D., Jackson, M.G., 2016. Preservation of Earth-forming events in the tungsten isotopic composition of modern flood basalts. Science **352**: 809–812.

Robillard, I., Francis, D., Ludden, J.N., 1992. The relationship between E-and N-type magmas in the Baffin Bay lavas. Contrib. Mineral. Petrol. **112**: 230–241.

Saunders, A.D., Fitton, J.G., Kerr, A.C., Norry, M.J. & Kent, R.W., 1997. The North Atlantic Igneous Province. In: Mahoney, J.J. & Coffin, M.F. (eds) *Large Igneous Provinces: Continental, Oceanic and Planetary Flood Volcanism. Geophysical Monograph, American Geophysical Union*, **100**: 45-93.

Starkey, N. A., Stuart, F. M., Ellam, R. M., Fitton, J. G., Basu, S. and Larsen, L. M., 2009. Helium isotopes in early Iceland plume picrites: Constraints on the composition of high 3He/4He mantle. *Earth and Planetary Science Letters*, **277**: 91-100.

Starkey, N., 2009. Evolution of the Earth's mantle-crust-atmosphere system from the trace element and isotope geochemistry of the plume-mantle reservoir. PhD Thesis, The University of Edinburgh.

Starkey, N.A., Fitton, J.G., Stuart, F.M. &Larsen, L.M., 2012. Melt inclusions in olivines from early Iceland plume picrites support high $^{3}He/^{4}He$ in both enriched and depleted mantle. *Chemical Geology*, **306-307**: 54-62.

Storey, M., Duncan, R. A., Pedersen, A. K., Larsen, L. M. and Larsen, H. C., 1998. $^{40}Ar/^{39}Ar$ geochronology of the West Greenland Tertiary volcanic province. *Earth and Planetary Science Letters,* **160**: 569-586.

Stuart, F.M., Lass-Evans, S., Fitton, J.G. & Ellam, R.M., 2003. High $^{3}He/^{4}He$ ratios in picritic basalts from Baffin Island and the role of a mixed reservoir in mantle plumes. *Nature*, **424**: 57-59.

Su, Y., 2003. Global MORB chemistry compilation at the segment scale. PhD Thesis. Department of Earth and Environmental Sciences, Colombia University.

Thompson, G., and Bankston, DC., 1970. Sample Contamination from Grinding and Sieving Determined by Emission Spectrometry. *Applied Spectroscopy*, **24(2)**: 210-219.

White, W.M., and Klein, E.M., (2014). Composition of the Oceanic Crust. *Treatise on Geochemistry: Second Edition*, **4**: 457-496.

Willhite, L.N., Jackson, M.G., Blichert-Toft, J., Bindeman, I., Kurz, M. D.,Halldórsson, S.A., et al., (2019). Hot and heterogenous high- $^{3}He/^{4}He$ components: New constraints from proto-Iceland plume lavas from Baffin Island. *Geochemistry, Geophysics, Geosystems*, **20**: 5939 – 5967.

Willis, J., 2010. XRF Sample Preparation – Glass beads by borate fusions. *PANalytical B.V.* ISBN: 978-90-809086-9-7.

Yaxley, G.M., Kamenetsky, V.S., Kamenetsky, M., Norman, M.D & Francis, D., 2004. Origins of compositional heterogeneity in olivine-hosted melt inclusions from the Baffin Island picrites. *Contributions to Mineralogy and Petrology*, **148**: 426-442.

Appendix I – Bulk Rock Major and Trace Elements

Sample	SiO_2	TiO_2	Al_2O_3	Fe_2O_3	MnO	MgO	CaO	Na_2O	K_2O	P_2O_5	LOI	Total
	wt.%	*wt.%*	*wt.%*	*wt.%*	*wt.%*	*wt.%*	*wt.%*	*wt.%*	*wt.%*	*wt.%*	*wt.%*	*wt.%*
N-Type												
1	45.75324	1.164369	14.22505	10.63318	0.170951	9.258917	12.55163	0.930735	0.103521	0.099722	5.026319	**99.9863**
4	46.32012	0.958603	10.4292	11.97903	0.181683	19.290512	9.299958	1.323977	0.077291	0.092347	-0.37686	**99.87987**
6	42.88349	0.523567	8.274127	11.28023	0.167659	26.503874	7.147575	0.587297	0.039219	0.051965	1.95175	**99.89992**
7	43.07619	0.581888	8.675949	11.116	0.166808	24.283153	7.73426	0.509152	0.063038	0.059159	3.009408	**99.6929**
9	43.76081	0.539211	8.191821	11.71613	0.174421	27.284477	6.718709	0.876093	0.024917	0.051828	0.331212	**100.161**
13	43.34522	0.706901	9.736709	11.32504	0.169656	22.173293	8.701221	0.585997	0.050702	0.063377	2.489518	**99.72419**
15	45.00384	0.704927	9.747513	11.39633	0.172249	22.833475	8.399389	1.047434	0.05277	0.111514	0.435284	**100.2996**
16	45.77864	0.834178	11.95588	11.26991	0.173245	18.29183	10.25348	1.25377	0.022031	0.096136	-0.14152	**100.0792**
23	44.97193	0.740813	10.96043	11.22002	0.171725	20.24156	9.364991	1.124198	0.017971	0.060902	0.158983	**99.3591**
24	45.60616	0.71397	11.7721	10.80336	0.168864	18.833786	9.457381	1.091198	0.02765	0.055301	1.249675	**100.0522**
25	44.47577	0.560648	8.899166	11.63822	0.174513	25.713605	7.487014	0.915692	0.033097	0.047139	-0.29524	**100.1192**

Table A1.1: XRF data of the major element concentrations for N-Type MORB's.

Errors	**SiO_2**	**TiO_2**	**Al_2O_3**	**Fe_2O_3**	**MnO**	**MgO**	**CaO**	**Na_2O**	**K_2O**	**P_2O_5**
Sample	*wt.%*	*wt.%*	*wt.%*	*wt.%*	*wt.%*	*wt.%*	*wt.%*	*wt.%*	*wt.%*	*wt.%*
N-Type										
1	0.249312	0.053777	0.021736	0.082177	0.010618	0.099141	0.069127	0.003178	0.056368	0.007587
4	0.245971	0.054951	0.02173	0.098222	0.010336	0.092219	0.069675	0.003179	0.051009	0.007587
6	0.24219	0.055321	0.021727	0.115539	0.010033	0.089934	0.069305	0.003025	0.048991	0.007506
7	0.243198	0.055184	0.021732	0.110872	0.010047	0.090527	0.069275	0.003025	0.049642	0.007545
9	0.242426	0.055656	0.02173	0.116356	0.010035	0.089726	0.06948	0.003027	0.048502	0.007506
13	0.243253	0.055061	0.021734	0.1057	0.010132	0.091732	0.069415	0.003175	0.05062	0.007545
15	0.244425	0.055077	0.021734	0.106145	0.010126	0.091501	0.069264	0.003026	0.050104	0.007586
16	0.245231	0.054871	0.02173	0.096341	0.010224	0.094344	0.069133	0.003174	0.052166	0.007587
23	0.244196	0.054975	0.021731	0.100413	0.01019	0.093025	0.069122	0.003025	0.051131	0.007545
24	0.246027	0.054807	0.021729	0.097956	0.010131	0.094324	0.06889	0.003025	0.051381	0.007506
25	0.243095	0.055466	0.021729	0.112269	0.010038	0.090416	0.069374	0.003026	0.049134	0.007507

Table A1.2: XRF data of the errors on the major element concentrations for N-Type MORB's.

Sample	SiO_2	TiO_2	Al_2O_3	Fe_2O_3	MnO	MgO	CaO	Na_2O	K_2O	P_2O_5	LOI	Total
	wt.%	*wt.%*	*wt.%*	*wt.%*	*wt.%*	*wt.%*	*wt.%*	*wt.%*	*wt.%*	*wt.%*	*wt.%*	*wt.%*
E-Type												
2	46.74663	1.001664	12.16434	12.26192	0.185198	15.198204	10.47465	1.433793	0.072685	0.096582	0.43239	**100.3108**
3	44.65206	0.583983	8.722551	12.38425	0.180924	25.207751	7.115342	1.080519	0.120616	0.067344	-0.51366	**100.054**
5	44.27435	0.572982	8.638653	12.17936	0.180679	24.951673	6.763984	1.005214	0.121784	0.069876	0.176245	**99.38421**
8	45.42388	0.791392	11.21973	11.374	0.172303	19.640538	9.408545	1.204117	0.043076	0.17631	-0.17545	**99.59795**
10	45.43566	0.699428	10.26499	11.8943	0.179134	21.56151	8.171737	1.323379	0.145924	0.081516	-0.63391	**99.49204**
11	46.99684	0.999063	13.55116	11.35163	0.177478	13.656852	10.83515	1.583345	0.087742	0.096716	0.292607	**99.82665**
12	44.24651	0.58223	8.572393	12.3709	0.181072	25.962277	6.395532	0.954378	0.123049	0.061024	-0.03956	**99.89431**
14	47.29135	0.964925	13.63007	11.01456	0.172165	13.415864	10.82438	1.645578	0.176169	0.107103	-0.09533	**99.33113**
17	46.09958	0.786332	12.06805	11.61858	0.177398	17.296314	9.771844	1.324506	0.074746	0.07375	0.337882	**99.91988**
18	46.63822	0.942812	12.30949	12.03983	0.18277	15.80508	10.62161	1.457163	0.067914	0.090885	0.126542	**100.5305**
19	46.17321	0.82225	11.77591	11.15897	0.17126	18.219704	9.849977	1.305986	0.050076	0.088134	-0.15193	**99.76525**
20	46.49924	0.96176	13.39691	10.54162	0.168356	12.729287	10.29683	1.540364	0.183837	0.1074	3.238083	**99.83336**
21	46.93878	0.934874	12.90502	11.83051	0.183211	14.351896	9.609195	1.443905	0.190144	0.108937	0.96373	**99.68578**
22	47.75106	1.067998	14.60228	11.46703	0.179328	10.592307	11.83565	1.621922	0.097634	0.095642	0.372542	**99.78658**
26	45.21008	0.623885	10.02335	11.64787	0.172799	22.93205	7.954787	1.159362	0.128595	0.064297	-0.46395	**99.85966**
27	44.84757	0.91549	12.90278	10.56394	0.166106	13.766722	10.80069	0.850575	0.11742	0.091644	4.52474	**99.73014**

Table A1.3: XRF data of the major element concentrations for E-Type MORB's.

Errors	**SiO_2**	**TiO_2**	**Al_2O_3**	**Fe_2O_3**	**MnO**	**MgO**	**CaO**	**Na_2O**	**K_2O**	**P_2O_5**
Sample	*wt.%*	*wt.%*	*wt.%*	*wt.%*	*wt.%*	*wt.%*	*wt.%*	*wt.%*	*wt.%*	*wt.%*
E-Type										
2	0.247245	0.05469	0.021731	0.090728	0.010422	0.09472	0.069987	0.003182	0.052536	0.007587
3	0.243208	0.055425	0.021735	0.110957	0.010043	0.090215	0.069957	0.003178	0.04879	0.007544
5	0.243106	0.055351	0.021735	0.11078	0.010041	0.090197	0.069868	0.003179	0.048528	0.007544
8	0.244637	0.054877	0.021727	0.099049	0.010207	0.093311	0.069201	0.003174	0.051144	0.007695
10	0.244348	0.055126	0.021732	0.102854	0.010122	0.091984	0.069559	0.003177	0.049774	0.007543
11	0.247579	0.054611	0.021729	0.088006	0.01042	0.096882	0.069255	0.003177	0.052996	0.007587
12	0.242929	0.055365	0.021735	0.113004	0.010043	0.090081	0.06999	0.003179	0.048224	0.007545
14	0.247752	0.054617	0.021741	0.087536	0.01034	0.096916	0.068965	0.003174	0.05293	0.007587
17	0.246137	0.054778	0.021731	0.094588	0.010207	0.094596	0.069445	0.003177	0.051633	0.007544
18	0.246856	0.05469	0.021732	0.091724	0.010331	0.094904	0.069796	0.00318	0.052674	0.007587
19	0.245861	0.054866	0.021734	0.09621	0.010219	0.094084	0.069057	0.003025	0.051667	0.007587
20	0.249125	0.054612	0.02174	0.087137	0.010416	0.097276	0.068894	0.003175	0.05272	0.007587
21	0.248033	0.054605	0.02174	0.089385	0.010331	0.095991	0.069683	0.003181	0.051519	0.007587
22	0.248921	0.054365	0.021738	0.083357	0.010459	0.098625	0.069375	0.003178	0.054377	0.007587
26	0.244133	0.055233	0.021734	0.105872	0.010052	0.091724	0.069367	0.003025	0.049591	0.007545
27	0.247292	0.054198	0.021735	0.089226	0.010338	0.096724	0.069007	0.003175	0.053597	0.007587

Table A1.4: XRF data of the errors on the major element concentrations for E-Type MORB's.

Sample	Rb	Ba	Sr	Nb	Zr	Hf	Y	Ga	Zn	Cu	Ni	Co	Cr	V	Sc	La	Ce	Nd	Pb	Th	U	W
	ppm	*ppm*	*ppm*	*ppm*	*ppm*	*ppm*	*ppm*	*ppm*	*ppm*	*ppm*	*ppm*	*ppm*	*ppm*	*ppm*	*ppm*	*ppm*	*ppm*	*ppm*	*ppm*	*ppm*	*ppm*	*ppm*
N-Type																						
1	1.4	26.2	118.3	1.3	59.5	0	23.6	15.1	77	172	188.6	48.4	330.5	353	57.9	4.5	1.1	7.6	8.3	7.4	0.2	11.7
4	0.9	19.9	83.7	3.8	54.5	0	19.1	12.6	77.2	130.3	866.2	77.6	1318.1	272.8	42.8	0	4.6	7.9	10.8	11.3	0	11.5
6	0	20.7	36.9	0.1	27.9	0	11.1	8.2	71	80.5	1351.4	97.7	2237	169.1	32.4	0	1.2	5	1.3	1.3	0	4.6
7	0	15.6	62.9	1.5	31.9	0	11.1	9.3	71.8	63.3	1205	91.8	1899.1	190.5	35.7	0	0	10.8	5	4.5	0	2.7
9	0	6.8	50.3	1.5	28.9	0	12.2	8.9	71	77.3	1347.8	101.7	2199.7	176.7	34.5	0	14.9	12.4	1.5	2.8	0	7.6
13	0.2	11.5	47	0	36.7	0	14	10.4	74.4	112.6	1050.3	90.7	1727.9	231.6	40.2	0	9.4	0.9	5.3	0.9	0	7.1
15	0.7	10.6	64.5	2	37.5	0	14.8	11.7	72.3	104	1056.6	87.3	1793.4	219.7	37.1	0	9.4	7.7	6.4	5.5	0	10.3
16	0.8	6.7	86.6	3.7	45.4	3.5	17.9	14.2	73.4	124.4	763.6	77.1	1327.4	253.4	44.7	2.6	2.4	10	9.7	7.7	0	8.5
23	0	17.4	70.5	3.1	40.4	0.7	15.5	11.8	70.2	115.4	904.9	82.4	1443.3	228.9	41.9	0.9	8.2	16.1	5.7	7.9	0	5.9
24	0	27.2	68.3	0	34.7	0	15.3	13.8	69.8	95.1	769.7	73.5	1219.3	234.1	43	0	2.9	16.8	4.1	0	0	9.2
25	0	20.3	62.6	2.1	30	0	11	9.3	70	84.8	1253.6	95.3	2111.9	178.5	34	5.4	0	0	4.7	0.9	1.6	8

Table A1.5: XRF data of the trace element concentrations for N-Type MORB's.

Errors	**Rb**	**Ba**	**Sr**	**Nb**	**Zr**	**Hf**	**Y**	**Ga**	**Zn**	**Cu**	**Ni**	**Co**	**Cr**	**V**	**Sc**	**La**	**Ce**	**Nd**	**Pb**	**Th**	**U**	**W**
Sample	*ppm*	*ppm*	*ppm*	*ppm*	*ppm*	*ppm*	*ppm*	*ppm*	*ppm*	*ppm*	*ppm*	*ppm*	*ppm*	*ppm*	*ppm*	*ppm*	*ppm*	*ppm*	*ppm*	*ppm*	*ppm*	*ppm*
N-Type																						
1	2.32	19.62	4.04	4.11	5.58	3.79	1.68	1.86	3.04	3.65	3.68	3.37	7.04	7.62	3.55	11.54	23.80	10.04	11.08	9.44	3.12	5.36
4	2.31	19.47	4.02	4.10	5.58	3.78	1.66	1.85	3.02	3.49	5.04	3.45	10.46	7.06	3.41	11.45	23.53	9.92	11.07	9.44	3.10	5.32
6	2.29	19.29	4.00	4.11	5.59	3.73	1.64	1.82	3.00	3.30	5.97	3.46	13.34	6.38	3.32	11.17	23.28	9.73	11.06	9.43	3.05	5.23
7	2.29	19.31	4.01	4.11	5.59	3.73	1.65	1.82	3.00	3.27	5.67	3.45	12.30	6.50	3.34	11.17	23.34	9.75	11.06	9.43	3.06	5.25
9	2.29	19.29	4.01	4.11	5.59	3.73	1.64	1.82	3.00	3.30	5.95	3.48	13.20	6.38	3.32	11.11	23.18	9.66	11.06	9.43	3.05	5.23
13	2.29	19.40	4.01	4.11	5.59	3.74	1.65	1.83	3.01	3.40	5.39	3.44	11.78	6.80	3.39	11.32	23.42	9.85	11.07	9.43	3.06	5.26
15	2.29	19.36	4.02	4.11	5.59	3.74	1.65	1.83	3.00	3.37	5.38	3.43	11.97	6.68	3.36	11.26	23.37	9.80	11.06	9.43	3.06	5.25
16	2.31	19.45	4.02	4.10	5.58	3.76	1.66	1.85	3.01	3.45	4.83	3.42	10.53	6.93	3.44	11.39	23.56	9.89	11.07	9.43	3.08	5.30
23	2.31	19.39	4.02	4.10	5.59	3.74	1.65	1.83	3.01	3.42	5.10	3.42	10.85	6.78	3.41	11.32	23.48	9.83	11.07	9.43	3.08	5.30
24	2.29	19.39	4.02	4.11	5.59	3.73	1.65	1.83	3.00	3.35	4.80	3.38	10.11	6.78	3.40	11.24	23.40	9.78	11.06	9.43	3.05	5.23
25	2.29	19.27	4.01	4.11	5.59	3.73	1.65	1.84	3.00	3.32	5.78	3.46	12.96	6.42	3.34	11.17	23.34	9.78	11.06	9.43	3.05	5.25

Table A1.6: XRF data of the errors on the trace element concentrations for N-Type MORB's.

Sample	Rb	Ba	Sr	Nb	Zr	Hf	Y	Ga	Zn	Cu	Ni	Co	Cr	V	Sc	La	Ce	Nd	Pb	Th	U	W
	ppm	*ppm*	*ppm*	*ppm*	*ppm*	*ppm*	*ppm*	*ppm*	*ppm*	*ppm*	*ppm*	*ppm*	*ppm*	*ppm*	*ppm*	*ppm*	*ppm*	*ppm*	*ppm*	*ppm*	*ppm*	*ppm*
E-Type																						
2	0	54.3	111.2	4.4	54.1	0	19.3	14.6	79.9	141.5	551.4	74.3	1187.8	271.4	45.7	0	16.5	6.9	3.7	2	0	6.8
3	1.2	41.5	74.6	7.9	40.5	0	12.3	10.7	79	66.5	1113.3	98.4	2109.8	173	34.8	4.7	17.1	4.6	7	6.8	0	8.8
5	2.2	51.4	69.5	0	28.3	0	10.3	9.4	75.7	66.2	1145.5	96.3	2083	173.6	33.8	0	10.4	11.7	0	0	0	10.4
8	0.7	30.2	88.6	0	41.2	0	14.4	12.5	72.5	101.1	856.8	78	1436.3	225.7	41.6	0	10.8	4.2	0	0	0	8.9
10	2.9	54.9	86	5	43.1	0	13.6	10.6	81.2	79.1	911.1	84.7	1711.2	196.2	36.2	3.4	20.2	18.5	5.7	2.9	0	9.8
11	0	40.1	116.6	7.2	61.7	0.4	20.7	14.6	75.2	75.1	502	67	922.1	270	47.5	3.5	1.6	3.2	5.8	6.1	0	14.8
12	2.9	48.3	75.3	4.4	37.3	0	12.4	9.6	79.9	70.9	1181.5	100.2	2285	175.5	33	0	9.9	9.3	3.7	0.1	0	8.5
14	2.4	71.9	117.7	7.3	60.3	0	19.6	14.9	74.6	104.6	466.2	63.7	853.9	250.9	45.5	6.9	7.4	12.2	10.7	8.2	0	11.1
17	0	51.7	100.4	5.9	45.8	0.2	16.7	13.3	75.7	93.6	703.7	75.9	1384.4	225	44.2	4.9	7.6	9.8	8.1	6.8	0	6.8
18	0	46.1	113	6.4	54.9	0	19.3	14.5	78.3	125.7	596.1	78.2	1181.5	256	44.9	0	29.3	10.5	11.7	11	0.5	6.3
19	0	23.1	95.7	4.5	47.8	0	17	15	71.6	109.7	769.7	74.5	1391	229.6	43.2	0	5.2	15	5.5	8.1	0	12.1
20	0.8	73.9	133.6	4.7	60.4	0	20.3	16	74	102	416.6	61.4	837.1	264.4	47.7	4.3	23.7	11.5	7.9	7.8	0.2	8.1
21	2.2	78.9	113.1	7	59.6	0	19.7	14.9	82.4	80.5	542.8	72	1085.9	253.9	44.5	3.4	12.3	9.6	8	10	0	13.2
22	0.3	46.8	129.6	0.7	53.9	2.1	19.4	15.8	73.9	108.5	245.1	58.7	495.3	294.3	45.9	0	3.4	9.4	4.1	2.9	0	4.2
26	1	50.1	83.1	6.9	41	0.1	13.2	12	76.2	67.6	996.8	88.3	1900.8	188.2	34.8	0	17.2	11.9	8	5.3	0	9.8
27	1.9	64.7	132.9	4	57.6	0	17.8	11.5	73.5	136.1	498.2	67.4	874	255.5	45.7	0	0	16.4	0	0	0	4.3

Table A1.7: XRF data of trace element concentrations for E-Type MORB's.

Errors	Rb	Ba	Sr	Nb	Zr	Hf	Y	Ga	Zn	Cu	Ni	Co	Cr	V	Sc	La	Ce	Nd	Pb	Th	U	W
Sample	*ppm*	*ppm*	*ppm*	*ppm*	*ppm*	*ppm*	*ppm*	*ppm*	*ppm*	*ppm*	*ppm*	*ppm*	*ppm*	*ppm*	*ppm*	*ppm*	*ppm*	*ppm*	*ppm*	*ppm*	*ppm*	*ppm*
E-Type																						
2	2.32	19.50	4.04	4.10	5.58	3.79	1.66	1.86	3.04	3.54	4.42	3.45	10.06	7.07	3.44	11.49	23.74	10.01	11.08	9.44	3.12	5.36
3	2.31	19.32	4.02	4.09	5.59	3.78	1.65	1.83	3.02	3.29	5.53	3.49	12.92	6.40	3.32	11.15	23.34	9.78	11.07	9.43	3.08	5.28
5	2.29	19.30	4.01	4.11	5.59	3.73	1.64	1.82	3.00	3.26	5.56	3.45	12.83	6.38	3.32	11.19	23.23	9.75	11.06	9.43	3.03	5.23
8	2.29	19.42	4.02	4.11	5.59	3.73	1.65	1.83	3.00	3.37	4.99	3.41	10.84	6.76	3.39	11.34	23.47	9.82	11.07	9.43	3.06	5.25
10	2.31	19.39	4.02	4.10	5.58	3.76	1.65	1.83	3.01	3.33	5.10	3.45	11.71	6.56	3.36	11.24	23.40	9.80	11.07	9.43	3.06	5.26
11	2.31	19.56	4.04	4.09	5.58	3.78	1.66	1.85	3.02	3.33	4.29	3.40	9.16	7.07	3.46	11.47	23.72	9.96	11.08	9.44	3.10	5.32
12	2.31	19.32	4.02	4.10	5.59	3.74	1.65	1.84	3.01	3.29	5.64	3.50	13.46	6.40	3.32	11.15	23.31	9.77	11.07	9.44	3.06	5.28
14	2.31	19.55	4.03	4.09	5.58	3.78	1.66	1.85	3.02	3.40	4.22	3.38	8.91	7.00	3.46	11.43	23.67	9.90	11.07	9.44	3.10	5.30
17	2.31	19.46	4.03	4.10	5.59	3.76	1.66	1.85	3.02	3.37	4.71	3.43	10.68	6.77	3.42	11.34	23.51	9.90	11.07	9.44	3.08	5.32
18	2.32	19.52	4.04	4.10	5.58	3.79	1.66	1.86	3.04	3.48	4.51	3.47	10.05	7.00	3.44	11.47	23.70	9.97	11.08	9.44	3.12	5.36
19	2.31	19.45	4.02	4.10	5.58	3.76	1.65	1.85	3.01	3.39	4.82	3.40	10.70	6.81	3.41	11.32	23.50	9.83	11.07	9.43	3.08	5.26
20	2.31	19.55	4.03	4.10	5.58	3.74	1.66	1.84	3.01	3.38	4.10	3.37	8.84	7.05	3.44	11.41	23.56	9.87	11.07	9.43	3.08	5.26
21	2.32	19.52	4.04	4.10	5.58	3.79	1.66	1.85	3.04	3.35	4.40	3.44	9.69	6.96	3.44	11.41	23.64	9.94	11.08	9.44	3.10	5.34
22	2.31	19.58	4.04	4.11	5.58	3.78	1.66	1.84	3.02	3.42	3.79	3.39	7.64	7.25	3.47	11.54	23.77	9.96	11.08	9.44	3.10	5.34
26	2.31	19.34	4.02	4.10	5.59	3.74	1.65	1.83	3.01	3.29	5.27	3.44	12.30	6.48	3.36	11.19	23.35	9.80	11.07	9.43	3.06	5.26
27	2.31	19.55	4.04	4.10	5.58	3.78	1.66	1.85	3.01	3.50	4.29	3.40	8.98	7.00	3.46	11.43	23.74	9.92	11.07	9.44	3.08	5.30

Table A1.8: XRF data of the errors on the trace element concentrations for E-Type MORB's.

Sample	Y	La	Ce	Pr	Nd	Sm	Eu	Gd	Tb	Dy	Ho	Er	Tm	Yb	Lu
	ppm	ppm	ppm	ppm	ppm	ppm	ppm	ppm	ppm	ppm	ppm	ppm	ppm	ppm	ppm
N-Type															
1	15.7235	10.3343	12.6610	14.3542	16.5967	17.2498	17.8702	19.2407	17.9338	17.3106	16.8597	16.7668	15.7534	15.7388	16.5401
4	12.9474	10.5771	12.4758	14.1100	15.8938	14.1056	14.5232	16.2953	14.5021	15.3833	13.1395	13.5801	11.6729	13.8432	12.3840
6	7.4297	4.9678	5.8569	7.0693	7.7237	7.7671	8.4679	8.1437	8.2167	8.2867	7.2736	7.6537	6.9112	7.8044	7.5504
7	8.1684	5.3271	6.5304	8.2083	8.9603	8.2670	9.3267	9.6428	9.0674	9.2243	8.4657	9.1604	8.2023	8.4163	7.3402
9	7.8972	4.8651	5.7044	6.7913	7.7636	8.9445	8.4113	8.8452	8.7797	9.0182	8.2958	7.9579	7.8344	8.5497	7.8373
13	10.0183	6.9912	8.0240	9.9570	10.4138	10.2145	10.9512	11.5750	11.4007	11.1379	10.4012	10.7034	9.9690	10.8135	10.2366
15	10.1743	6.2003	7.7301	9.1277	9.9350	10.1660	10.7436	10.3024	11.0769	11.5477	11.4796	10.7307	9.5252	10.9928	10.0856
16	11.8593	8.2009	9.2434	11.4737	11.9562	13.1165	12.7404	14.2694	12.6708	13.1553	12.1831	12.4469	11.9836	12.0567	11.0956
23	10.7702	6.5475	7.8556	9.1120	10.1339	10.9541	10.6961	12.7444	11.4336	11.5430	10.7626	12.0666	10.4022	11.2195	12.2789
24	10.6496	6.1591	7.3120	8.8747	9.8842	11.4310	10.5160	11.8635	11.0682	11.9337	10.4641	11.4847	9.9096	11.1472	9.6375
25	7.7234	5.4133	6.2439	7.3480	7.9775	7.7486	8.4864	8.9297	8.2738	8.7706	7.9659	8.1793	6.9627	7.2310	7.0913

Table A1.8: LA-ICP-MA data of the REE concentrations for N-Type MORB's.

ERRORS	Y	La	Ce	Pr	Nd	Sm	Eu	Gd	Tb	Dy	Ho	Er	Tm	Yb	Lu
	ppm	ppm	ppm	ppm	ppm	ppm	ppm	ppm	ppm	ppm	ppm	ppm	ppm	ppm	ppm
N-Type															
1	0.42678	0.69775	0.47228	1.12995	1.24461	2.33692	1.98820	1.96155	1.85043	1.41831	1.33553	1.41215	1.98216	1.69937	2.00874
4	0.40304	0.75612	0.50411	1.15477	1.33647	2.06147	1.81539	2.04830	1.56891	1.40116	1.28269	1.29708	1.71142	1.52683	1.71867
6	0.31792	0.47316	0.35361	0.79870	0.90731	1.66133	1.40378	1.42274	1.21471	0.95169	0.90439	0.99992	1.28882	1.25317	1.39188
7	0.31572	0.53482	0.36567	0.96776	1.01616	1.60340	1.45495	1.58514	1.25725	1.08181	0.97283	1.05923	1.45900	1.21670	1.31360
9	0.31186	0.48199	0.35572	0.83844	0.89871	1.79683	1.42389	1.41093	1.24997	1.10459	1.01402	1.01083	1.40743	1.22405	1.54131
13	0.36980	0.57748	0.41921	1.02531	1.02173	1.94155	1.63388	1.75260	1.45657	1.19512	1.12780	1.22963	1.70352	1.44863	1.58136
15	0.38989	0.58598	0.42091	0.97578	1.13087	1.82642	1.63397	1.70801	1.51852	1.18134	1.24294	1.17406	1.68665	1.58208	1.63565
16	0.42216	0.68759	0.42948	1.07737	1.12824	2.15671	1.96397	1.93326	1.67831	1.26235	1.30884	1.32423	1.91360	1.58525	1.77096
23	0.40446	0.58698	0.44859	1.04319	1.08201	2.06056	1.72200	1.89773	1.46013	1.18786	1.25694	1.23573	1.76797	1.54200	1.89399
24	0.43635	0.55102	0.39789	1.00268	1.03106	2.21354	1.70539	1.78623	1.48905	1.23296	1.20962	1.26711	1.73111	1.46594	1.67506
25	7.7234	5.4133	6.2439	7.3480	7.9775	7.7486	8.4864	8.9297	8.2738	8.7706	7.9659	8.1793	6.9627	7.2310	7.0913

Table A1.9: LA-ICP-MA data of the errors on the REE concentrations for N-Type MORB's.

Sample	Y	La	Ce	Pr	Nd	Sm	Eu	Gd	Tb	Dy	Ho	Er	Tm	Yb	Lu
	ppm	ppm	ppm	ppm	ppm	ppm	ppm	ppm	ppm	ppm	ppm	ppm	ppm	ppm	ppm
E-Type															
2	13.3665	18.1476	16.8689	17.5822	17.3555	17.0112	16.6554	16.9409	14.9215	15.3086	13.2931	13.6005	13.1831	12.9116	12.7935
3	8.0447	14.2626	12.1102	11.9303	11.9081	10.1619	10.5702	9.0472	9.4056	8.9227	8.1795	8.2150	8.7839	8.3217	8.1856
5	8.3297	15.0882	12.0392	12.0814	12.1626	9.1359	9.1974	9.6571	9.6017	9.3412	8.3214	8.2284	8.7140	8.2387	8.3315
8	10.7874	14.3892	13.8097	13.5566	13.3817	12.8240	12.6390	12.3866	12.3158	12.4506	11.1842	11.6413	10.6520	10.4414	9.6464
10	9.5950	16.2329	13.7243	13.5285	13.6398	11.1218	11.2847	11.1272	9.9543	10.7016	9.6354	9.8236	9.3354	9.8044	9.8343
11	14.0692	24.2218	20.6254	20.2820	19.2764	16.1942	17.4060	16.7082	14.7596	16.2992	14.7925	14.5969	13.9176	13.7454	12.8444
12	8.3908	14.9556	12.8332	12.7340	11.4867	9.5945	10.4235	10.6839	9.2638	10.0232	8.6906	9.2164	8.3565	8.8212	8.2323
14	13.2090	22.1775	19.6594	19.2104	19.1219	16.7425	15.8298	16.0395	14.9008	15.1260	13.9322	14.7510	14.2704	14.8160	12.4962
17	10.9995	15.7361	14.4673	14.6011	14.2882	13.1319	11.9797	13.1360	12.1020	11.3635	10.6599	11.8410	10.7364	9.5584	9.9956
18	12.5074	16.4205	15.4132	15.8999	16.3664	16.0384	15.3832	15.2610	14.1684	13.2849	12.7649	13.8466	12.2100	13.1473	12.2816
19	11.2280	14.9542	14.6253	14.4642	13.3692	12.5481	12.4067	13.5922	12.9085	12.7687	11.9612	12.1247	11.9576	10.4974	11.5527
20	12.8837	23.2106	20.0271	18.4758	18.5022	16.3706	15.6759	16.8914	15.8821	15.2083	14.1161	14.2084	14.8475	14.0515	11.8171
21	11.1727	19.6072	16.0477	15.3576	14.9041	13.7514	13.3994	13.1284	12.9083	12.8595	11.0383	11.2651	10.7413	10.7250	9.6610
22	14.0524	16.6538	15.9564	16.9390	17.2434	17.0682	16.9612	18.3057	15.1896	15.6453	14.9577	15.4057	14.1404	14.5293	13.6113
26	8.5995	14.0461	12.6302	11.9551	11.0001	9.4513	9.5851	10.1186	9.5475	9.6030	8.4781	9.1482	8.2228	8.2000	8.0725
27	12.8952	21.4083	18.5482	18.3379	17.0620	15.1372	14.4920	15.7481	13.6963	14.5657	12.8078	13.6825	12.7901	13.3639	11.6439

Table A1.10: LA-ICP-MA data of the REE concentrations for E-Type MORB's.

ERRORS	Y	La	Ce	Pr	Nd	Sm	Eu	Gd	Tb	Dy	Ho	Er	Tm	Yb	Lu
	ppm	ppm	ppm	ppm	ppm	ppm	ppm	ppm	ppm	ppm	ppm	ppm	ppm	ppm	ppm
E-Type															
2	0.40254	0.93837	0.58192	1.32126	1.38595	2.35732	2.06473	2.05862	1.63329	1.41294	1.19439	1.27718	1.90731	1.67264	1.89779
3	0.30400	0.85286	0.49152	1.09020	1.11340	1.84102	1.58776	1.46603	1.36961	0.94771	1.06649	1.00462	1.55471	1.24179	1.45722
5	0.33579	0.95349	0.51786	1.11443	1.13776	1.78711	1.49758	1.52161	1.43099	1.08597	0.96783	1.06733	1.44823	1.20976	1.42644
8	0.37820	0.86390	0.55384	1.16397	1.22476	2.13414	1.86247	1.76932	1.58813	1.23578	1.13555	1.33058	1.68340	1.41891	1.61215
10	0.37025	0.92321	0.56009	1.22425	1.17216	1.91171	1.67636	1.71178	1.37805	1.09604	1.07303	1.21694	1.61720	1.35557	1.58243
11	0.43815	1.12276	0.64873	1.45158	1.48484	2.45850	2.18928	2.12083	1.72316	1.52598	1.39851	1.42101	2.06668	1.71411	1.97612
12	0.32534	0.93913	0.52287	1.17381	1.17520	1.89729	1.66478	1.70089	1.31886	1.15875	0.99853	1.03753	1.59548	1.26873	1.36307
14	0.43142	1.14698	0.71228	1.47985	1.45198	2.53285	1.94397	2.08356	1.65640	1.21894	1.35567	1.34754	2.03555	1.66469	1.86556
17	0.38769	0.93188	0.54137	1.24163	1.29545	2.16968	1.71089	1.83822	1.52994	1.13514	1.15567	1.24661	1.77229	1.38827	1.50150
18	0.41586	0.95976	0.55409	1.33441	1.41560	2.33323	2.04740	2.13345	1.64588	1.38244	1.26504	1.42777	1.83708	1.63743	1.84722
19	0.40824	0.90211	0.56484	1.35205	1.23970	2.29933	1.94206	1.97833	1.59509	1.21762	1.23898	1.29041	1.90783	1.42975	1.82995
20	0.43430	1.12331	0.72309	1.34628	1.65670	2.58720	1.94043	2.05179	1.86116	1.34558	1.42966	1.45674	2.23479	1.66300	1.78919
21	0.52733	1.15865	0.84639	1.70788	1.24390	1.98734	1.79385	1.81413	1.59987	1.19756	1.14649	1.33456	1.46120	1.30578	1.34596
22	0.46879	0.97339	0.60981	1.26161	1.31823	2.45400	2.17339	2.16005	1.84343	1.45904	1.39738	1.48822	1.98151	1.66914	1.89876
26	0.33515	0.89968	0.54370	1.07821	1.01165	1.91285	1.63724	1.55566	1.38964	1.03993	1.00479	1.11340	1.42035	1.28385	1.53495
27	0.40309	1.13243	0.67146	1.36382	1.40365	2.39822	1.85316	1.99939	1.73252	1.36309	1.28269	1.30527	1.98248	1.65063	1.82100

Table A1.11: LA-ICP-MA data of the errors on the REE concentrations for E-Type MORB's.

Appendix II – Minerals Major and Trace Elements

Sample	Mineral	Ti	Fe	Ni	Cr	Mn	Si	Al	Ca	Mg	O	K	S	Na	P	Total
		wt.%	wt.%	wt.%	wt.%	wt.%	wt.%	wt.%	wt.%	wt.%	wt.%	wt.%	wt.%	wt.%	wt.%	wt.%
2	Plagioclase 4	0.050	0.613			0.031	24.349	15.181	9.195	0.089	46.241	0.074		2.966		98.789
10	Plagioclase 2	0.031	0.570			0.018	23.093	16.206	10.323	0.048	45.926	0.093		2.408		98.716
14	Plagioclase 2	0.027	0.464			0.004	23.311	15.942	10.458	0.121	45.981	0.065		2.361		98.733
14	Plagioclase 4	0.046	0.689			0.000	24.528	14.951	8.955	0.109	46.204	0.104		3.076		98.636
19	Plagioclase 5	0.022	0.494			0.000	22.830	16.357	11.243	0.151	45.921	0.060		1.741		98.813
Samples with total wt.% of 97.5-102.5%																
Sample	**Mineral**	**Ti**	**Fe**	**Ni**	**Cr**	**Mn**	**Si**	**Al**	**Ca**	**Mg**	**O**	**K**	**S**	**Na**	**P**	**Total**
		wt.%	wt.%	wt.%	wt.%	wt.%	wt.%	wt.%	wt.%	wt.%	wt.%	wt.%	wt.%	wt.%	wt.%	wt.%
2	Plagioclase 1	0.051	0.775			0.000	24.133	15.142	9.062	0.070	46.003	0.113		3.155		98.495
2	Plagioclase 2	0.031	0.657			0.033	23.080	15.875	10.417	0.063	45.664	0.057		2.346		98.221
2	Plagioclase 3	0.053	0.597			0.038	24.291	14.965	8.890	0.089	45.939	0.080		3.189		98.131
10	Plagioclase 1	0.024	0.463			0.009	22.821	16.341	10.864	0.097	45.795	0.044		2.006		98.463

10	Plagioclase 3	0.044	0.492			0.000	24.103	15.276	8.982	0.071	45.954	0.151		3.085		98.146
14	Plagioclase 1	0.035	0.460			0.000	23.402	15.888	10.220	0.145	45.932	0.062		2.285		98.424
14	Plagioclase 3	0.027	0.413			0.003	22.891	16.068	10.750	0.154	45.624	0.053		2.040		98.023
14	Plagioclase 5	0.032	0.433			0.000	23.085	15.969	10.610	0.146	45.739	0.037		2.148		98.197
14	Plagioclase 6	0.027	0.387			0.000	22.529	16.251	11.075	0.161	45.436	0.050		1.876		97.767
14	Plagioclase 7	0.021	0.450			0.006	22.774	16.291	10.902	0.150	45.685	0.020		1.857		98.156
14	Plagioclase 8	0.061	0.614			0.000	25.051	14.443	8.055	0.081	46.113	0.129		3.491		98.024
19	Plagioclase 2	0.018	0.466			0.000	22.013	16.784	11.765	0.139	45.432	0.026		1.388		98.027
19	Plagioclase 3	0.021	0.446			0.031	22.467	16.477	11.431	0.151	45.656	0.029		1.675		98.383
19	Plagioclase 6	0.026	0.376			0.002	21.794	16.943	11.889	0.130	45.340	0.033		1.362		97.896
19	Plagioclase 7	0.018	0.418			0.000	22.154	16.614	11.600	0.153	45.421	0.016		1.562		97.926

Table A2.1: EMPA data of major element concentrations for plagioclases analysed.

Errors	Mineral	Ti	Fe	Ni	Cr	Mn	Si	Al	Ca	Mg	O	K	S	Na	P
Sample		wt.%	wt.%	wt.%	wt.%	wt.%	wt.%	wt.%	wt.%	wt.%	wt.%	wt.%	wt.%	wt.%	wt.%
2	Plagioclase 4	0.014	0.102			0.067	0.607	0.299	0.313	0.012		0.038		0.187	
10	Plagioclase 2	0.014	0.097			0.070	0.586	0.310	0.338	0.011		0.039		0.165	
14	Plagioclase 2	0.014	0.096			0.070	0.590	0.307	0.341	0.013		0.036		0.164	
14	Plagioclase 4	0.014	0.106			0.068	0.612	0.297	0.308	0.013		0.041		0.188	
19	Plagioclase 5	0.013	0.093			0.068	0.578	0.310	0.356	0.013		0.033		0.140	
Samples with total wt.% of 97.5-102.5%															
Errors	**Mineral**	**Ti**	**Fe**	**Ni**	**Cr**	**Mn**	**Si**	**Al**	**Ca**	**Mg**	**O**	**K**	**S**	**Na**	**P**
Sample		wt.%	wt.%	wt.%	wt.%	wt.%	wt.%	wt.%	wt.%	wt.%	wt.%	wt.%	wt.%	wt.%	wt.%
2	Plagioclase 1	0.014	0.110			0.068	0.604	0.299	0.310	0.011		0.039		0.192	
2	Plagioclase 2	0.014	0.103			0.068	0.586	0.307	0.340	0.011		0.035		0.165	
2	Plagioclase 3	0.014	0.102			0.061	0.606	0.296	0.305	0.012		0.039		0.193	
10	Plagioclase 1	0.013	0.092			0.069	0.582	0.312	0.350	0.012		0.036		0.153	
10	Plagioclase 3	0.014	0.098			0.069	0.604	0.300	0.308	0.011		0.044		0.190	
14	Plagioclase 1	0.014	0.094			0.064	0.592	0.307	0.336	0.013		0.036		0.161	
14	Plagioclase 3	0.014	0.090			0.065	0.583	0.309	0.348	0.014		0.034		0.152	

14	Plagioclase 5	0.013	0.091			0.069	0.586	0.308	0.344	0.013		0.036		0.156	
14	Plagioclase 6	0.013	0.088			0.072	0.577	0.311	0.355	0.014		0.034		0.145	
14	Plagioclase 7	0.014	0.089			0.065	0.581	0.312	0.351	0.013		0.037		0.143	
14	Plagioclase 8	0.014	0.100			0.072	0.621	0.290	0.287	0.012		0.042		0.203	
19	Plagioclase 2	0.013	0.092			0.074	0.567	0.317	0.370	0.013		0.032		0.125	
19	Plagioclase 3	0.013	0.089			0.069	0.575	0.314	0.362	0.014		0.034		0.137	
19	Plagioclase 6	0.014	0.088			0.068	0.564	0.319	0.373	0.013		0.031		0.126	
19	Plagioclase 7	0.013	0.091			0.074	0.571	0.316	0.366	0.014		0.033		0.133	

Table A2.2: EMPA data of the errors on the major element concentrations for plagioclases analysed.

Sample	Mineral	Ti	Fe	Ni	Cr	Mn	Si	Al	Ca	Mg	O	K	S	Na	P	Total
		wt.%	wt.%	wt.%	wt.%	wt.%	wt.%	wt.%	wt.%	wt.%	wt.%	wt.%	wt.%	wt.%	wt.%	wt.%
2	Pyroxene 1	0.271	5.078		0.206	0.157	24.535	0.913	14.142	10.378	43.069	0.000		0.141		98.888
2	Pyroxene 2	0.364	4.732		0.599	0.145	23.775	1.895	14.281	9.968	43.013	0.005		0.169		98.944
2	Pyroxene 3	0.241	4.374		0.374	0.128	24.838	1.024	14.514	10.427	43.535	0.000		0.125		99.573
2	Pyroxene 4	0.375	4.591		0.560	0.097	23.975	1.738	14.854	9.812	43.162	0.003		0.166		99.332
2	Pyroxene 5	0.380	4.966		0.337	0.127	23.992	1.624	14.688	9.674	42.937	0.000		0.169		98.883
2	Pyroxene 7	0.270	5.221		0.174	0.159	24.520	0.919	13.907	10.465	43.058	0.001		0.170		98.864
2	Pyroxene 8	0.340	4.147		0.989	0.107	23.600	2.105	14.776	9.632	42.960	0.000		0.165		98.815
10	Pyroxene 1	0.445	5.186		0.572	0.141	23.911	1.477	13.290	10.407	42.873	0.010		0.198		98.509
10	Pyroxene 2	0.260	4.145		0.530	0.120	24.488	1.063	14.402	10.457	43.187	0.004		0.191		98.846
10	Pyroxene 3	0.318	4.064		0.837	0.126	24.035	1.717	14.491	10.127	43.232	0.013		0.194		99.153
10	Pyroxene 5	0.349	3.943		0.771	0.096	24.176	1.685	14.699	9.853	43.215	0.011		0.197		98.995
14	Pyroxene 1	0.468	7.877		0.061	0.185	24.158	1.054	12.599	9.654	42.554	0.000		0.159		98.767
14	Pyroxene 2	0.507	6.257		0.159	0.150	23.872	1.572	13.742	9.597	42.704	0.007		0.152		98.719

14	Pyroxene 3	0.560	4.596		0.627	0.123	23.506	2.206	14.565	9.379	42.807	0.000		0.172		98.535
14	Pyroxene 5	0.485	4.703		0.310	0.151	23.734	1.831	14.831	9.615	42.836	0.005		0.159		98.660
14	Pyroxene 6	0.550	7.146		0.038	0.198	23.850	1.419	13.523	9.391	42.562	0.000		0.165		98.840
14	Pyroxene 7	0.465	5.090		0.303	0.148	23.872	1.823	14.275	9.751	42.948	0.010		0.162		98.845
14	Pyroxene 8	0.465	5.705		0.250	0.137	23.940	1.673	14.183	9.753	43.000	0.002		0.151		99.259
14	Pyroxene 9	0.564	4.856		0.380	0.112	23.930	2.025	14.533	9.469	43.149	0.018		0.193		99.229
19	Pyroxene 2	0.363	4.184		0.649	0.141	23.857	2.015	14.715	9.739	43.101	0.000		0.175		98.928
Samples with total wt.% of 97.5-102.5%																
2	Pyroxene 6	0.327	4.183		0.723	0.100	23.533	1.953	14.912	9.718	42.734	0.000		0.163		98.333
10	Pyroxene 4	0.335	4.149		0.881	0.116	23.789	1.658	14.094	10.108	42.781	0.005		0.195		98.111
14	Pyroxene 4	0.448	5.332		0.259	0.149	23.895	1.648	13.882	9.706	42.666	0.000		0.160		98.141
19	Pyroxene 1	0.207	4.557		0.469	0.178	24.556	1.130	12.934	11.032	43.171	0.009		0.140		98.381

Table A2.3: EMPA data of major element concentrations for pyroxenes analysed.

Errors	Mineral	Ti	Fe	Ni	Cr	Mn	Si	Al	Ca	Mg	O	K	S	Na	P
wt.%	wt.%	wt.%	wt.%	wt.%	wt.%	wt.%	wt.%	wt.%	wt.%	wt.%	wt.%	wt.%	wt.%	wt.%	wt.%
2	Pyroxene 1	0.015	0.267		0.050	0.059	0.512	0.029	0.356	0.198		0.022		0.038	
2	Pyroxene 2	0.016	0.255		0.074	0.057	0.499	0.044	0.358	0.192		0.021		0.039	
2	Pyroxene 3	0.014	0.245		0.061	0.057	0.517	0.031	0.363	0.198		0.021		0.036	
2	Pyroxene 4	0.017	0.251		0.072	0.059	0.503	0.042	0.370	0.190		0.021		0.039	
2	Pyroxene 5	0.017	0.262		0.058	0.058	0.503	0.040	0.367	0.189		0.021		0.040	
2	Pyroxene 7	0.015	0.269		0.050	0.059	0.511	0.029	0.350	0.198		0.021		0.038	
2	Pyroxene 8	0.016	0.237		0.090	0.052	0.496	0.047	0.368	0.188		0.020		0.039	
10	Pyroxene 1	0.018	0.270		0.071	0.059	0.503	0.038	0.338	0.198		0.022		0.043	
10	Pyroxene 2	0.014	0.237		0.069	0.055	0.511	0.032	0.361	0.198		0.021		0.041	
10	Pyroxene 3	0.015	0.235		0.084	0.055	0.504	0.042	0.362	0.194		0.021		0.041	
10	Pyroxene 5	0.016	0.232		0.081	0.056	0.506	0.041	0.367	0.190		0.021		0.041	
14	Pyroxene 1	0.018	0.342		0.041	0.064	0.506	0.032	0.324	0.190		0.022		0.038	
14	Pyroxene 2	0.019	0.299		0.048	0.061	0.501	0.039	0.347	0.188		0.021		0.038	
14	Pyroxene 3	0.020	0.252		0.075	0.056	0.495	0.049	0.364	0.185		0.022		0.039	

14	Pyroxene 5	0.019	0.255		0.058	0.058	0.499	0.043	0.369	0.188		0.021		0.039	
14	Pyroxene 6	0.020	0.322		0.040	0.061	0.501	0.037	0.343	0.186		0.022		0.039	
14	Pyroxene 7	0.018	0.265		0.057	0.059	0.501	0.043	0.358	0.190		0.022		0.040	
14	Pyroxene 8	0.018	0.284		0.054	0.056	0.502	0.041	0.356	0.190		0.021		0.039	
14	Pyroxene 9	0.020	0.260		0.061	0.058	0.502	0.046	0.364	0.186		0.021		0.039	
19	Pyroxene 2	0.016	0.239		0.075	0.059	0.501	0.046	0.367	0.189		0.022		0.039	
Samples with total wt.% of 97.5-102.5%															
2	Pyroxene 6	0.016	0.239		0.079	0.056	0.495	0.045	0.371	0.189		0.020		0.039	
10	Pyroxene 4	0.016	0.237		0.085	0.056	0.500	0.041	0.355	0.194		0.021		0.040	
14	Pyroxene 4	0.018	0.275		0.054	0.057	0.502	0.041	0.350	0.189		0.022		0.039	

Table A2.4: EMPA data of the errors on the major element concentrations for pyroxenes analysed.

Laser Number	TiO2	FeO	NiO	Cr2O3	MnO	SiO2	Al2O3	CaO	MgO	Total
	wt.%	wt.%	wt.%	wt.%	wt.%	wt.%	wt.%	wt.%	wt.%	wt.%
Sample 2										
2_1_R	0.0116	15.0588	0.2894	0.0833	0.2078	38.7527	0.0798	0.3239	44.0759	98.8833
2_10_C	0.0043	13.6468	0.2861	0.0643	0.2147	39.2713	0.0449	0.3478	45.2641	99.1444
2_3_C	0.0065	13.5191	0.2799	0.0316	0.196	39.4124	0.0428	0.345	45.5798	99.413
2_4_C	0.0035	14.1014	0.263	0.0507	0.2256	39.5041	0.0437	0.3445	45.1015	99.6381
2_5_C	0.009	13.8564	0.2742	0.0586	0.1722	39.6144	0.0475	0.3258	45.1719	99.53
2_6_C	0.0051	14.4351	0.2567	0.0533	0.2024	39.6173	0.121	0.3614	44.1505	99.2029
2_7_R	0.0071	13.6209	0.2814	0.0585	0.2109	39.7958	0.0767	0.3168	45.2613	99.6294
Sample 10										
10_1_C	0.0183	15.8681	0.2757	0.0219	0.246	39.7084	0.0452	0.2777	43.5788	100.04
10_2_C	0.0156	13.3237	0.3073	0.0532	0.1832	40.0458	0.0781	0.317	45.6672	99.9911
10_3_C	0.0163	15.8419	0.3011	0.0526	0.2325	39.8209	0.0699	0.2939	43.4821	100.1112
10_4_C	0.0078	17.4728	0.2758	0.0458	0.2742	39.3979	0.0524	0.3121	42.3667	100.2054
Sample 14										
14_1_C	0.0011	12.2629	0.2934	0.0449	0.1862	40.009	0.0455	0.3085	46.3947	99.5463
14_10_C	0.011	9.7032	0.3825	0.1447	0.1255	40.9233	0.1247	0.3	47.9708	99.6857
14_2_C	0.0094	13.466	0.2896	0.1022	0.178	39.815	0.0796	0.3137	45.1344	99.3879
14_3_C	0.0109	10.586	0.3141	0.0819	0.1845	40.5793	0.0582	0.3172	47.6457	99.7777
14_4_C	0.0048	13.489	0.3228	0.0751	0.2083	39.944	0.0735	0.3028	45.4412	99.8613
14_5_R	0.011	13.8415	0.2396	0.0177	0.2261	39.7389	0.0583	0.3625	45.2366	99.7323
14_6_C	0.0114	12.0402	0.3653	0.0848	0.1748	40.0952	0.0794	0.2815	46.2955	99.428
14_7_C	0.0097	12.9828	0.2835	0.0369	0.198	40.1886	0.0495	0.3136	45.9065	99.969
14_8	0.0425	29.9187	0.1458	0.003	0.4391	36.4312	0.0399	0.2838	31.5214	98.8254
14_9	0.0116	13.9857	0.2481	0.0566	0.2006	40.1296	0.0512	0.3194	44.8157	99.8184
Sample 16										

16_1_C	0.0041	10.6723	0.3656	0.0741	0.1542	40.5842	0.0583	0.3318	47.9824	100.2271
16_2_C	0.0037	10.7641	0.3662	0.0689	0.1837	41.0306	0.0603	0.326	47.9096	100.7133
16_4_C	0.0027	10.7923	0.3568	0.053	0.1582	41.0898	0.0606	0.3405	48.1264	100.9804
16_5_C	0.0192	12.8483	0.2982	0.0411	0.1461	40.1216	0.0677	0.3539	46.3564	100.2524
Sample 19										
19_1_C	0.0157	12.815	0.2938	0.0802	0.2028	40.0149	0.1009	0.3483	46.1644	100.036
19_10_3	0.0089	12.3288	0.3144	0.0379	0.1986	40.5898	0.0549	0.3586	45.8662	99.7581
19_11_C	0.0198	10.5701	0.3295	0.0941	0.1661	40.0728	0.127	0.3483	47.4669	99.1945
19_12_C	0.0114	10.7245	0.3461	0.1122	0.1834	40.5436	0.0823	0.3145	47.3325	99.6504
19_13_C	0.0224	12.5205	0.2964	0.089	0.1945	39.9684	0.1122	0.3381	45.843	99.3844
19_14_C	0.0086	12.2115	0.3365	0.0484	0.1776	40.2844	0.0796	0.3417	46.4433	99.9316
19_15_C	0.0126	12.1517	0.2669	0.0484	0.1863	40.2682	0.0817	0.3519	46.3734	99.7412
19_3_C	0.012	12.8292	0.2988	0.0804	0.2178	40.0895	0.0629	0.3505	45.8879	99.8291
19_4_C	0.0132	12.5703	0.3213	0.0567	0.1715	40.0714	0.0495	0.3438	46.1679	99.7657
19_6_C	0.0118	13.8838	0.2433	0.0336	0.1762	40.0631	0.046	0.3918	44.791	99.6406
19_7_C	0.011	12.2593	0.3127	0.0641	0.1794	40.0901	0.0729	0.3548	46.0648	99.4091
19_8-_C	0.013	12.5811	0.3256	0.0675	0.186	39.5266	0.0748	0.3485	45.8424	98.9656

Table A2.5: EMPA data of the major element concentrations for the olivine cores analysed.

Samples	**La**	**Ce**	**Sm**	**Eu**	**Gd**	**Yb**	**Lu**
Sample 2 Olivine's	ppm	ppm	ppm	ppm	ppm	ppm	ppm
Oliv-2-1-R	0.164842	0.213027	0.247576	0.247209	0.28556	0.522946	0.646317
Oliv-2-10-C	0.004015	0.001764	0.010875	Below LOD	0.019513	0.306018	0.418461
Oliv-2-3-C	0.015358	0.009191	0.009661	0.018093	0.022827	0.2808	0.397635
Oliv-2-4-C	0.089873	0.044832	0.053805	0.063105	0.074818	0.313505	0.428235
Oliv-2-5-C	0.057658	0.03901	0.042003	0.043625	0.042835	0.2787	0.368837

Oliv-2-6-C	0.08321	0.078415	0.047306	0.048613	0.051464	0.359675	0.489654
Oliv-2-7-R	0.37181	0.190373	0.190206	0.218007	0.174276	0.416607	0.505733
Sample 10 Olivine's							
Oliv-10-1-C	0.02751	0.04127	0.069304	0.083923	0.077267	0.388479	0.491193
Oliv-10-2-C	0.03759	0.021355	0.02591	0.022634	0.03536	0.358074	0.521695
Oliv-10-3-C	0.067507	0.035264	0.02817	0.024947	0.027216	0.400664	0.559305
Oliv-10-4-C	0.076622	0.053075	0.037327	0.023959	0.055628	0.46834	0.576695
Sample 14 Olivine's							
Oliv-14-1-C	Below LOD	0.001152	0.008059	0.008914	0.017804	0.290865	0.406386
Oliv-14-10-C	0.001013	0.001046	0.008781	0.00554	0.014698	0.299966	0.432638
Oliv-14-2-C	0.033545	0.153433	0.020939	0.021019	0.026612	0.342646	0.480366
Oliv-14-3-C	Below LOD	0.0015	Below LOD	Below LOD	Below LOD	0.264908	0.327428
Oliv-14-4-C	0.032813	0.021912	0.028028	0.028716	0.027959	0.364588	0.569395
Oliv-14-5-R	0.020644	0.023197	0.022361	0.027676	0.035476	0.274591	0.388626
Oliv-14-6-C	0.044092	0.047111	0.014964	0.021929	0.028893	0.317503	0.434835
Oliv-14-7-C	0.119269	0.647311	0.057304	0.054881	0.070034	0.337858	0.452667
Oliv-14-9-C	0.031078	0.038672	0.020459	0.021394	0.026538	0.307539	0.437556
Sample 16 Olivine's							
Oliv-16-1-C	0.069502	0.152856	0.098715	0.083573	0.110342	0.372375	0.515309
Oliv-16-2-C	0.799928	0.871651	0.727362	0.821775	0.555422	0.814375	0.829547
Oliv-16-4-C	0.081899	0.286353	0.07157	0.073722	0.050029	0.296786	0.381714
Oliv-16-5-C	Below LOD	Below LOD	Below LOD	Below LOD	0.020504	0.264907	0.381202

Sample 19 Olivine's							
Oliv-19-1-C	0.0787	0.126844	0.018496	0.019927	0.041042	0.333565	0.480379
Oliv-19-10-3	1.087363	1.153946	0.799368	0.776696	0.774217	0.863077	1.041169
Oliv-19-12-C	3.533579	11.37779	2.851971	2.711179	2.609334	2.844222	2.70958
Oliv-19-13-C	0.014499	0.029719	0.01253	0.017638	0.036176	0.282721	0.487066
Oliv-19-14-C	0.029769	0.039531	0.01199	0.021633	0.028136	0.406812	0.552243
Oliv-19-15-C	0.159824	1.040754	0.080617	0.0626	0.091113	0.437958	0.538877
Oliv-19-16-C	0.291333	0.21594	0.066874	0.10443	0.08794	0.38088	0.474733
Oliv-19-3-C	0.206238	0.302681	0.066429	0.037373	0.053814	0.404172	0.418877
Oliv-19-4-C	0.040837	0.13821	0.032831	0.014586	0.048729	0.345616	0.423407
Oliv-19-6-C	0.482646	0.320439	0.158604	0.136618	0.114103	0.392876	0.534374
Oliv-19-7-C	2.467622	8.46633	0.963114	1.549671	0.878098	0.934603	1.019152
Oliv-19-8-C	1.311167	0.889645	0.333684	0.227568	0.265862	0.451055	0.584601

Table A2.6: LA-ICP-MS data of the REE concentrations for the olivine cores analysed. *Only REE'S La, Ce, Sm, Eu, Gd, Yb and Lu were analysed due to the thin sections not being thick enough to allow a full analysis.*

ERRORS	La	Ce	Sm	Eu	Gd	Yb	Lu
Sample 2 Olivine's	ppm	ppm	ppm	ppm	ppm	ppm	ppm
Oliv-2-1-R	0.029594	0.035587	0.069158	0.067867	0.079233	0.063473	0.06584
Oliv-2-10-C	0.002364	0.000733	0.008421	0.003828	0.007091	0.024858	0.040673
Oliv-2-3-C	0.005206	0.003565	0.004949	0.005992	0.005745	0.016918	0.022654
Oliv-2-4-C	0.01342	0.008637	0.012184	0.011302	0.0139	0.019402	0.032879
Oliv-2-5-C	0.009388	0.005717	0.010697	0.011645	0.008593	0.016451	0.023663
Oliv-2-6-C	0.006306	0.004412	0.011906	0.008108	0.008774	0.021936	0.029448
Oliv-2-7-R	0.023024	0.021798	0.023698	0.020733	0.018413	0.023248	0.027661
Sample 10 Olivine's							
Oliv-10-1-C	0.004098	0.004189	0.017732	0.014	0.012766	0.023825	0.037548
Oliv-10-2-C	0.004738	0.001784	0.008791	0.007593	0.008075	0.026258	0.035581
Oliv-10-3-C	0.008398	0.004289	0.010774	0.01067	0.010819	0.035212	0.048015
Oliv-10-4-C	0.015087	0.011642	0.011207	0.008495	0.01398	0.031282	0.029681
Sample 14 Olivine's							
Oliv-14-1-C	0.00156	0.00134	0.004336	0.004422	0.004532	0.018283	0.026612
Oliv-14-10-C	0.000986	0.000522	0.005028	0.003679	0.006413	0.023783	0.032629
Oliv-14-2-C	0.007793	0.028035	0.006611	0.005088	0.007731	0.021614	0.028059
Oliv-14-3-C	0.002058	0.000677	0.004208	0.004676	0.004127	0.019885	0.025122
Oliv-14-4-C	0.011291	0.007438	0.010418	0.009595	0.007033	0.026776	0.034455
Oliv-14-5-R	0.004472	0.005107	0.007484	0.008381	0.008543	0.01898	0.025579
Oliv-14-6-C	0.005861	0.003889	0.005502	0.005927	0.006876	0.020764	0.029949
Oliv-14-7-C	0.058669	0.047217	0.019732	0.01879	0.020083	0.021858	0.033734
Oliv-14-9-C	0.009483	0.011597	0.007233	0.006098	0.007072	0.022217	0.025308
Sample 16 Olivine's							

Oliv-16-1-C	0.013944	0.015681	0.029483	0.022086	0.032711	0.038675	0.041665
Oliv-16-2-C	0.196119	0.211252	0.239528	0.165492	0.156588	0.182806	0.13099
Oliv-16-4-C	0.013794	0.014445	0.030355	0.021984	0.013746	0.035659	0.045707
Oliv-16-5-C	0.000594	0.000318	0.004378	0.005382	0.006195	0.023947	0.037472
Sample 19 Olivine's							
Oliv-19-1-C	0.034696	0.026481	0.020291	0.011524	0.015782	0.049322	0.05274
Oliv-19-10-3	0.092785	0.14043	0.15853	0.115272	0.201722	0.12878	0.176642
Oliv-19-12-C	0.908645	4.669247	0.531712	0.580377	0.596414	0.894917	0.752531
Oliv-19-13-C	0.007101	0.019063	0.017519	0.011734	0.027767	0.062667	0.12507
Oliv-19-14-C	0.01228	0.006168	0.011557	0.013239	0.011896	0.058478	0.053332
Oliv-19-15-C	0.022303	0.196325	0.036134	0.013137	0.029026	0.053531	0.066419
Oliv-19-16-C	0.059711	0.032378	0.025417	0.044788	0.035034	0.048102	0.078561
Oliv-19-3-C	0.041804	0.140321	0.047232	0.025814	0.023223	0.042374	0.043225
Oliv-19-4-C	0.010236	0.012484	0.022404	0.008877	0.024573	0.04914	0.075272
Oliv-19-6-C	0.509497	0.303849	0.173515	0.110663	0.089377	0.041288	0.117509
Oliv-19-7-C	0.308049	1.972546	0.2026	1.214782	0.176271	0.101987	0.175298
Oliv-19-8-C	0.084421	0.059675	0.086607	0.014424	0.066576	0.063846	0.151509

Table A2.7: LA-ICP-MS data of errors on the REE concentrations for the olivine cores analysed.

Appendix III – QEMSCAN IMAGES

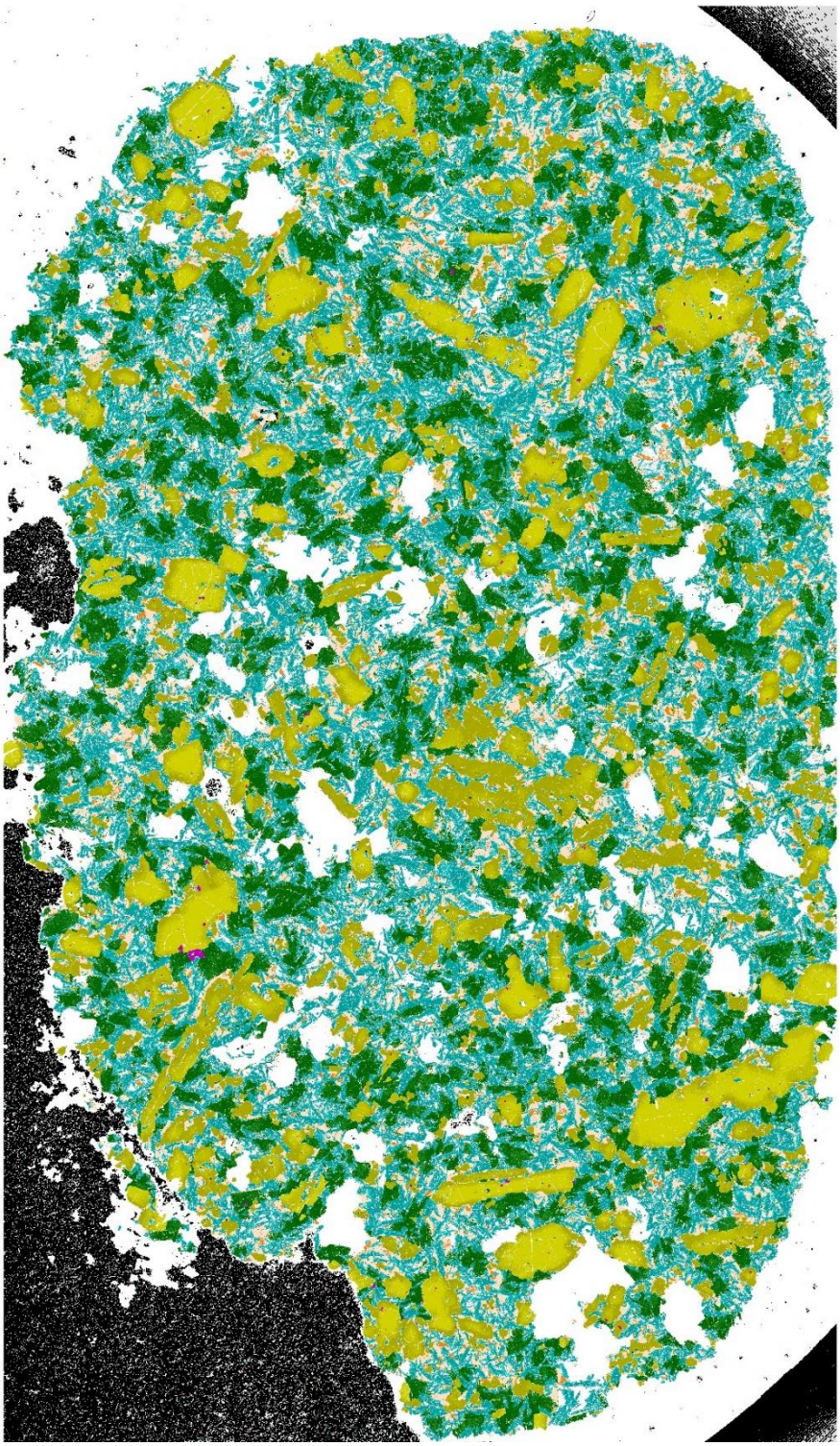

Figure: A3.1: QEMSCAN of Sample 2.

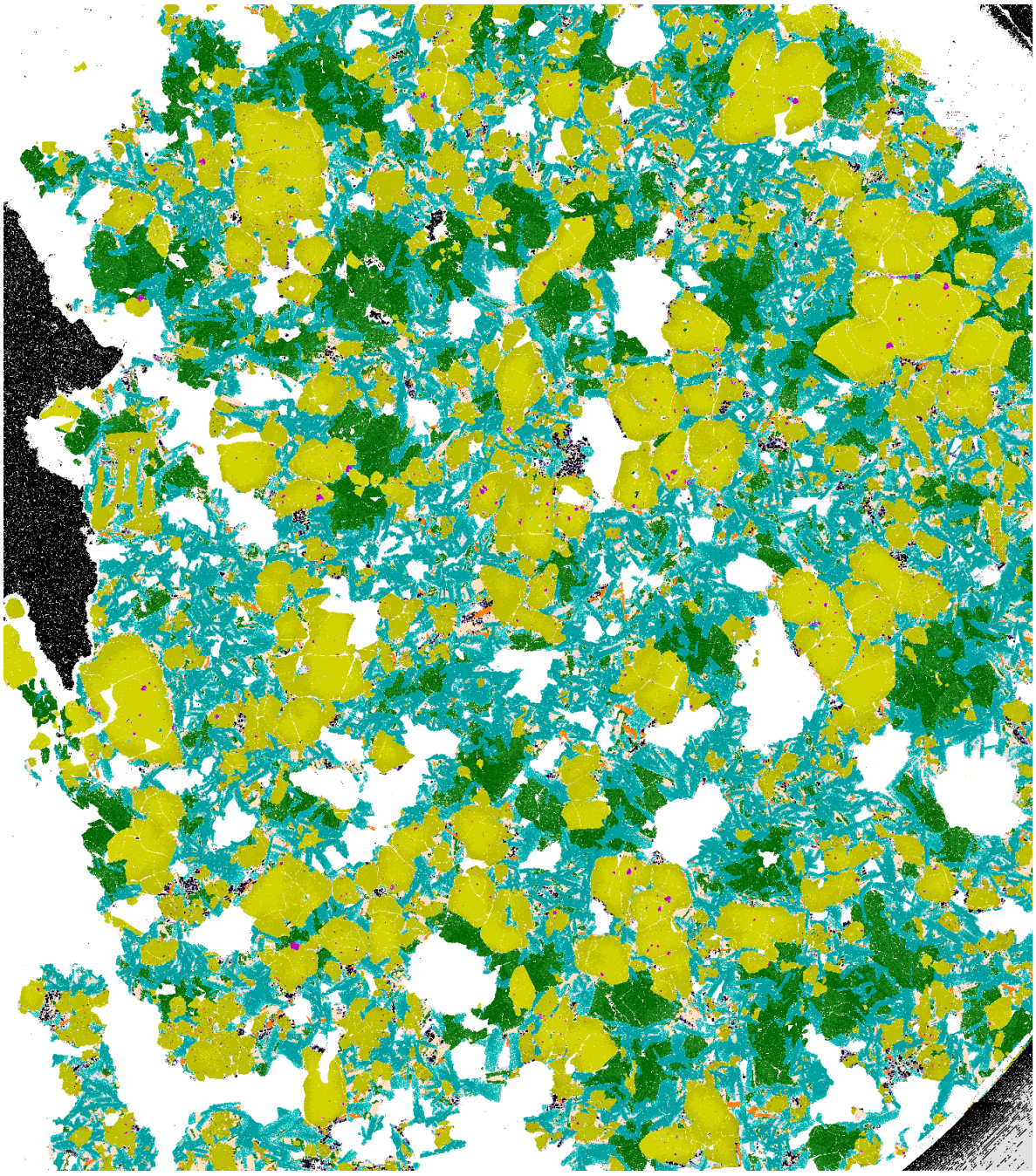

Figure A3.2: QEMSCAN of Sample 10.

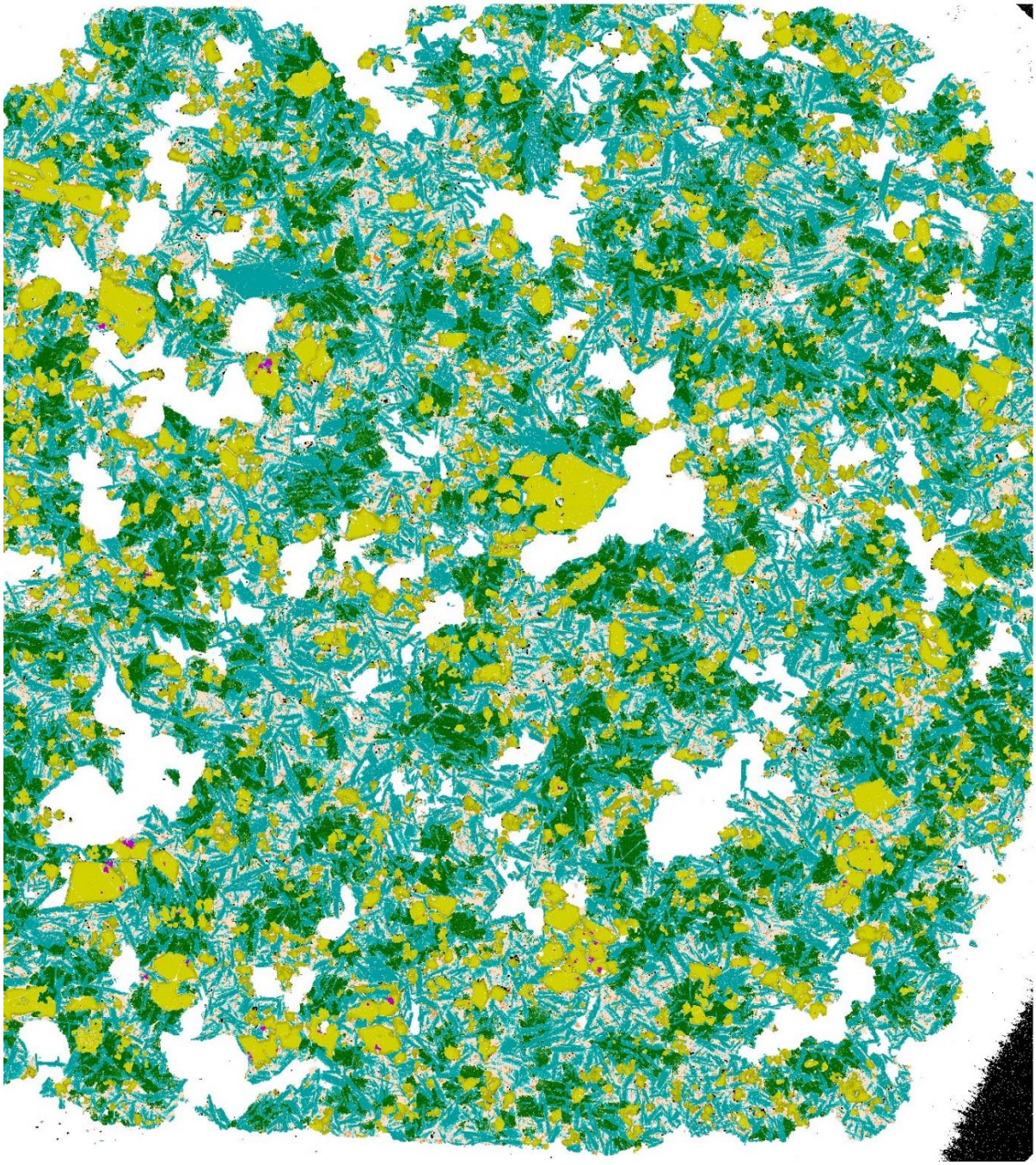

Figure A3.3: QEMSCAN of Sample 14.

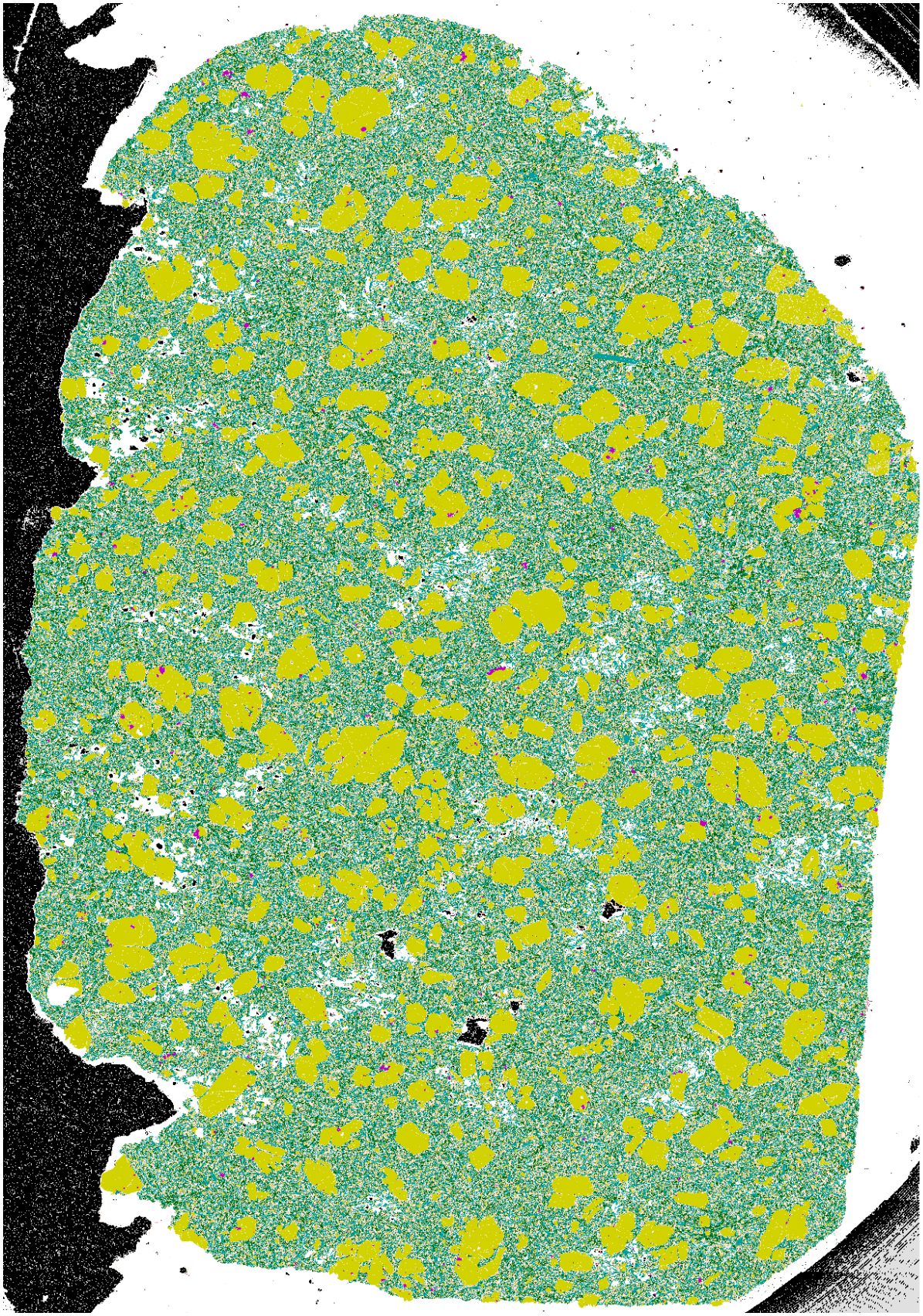

Figure A3.4: QEMSCAN of Sample 16.

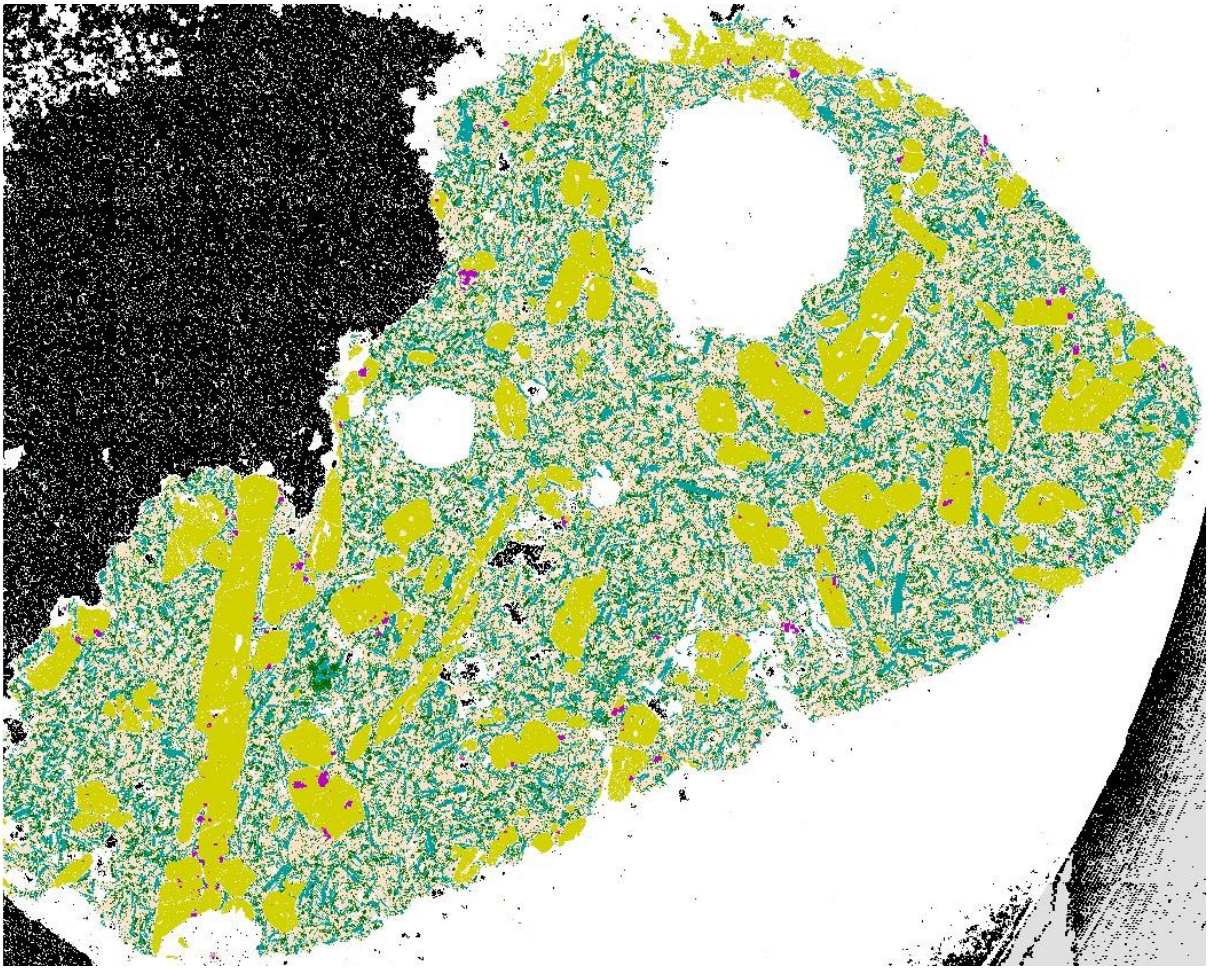

Figure A3.5: QEMSCAN of Sample 19.

Appendix IV – SEM Backscatter Images

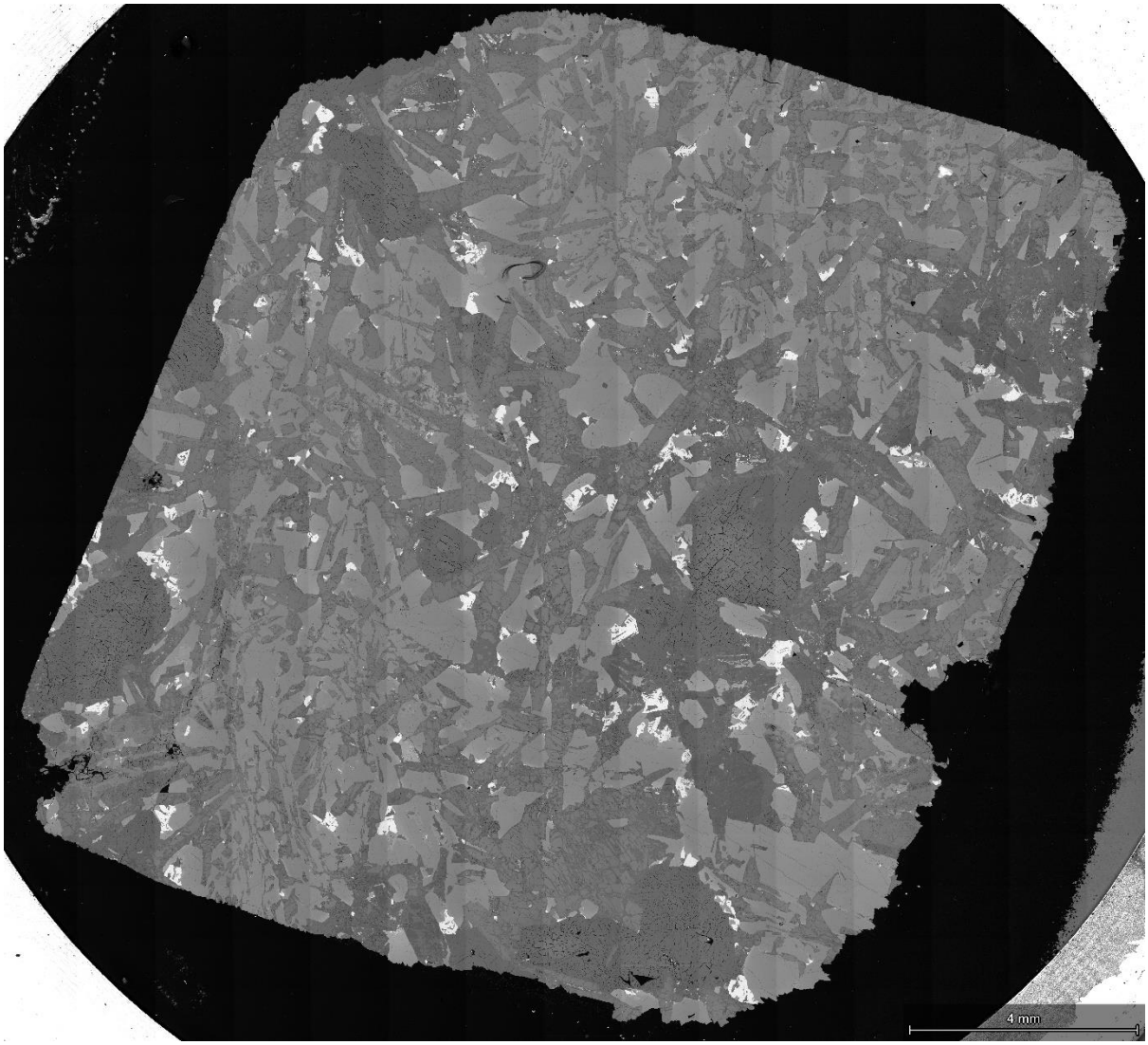

Figure A4.1: SEM Backscatter Image of Sample 1.

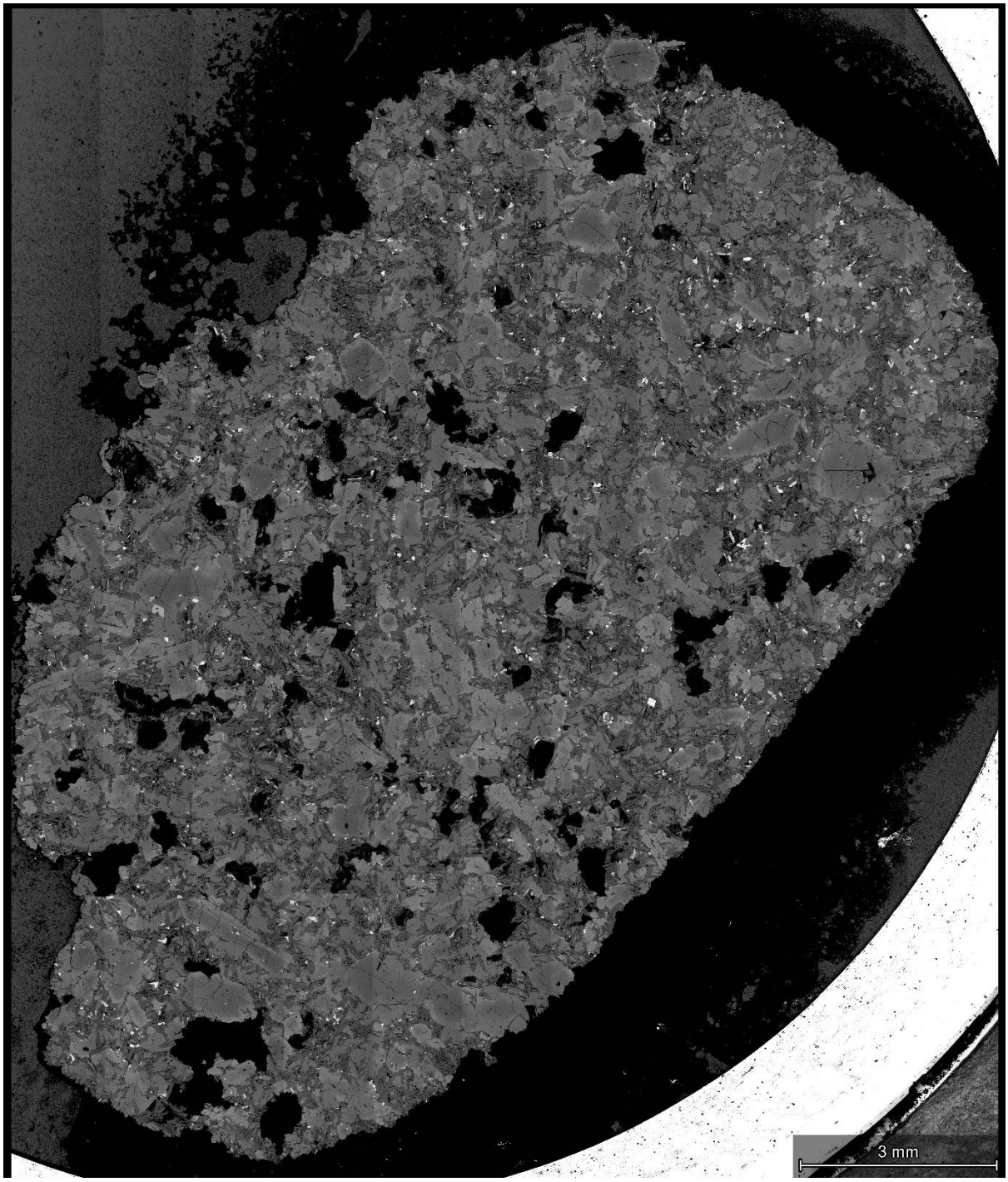

Figure A4.2: SEM Backscatter Image of Sample 2.

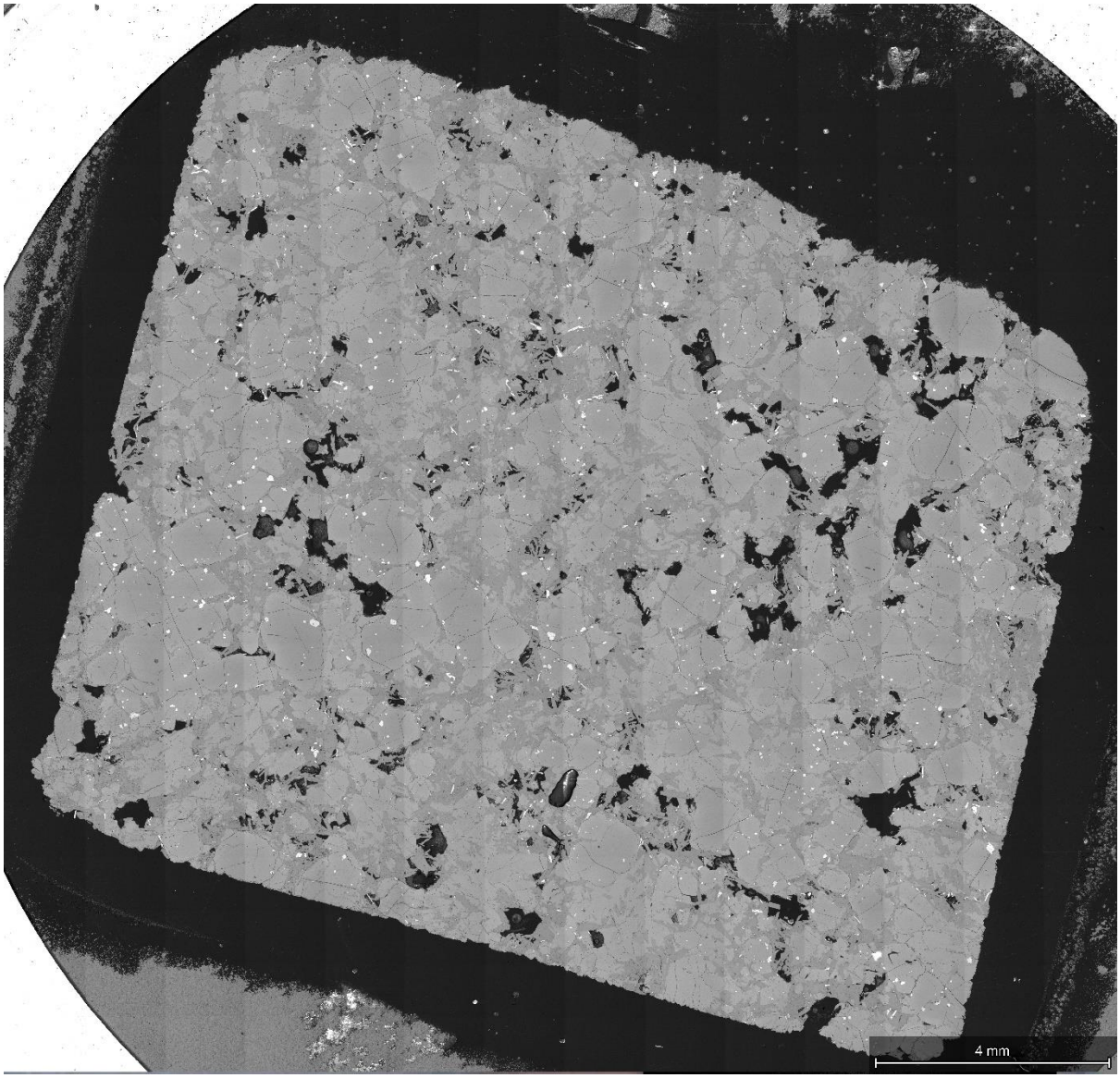

Figure A4.3: SEM Backscatter Image of Sample 3.

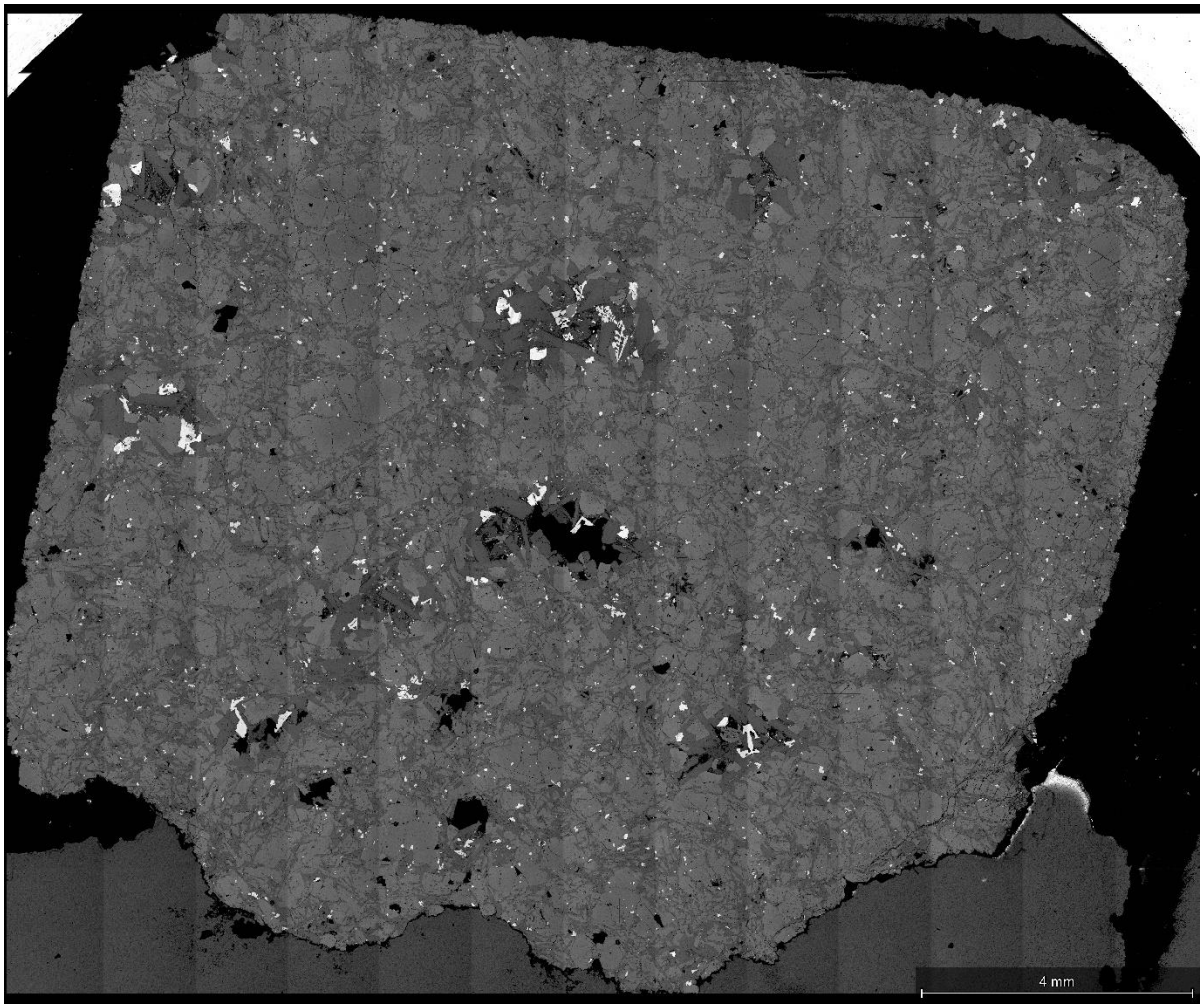

Figure A4.4: SEM Backscatter Image of Sample 4.

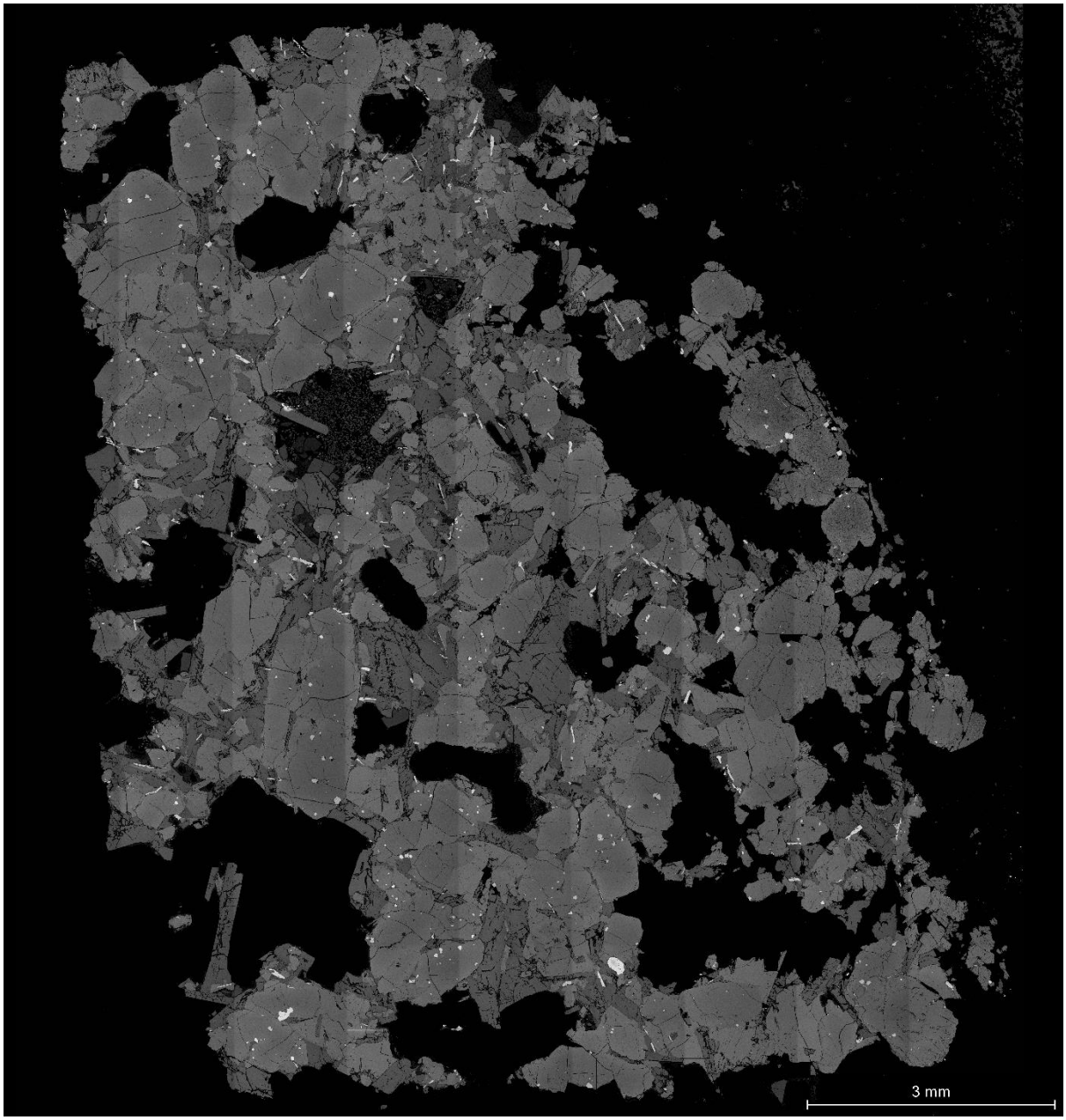

Figure A4.5: SEM Backscatter Image of Sample 5.

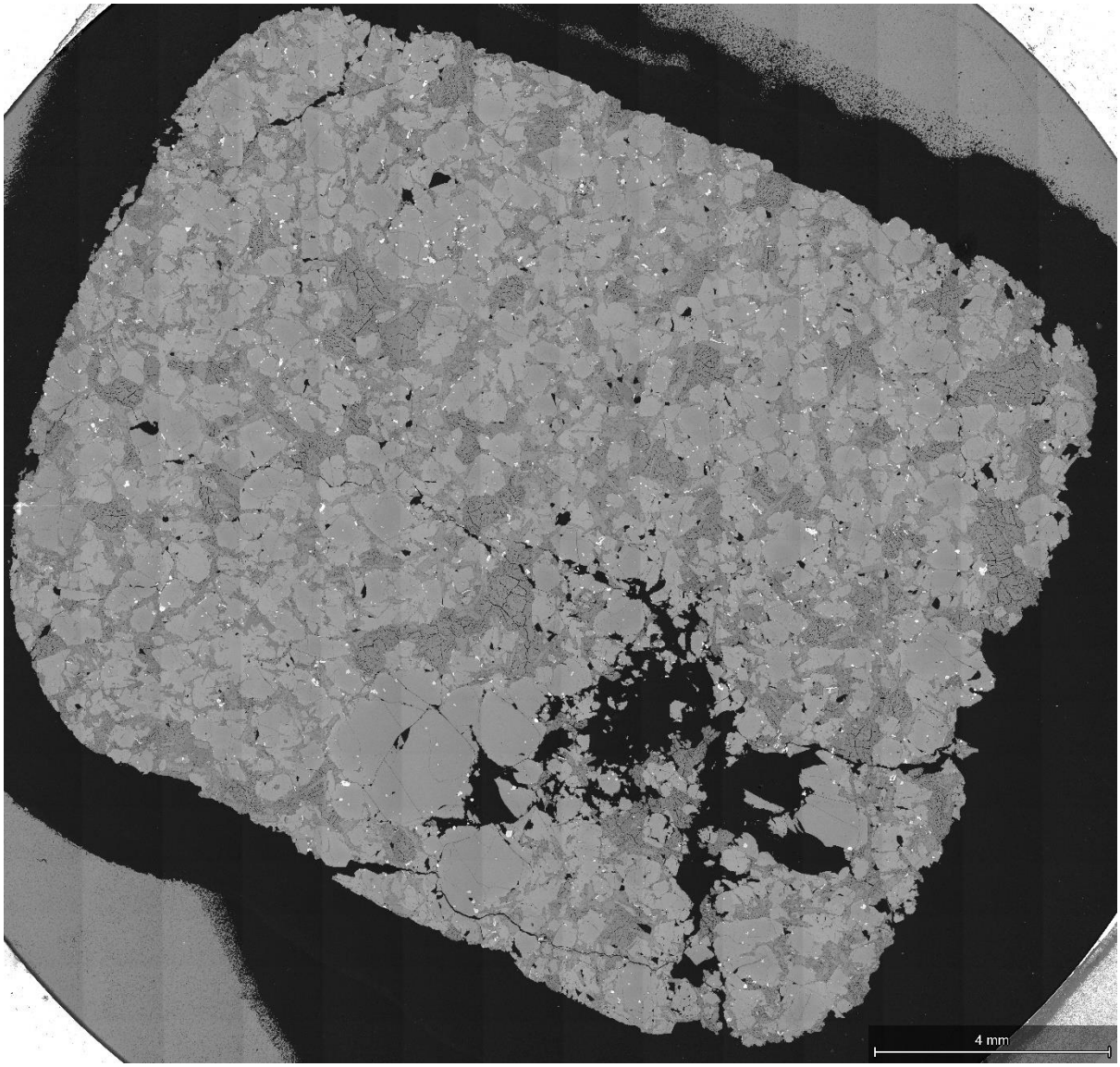

Figure A4.6: SEM Backscatter Image of Sample 6.

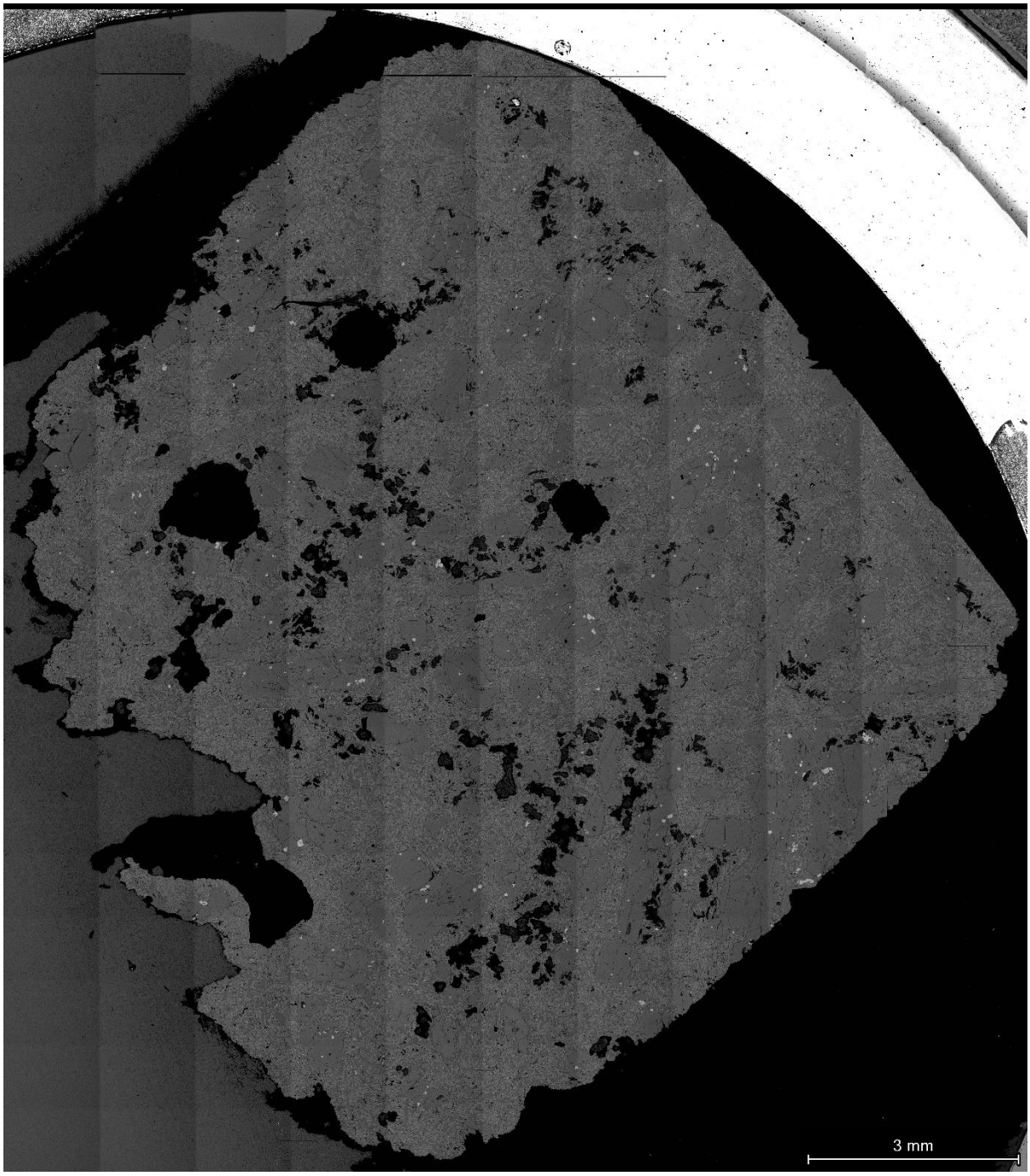

Figure A4.7: SEM Backscatter Image of Sample 7.

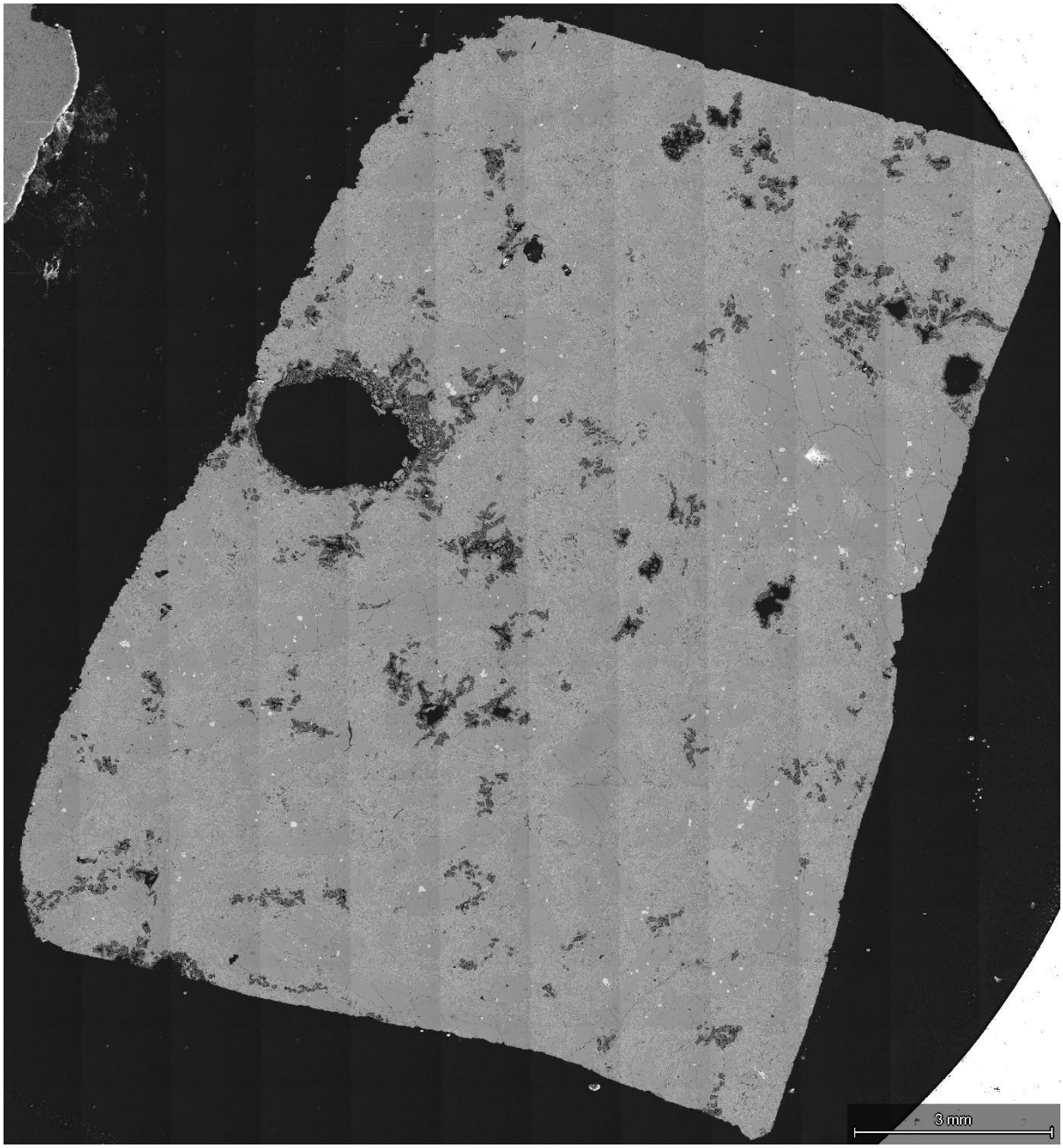

Figure A4.8: SEM Backscatter Image of Sample 8.

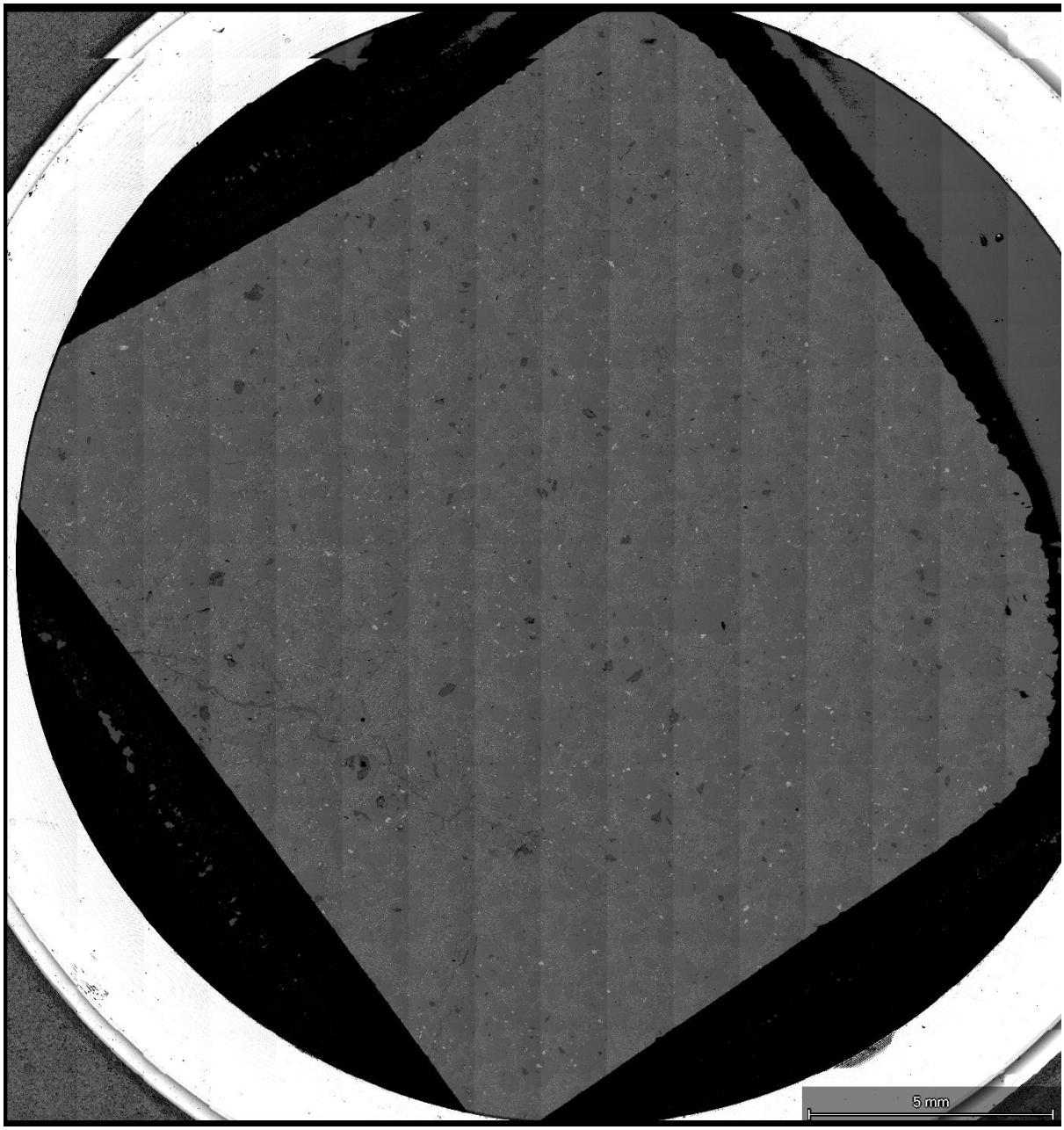

Figure A4.9: SEM Backscatter Image of Sample 9.

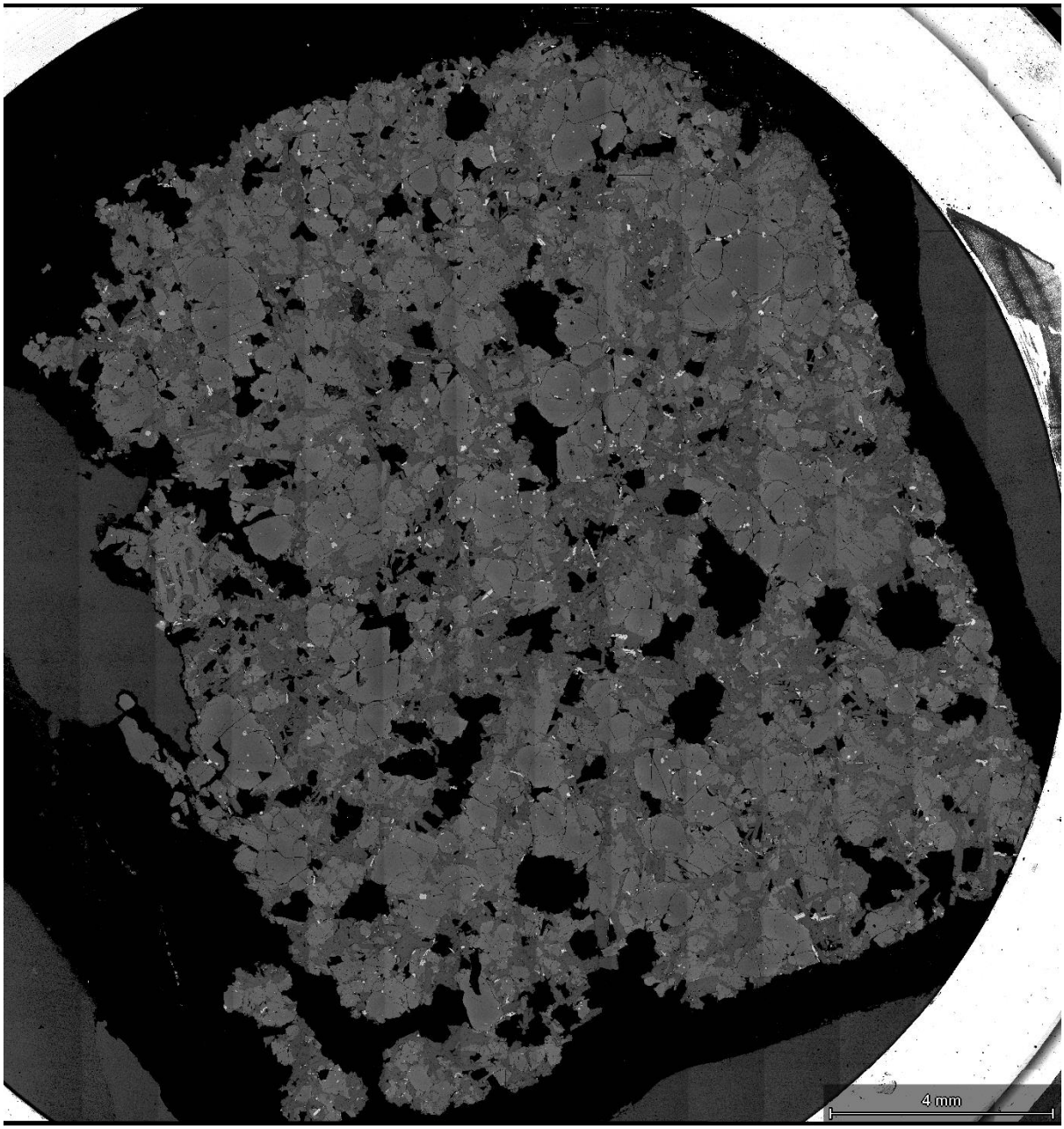

Figure A4.10: SEM Backscatter Image of Sample 10.

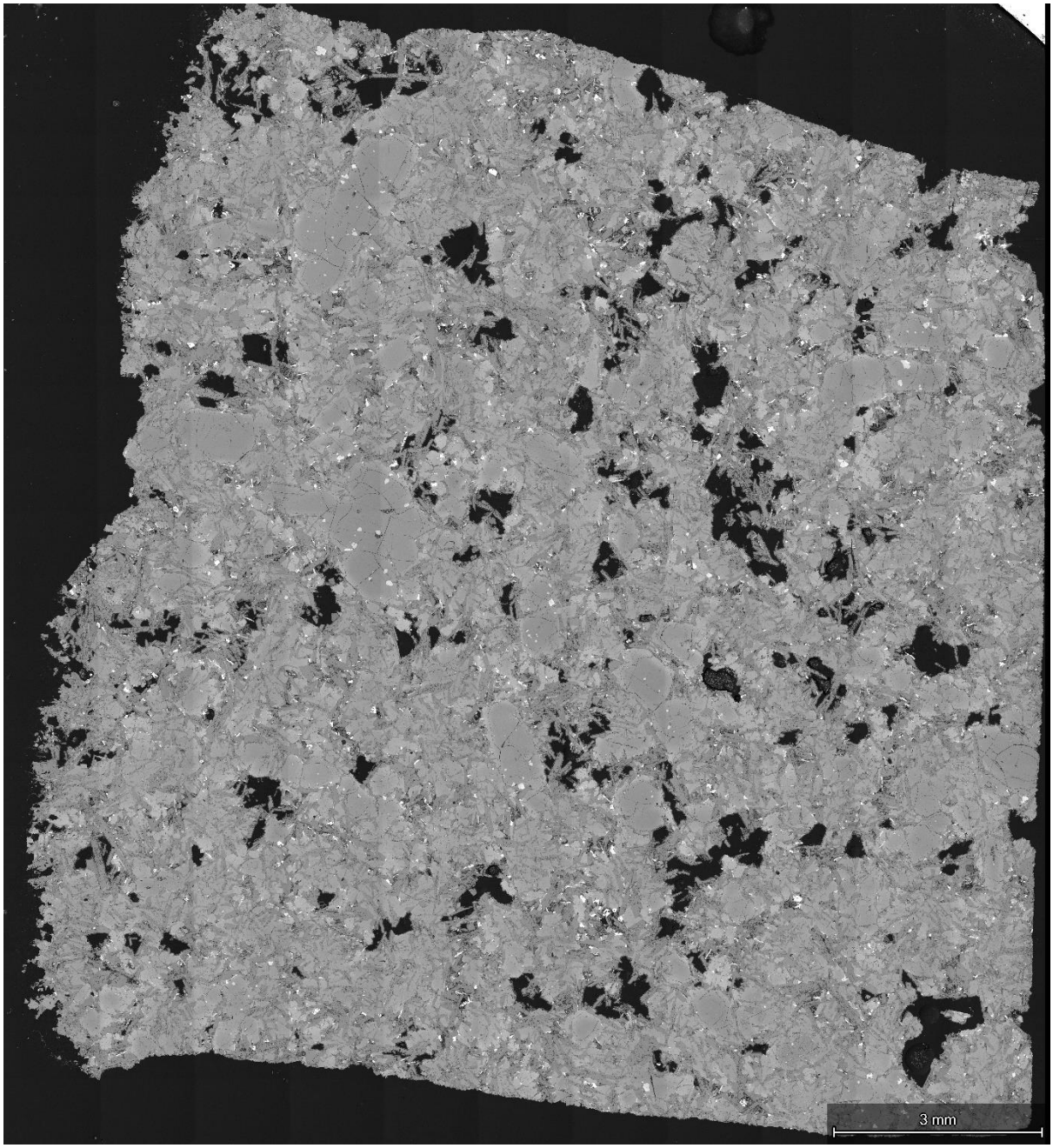

Figure A4.11: SEM Backscatter Image of Sample 11.

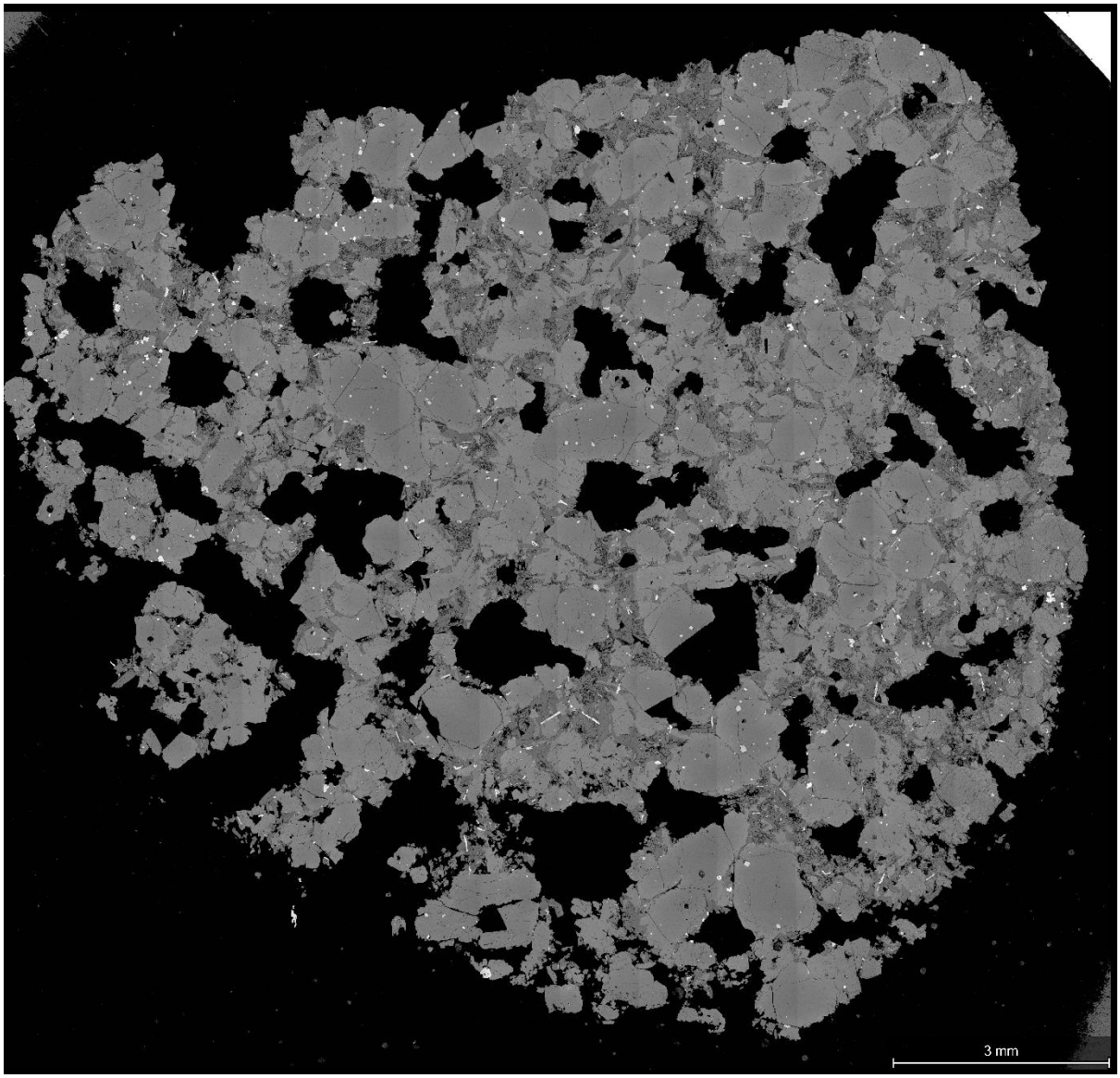

Figure A4.12: SEM Backscatter Image of Sample 12.

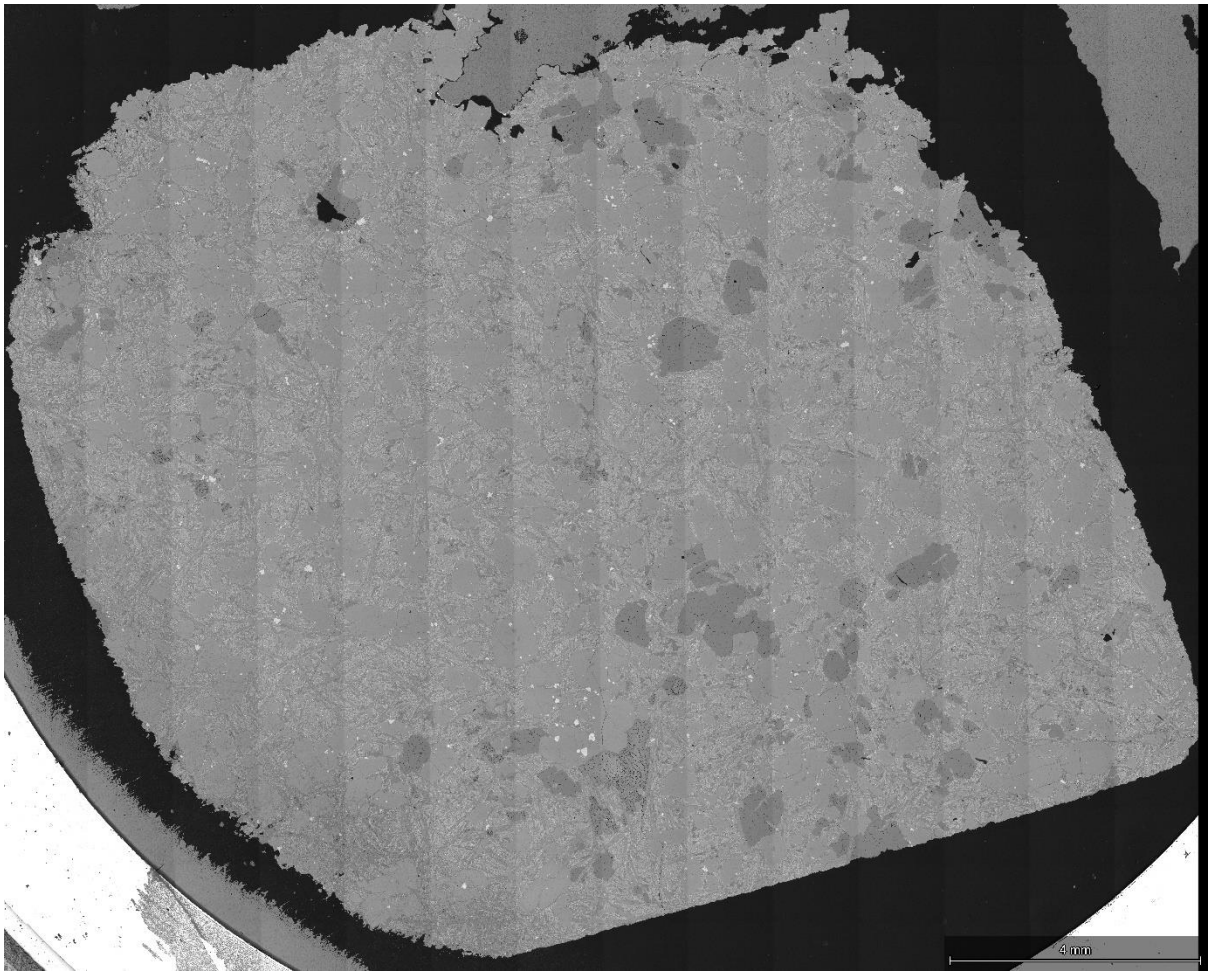

Figure A4.13: SEM Backscatter Image of Sample 13.

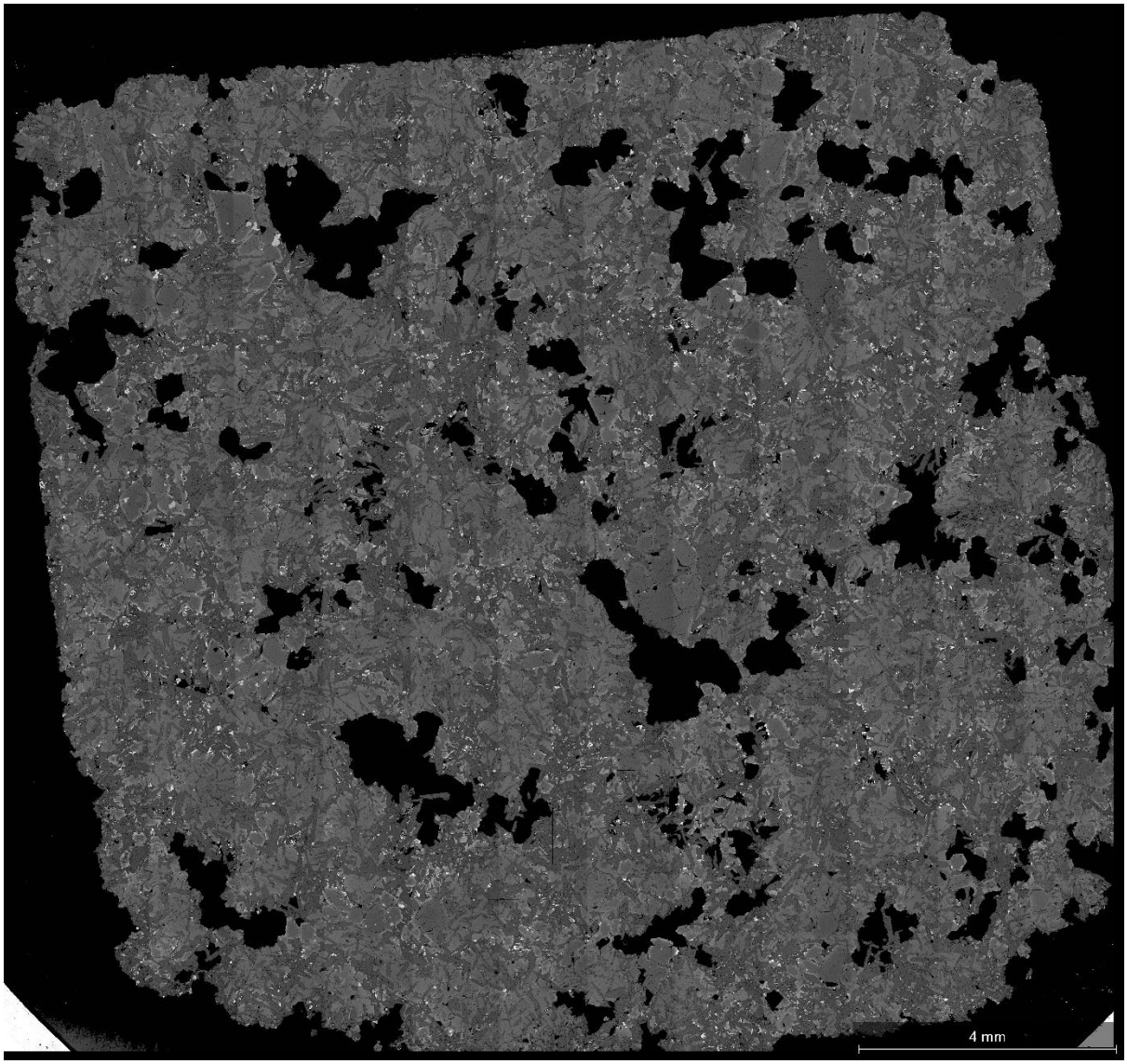

Figure A4.14: SEM Backscatter Image of Sample 14.

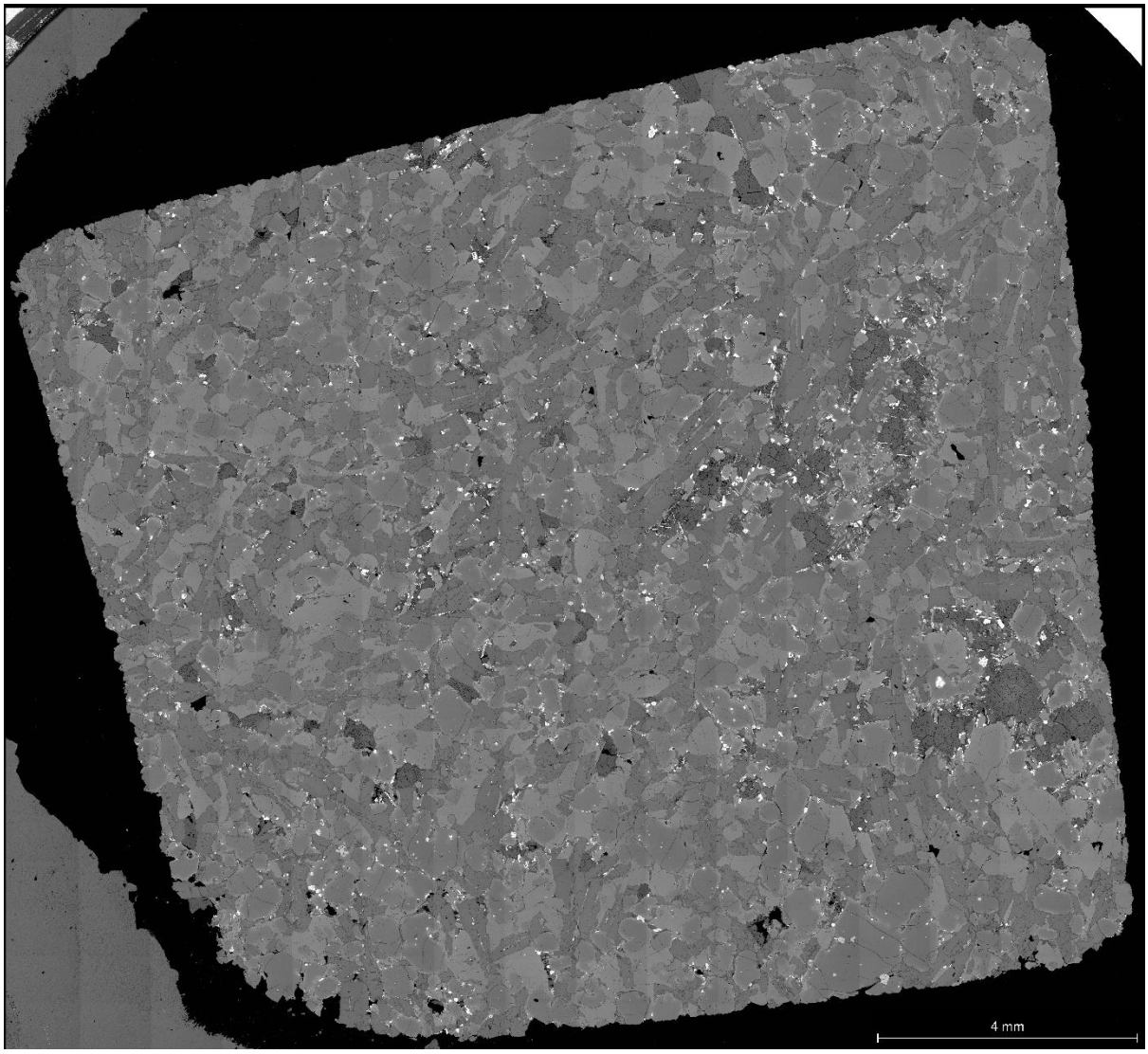

Figure A4.15: SEM Backscatter Image of Sample 15.

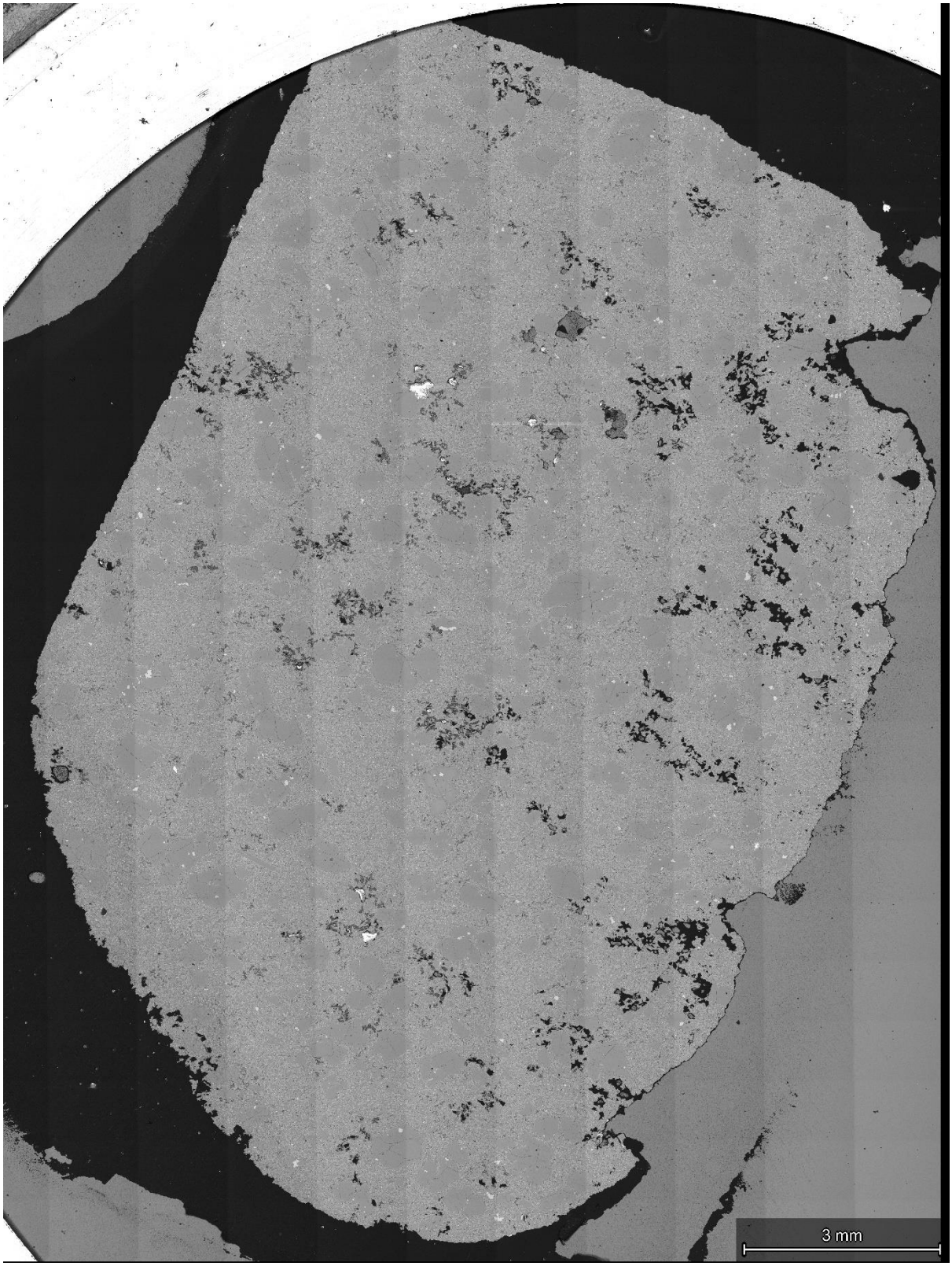

Figure A4.16: SEM Backscatter Image of Sample 16.

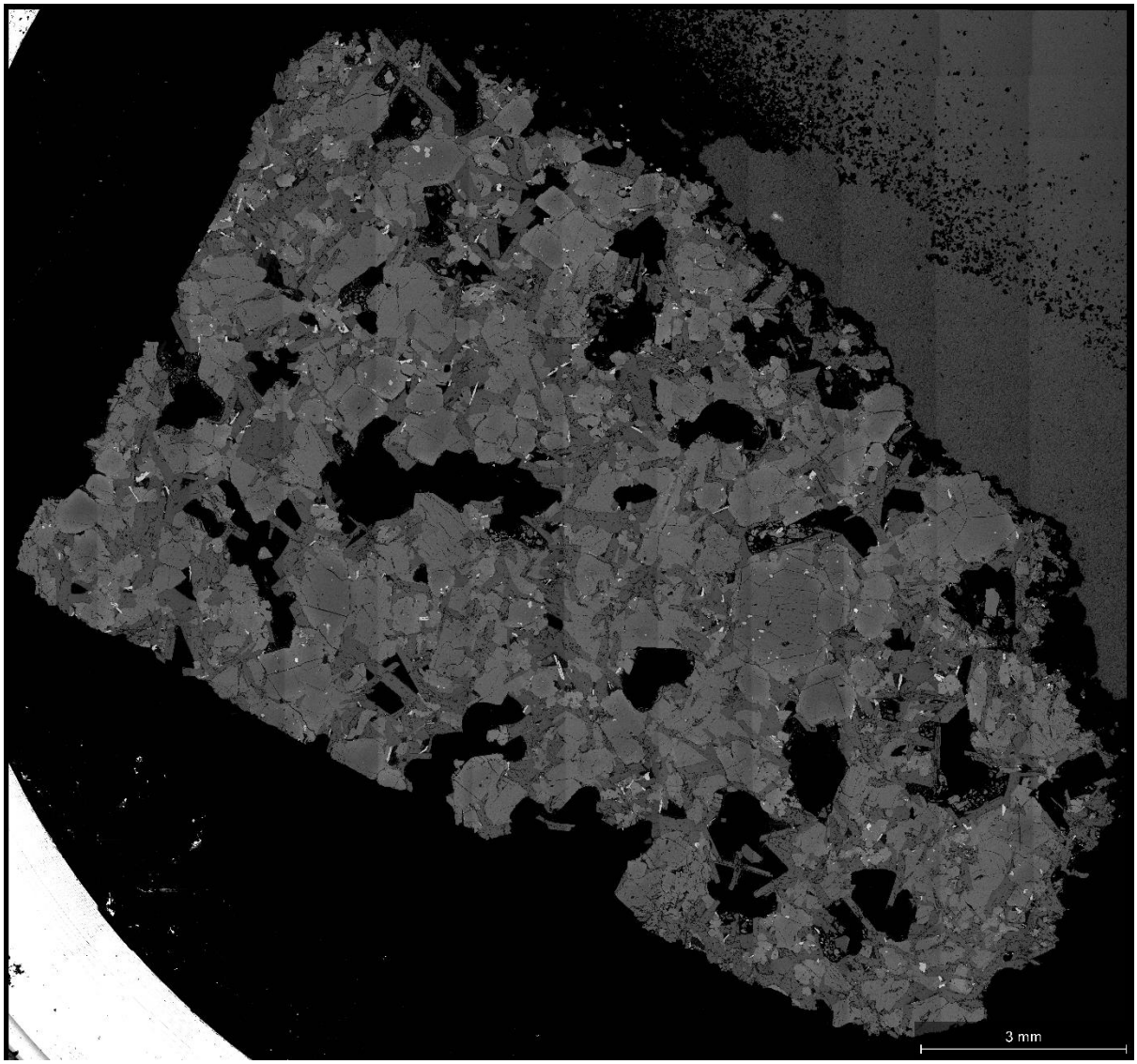

Figure A4.17: SEM Backscatter Image of Sample 17.

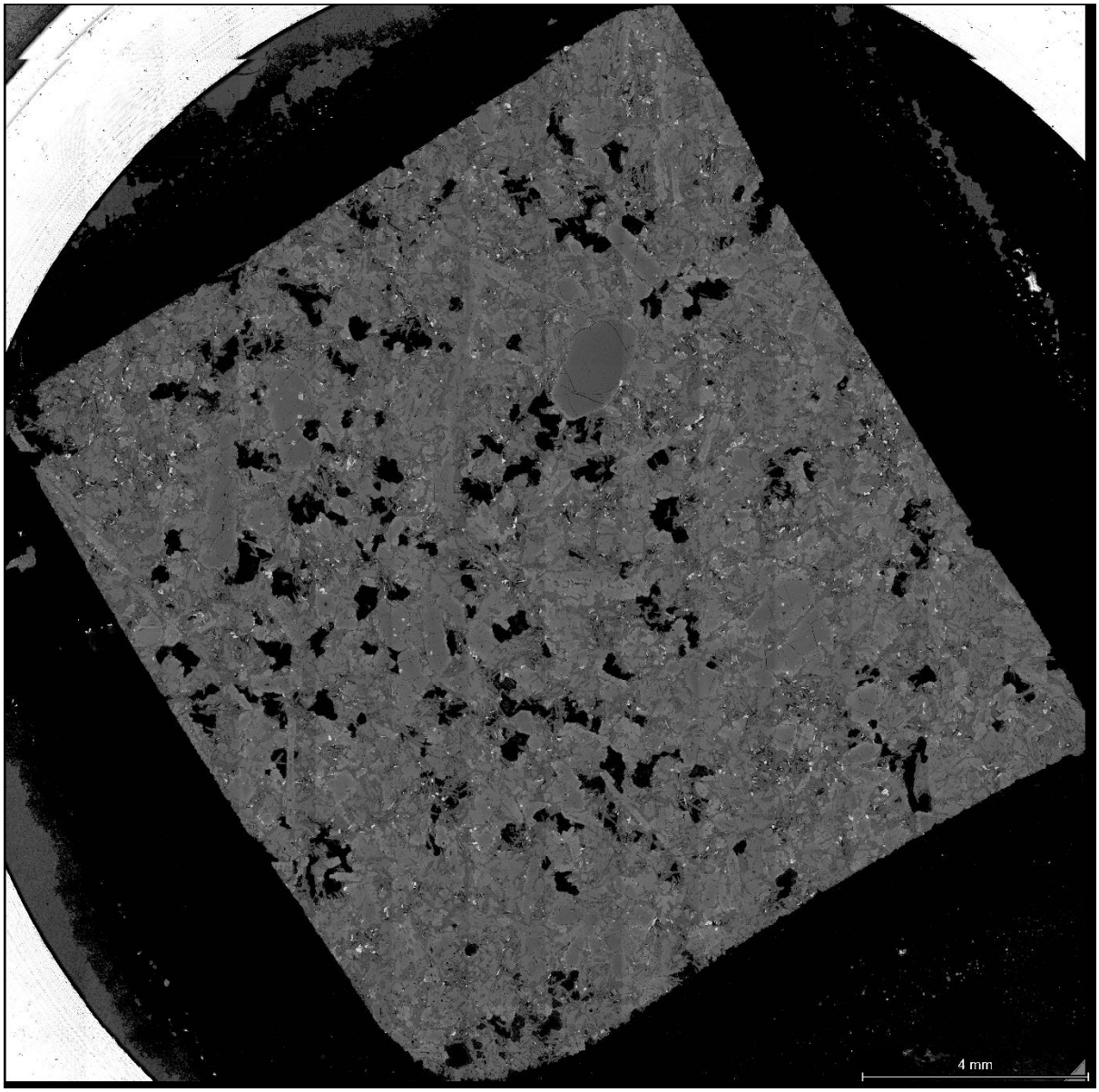

Figure A4.18: SEM Backscatter Image of Sample 18.

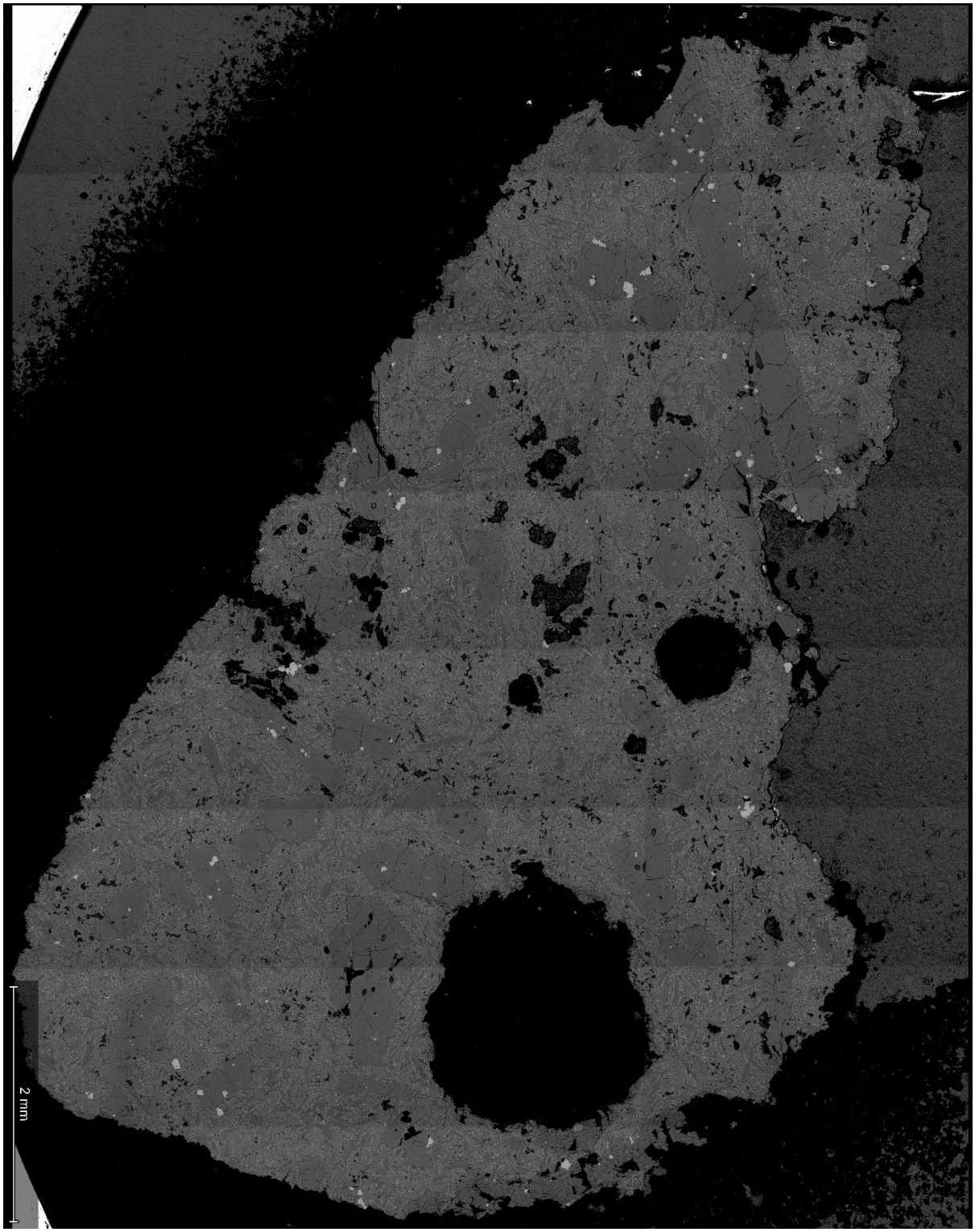

Figure A4.19: SEM Backscatter Image of Sample 19.

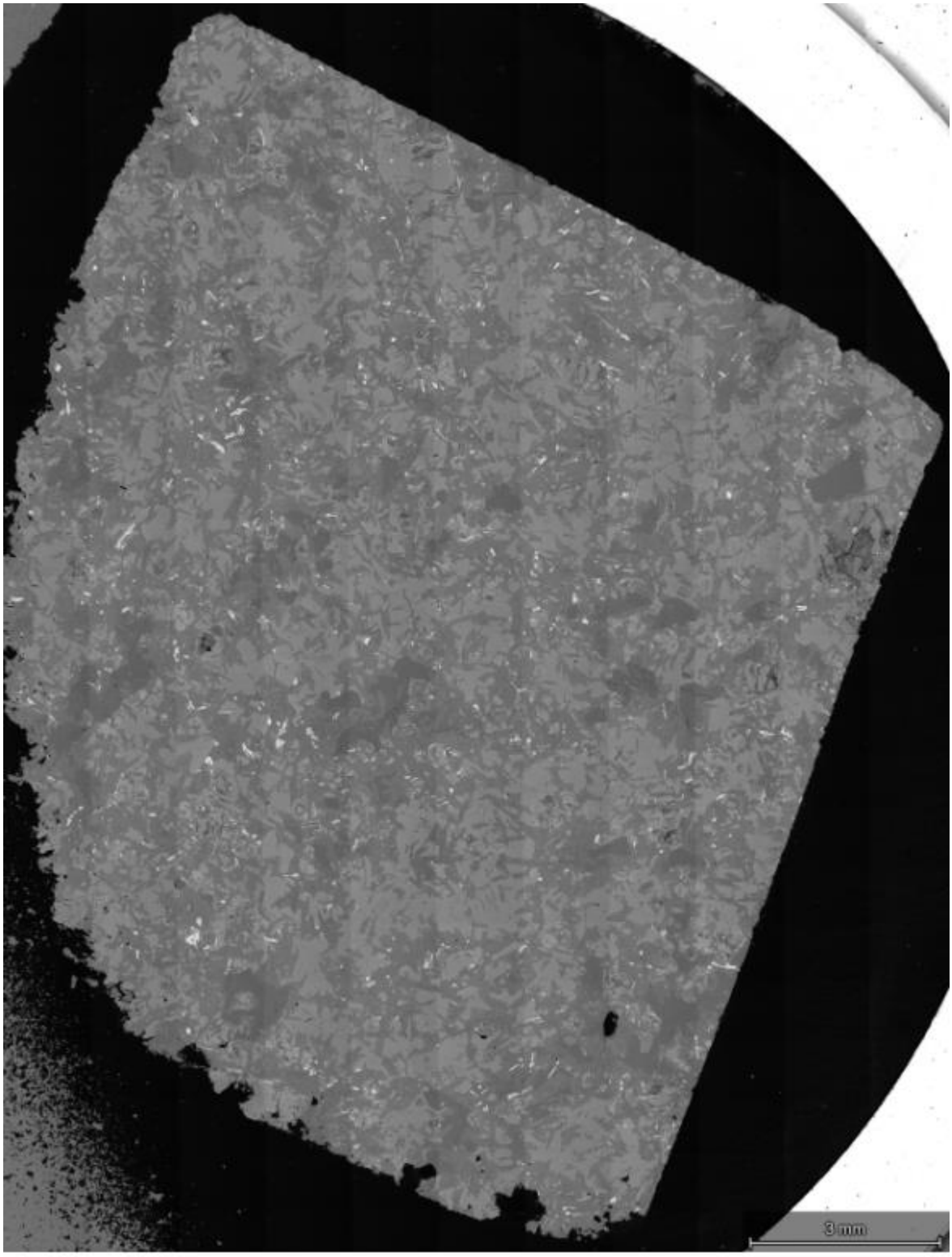

Figure A4.20: SEM Backscatter Image of Sample 20.

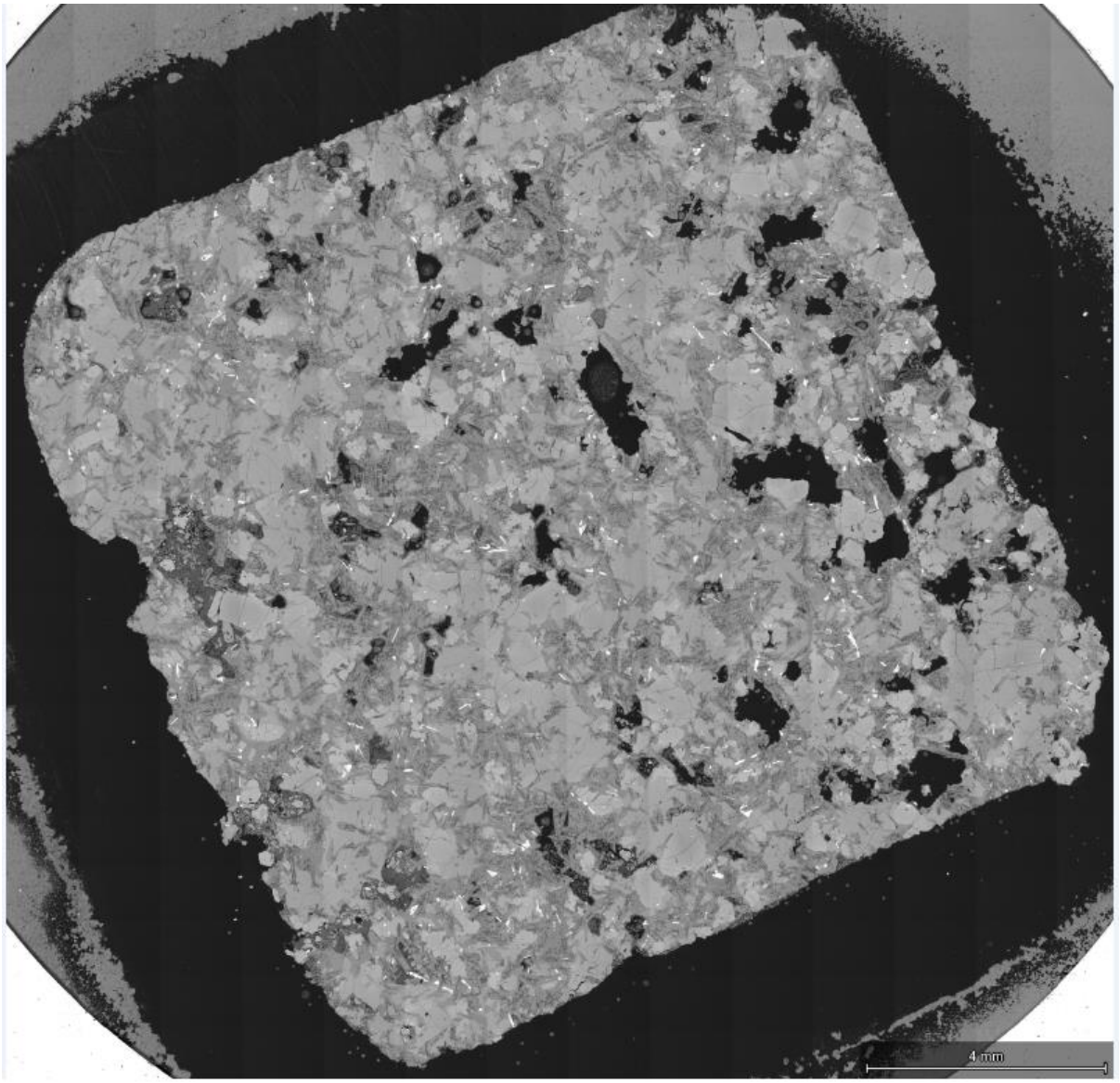

Figure A4.21: SEM Backscatter Image of Sample 21.

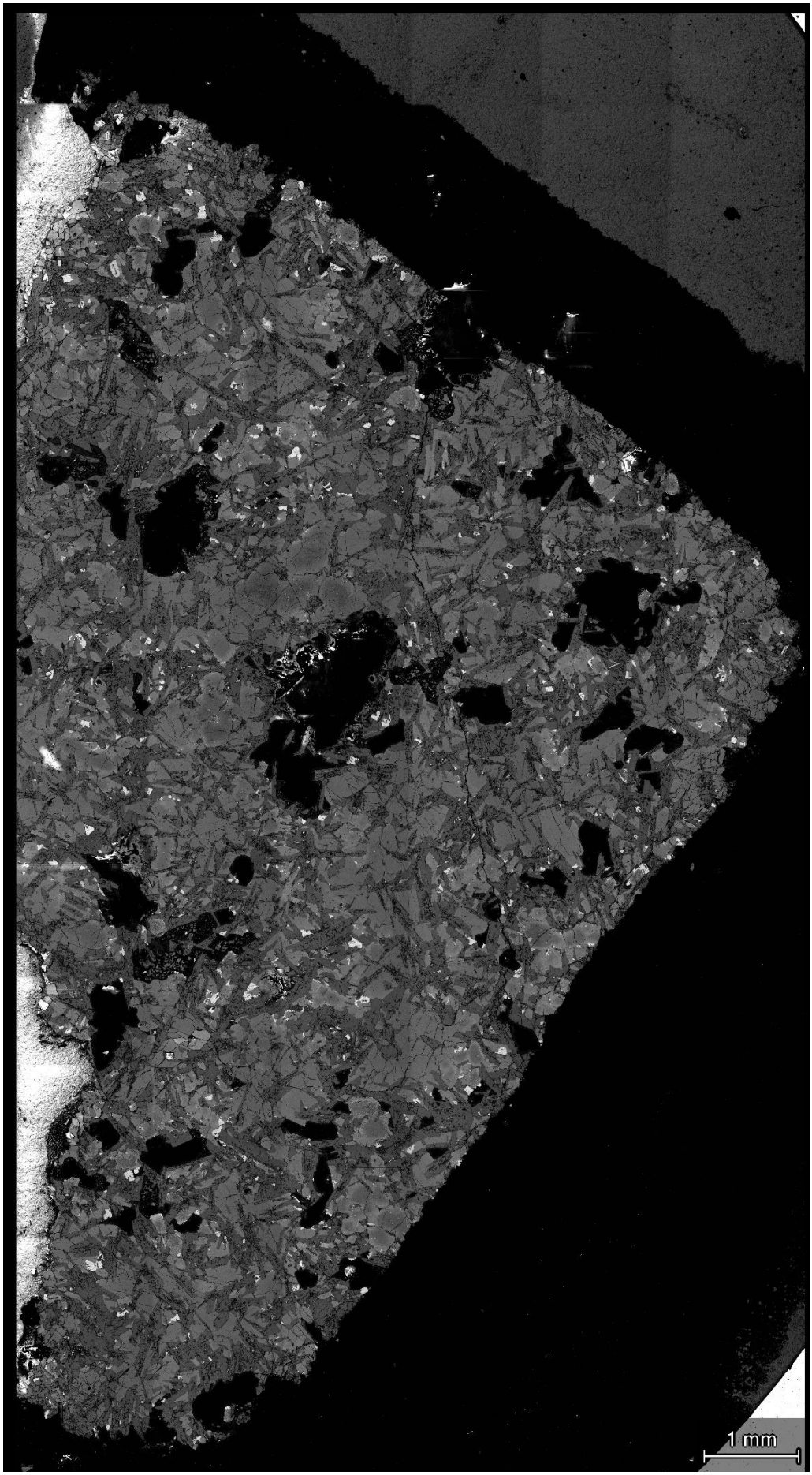
1 mm

Figure A4.22: SEM Backscatter Image of Sample 22.

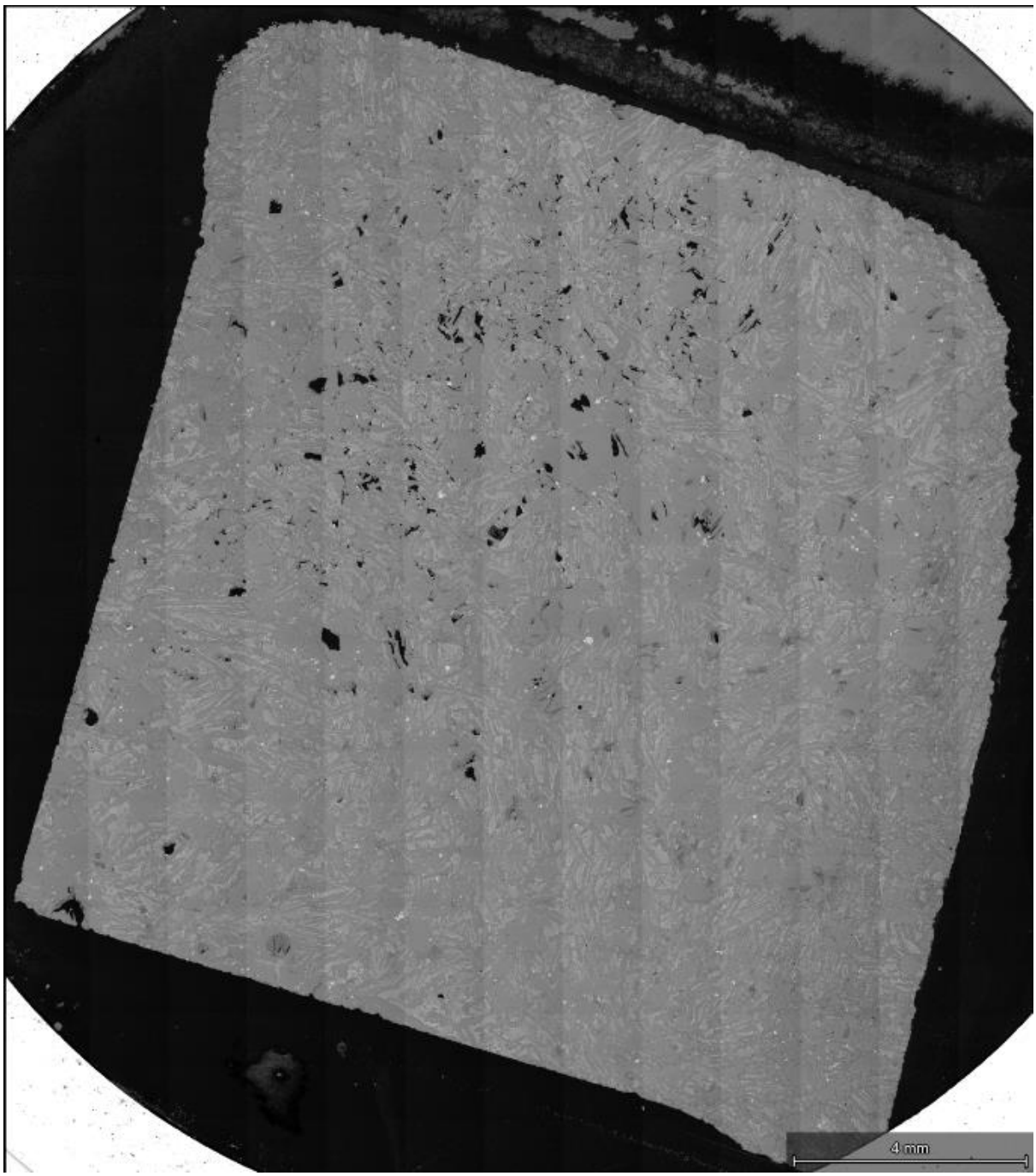

Figure A4.23: SEM Backscatter Image of Sample 23.

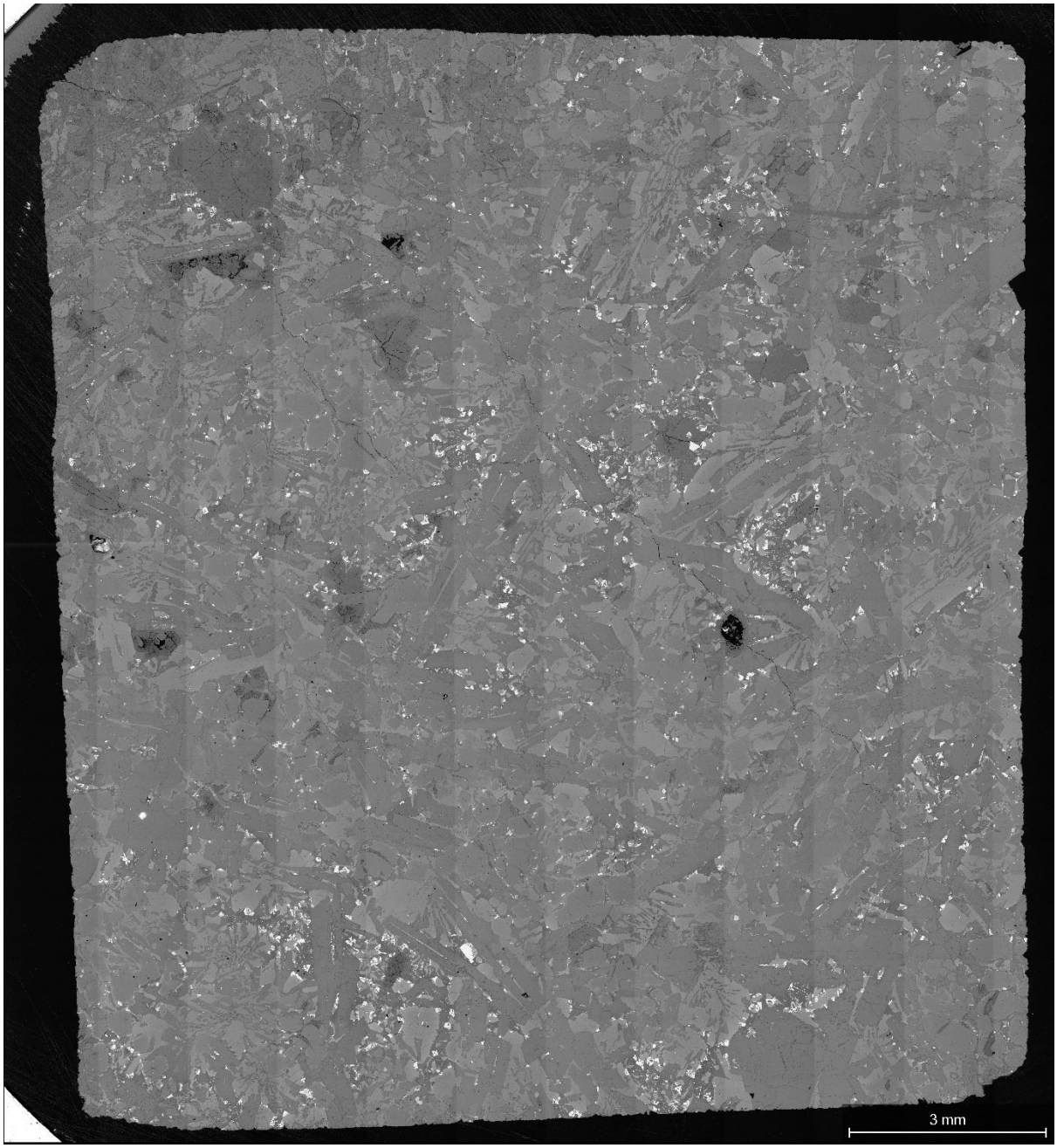

Figure A4.24: SEM Backscatter Image of Sample 24.

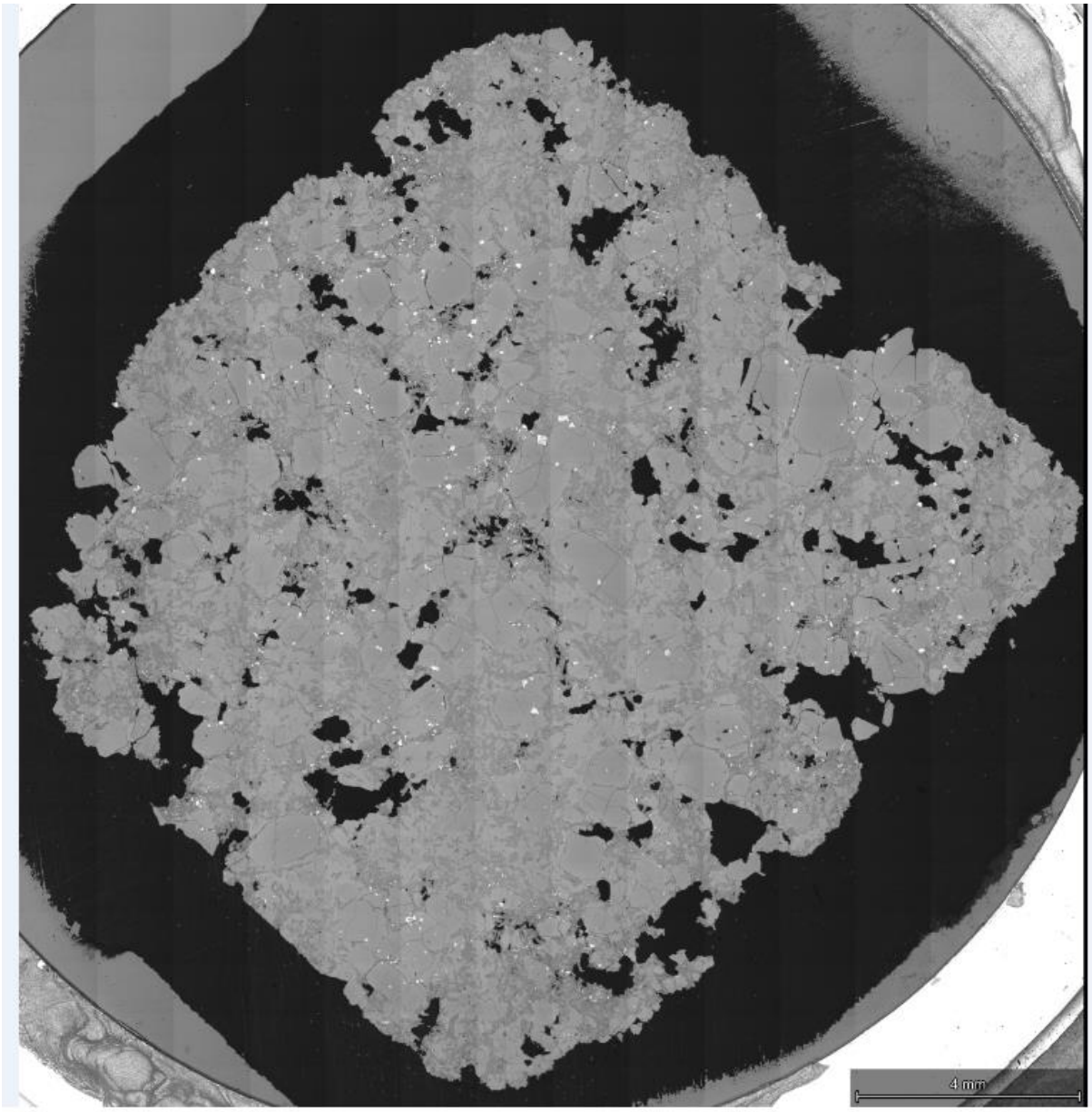

Figure A4.25: SEM Backscatter Image of Sample 25.

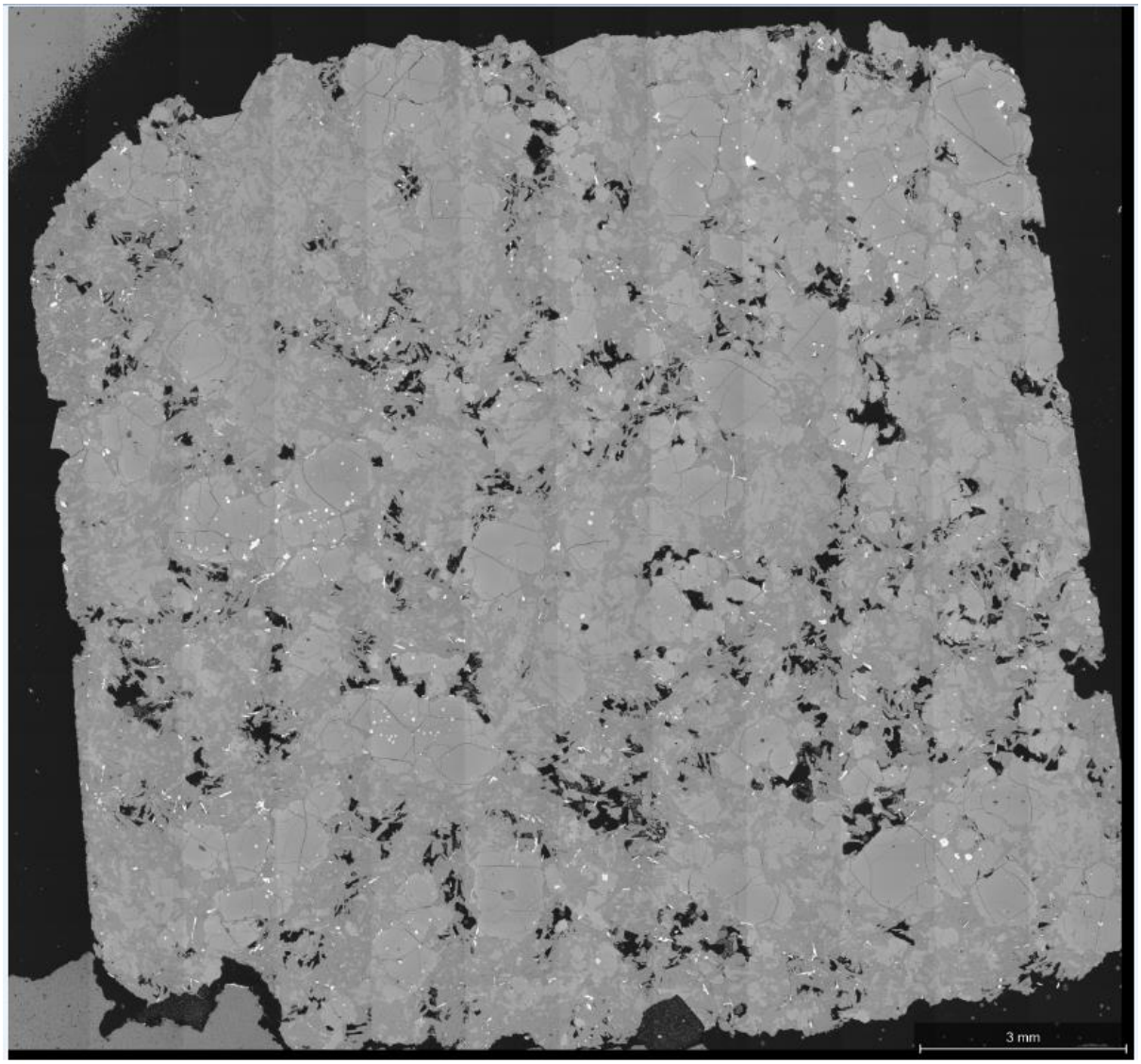

Figure A4.26: SEM Backscatter Image of Sample 26.

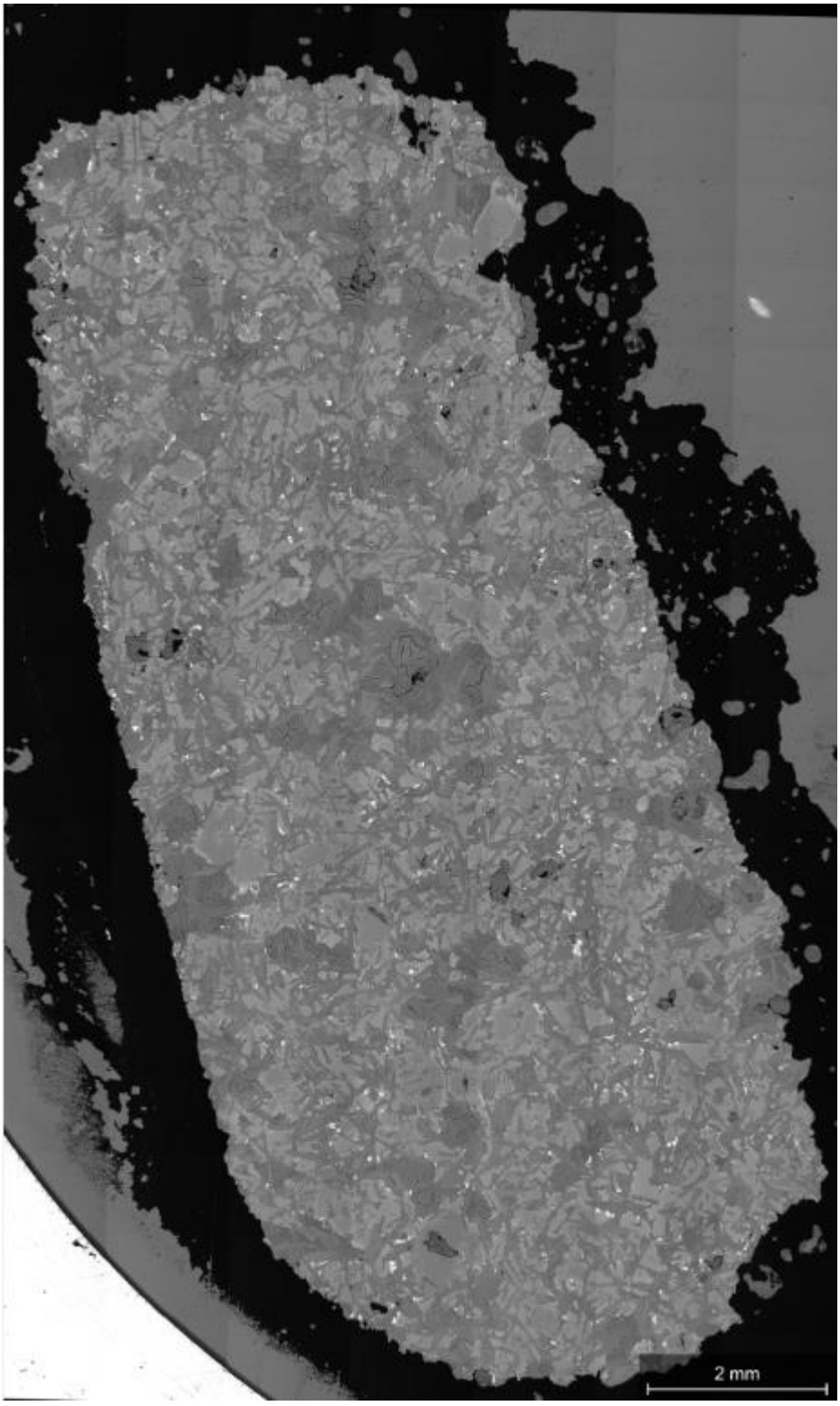

Figure A4.27: SEM Backscatter Image of Sample 27.

Appendix V – PPL Images

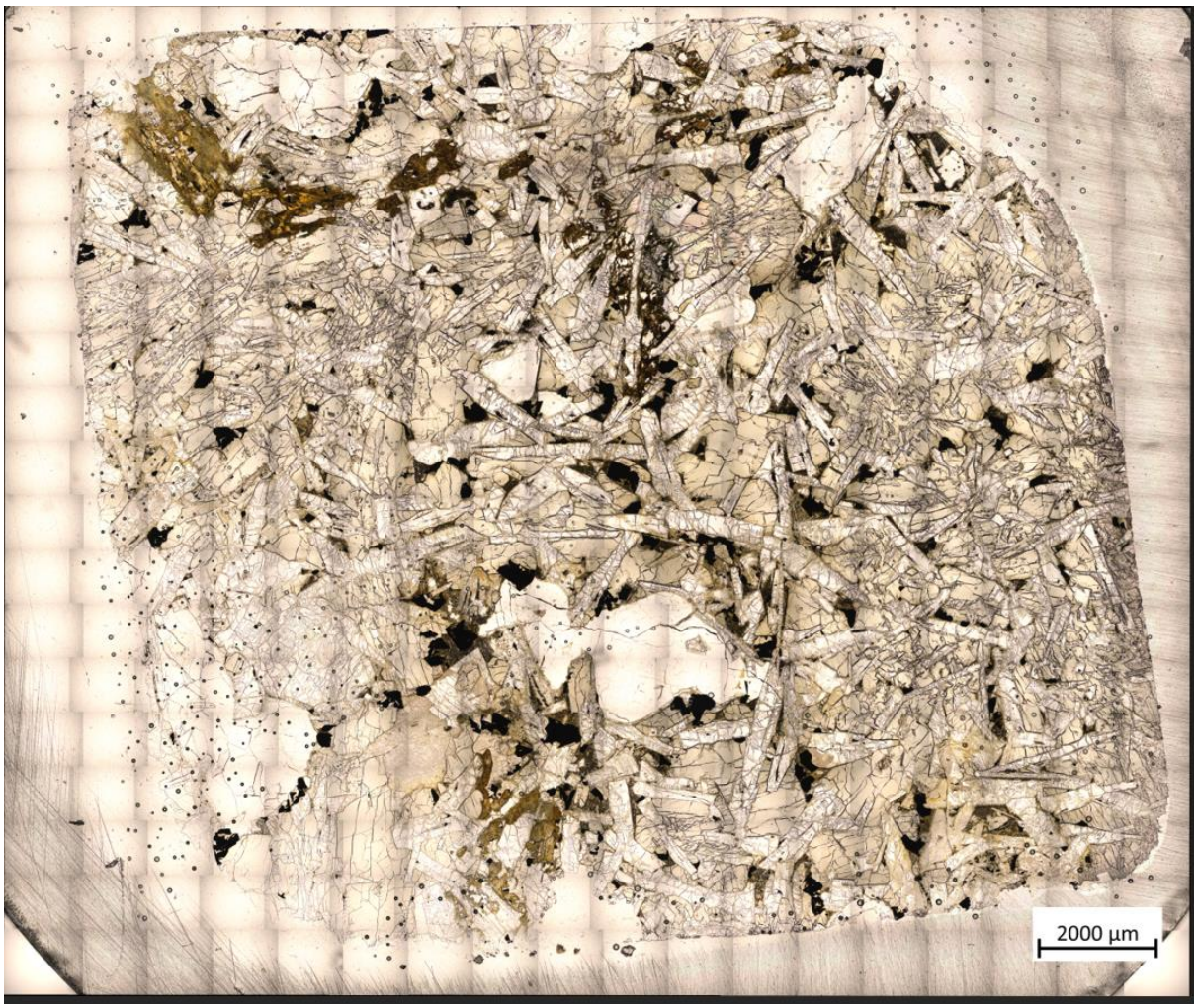

Figure A5.1: PPL Image of Sample 1.

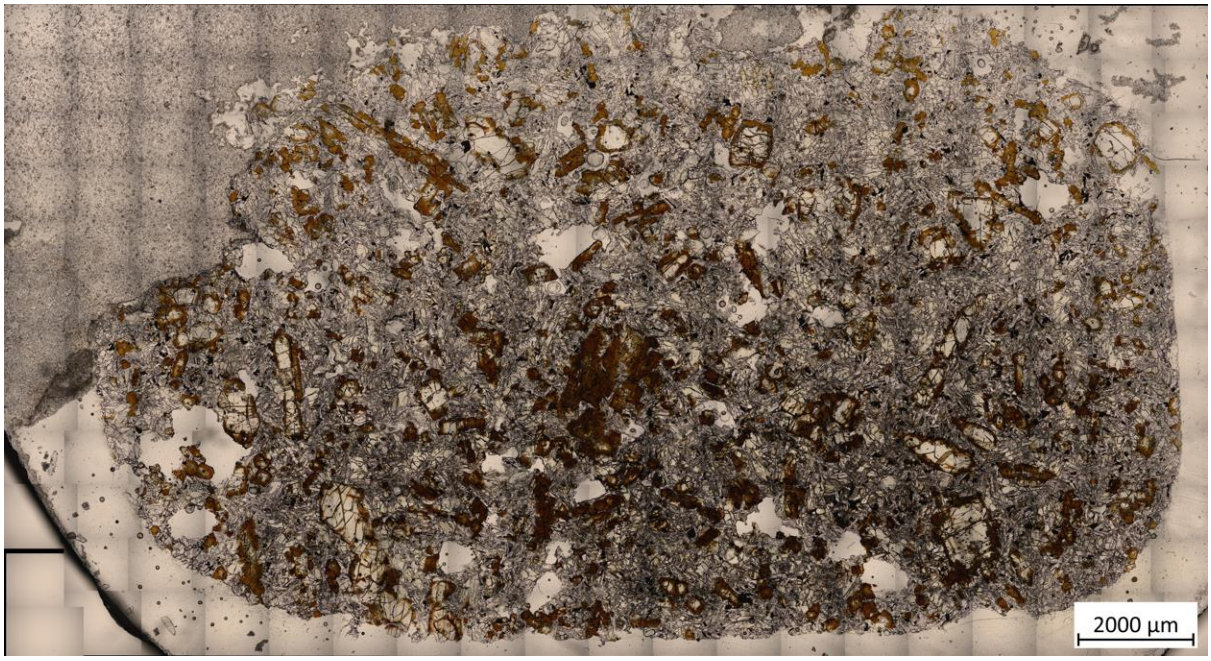

Figure A5.2: PPL Image of Sample 2.

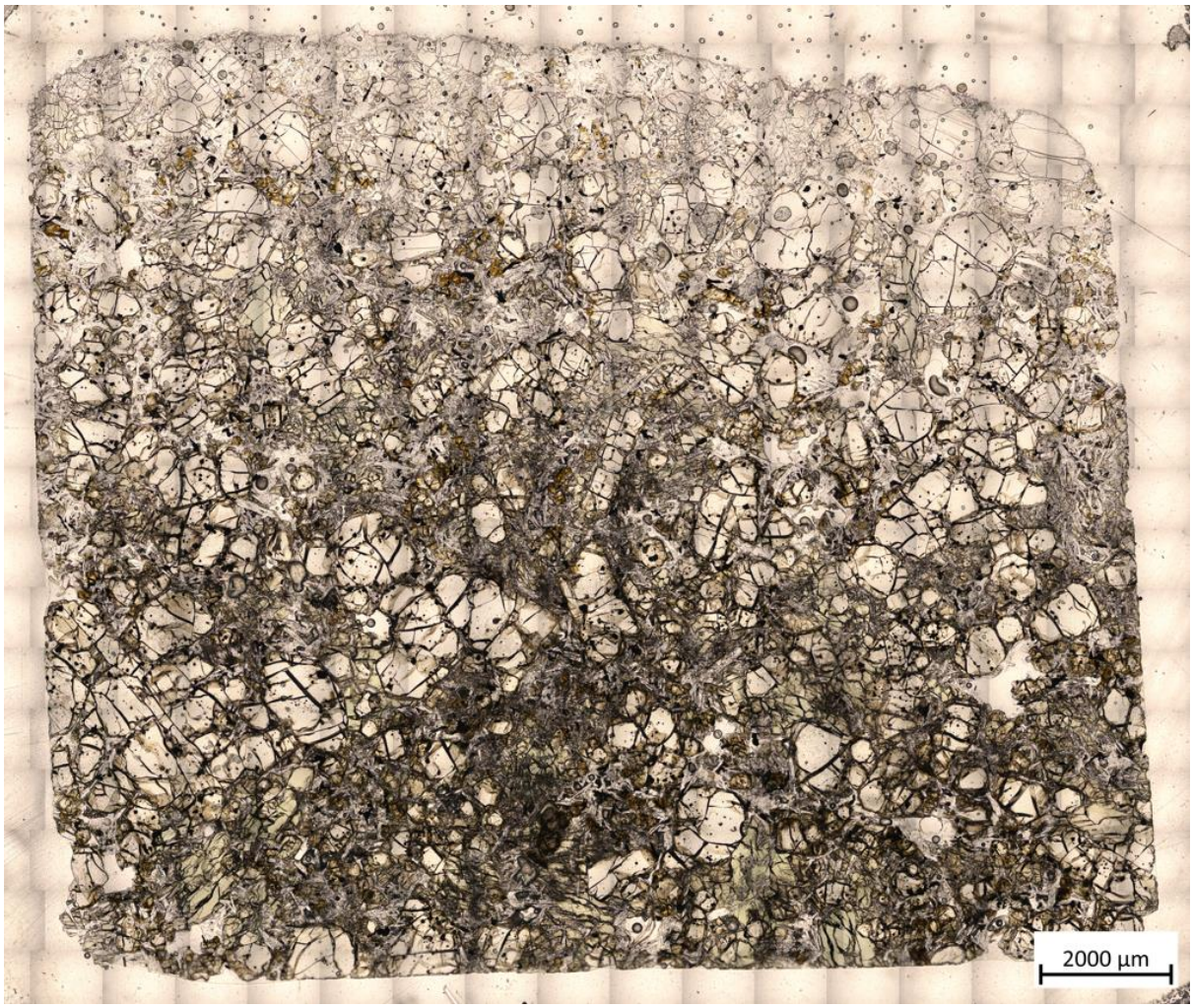

Figure A5.3: PPL Image of Sample 3.

Figure A5.4: PPL Image of Sample 4.

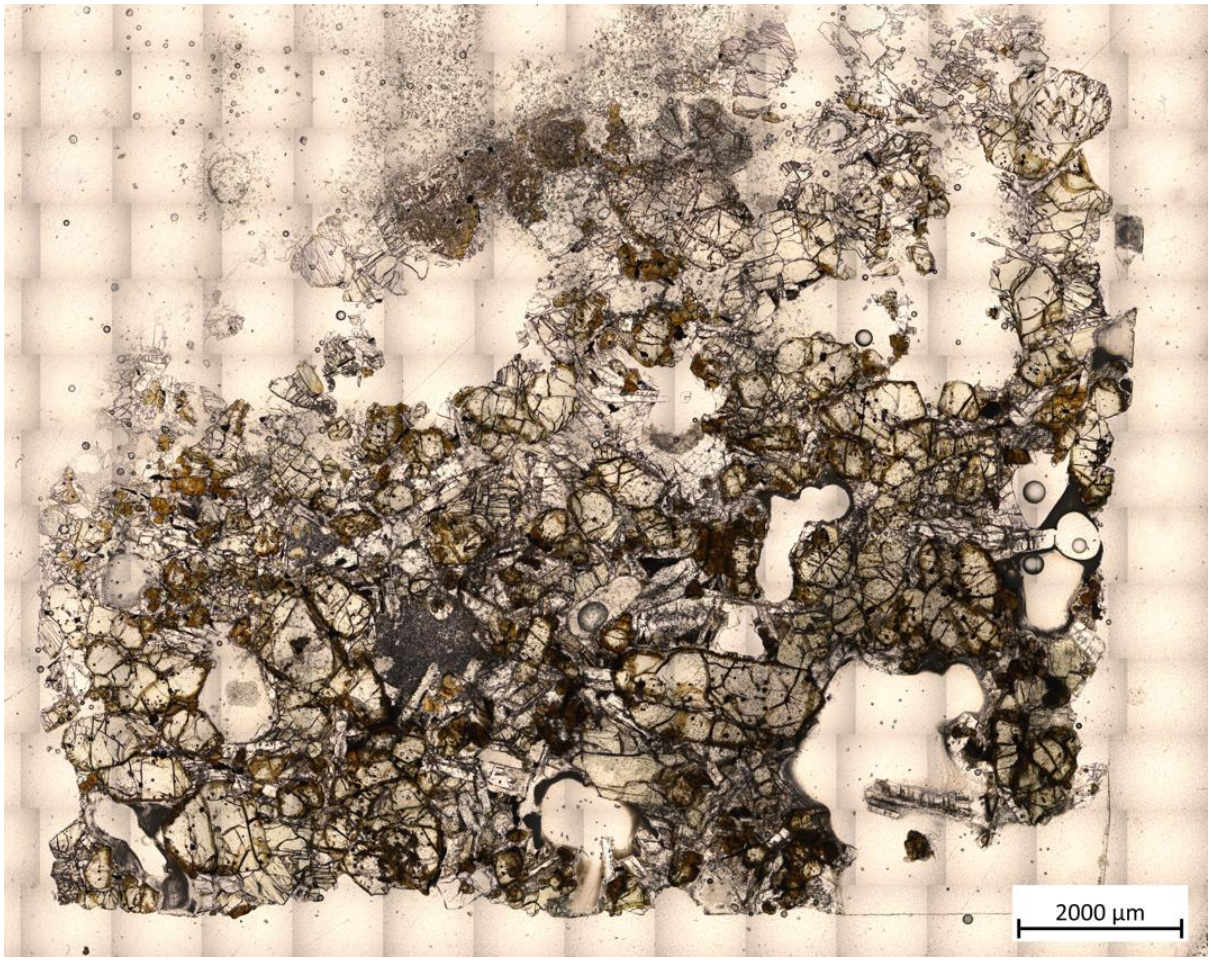

Figure A5.5: PPL Image of Sample 5.

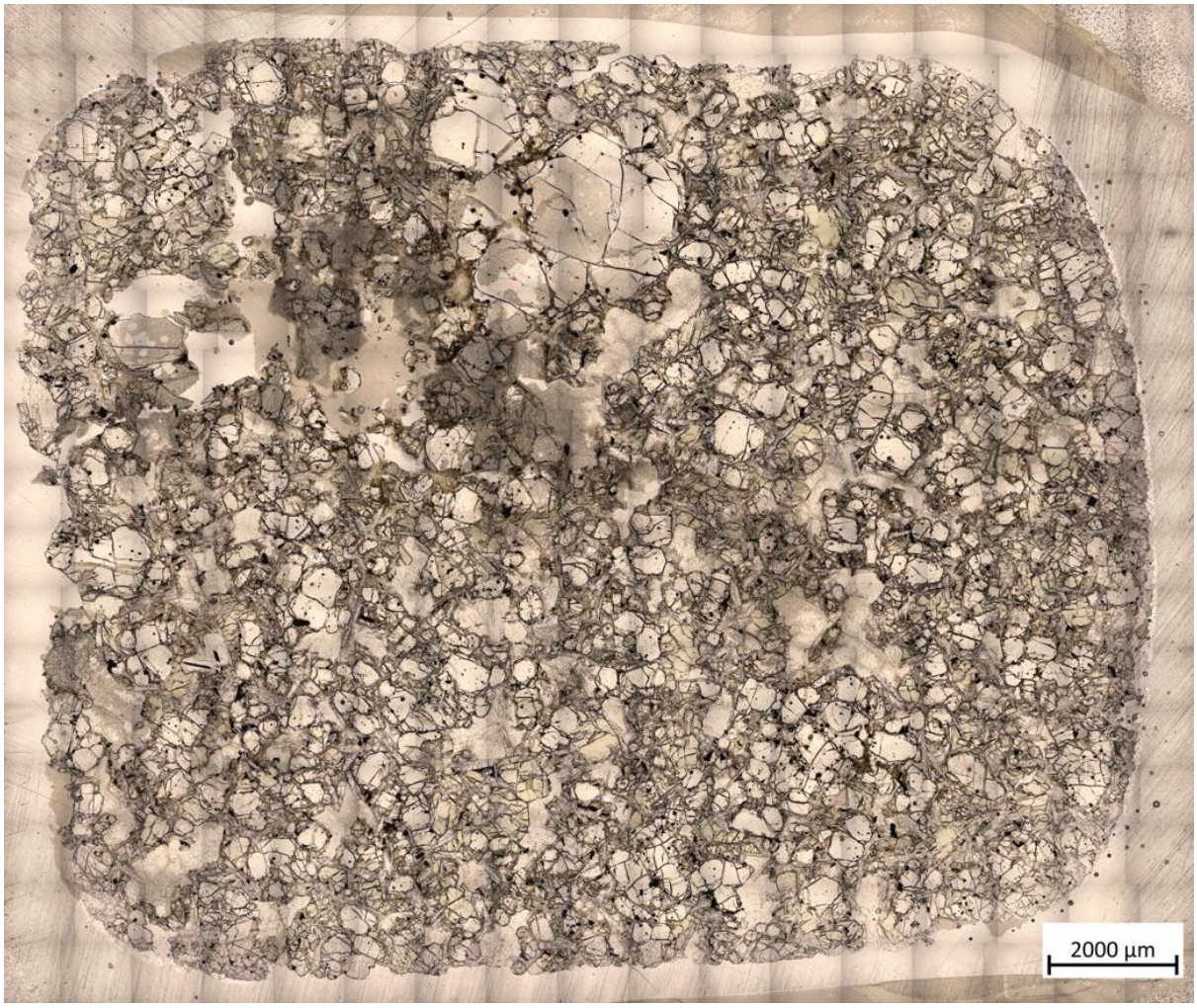

Figure A5.6: PPL Image of Sample 6.

Figure A5.7: PPL Image of Sample 7.

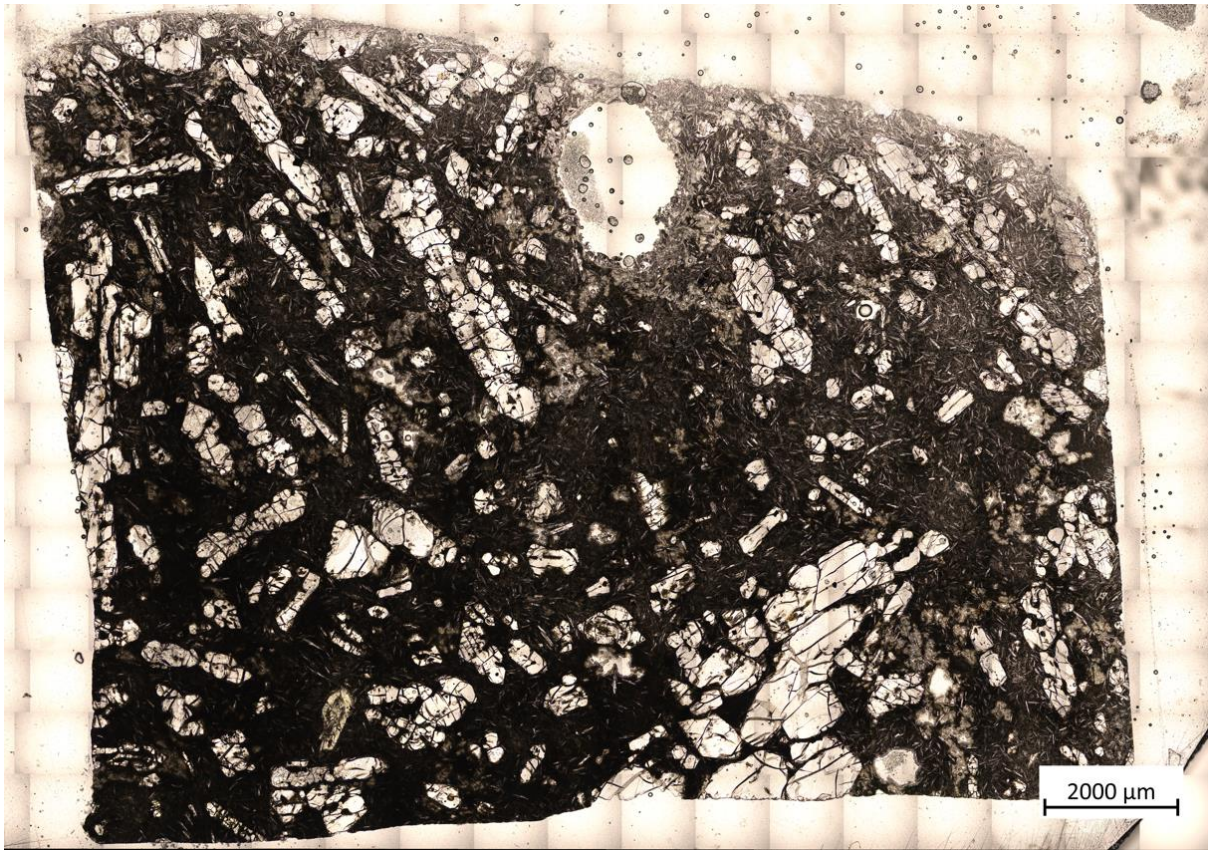

Figure A5.8: PPL Image of Sample 8.

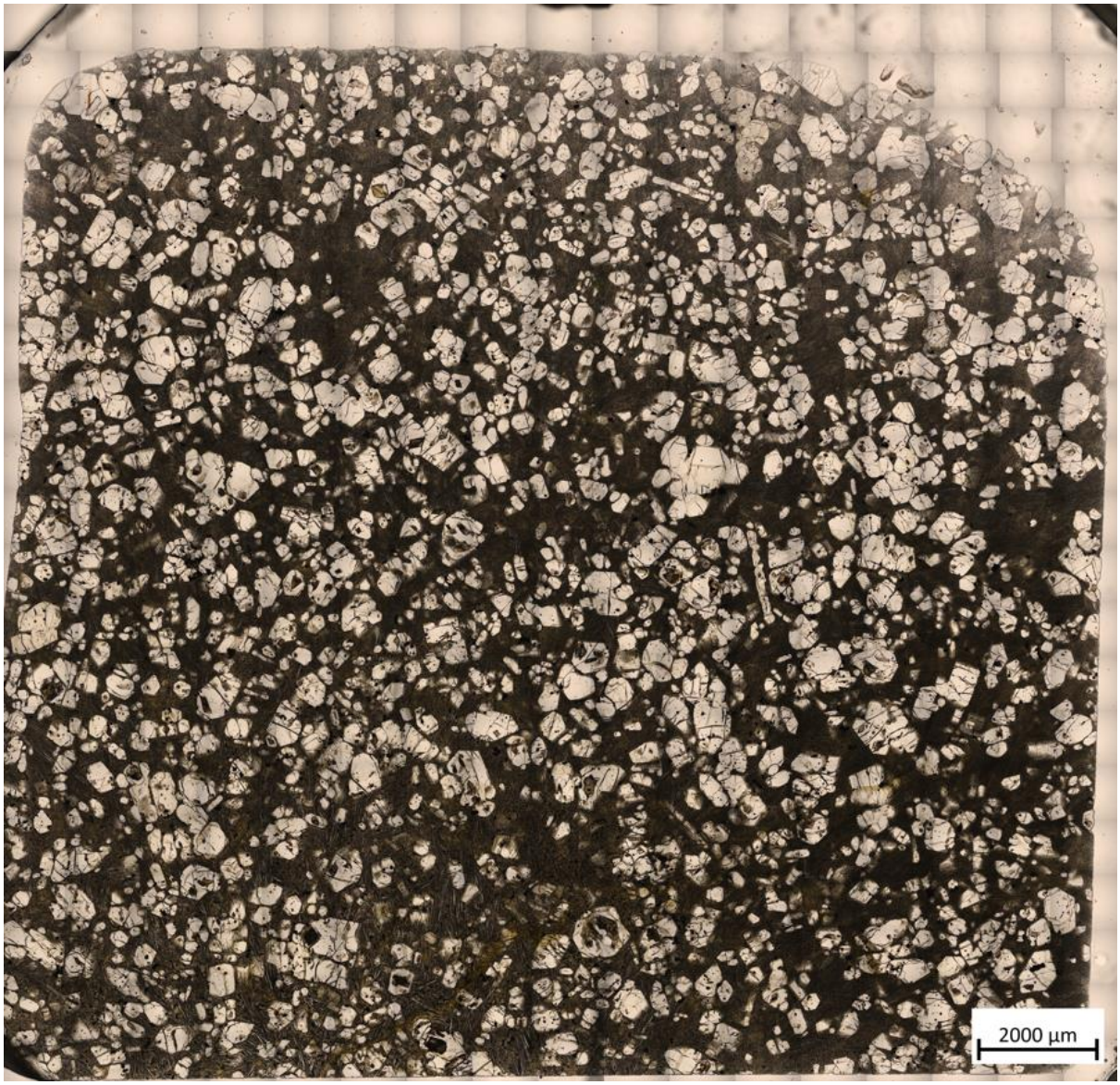

Figure A5.9: PPL Image of Sample 9.

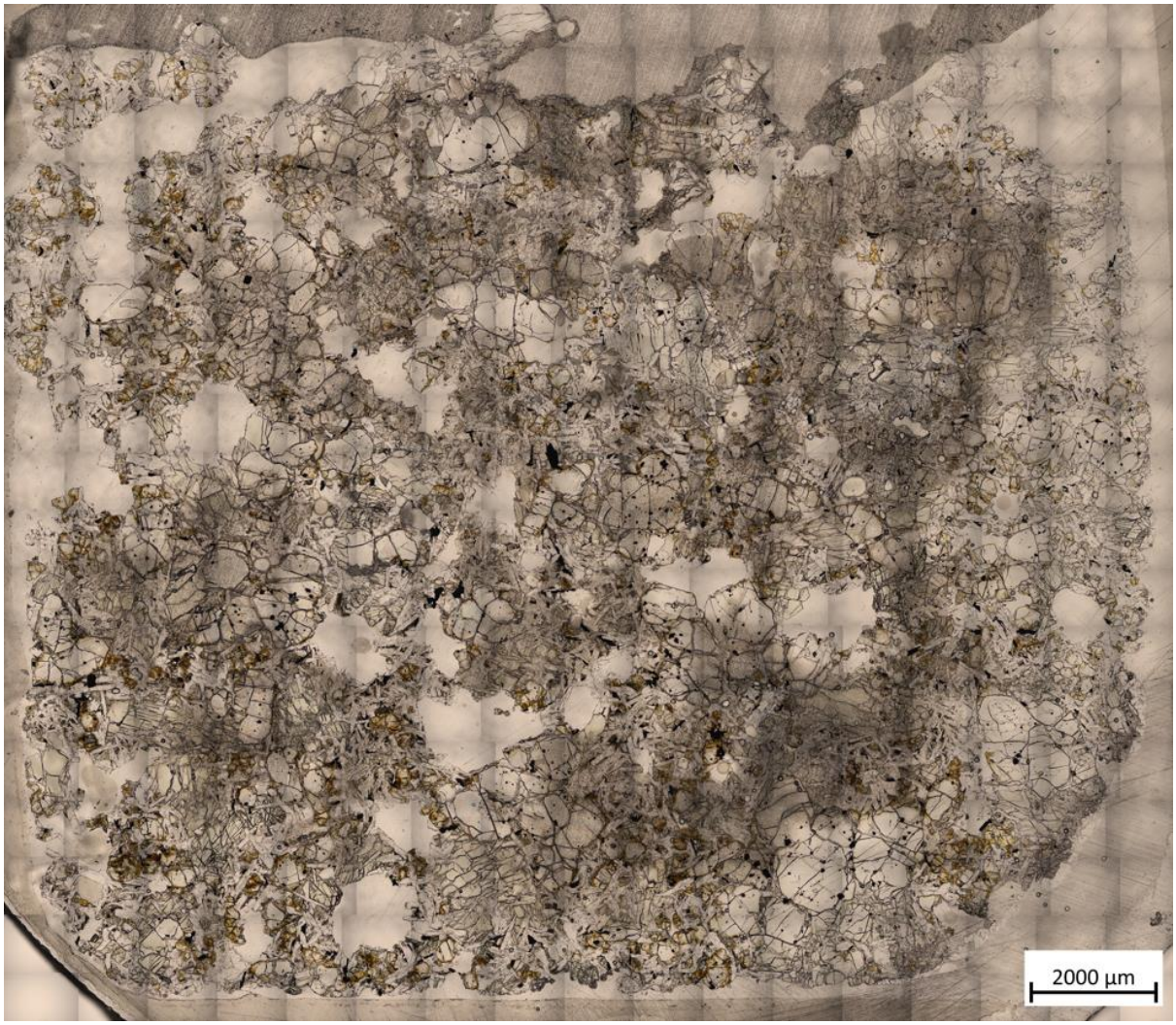

Figure A5.10: PPL Image of Sample 10.

Figure A5.11: PPL Image of Sample 11.

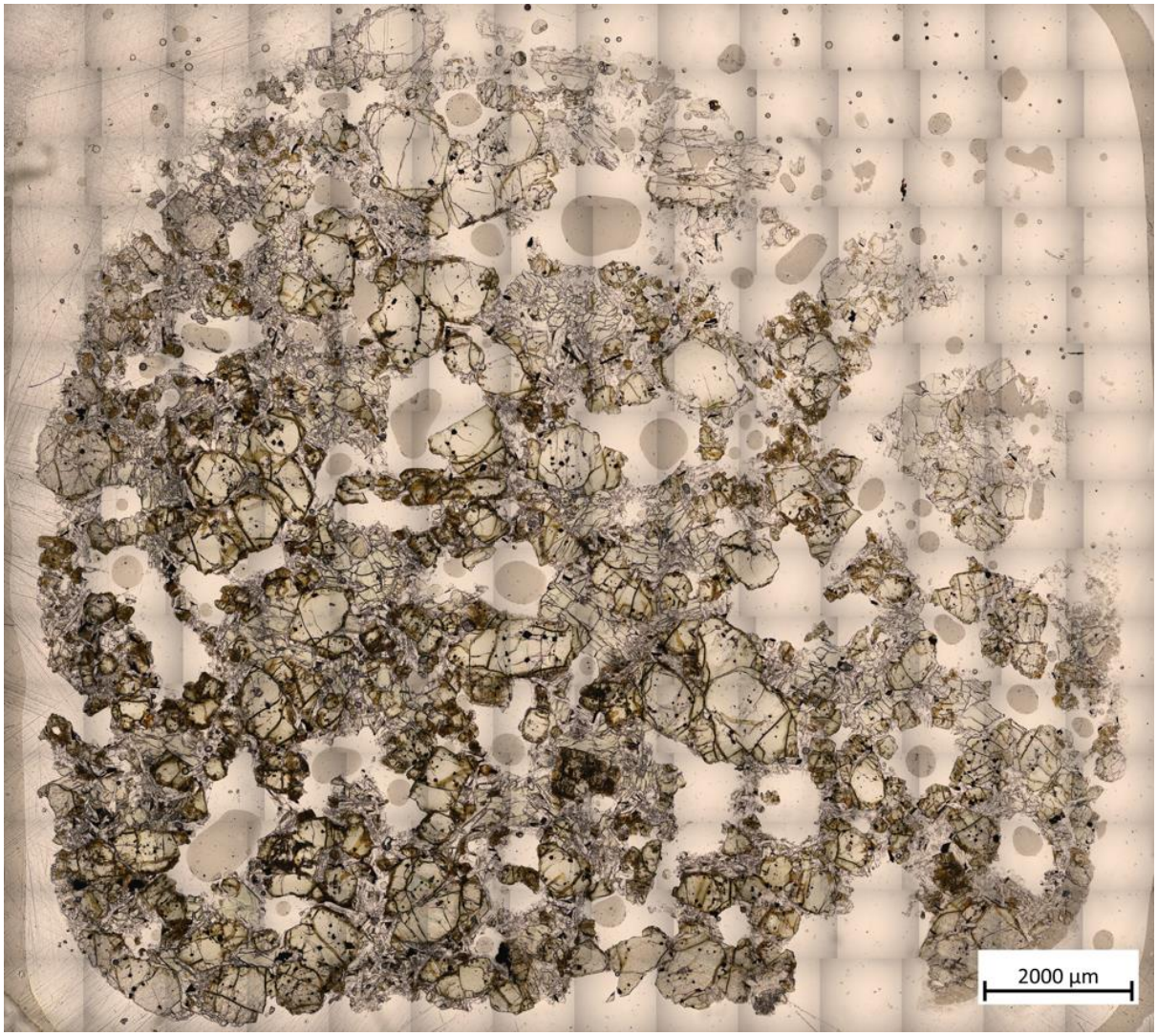

Figure A5.12: PPL Image of Sample 12.

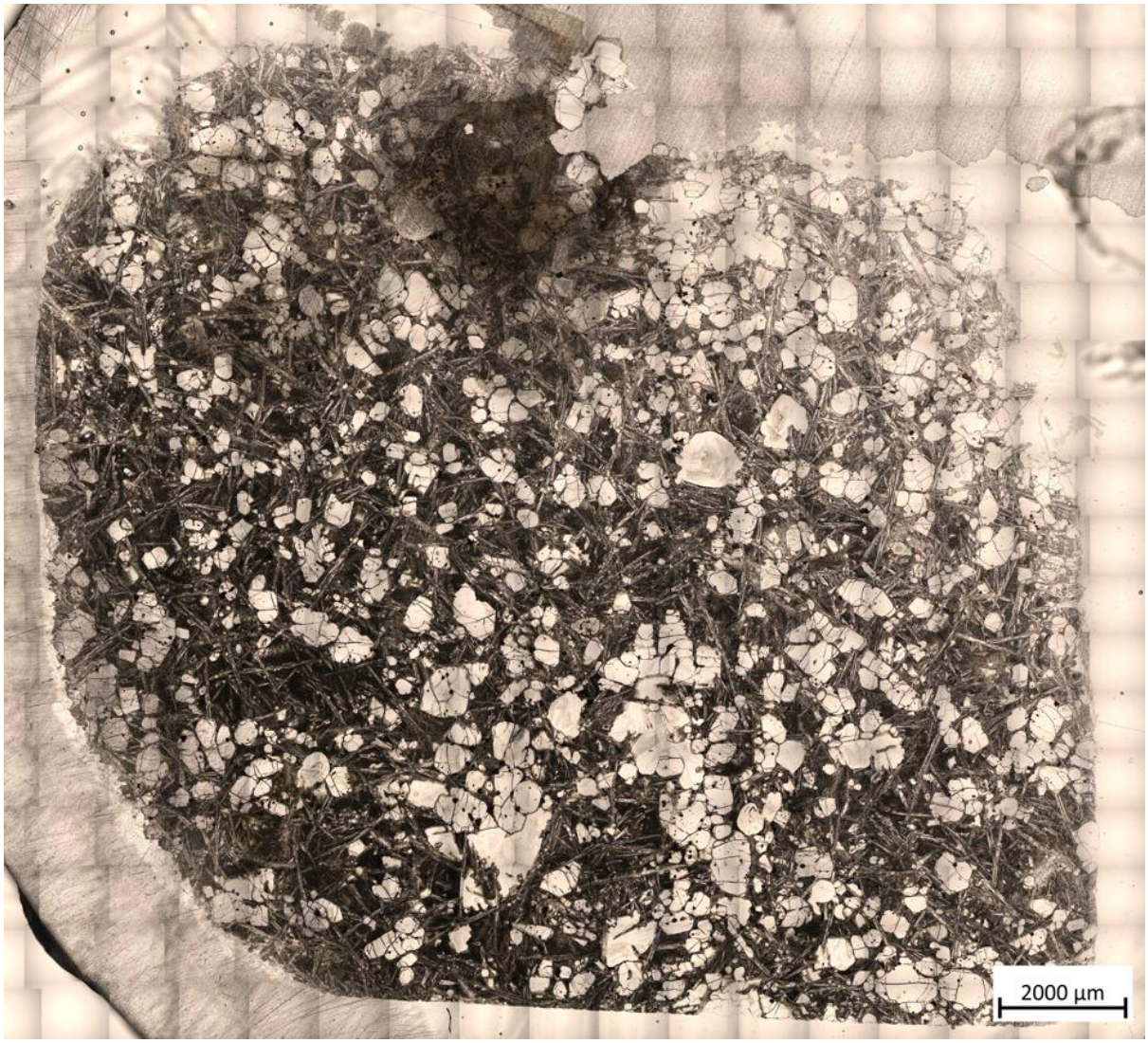

Figure A5.13: PPL Image of Sample 13.

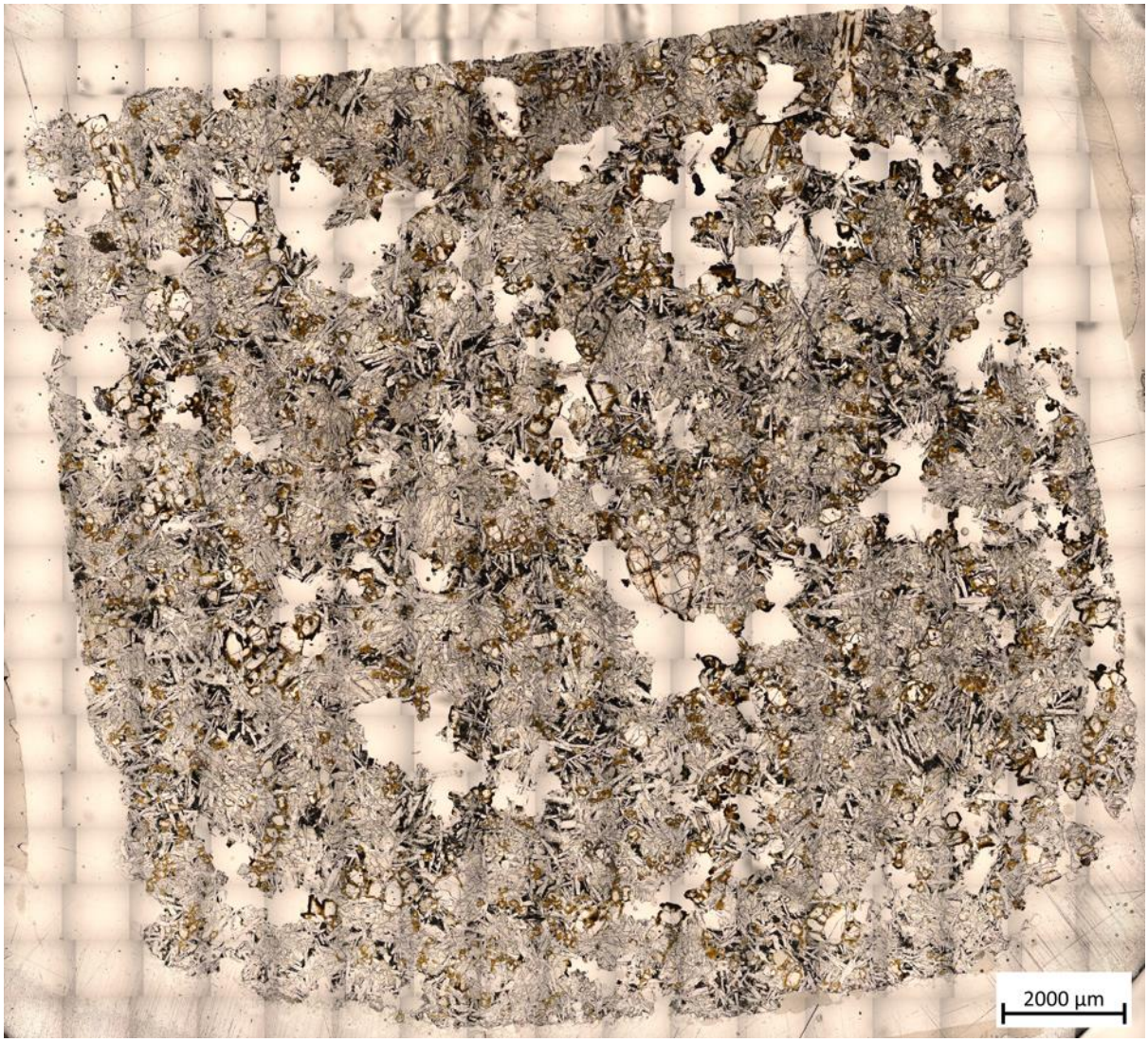

Figure A5.14: PPL Image of Sample 14.

Figure A5.15: PPL Image of Sample 15.

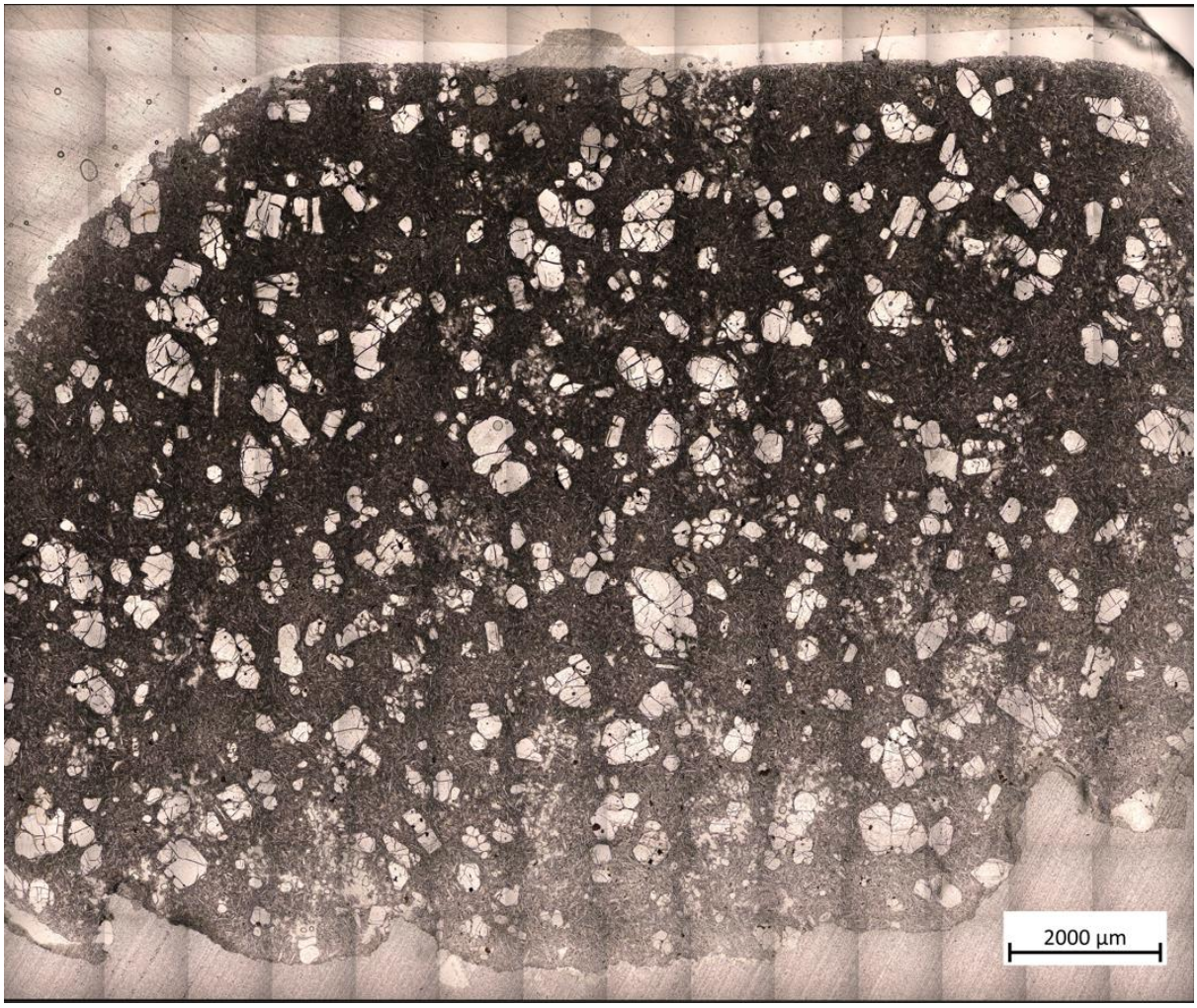

Figure A5.16: PPL Image of Sample 16.

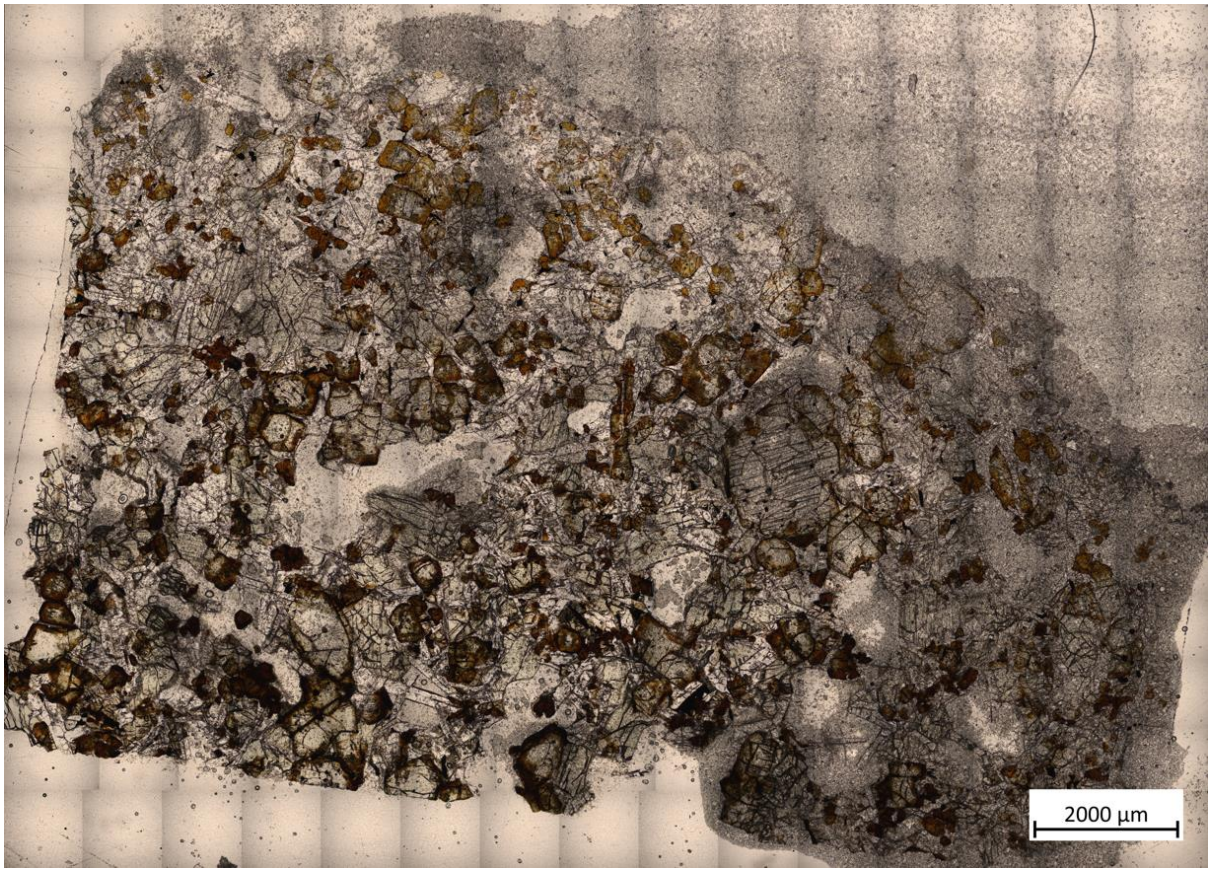

Figure A5.17: PPL Image of Sample 17.

Figure A5.18: PPL Image of Sample 18.

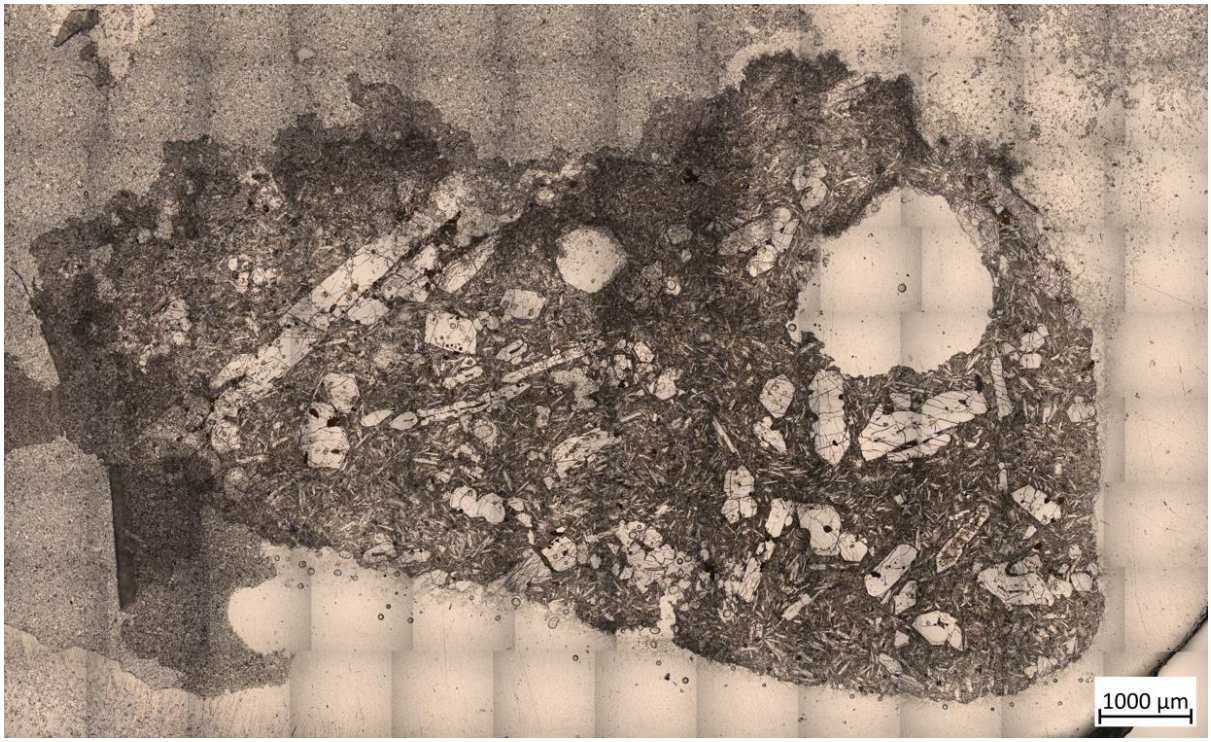

Figure A5.19: PPL Image of Sample 19.

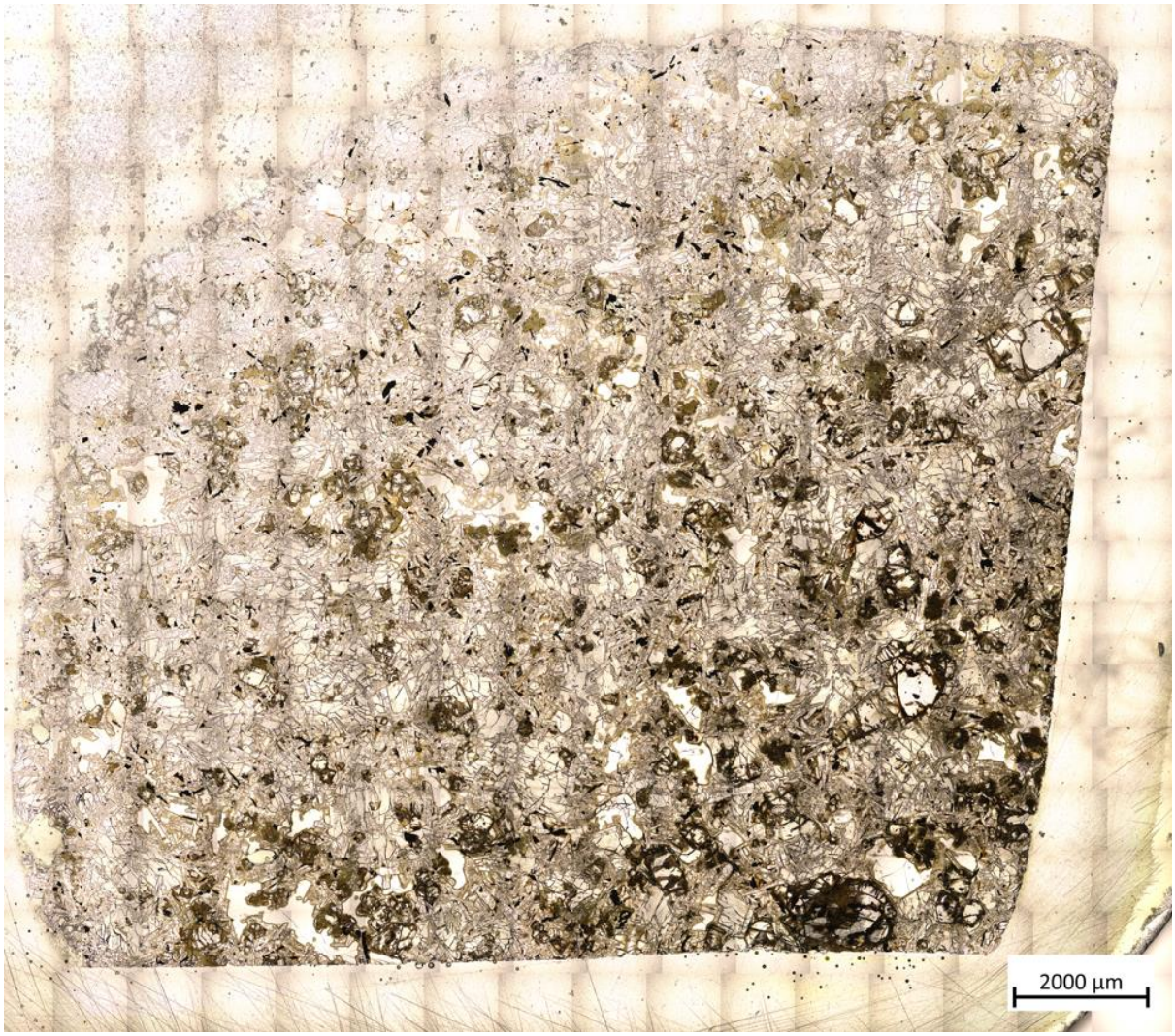

Figure A5.20: PPL Image of Sample 20.

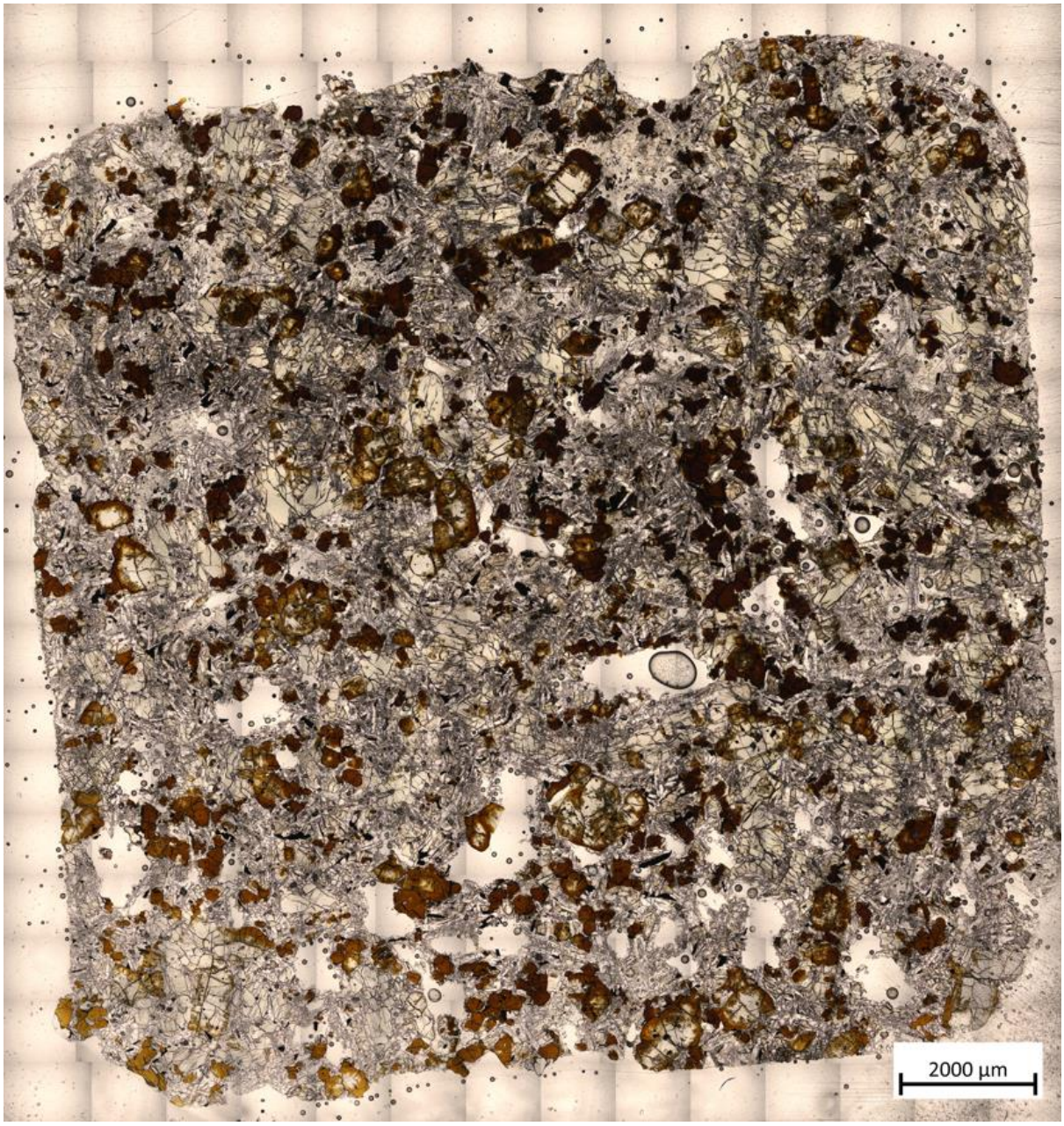

Figure A5.21: PPL Image of Sample 21.

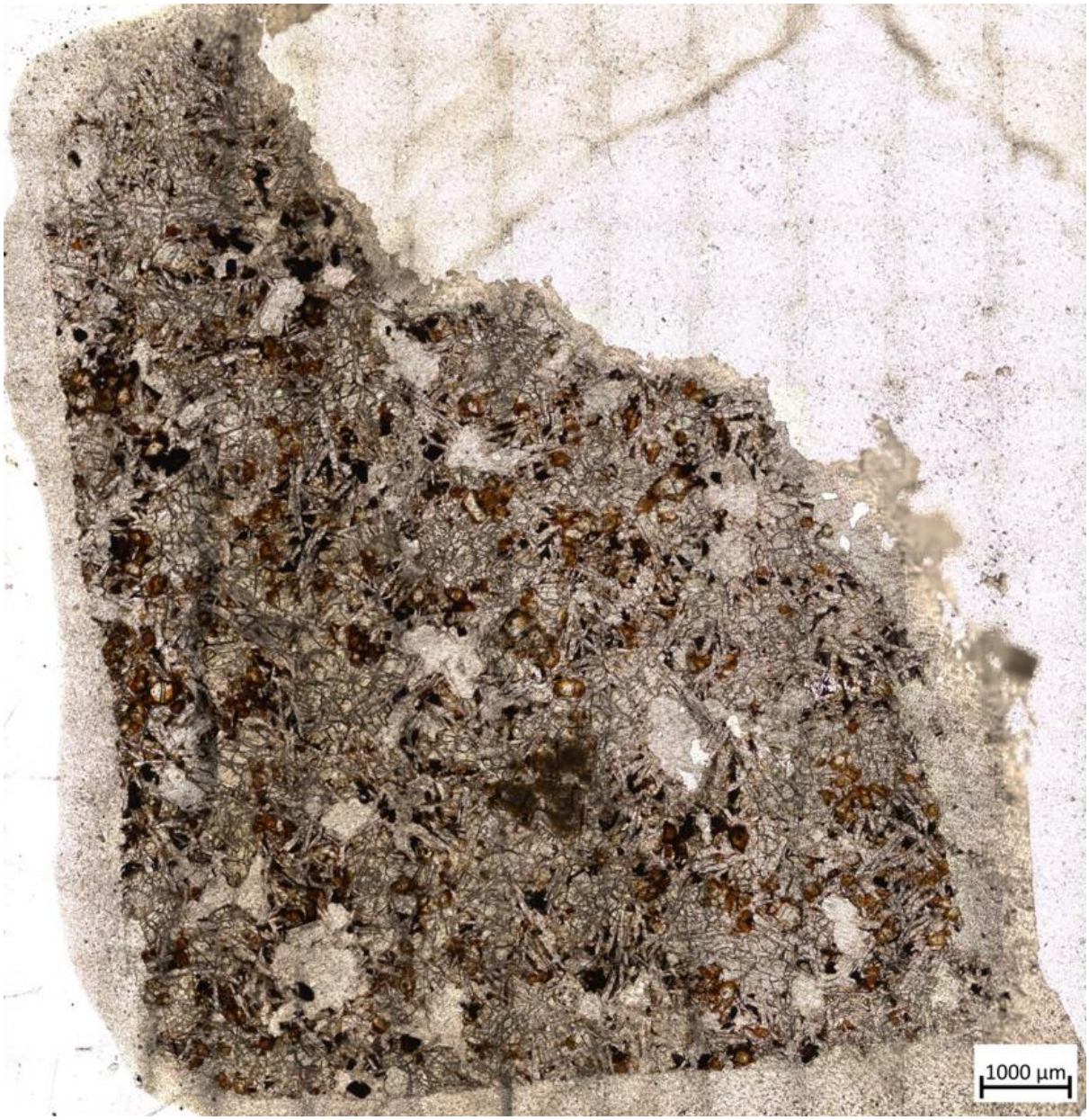

Figure A5.22: PPL Image of Sample 22.

Figure A5.23: PPL Image of Sample 23.

Figure A5.24: PPL Image of Sample 24.

Figure A5.25: PPL Image of Sample 25.

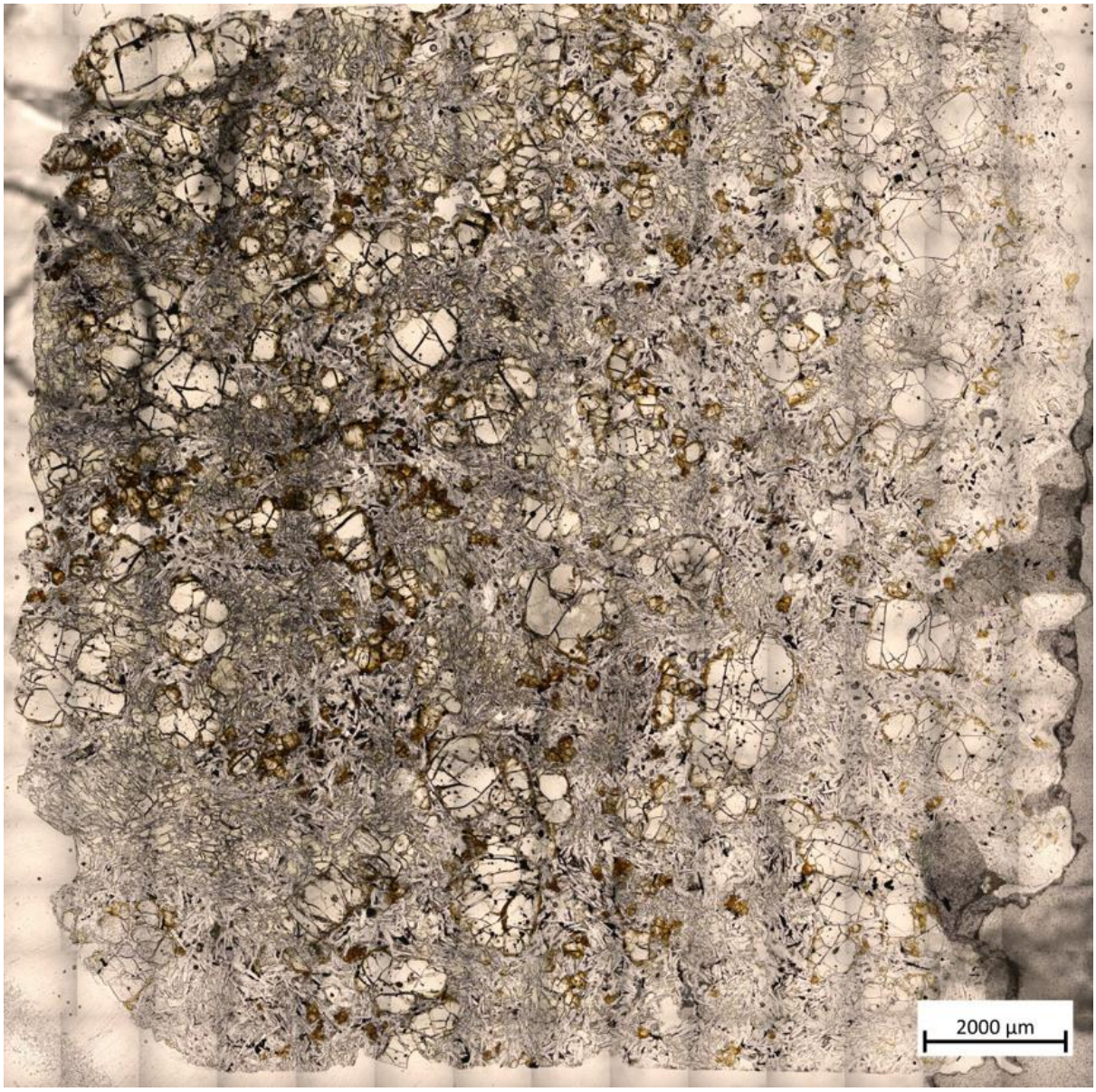

Figure A5.26: PPL Image of Sample 26.

Figure A5.27: PPL Image of Sample 27.

Appendix VI – XPL Images

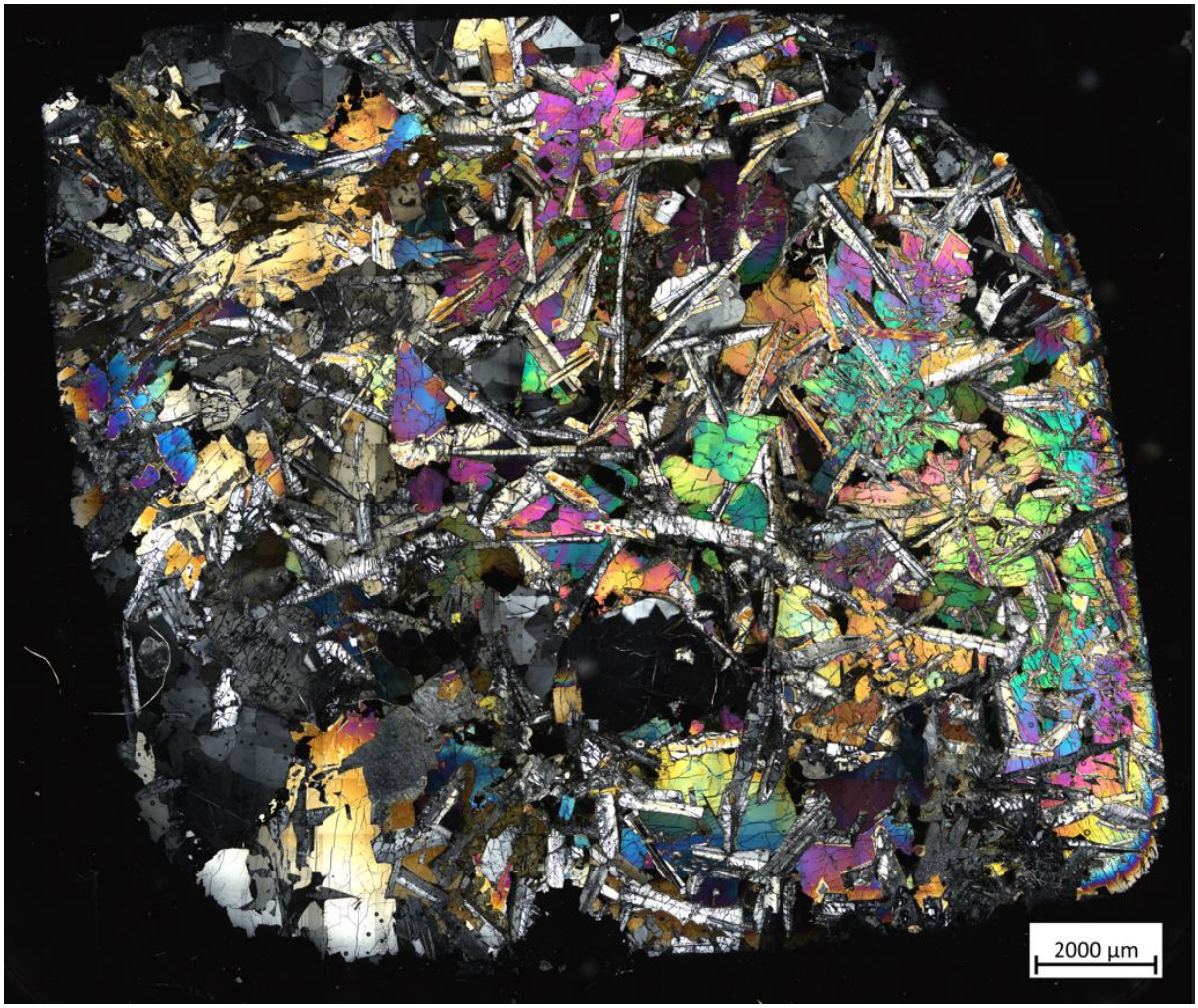

Figure A6.1: XPL Image of Sample 1.

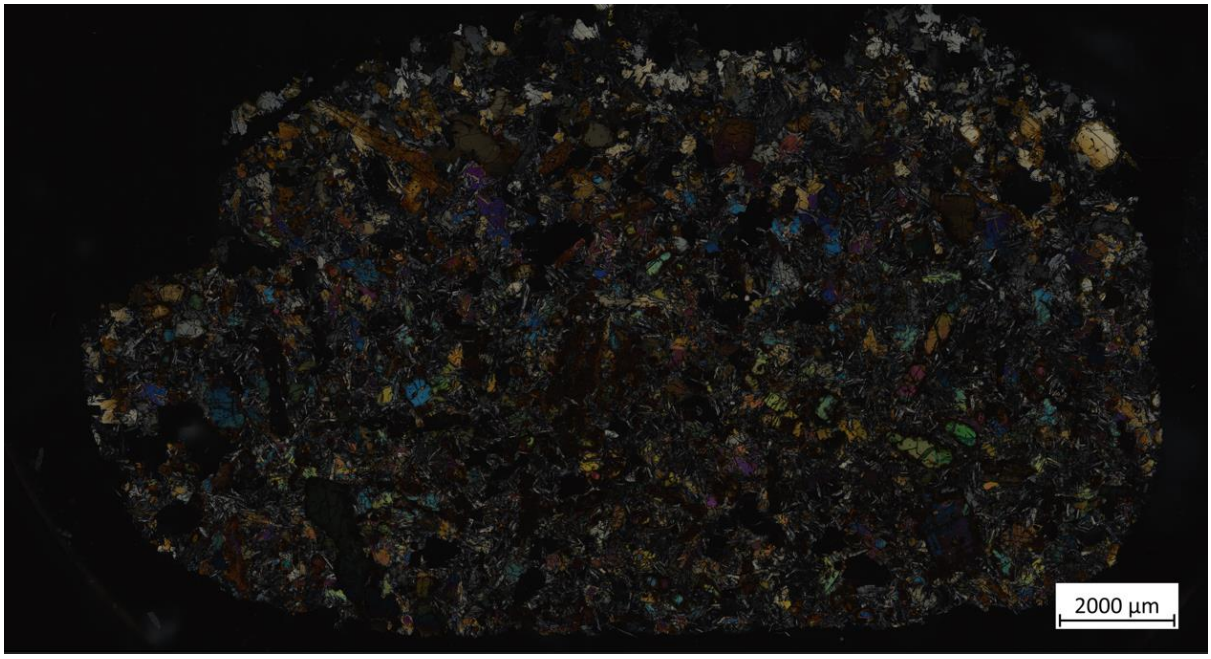

Figure A6.2: XPL Image of Sample 2.

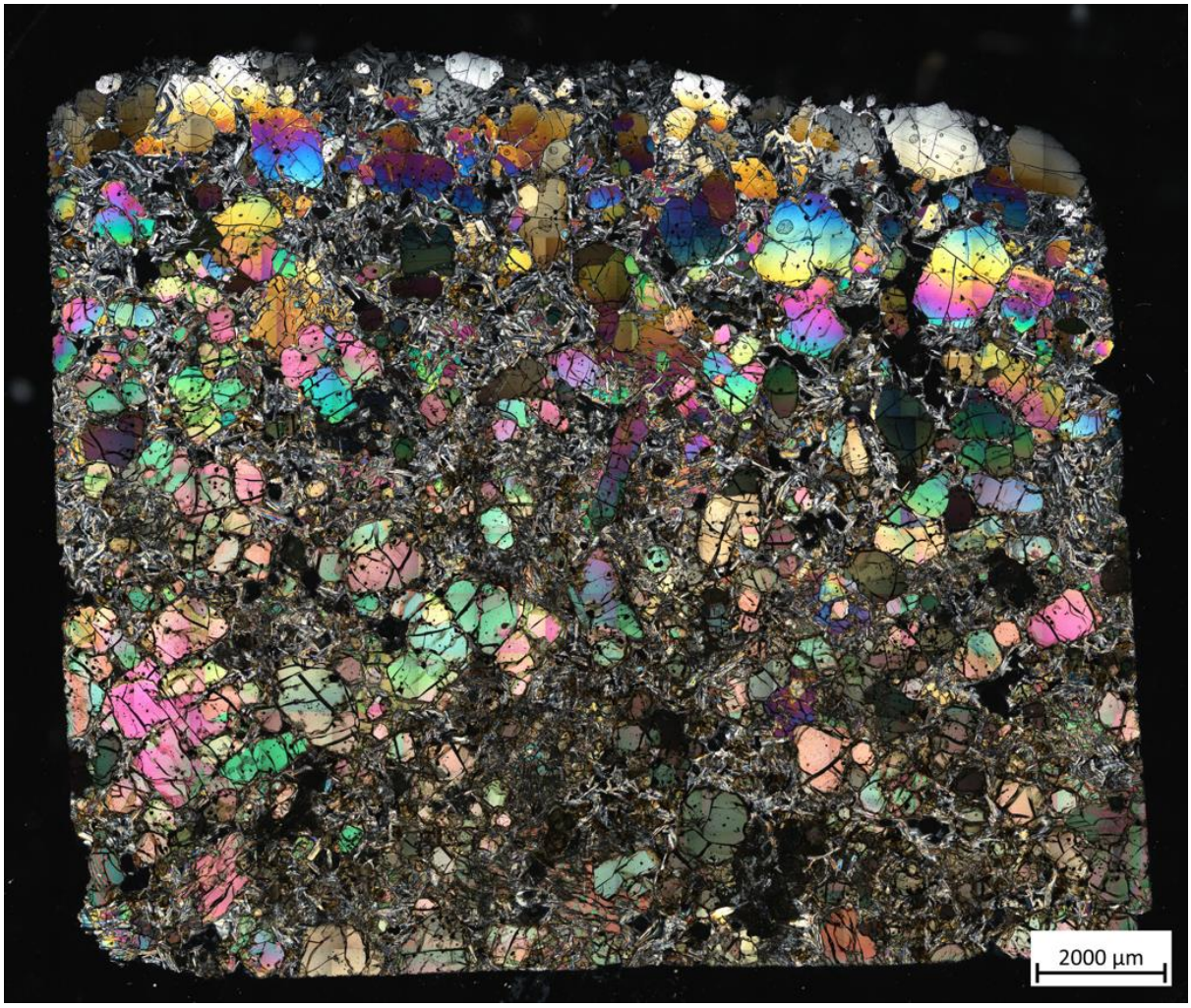

Figure A6.3: XPL Image of Sample 3.

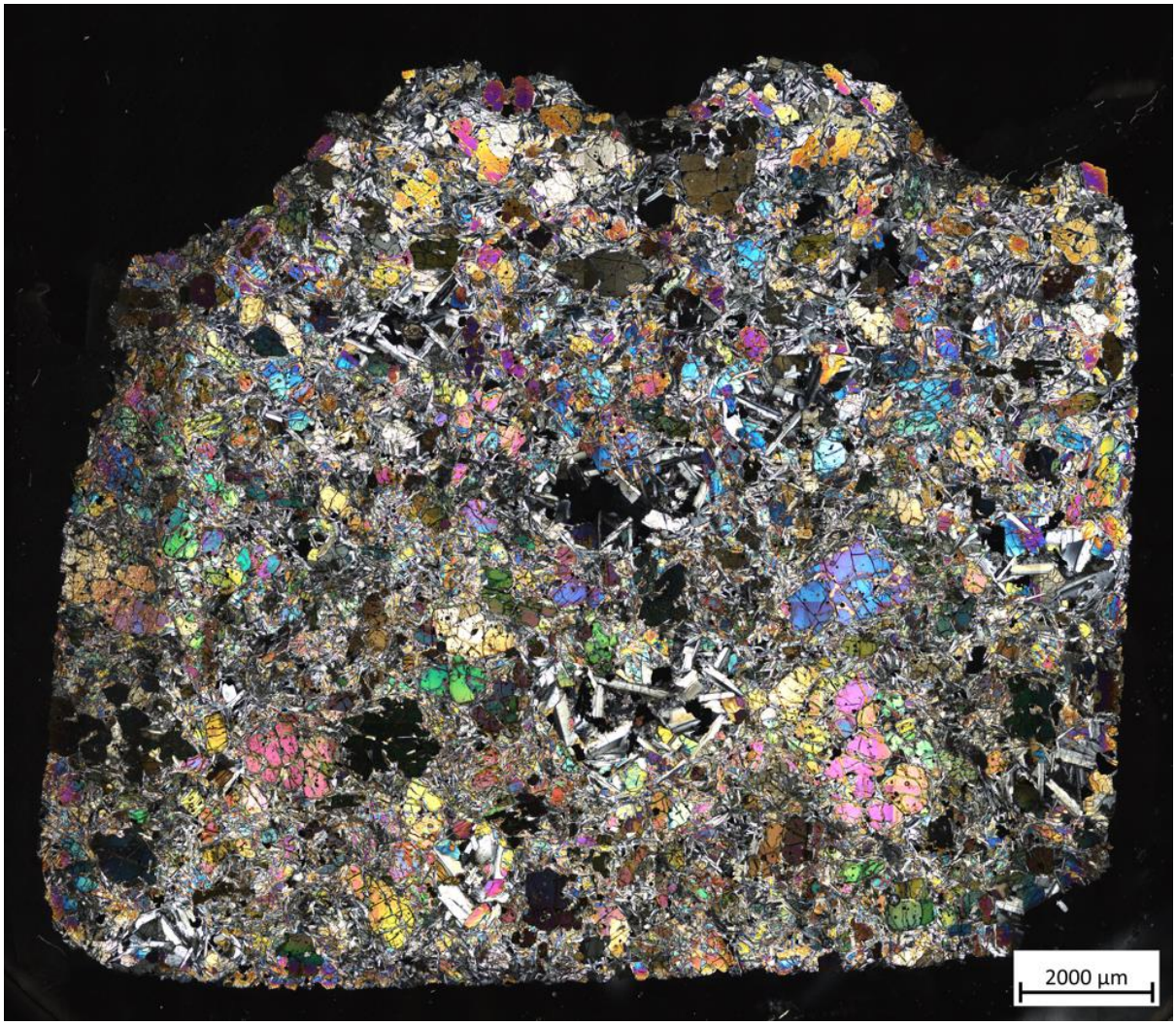

Figure A6.4: XPL Image of Sample 4.

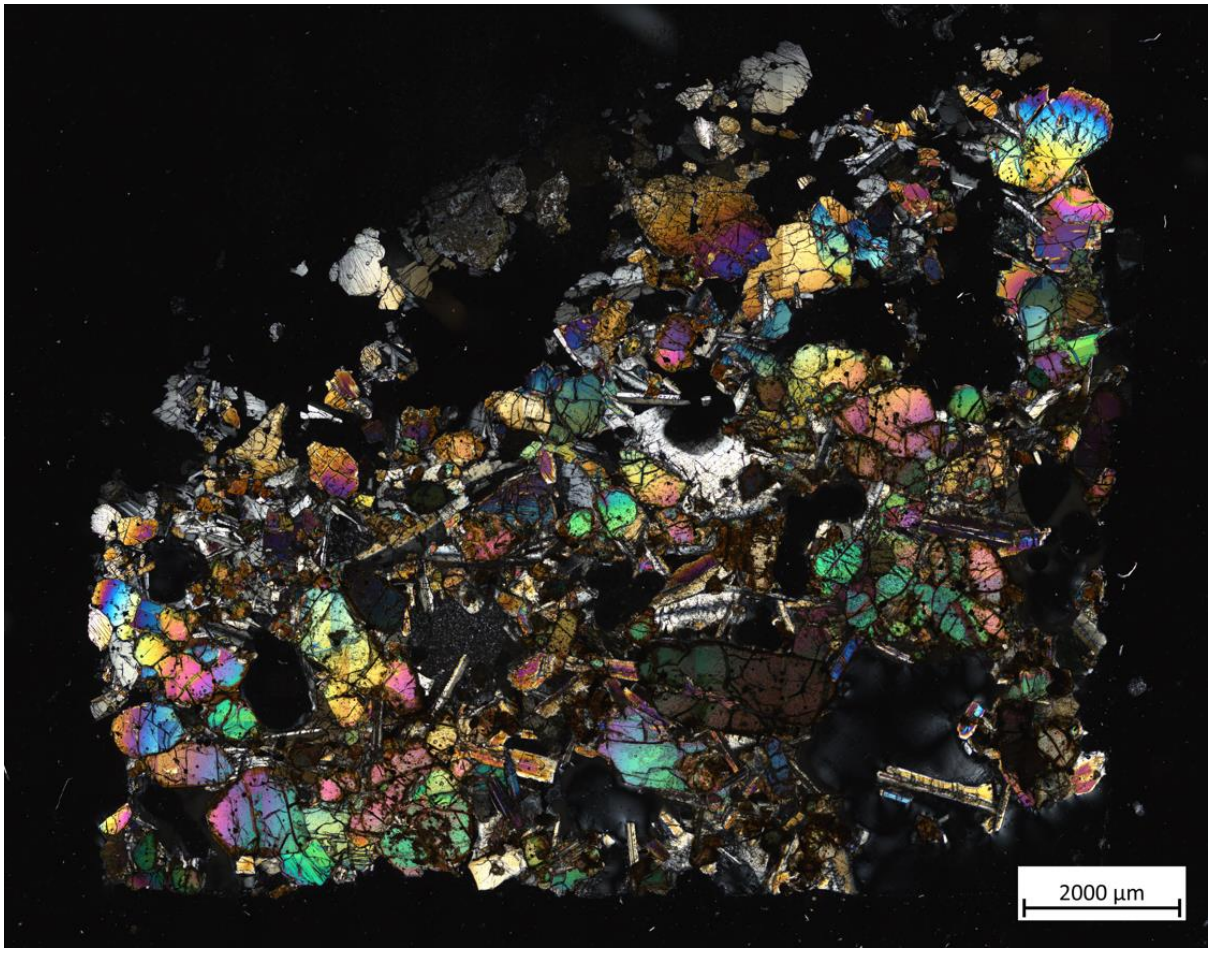

Figure A6.5: XPL Image of Sample 5.

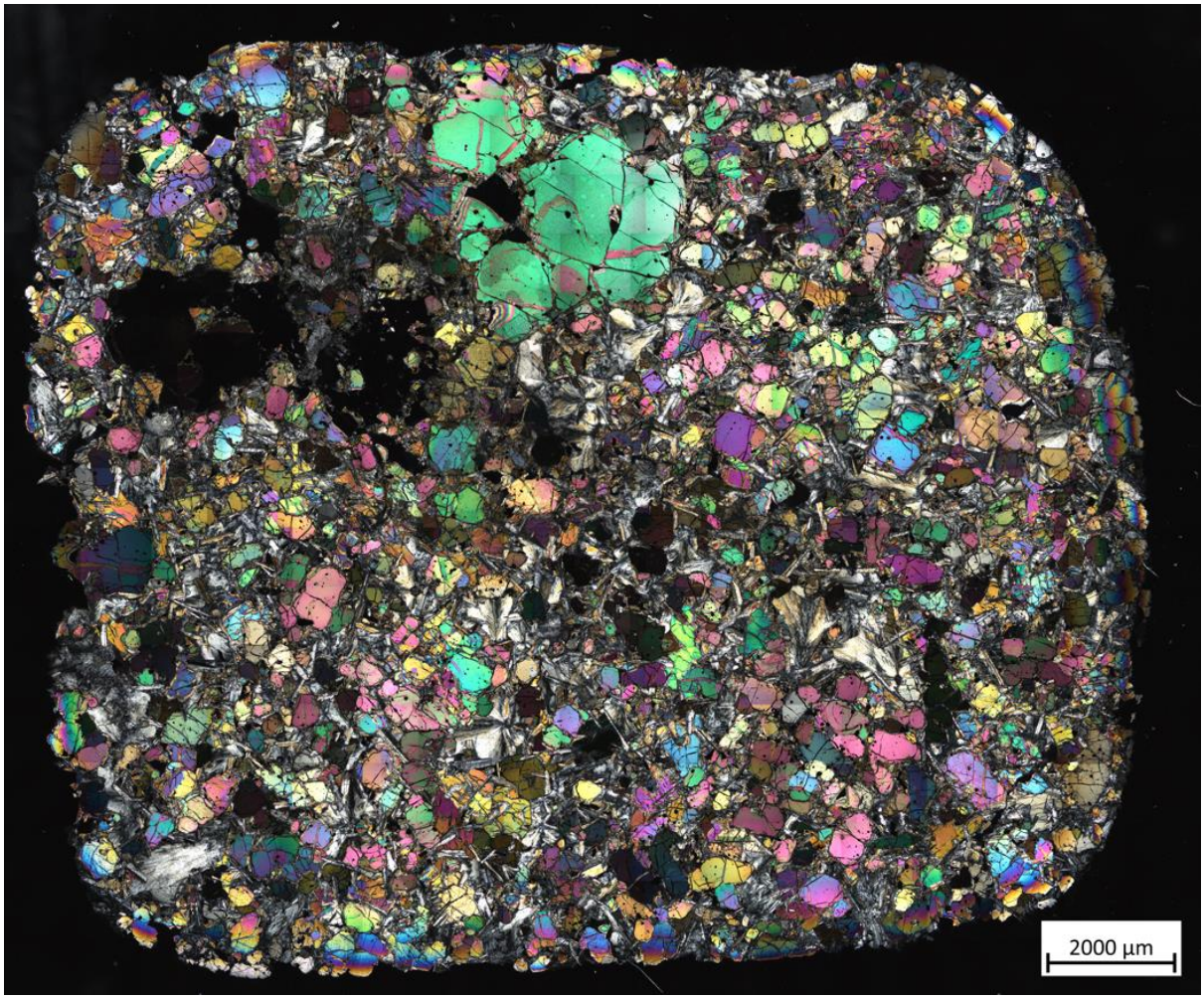

Figure A6.6: XPL Image of Sample 6.

Figure A6.7: XPL Image of Sample 7.

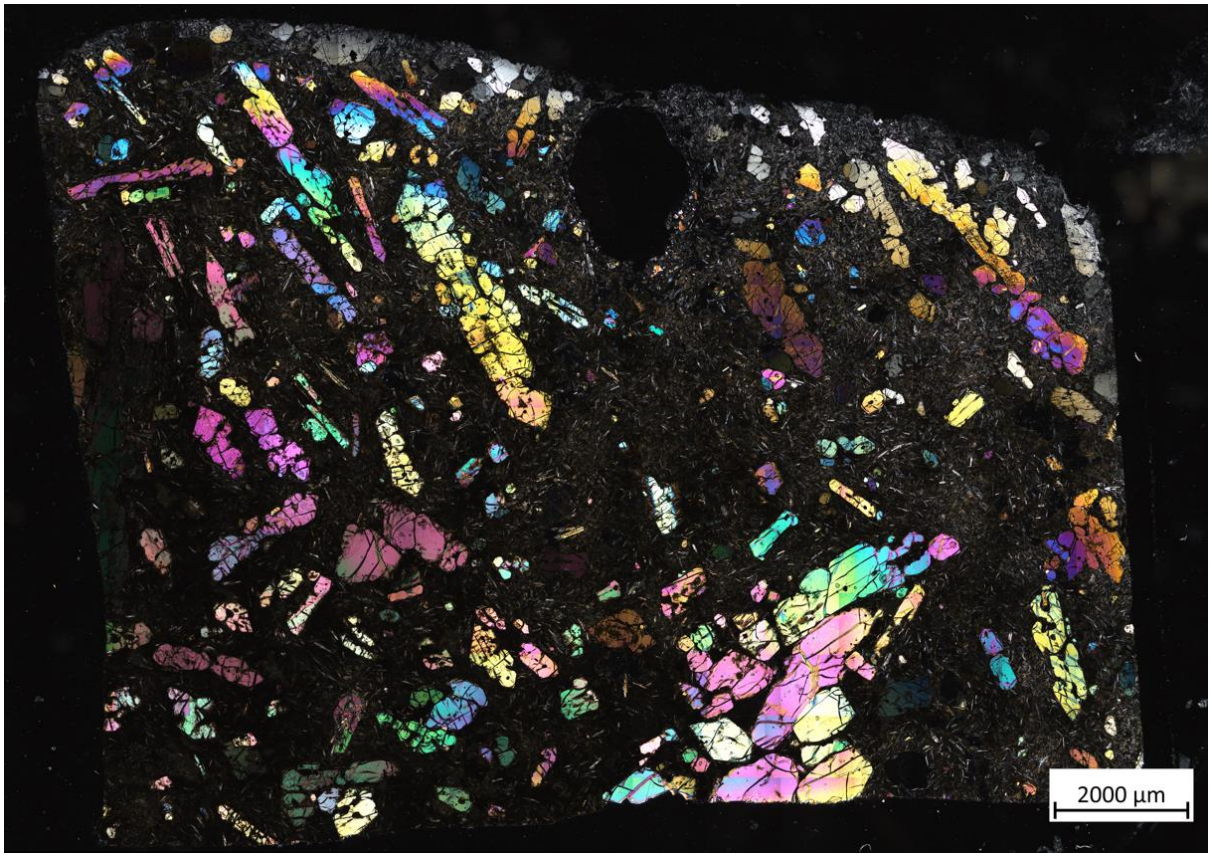

Figure A6.8: XPL Image of Sample 8.

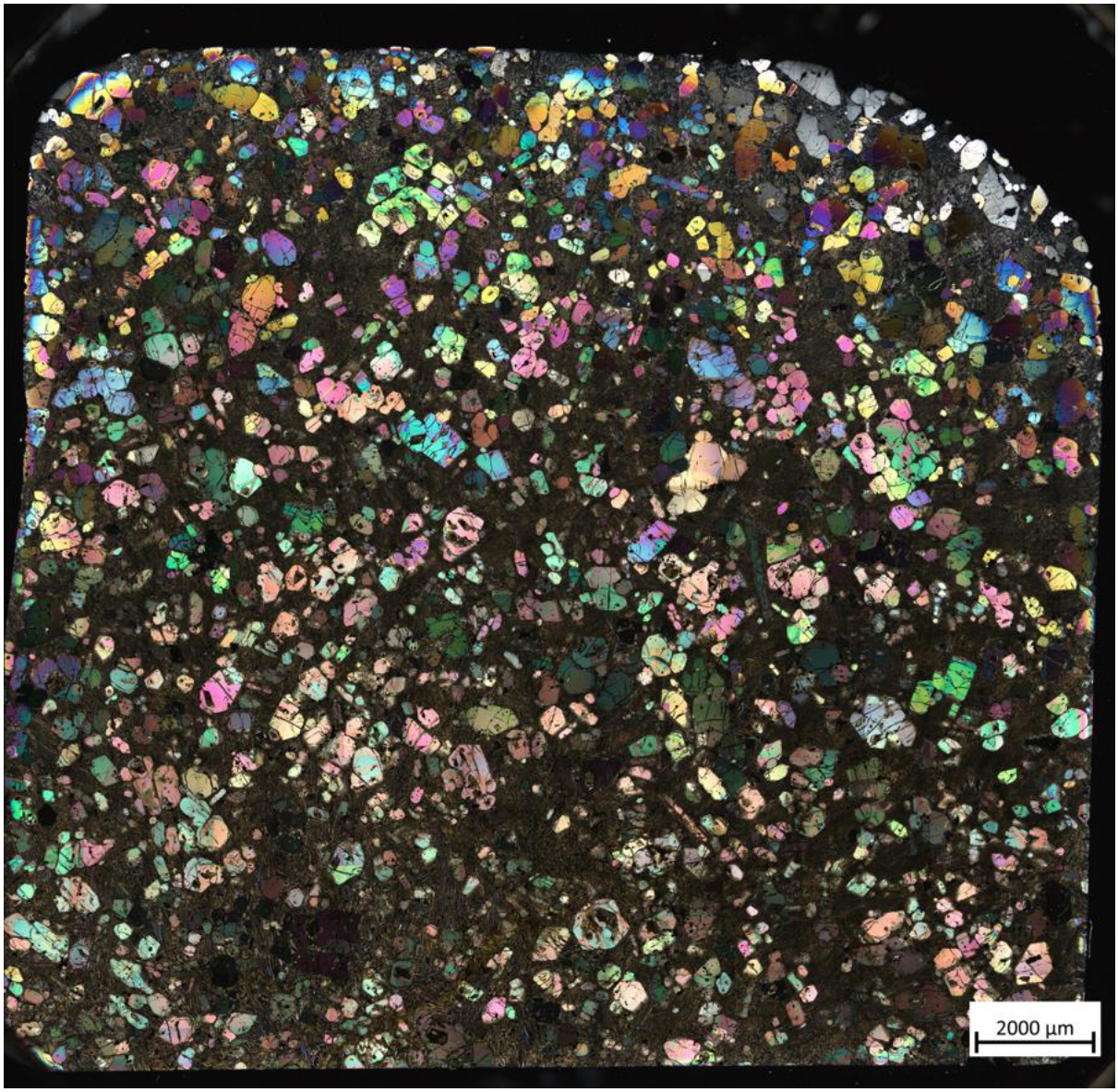

Figure A6.9: XPL Image of Sample 9.

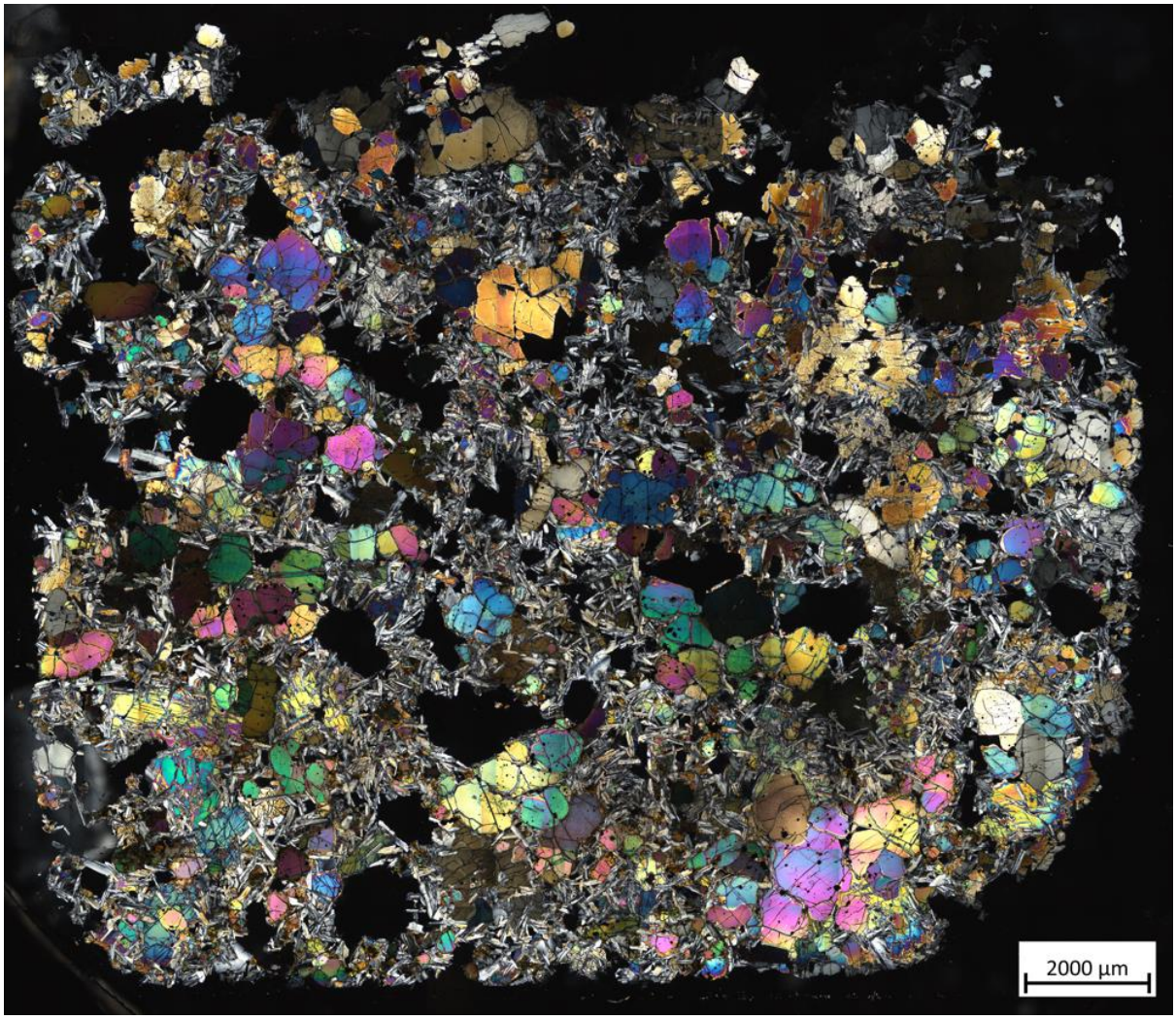

Figure A6.10:XPPL Image of Sample 10.

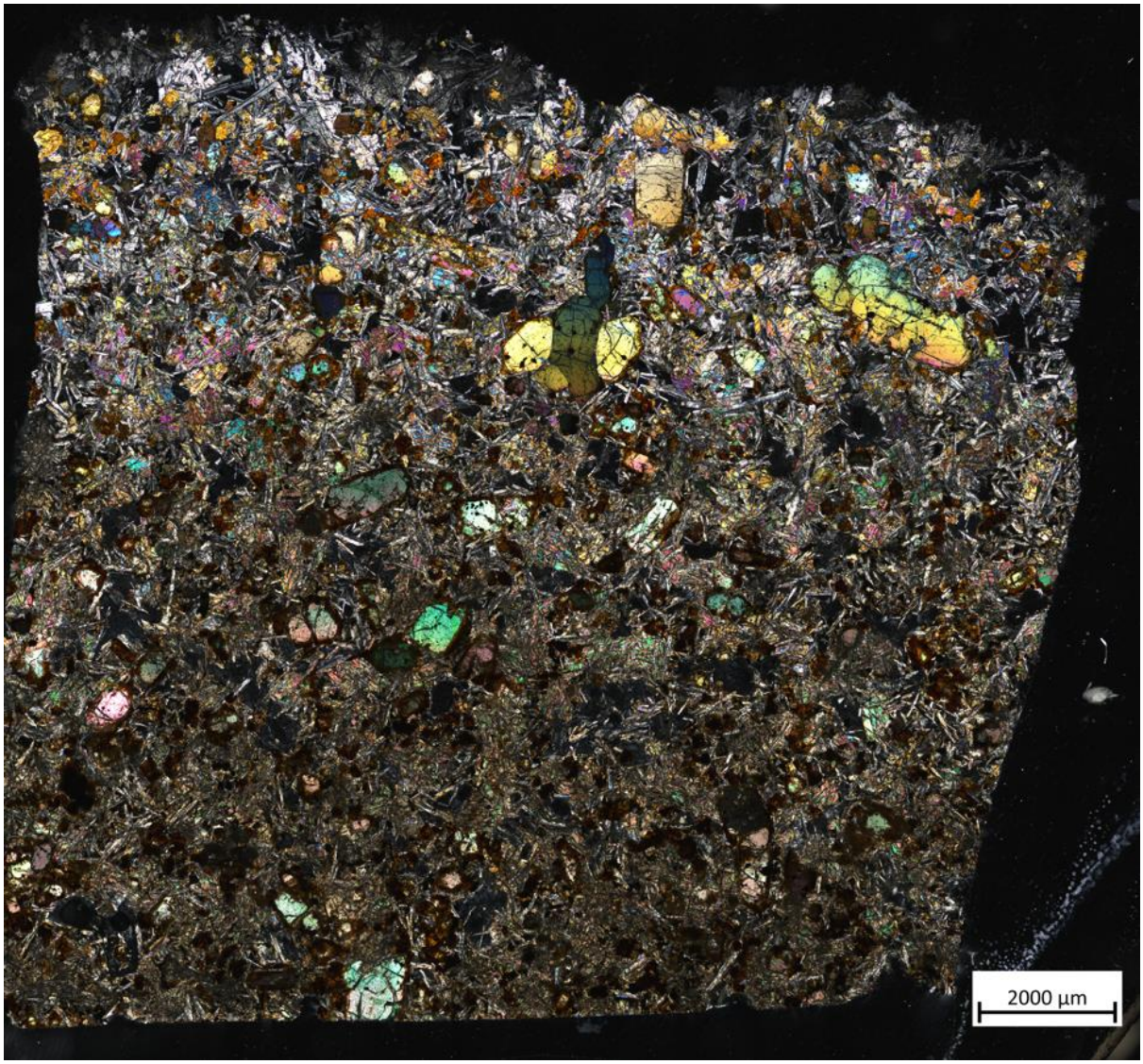

Figure A6.11: XPL Image of Sample 11.

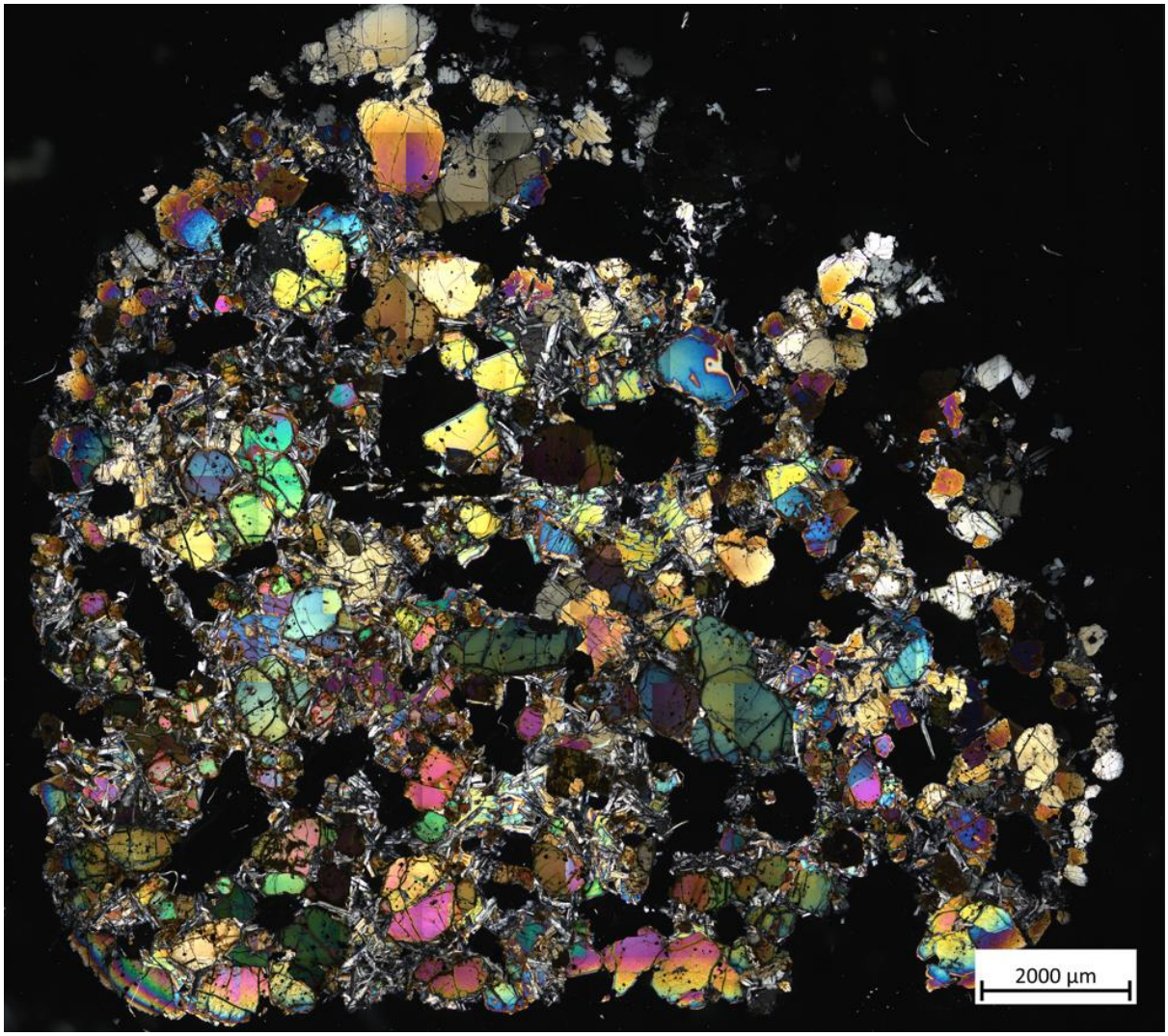

Figure A6.12: XPL Image of Sample 12.

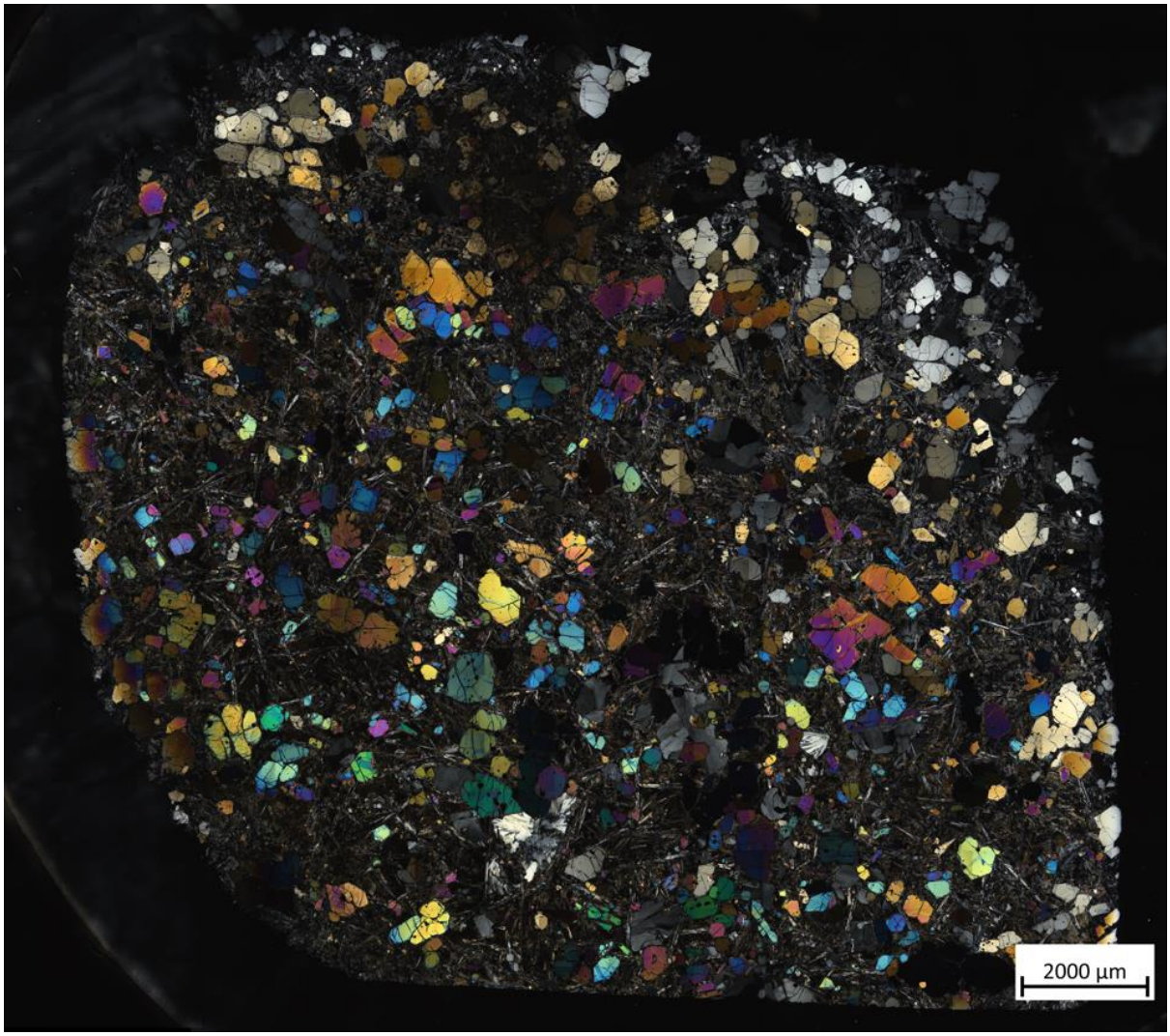

Figure A6.13: XPL Image of Sample 13.

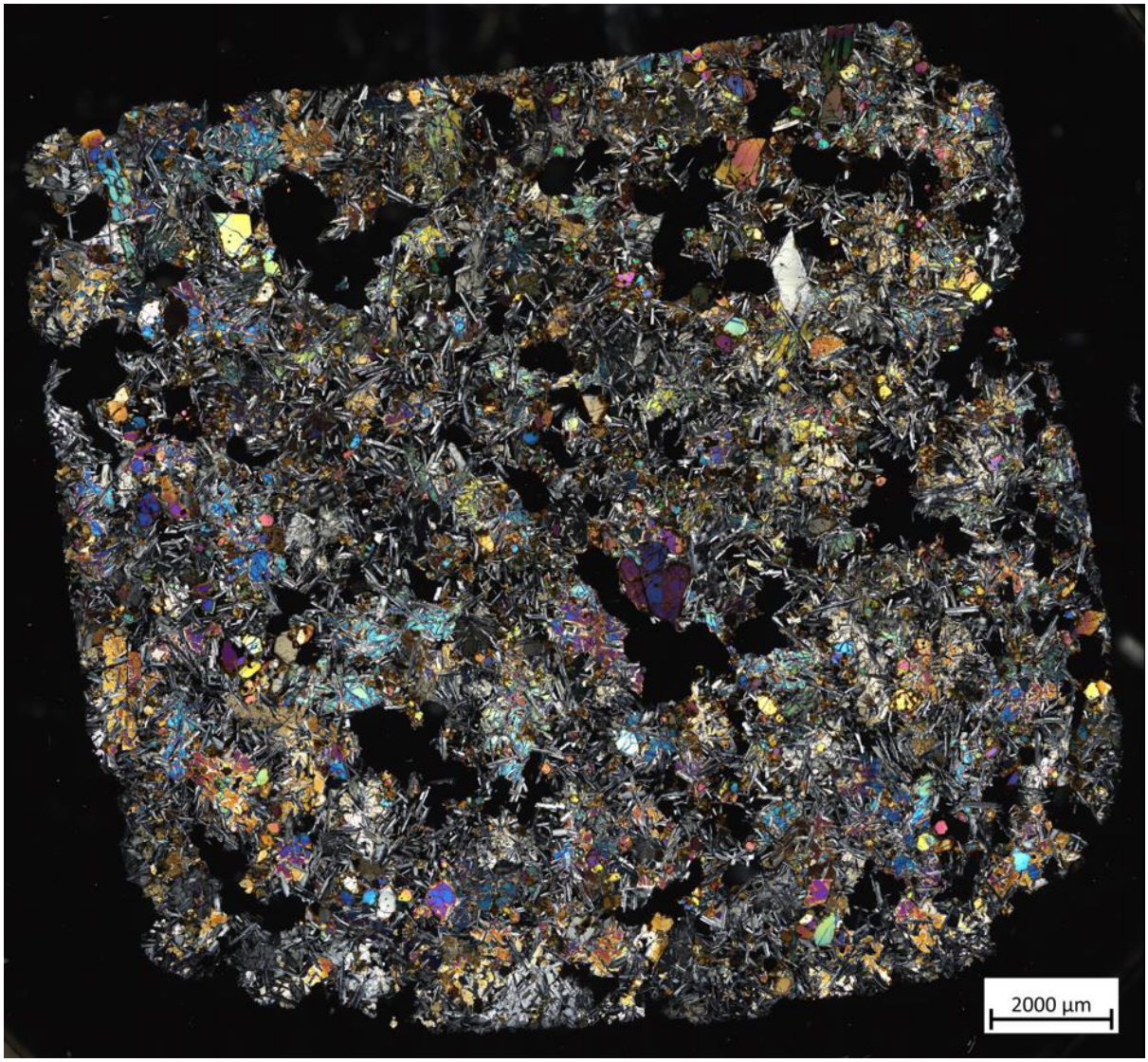

Figure A6.14: XPL Image of Sample 14.

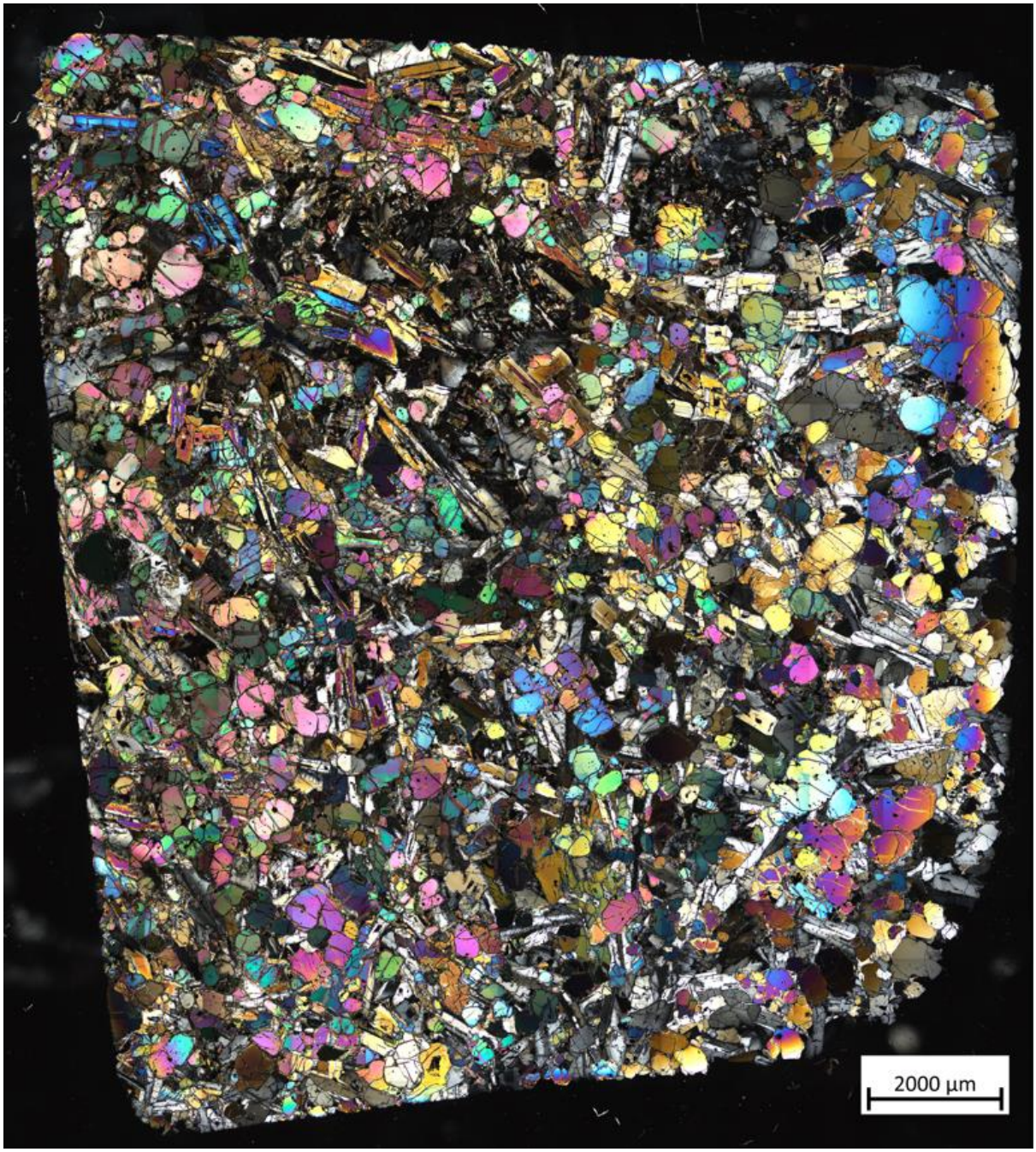

Figure A6.15: XPL Image of Sample 15.

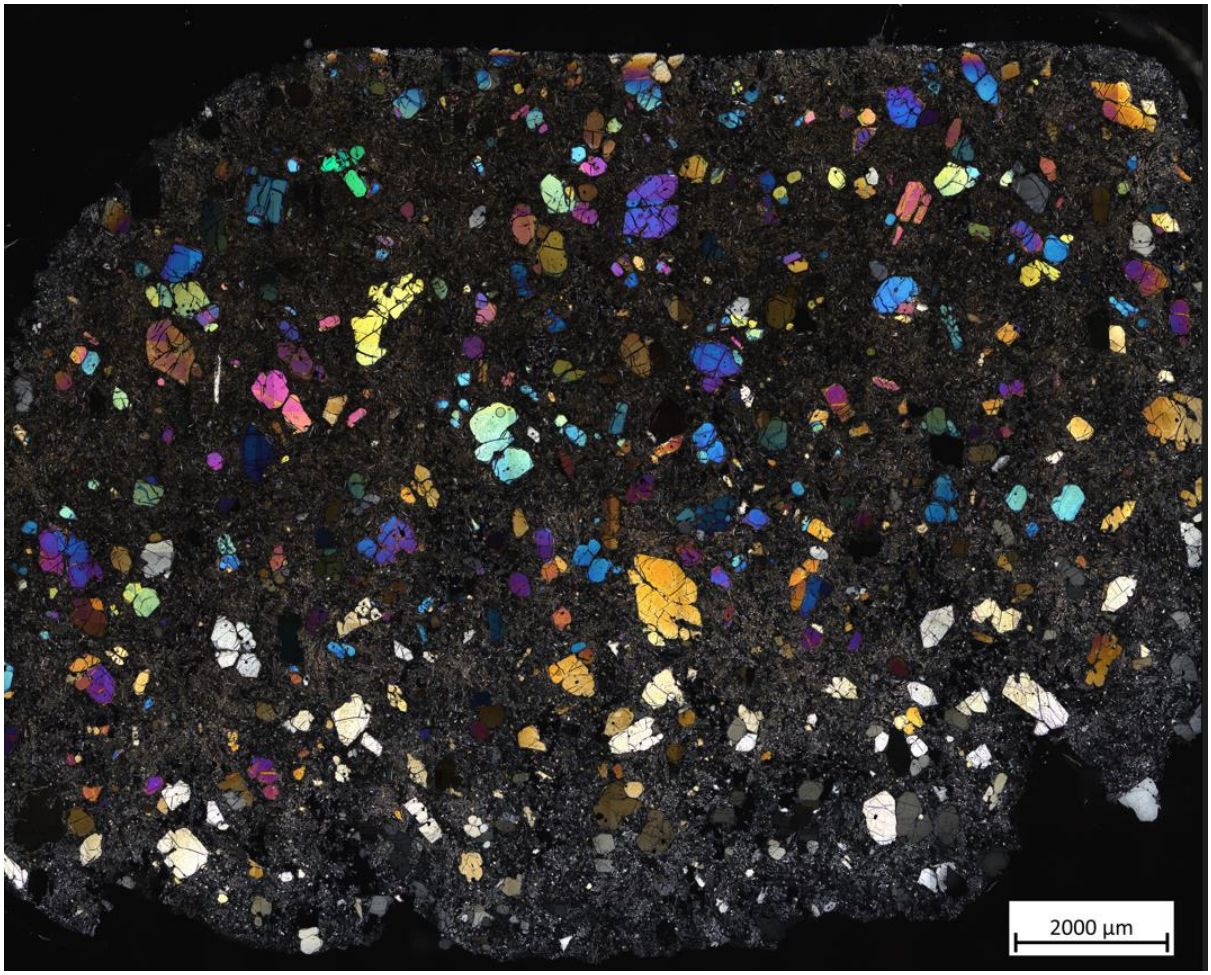

Figure A6.16: XPL Image of Sample 16.

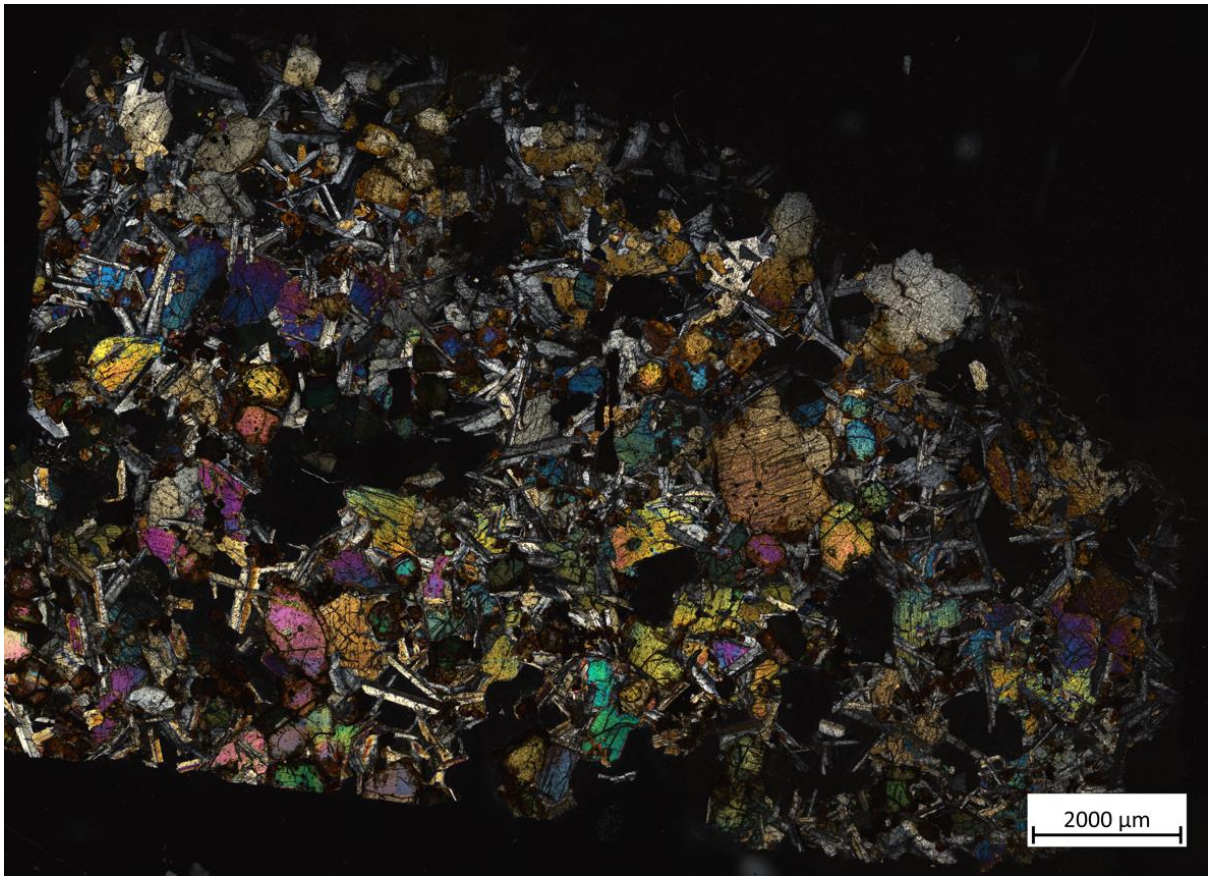

Figure A6.17: XPL Image of Sample 17.

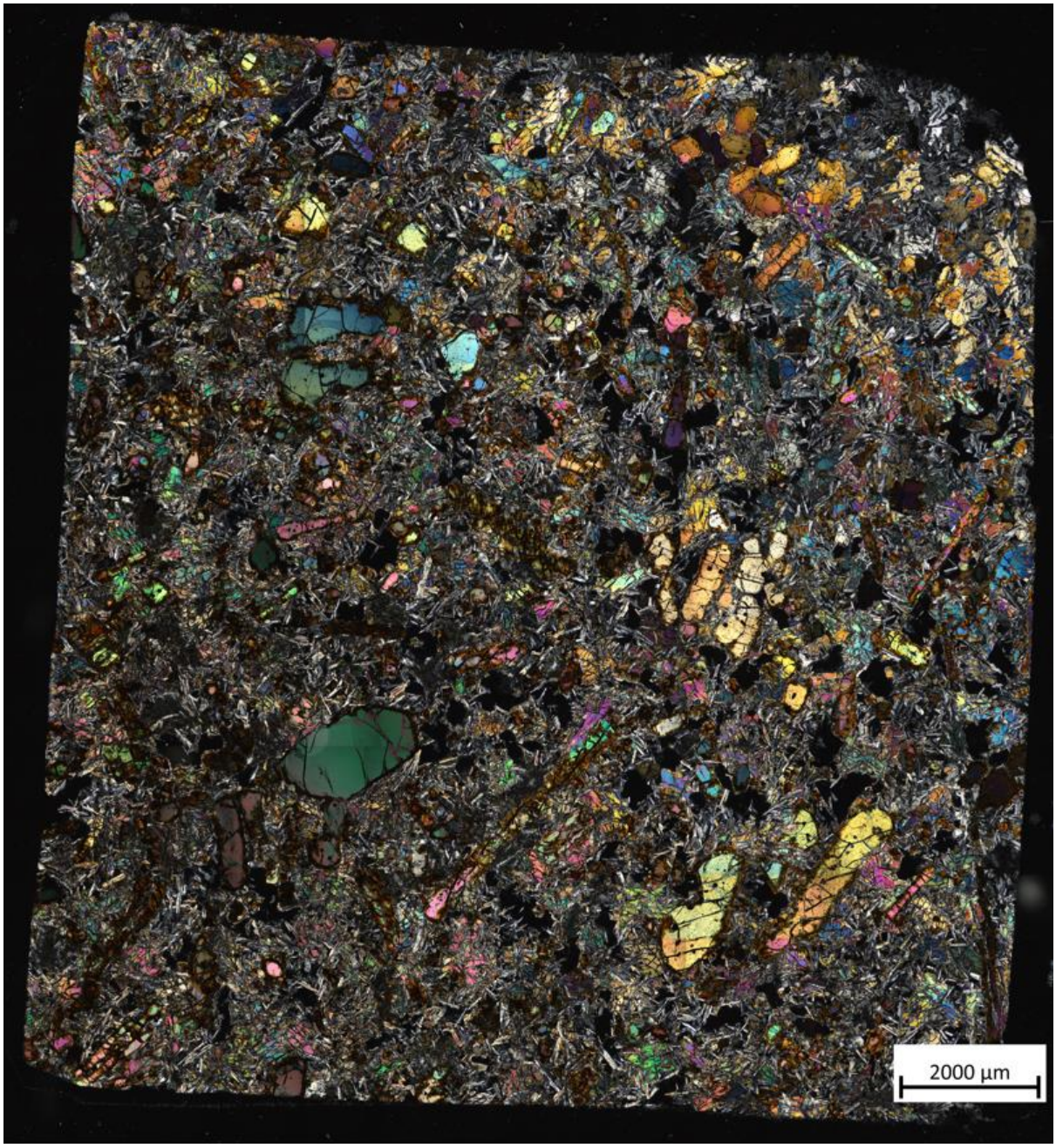

Figure A6.18: XPL Image of Sample 18.

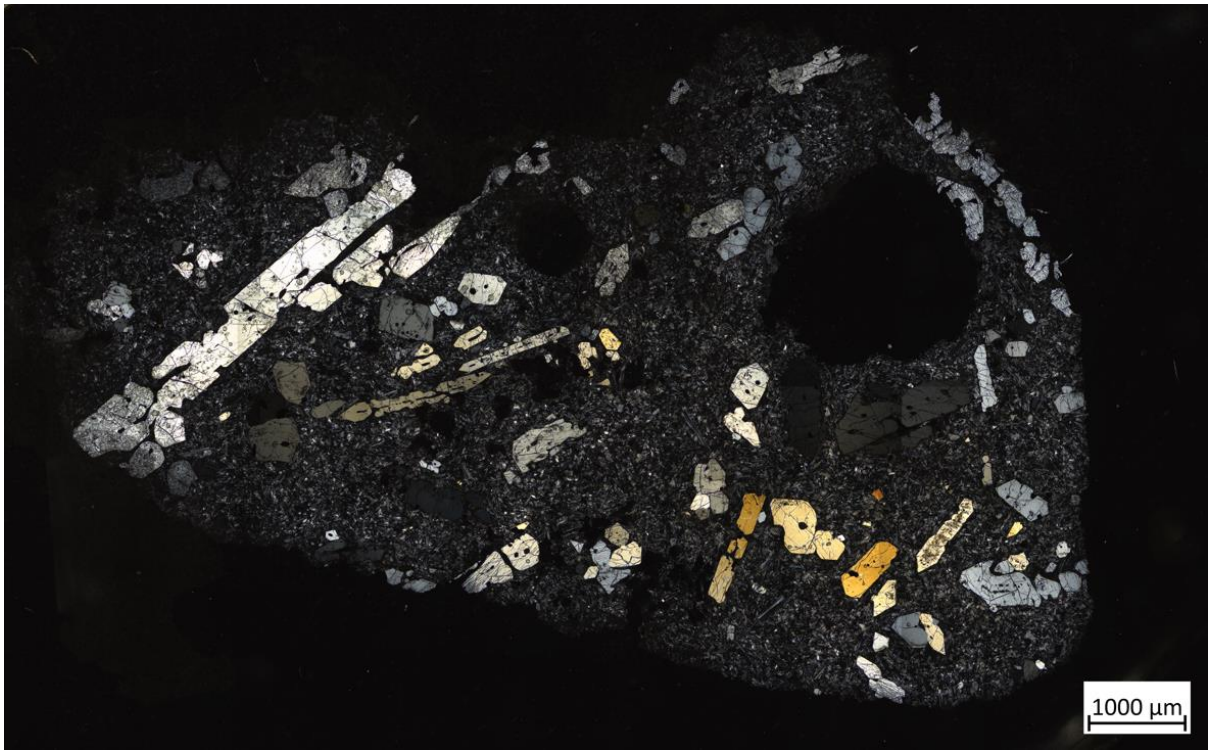

Figure A6.19: XPL Image of Sample 19.

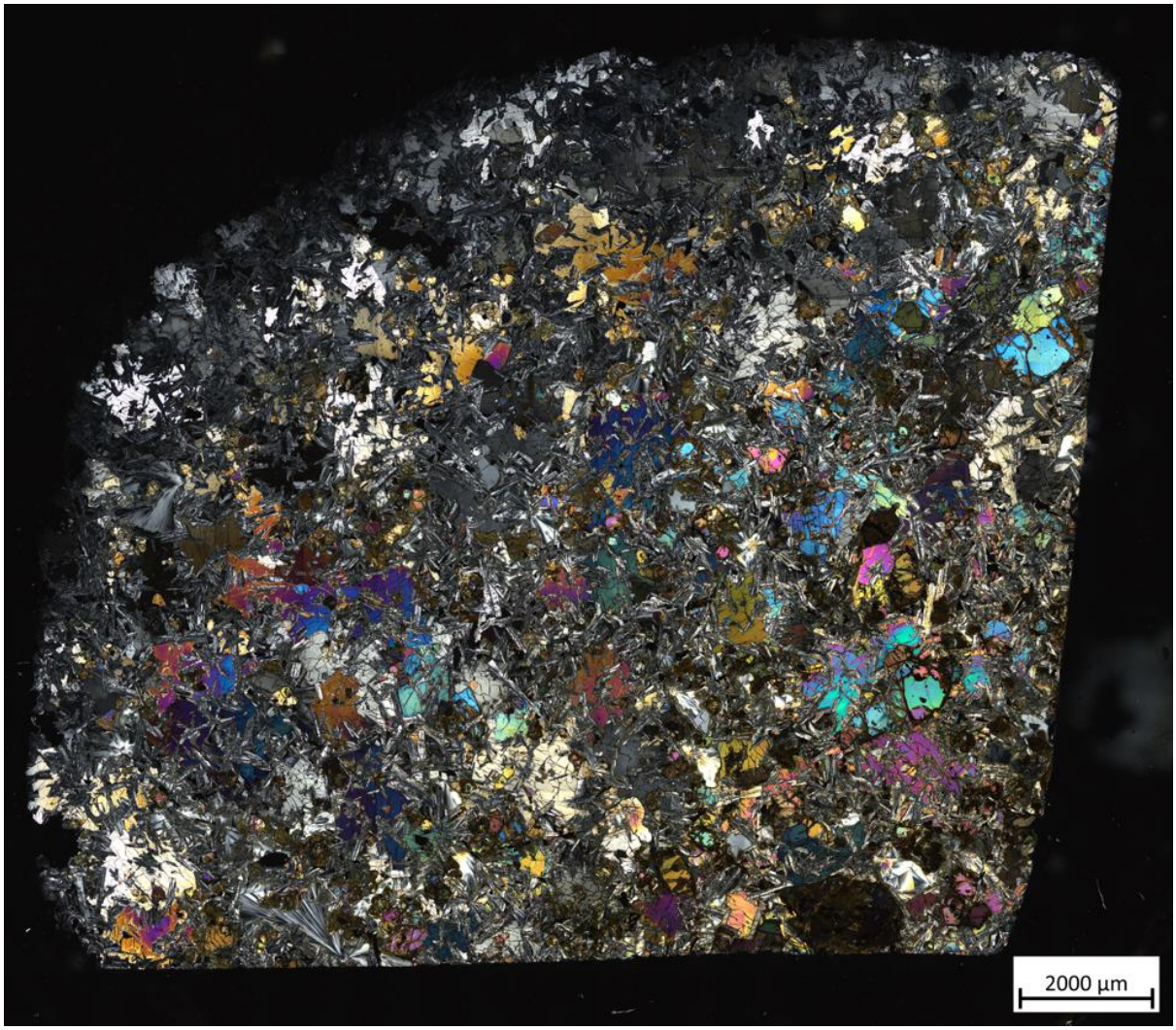

Figure A6.20: XPL Image of Sample 20.

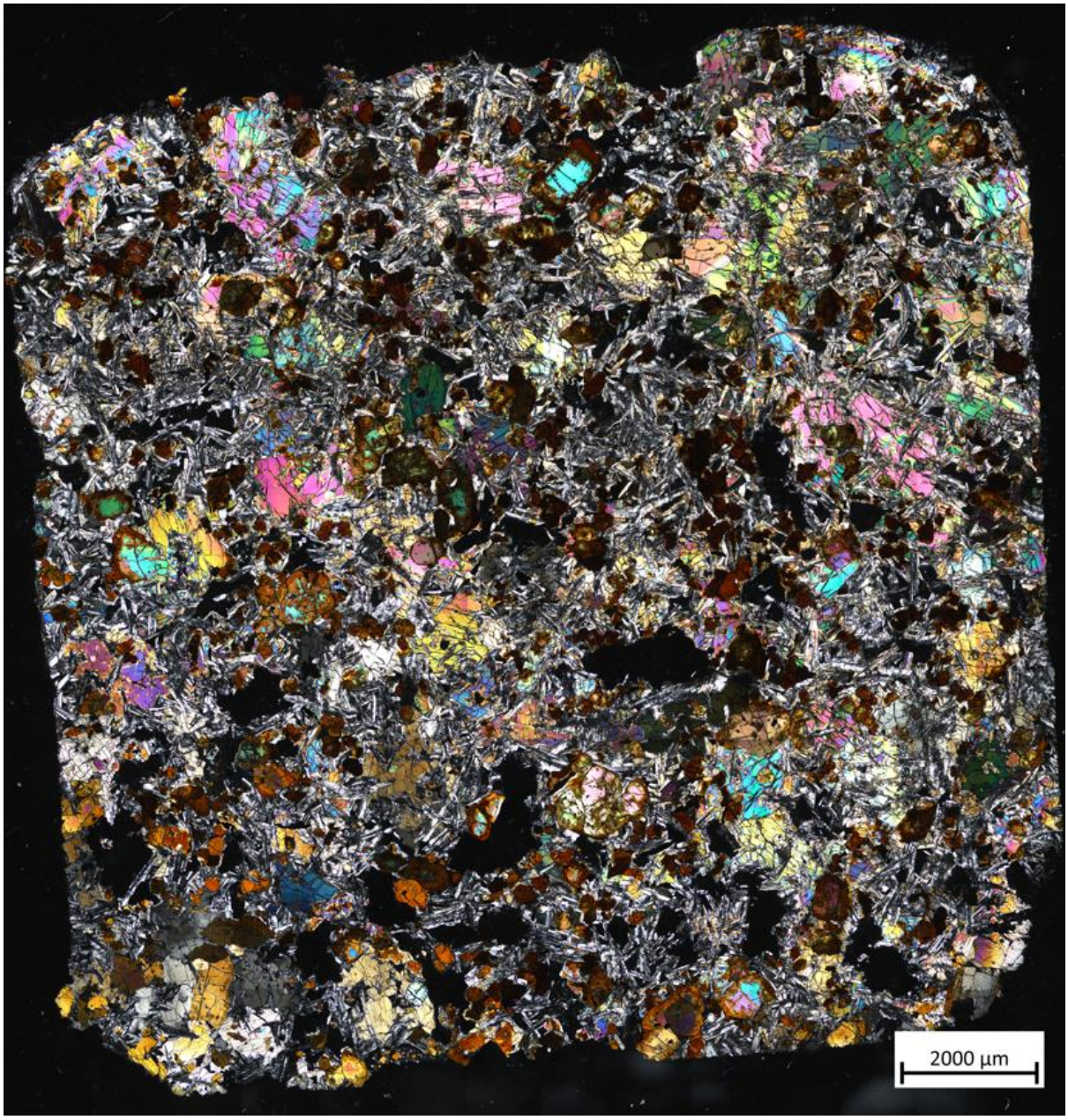

Figure A6.21: XPL Image of Sample 21.

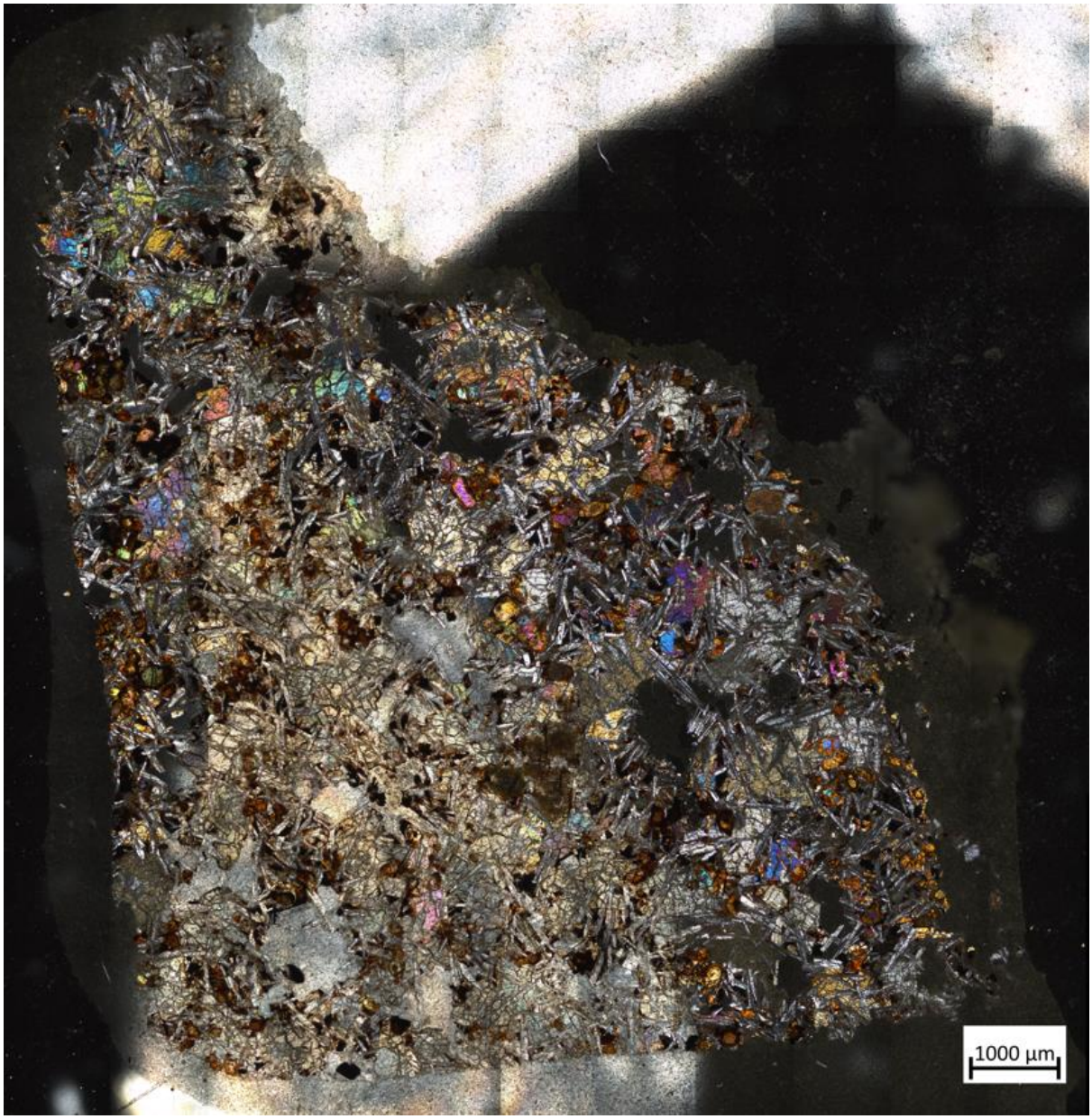

Figure A6.22: XPL Image of Sample 22.

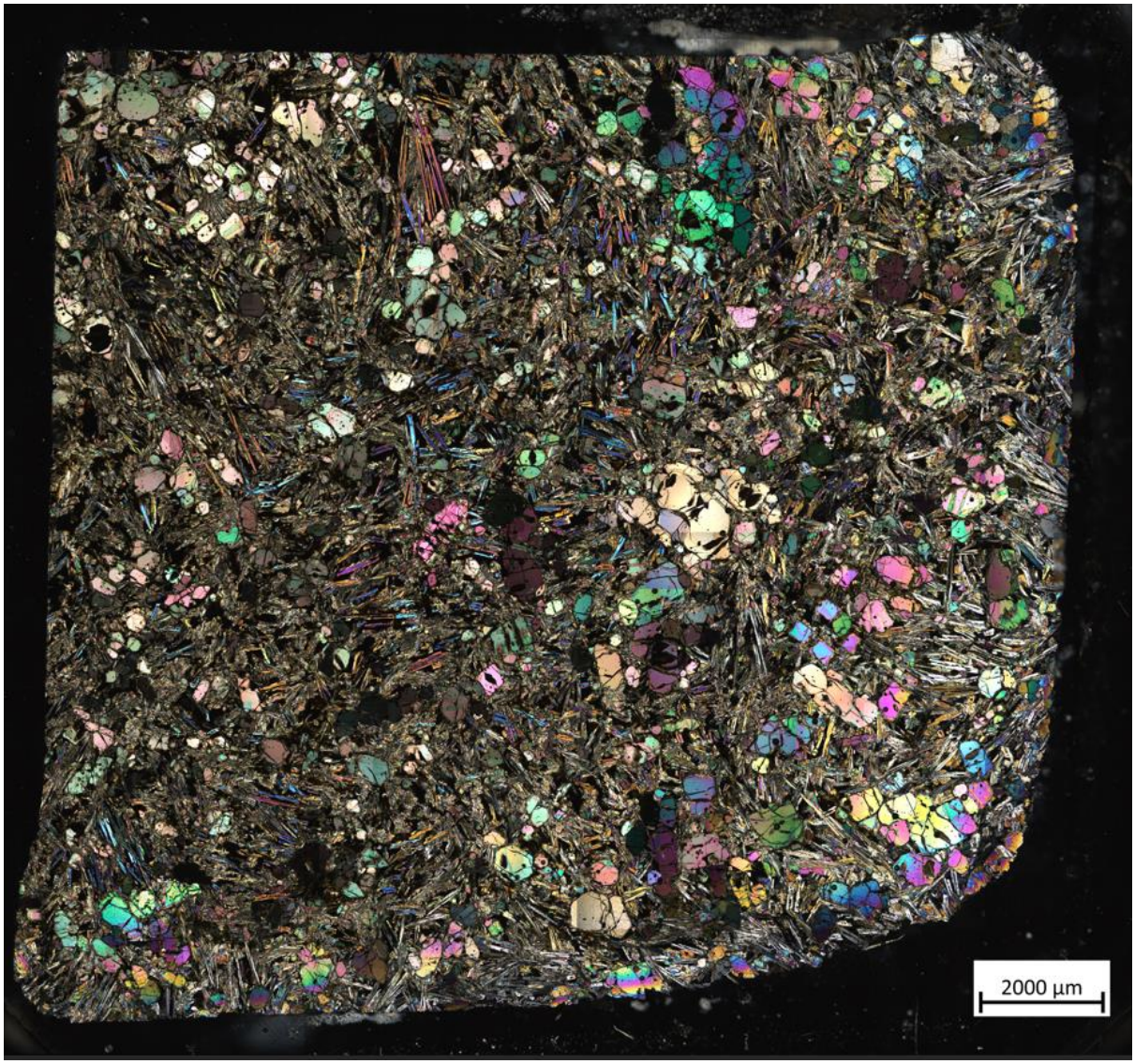

Figure A6.23: XPL Image of Sample 23.

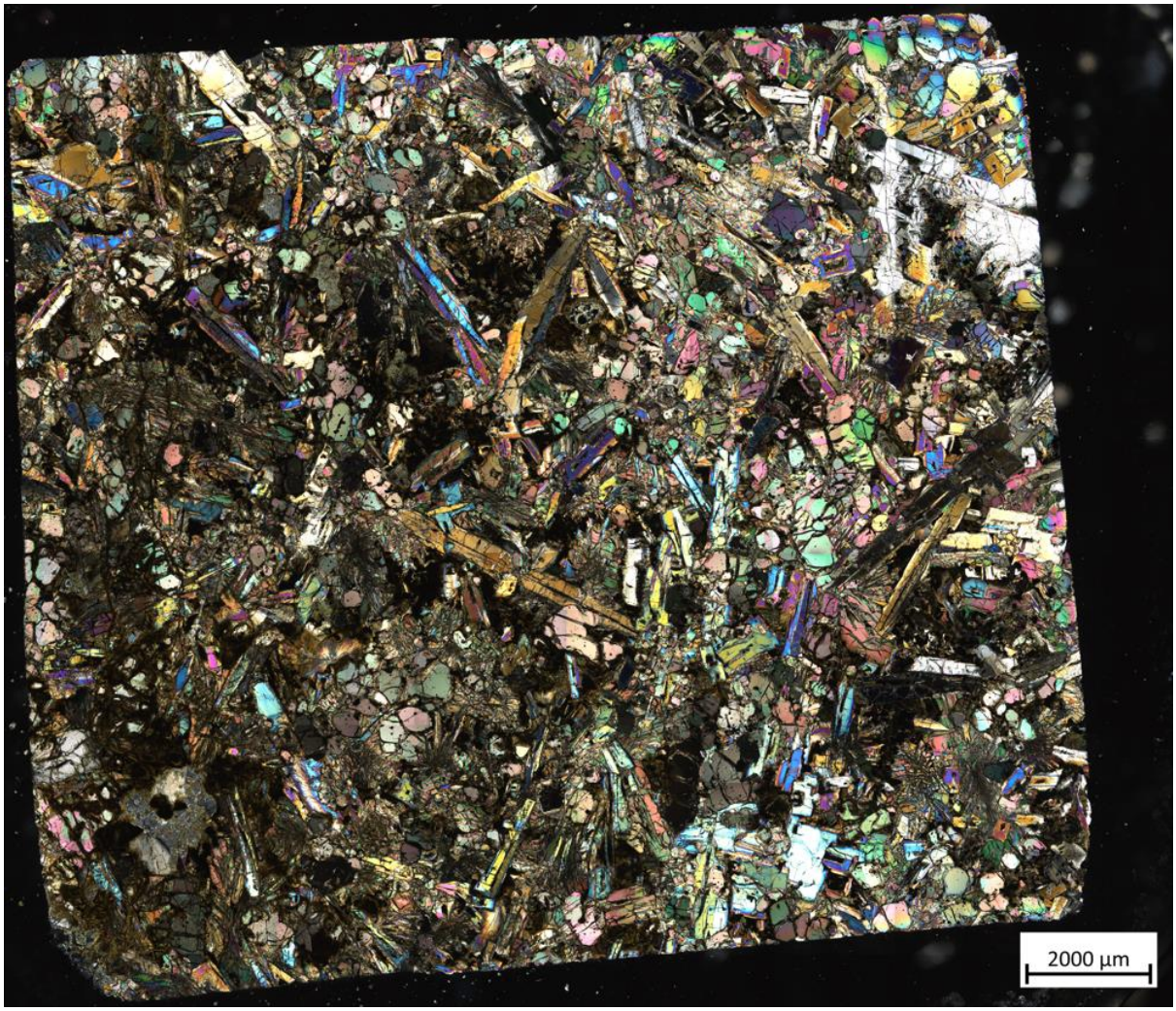

Figure A6.24: XPL Image of Sample 24.

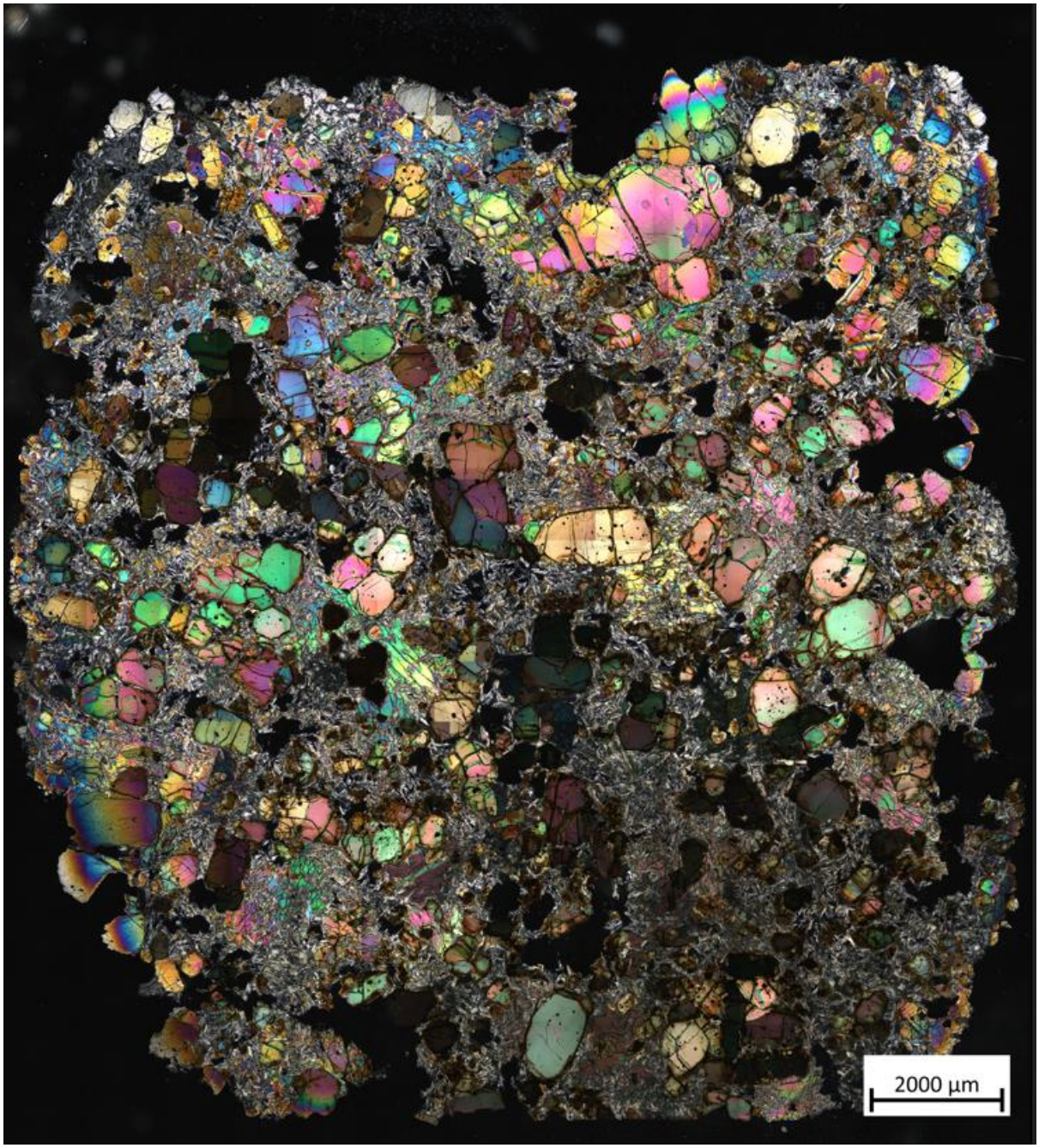

Figure A6.25: XPL Image of Sample 25.

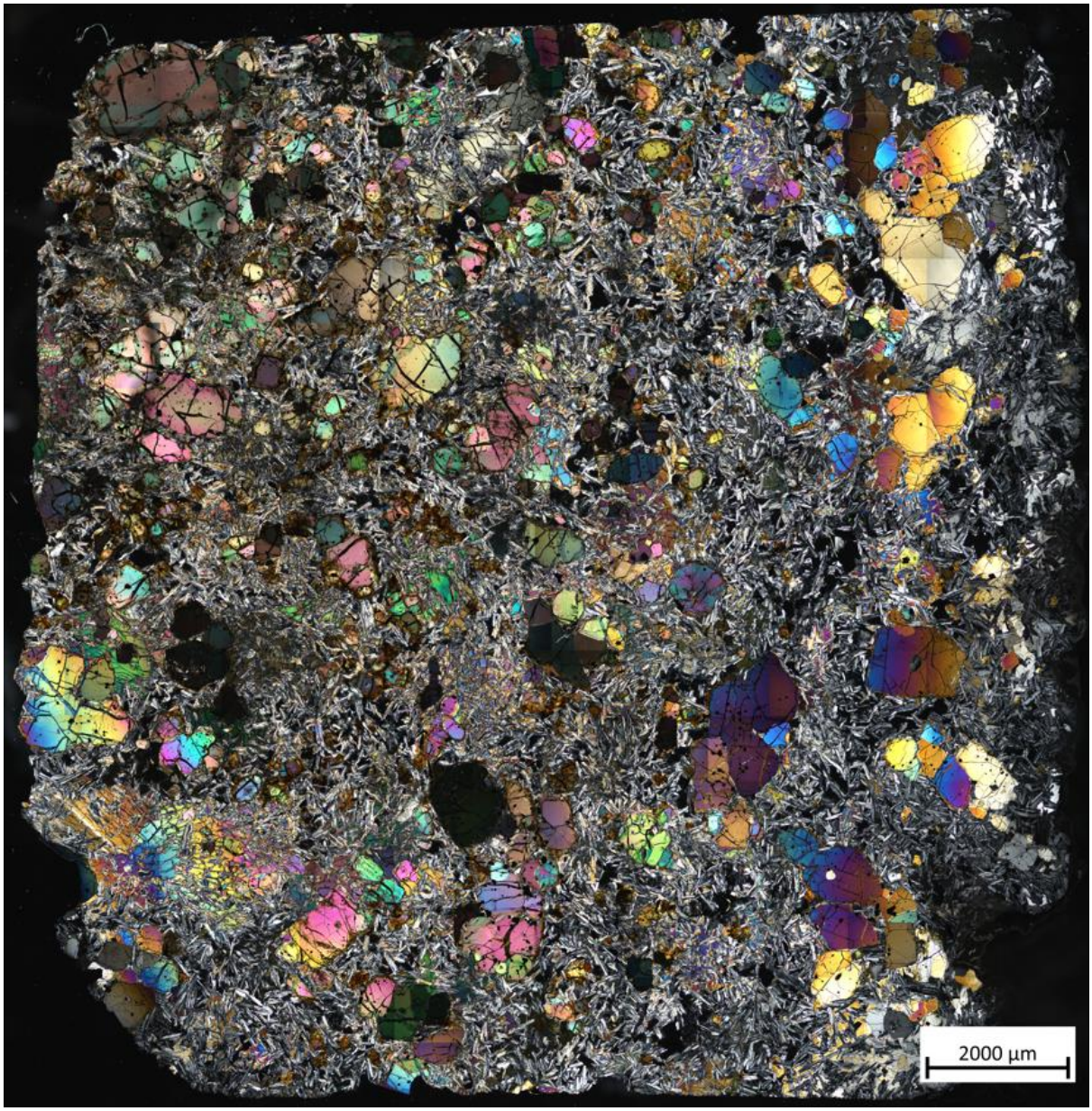

Figure A6.26: XPL Image of Sample 26.

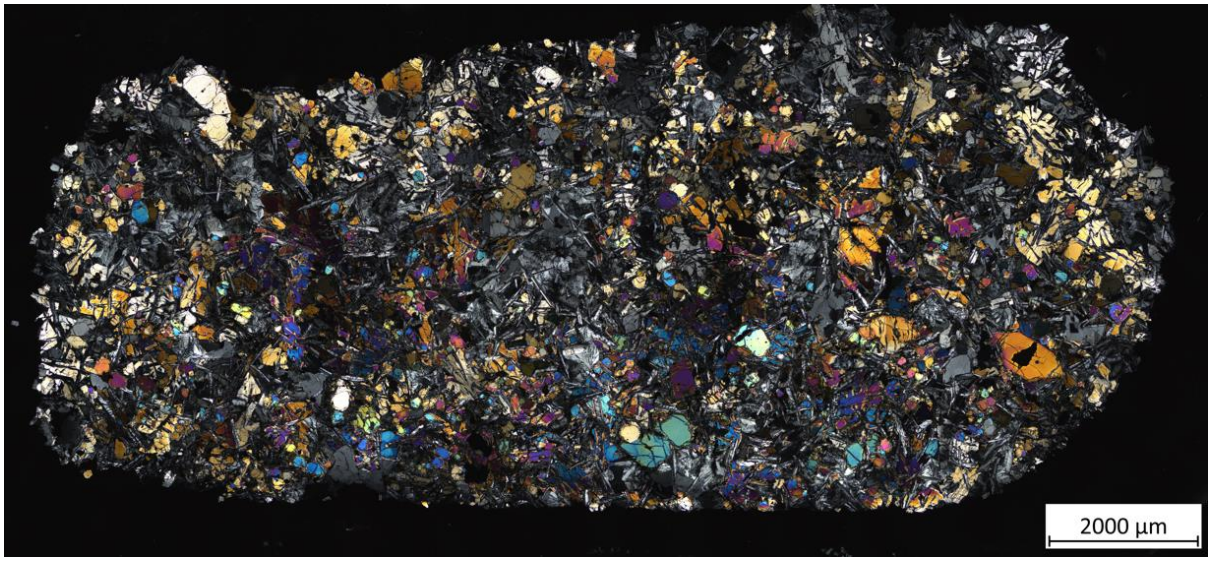

Figure A6.27: XPL Image of Sample 27.

Appendix VII – Reflected Light Images

Figure A7.1: Reflected Light Image of Sample 1.

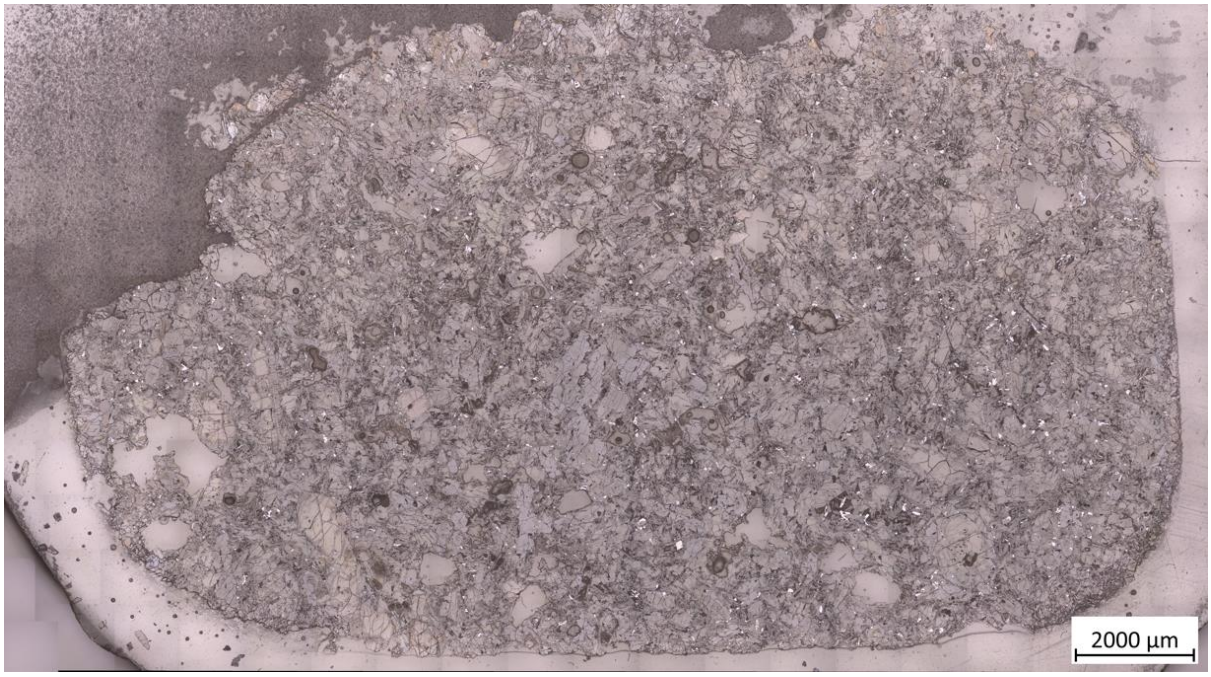

Figure A7.2: Reflected Light Image of Sample 2.

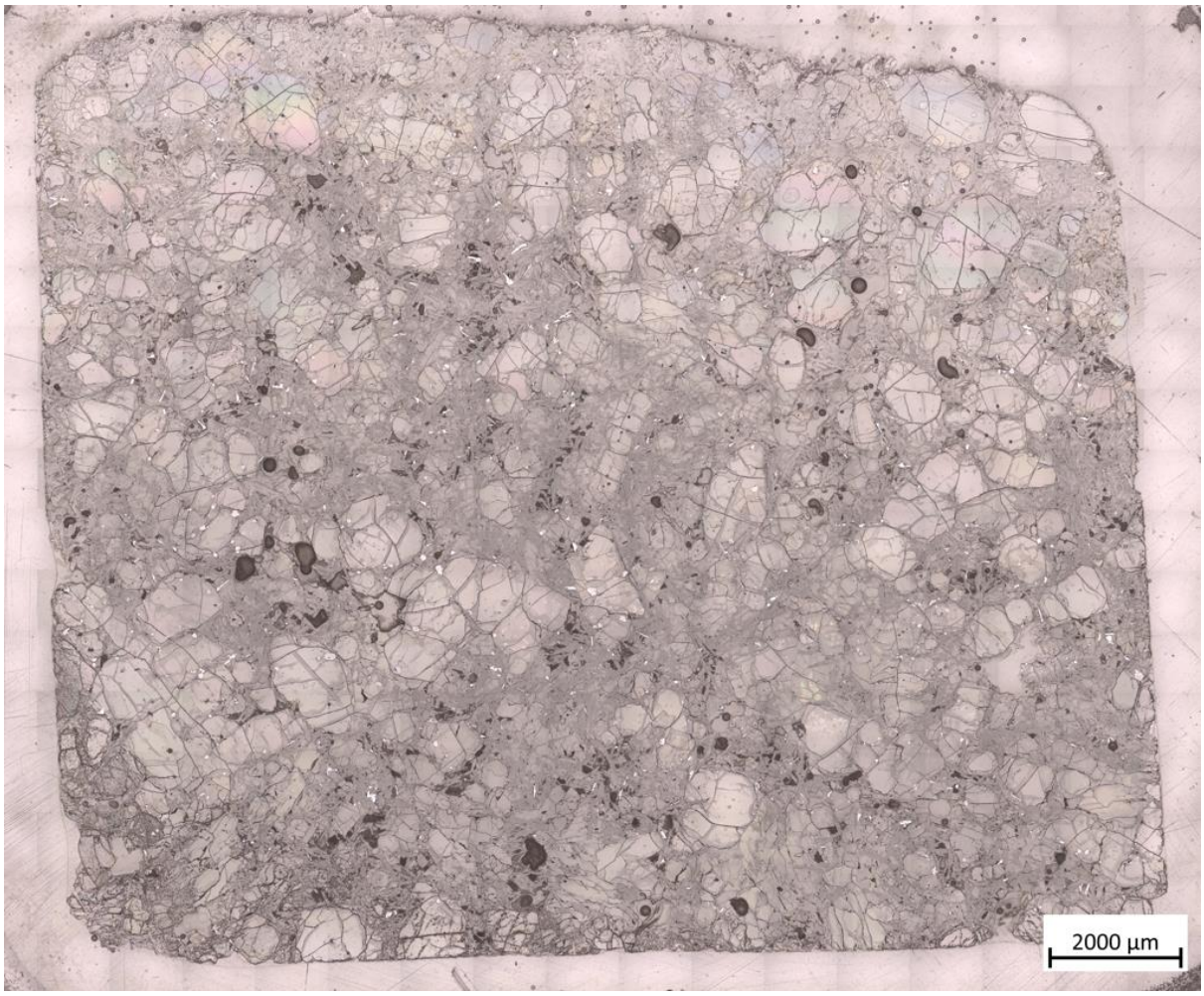

Figure A7.3: Reflected Light Image of Sample 3.

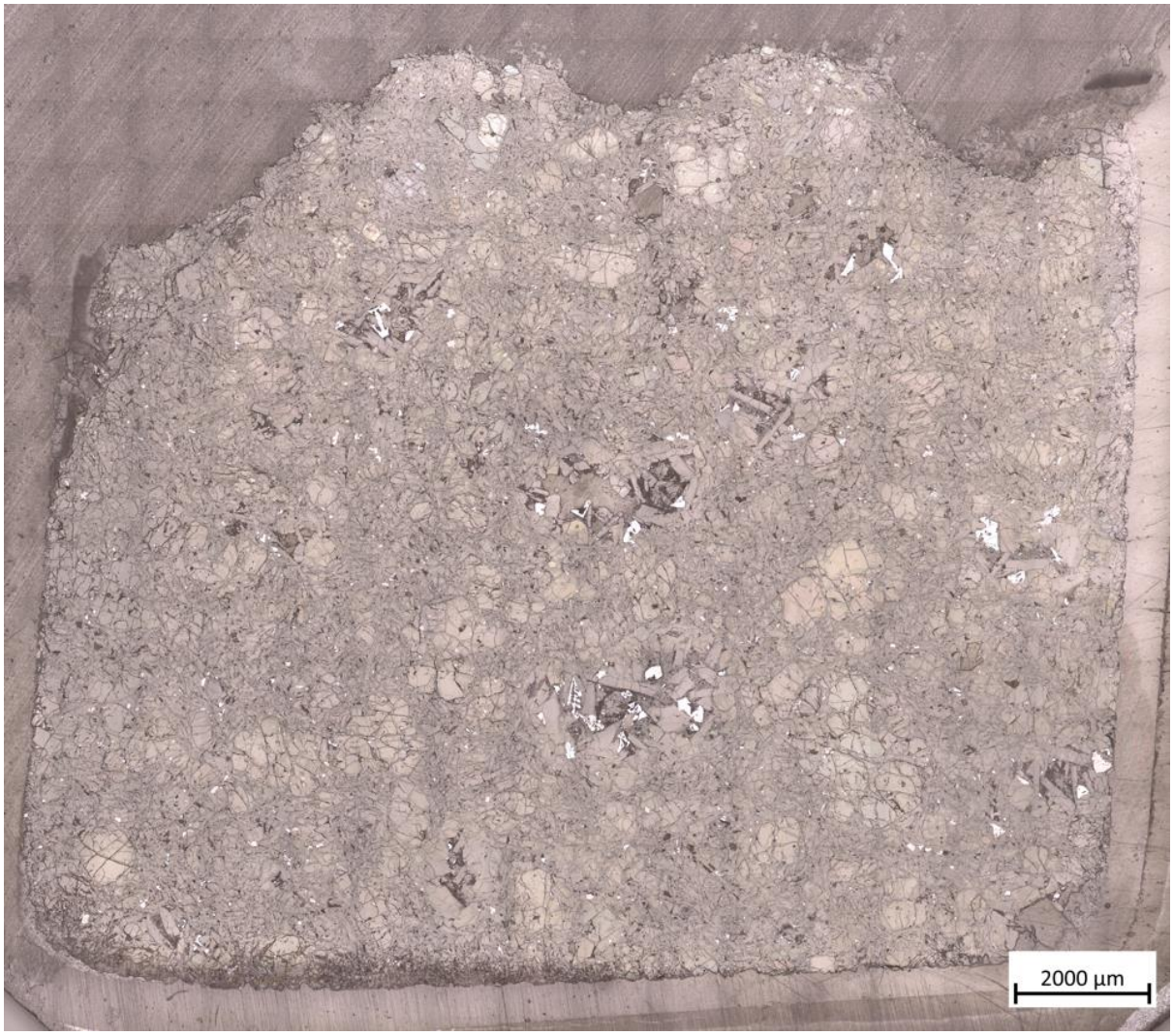

Figure A7.4: Reflected Light Image of Sample 4.

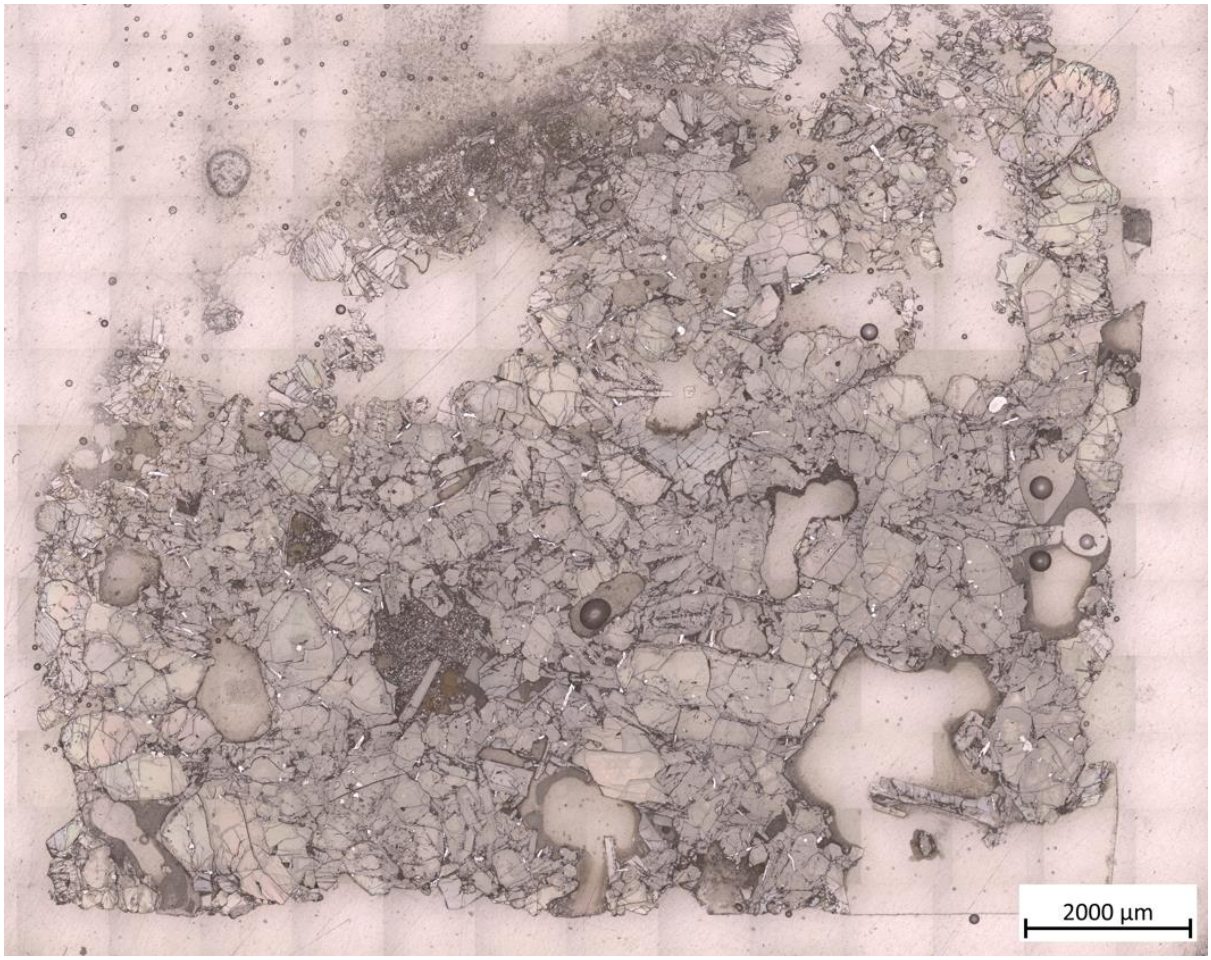

Figure A7.5: Reflected Light Image of Sample 5.

Figure A7.6: Reflected Light Image of Sample 6.

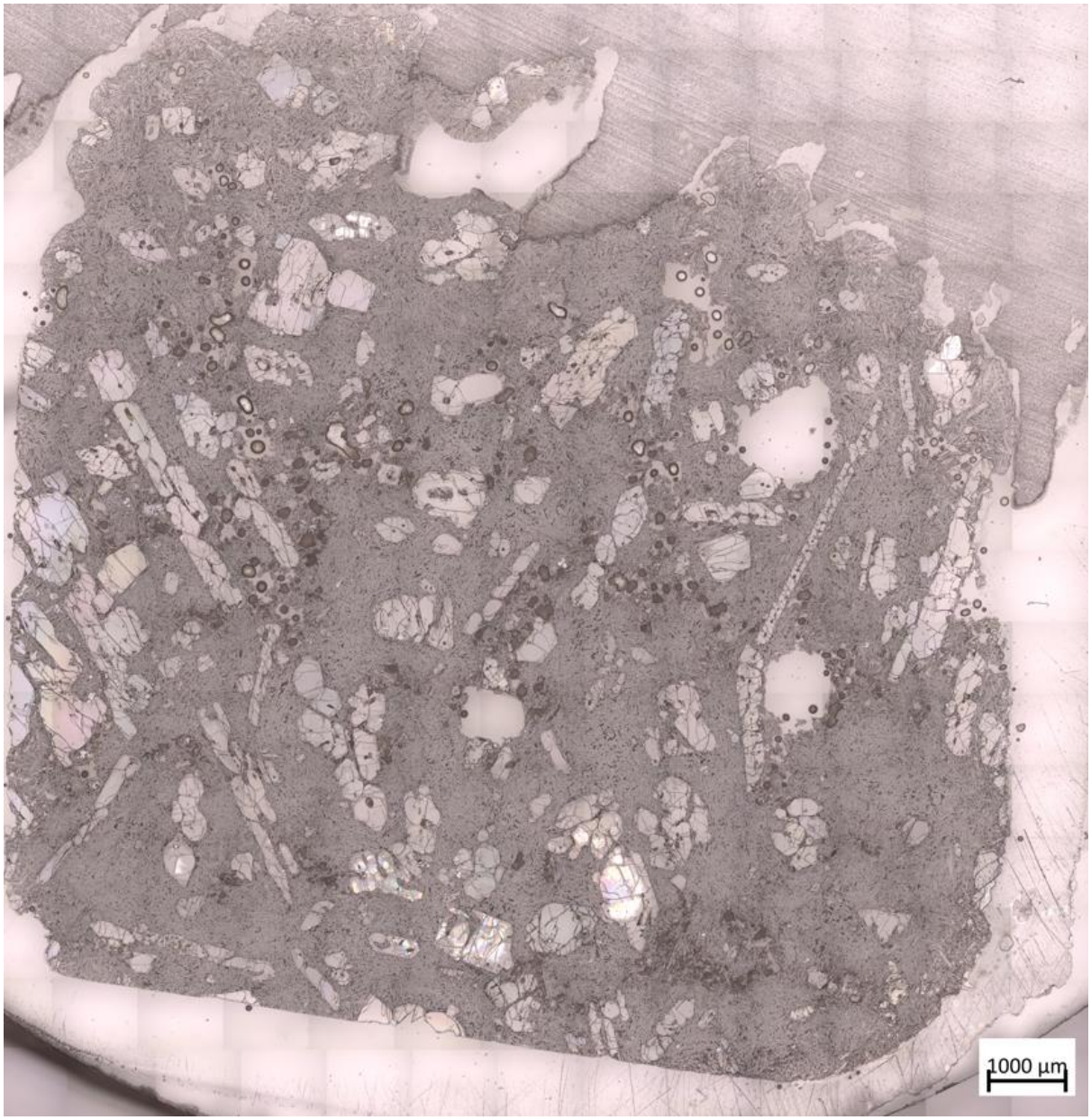

Figure A7.7: Reflected Light Image of Sample 7.

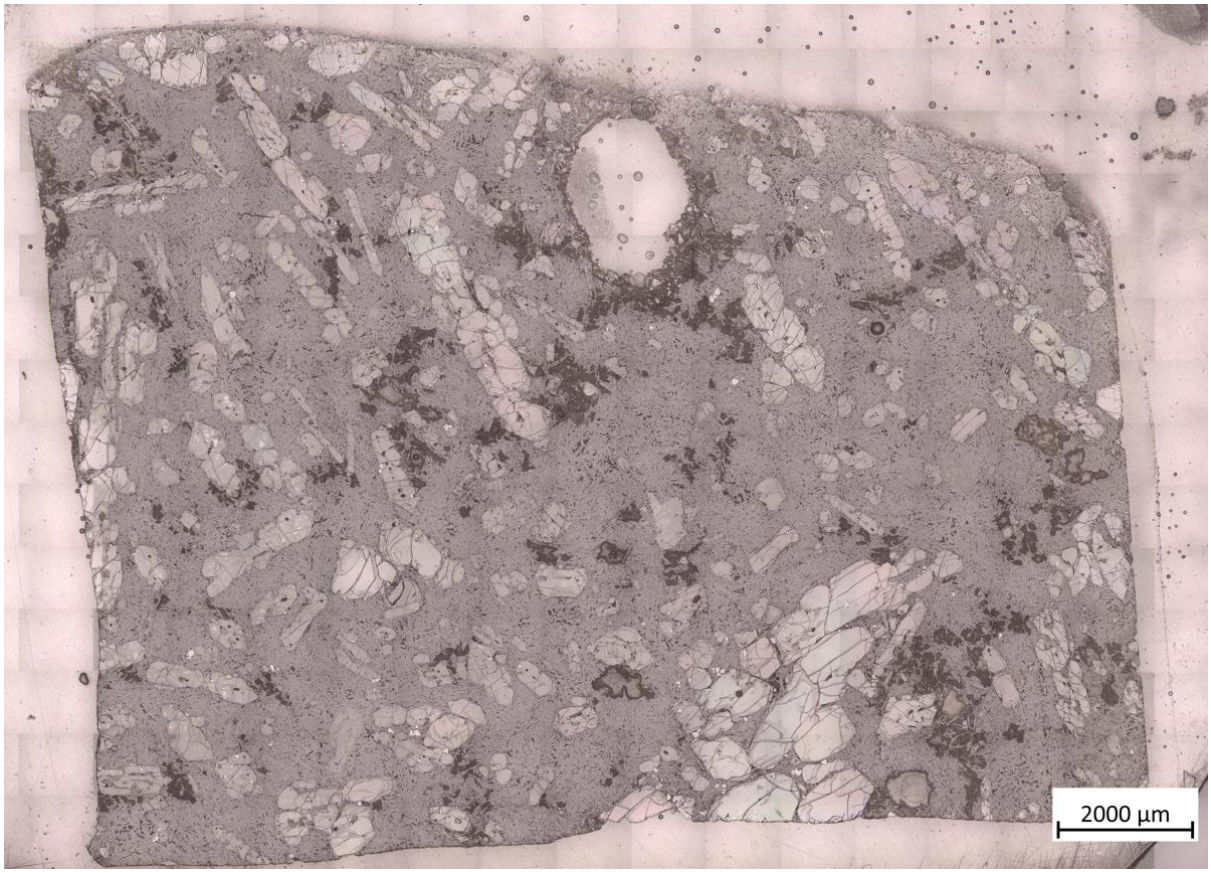

Figure A7.8: Reflected Light Image of Sample 8.

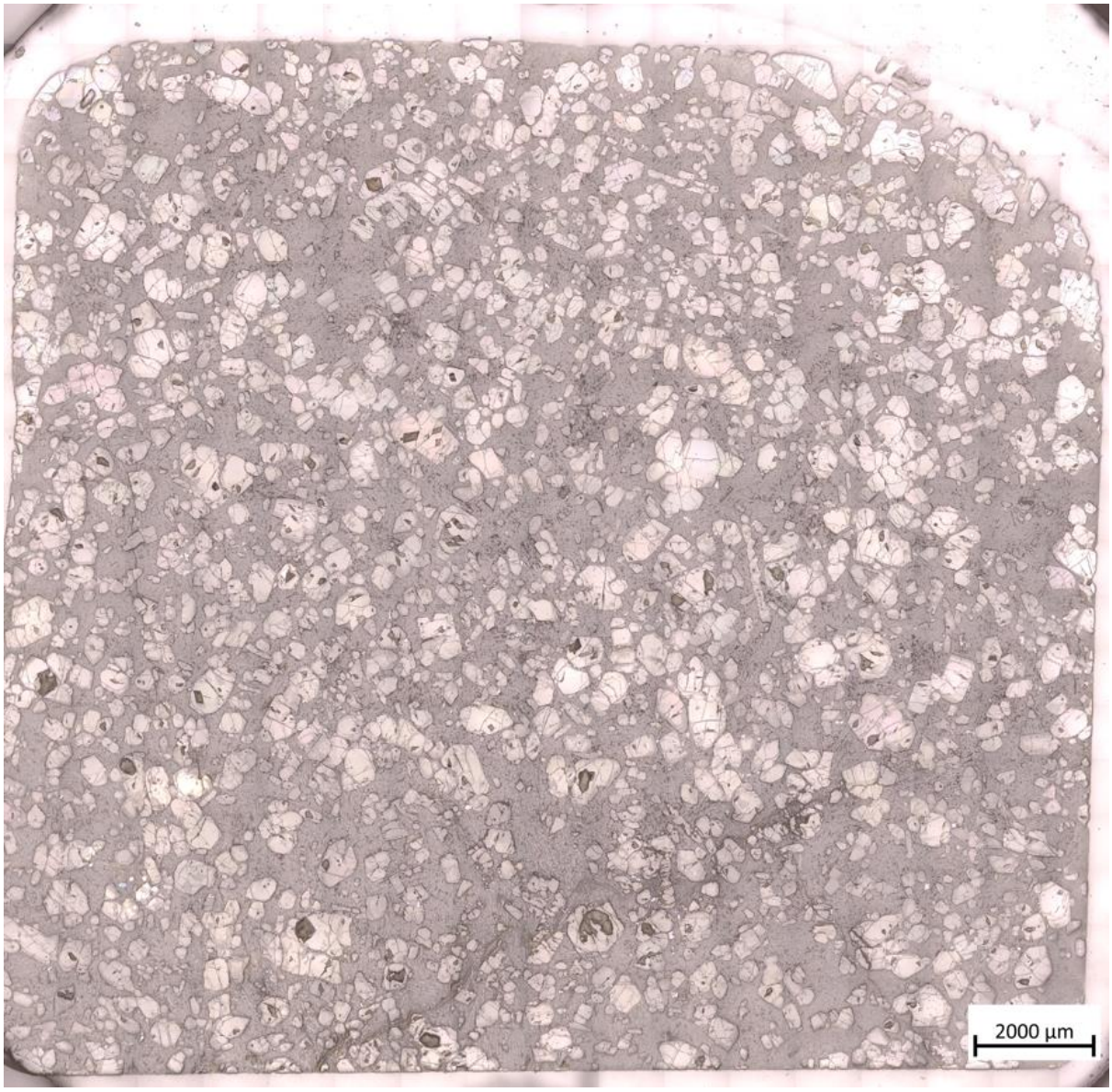

Figure A7.9: Reflected Light Image of Sample 9.

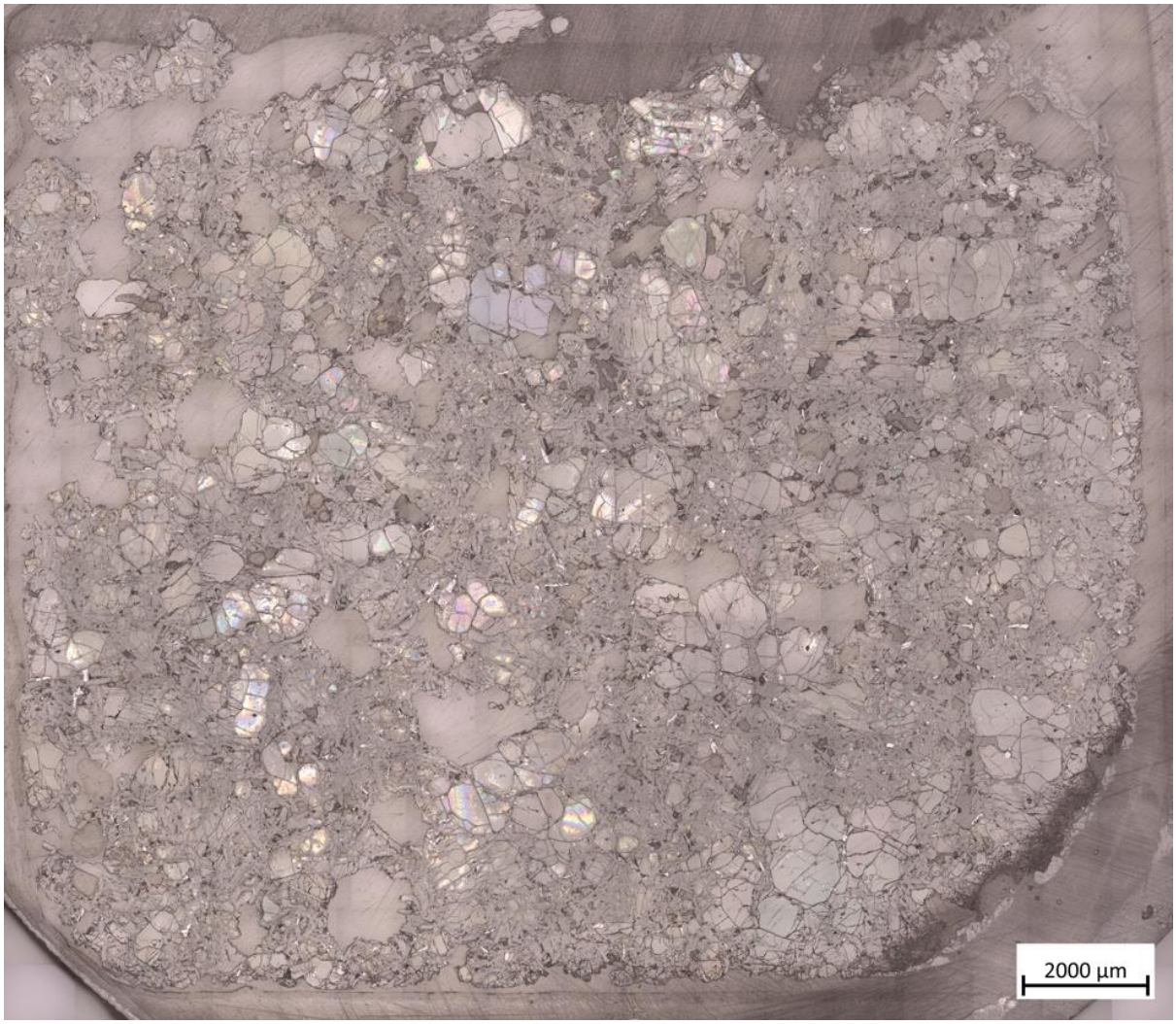

Figure A7.10: Reflected Light Image of Sample 10.

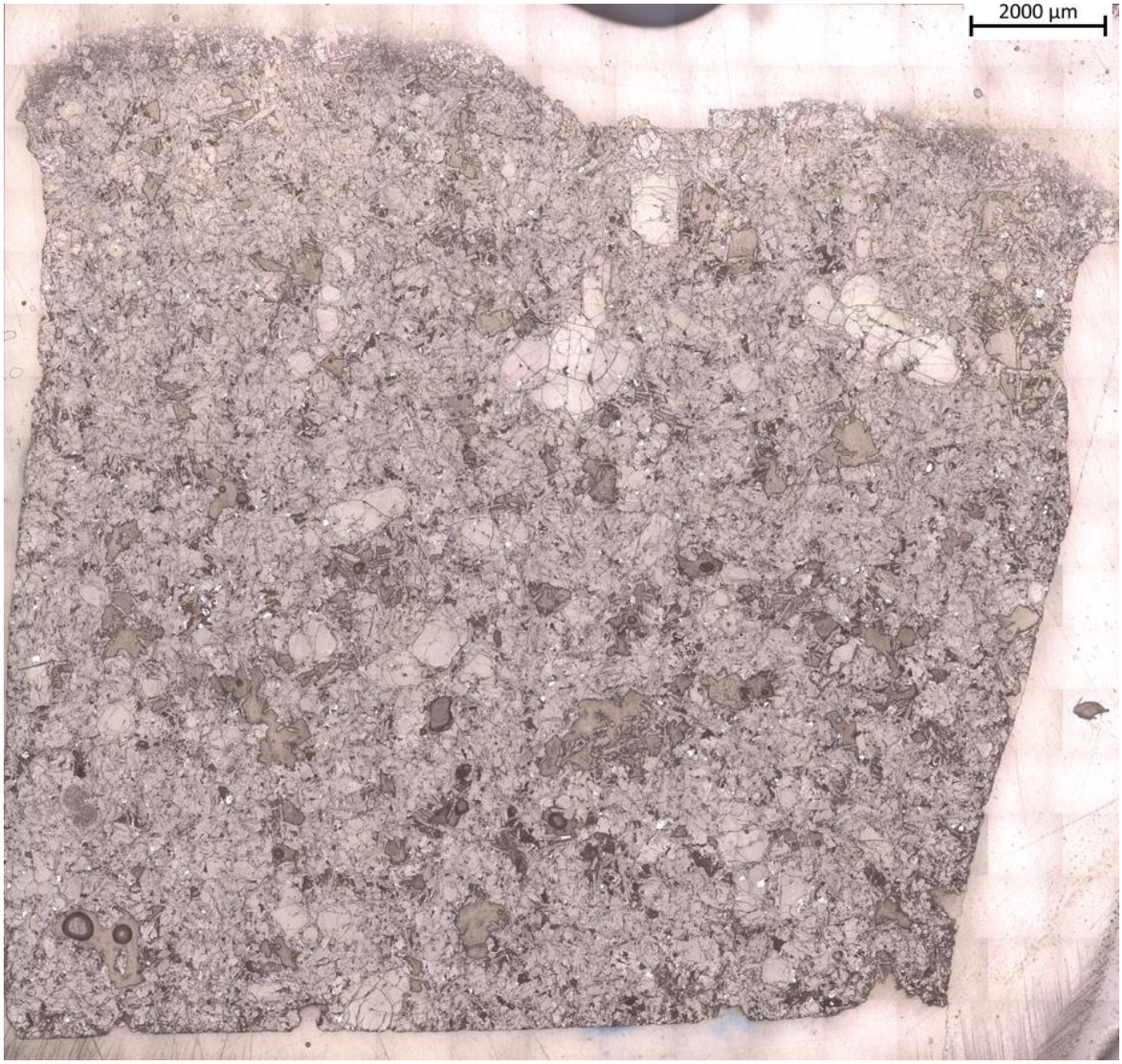

Figure A7.11: Reflected Light Image of Sample 11.

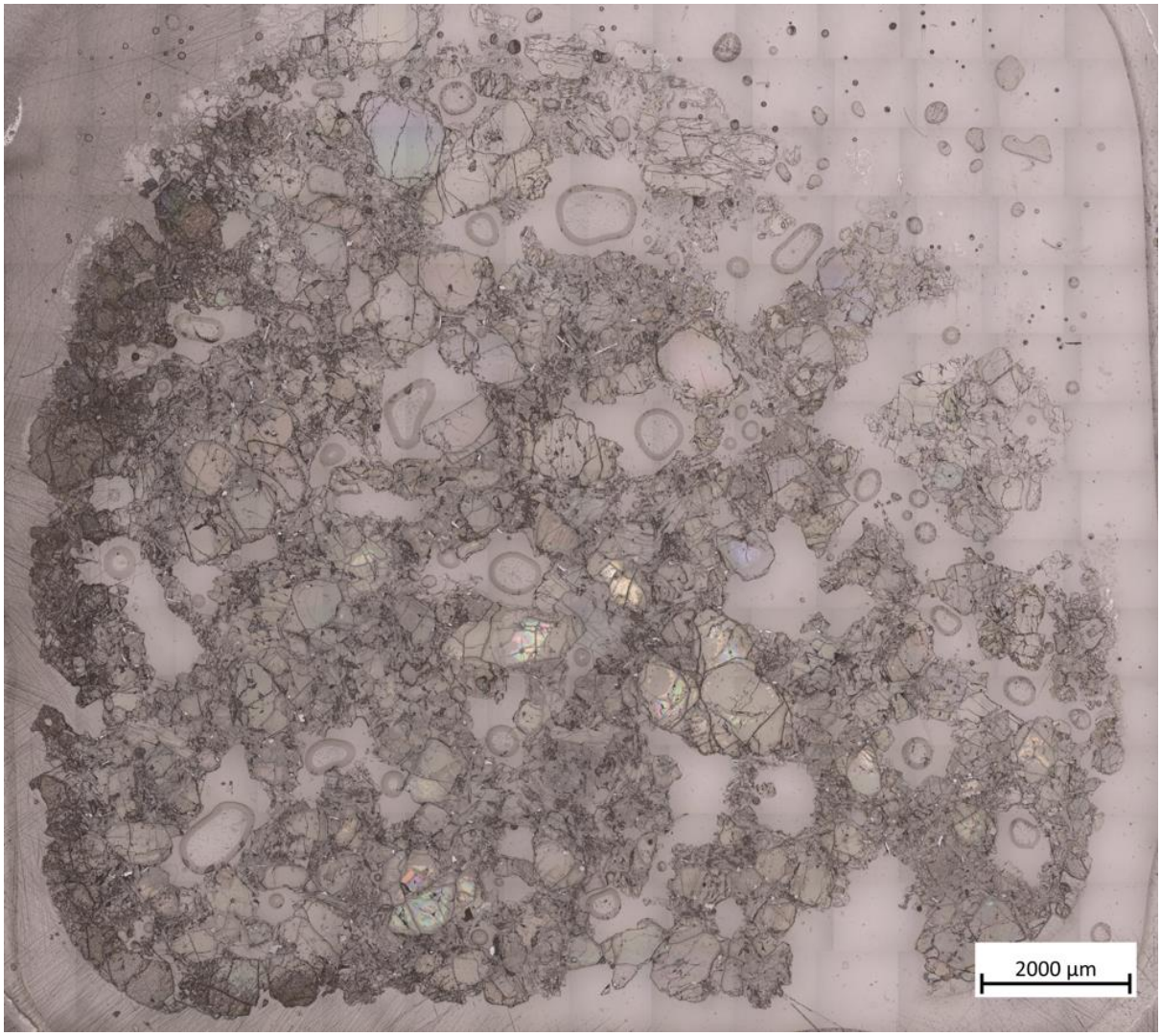

Figure A7.12: Reflected Light Image of Sample 12.

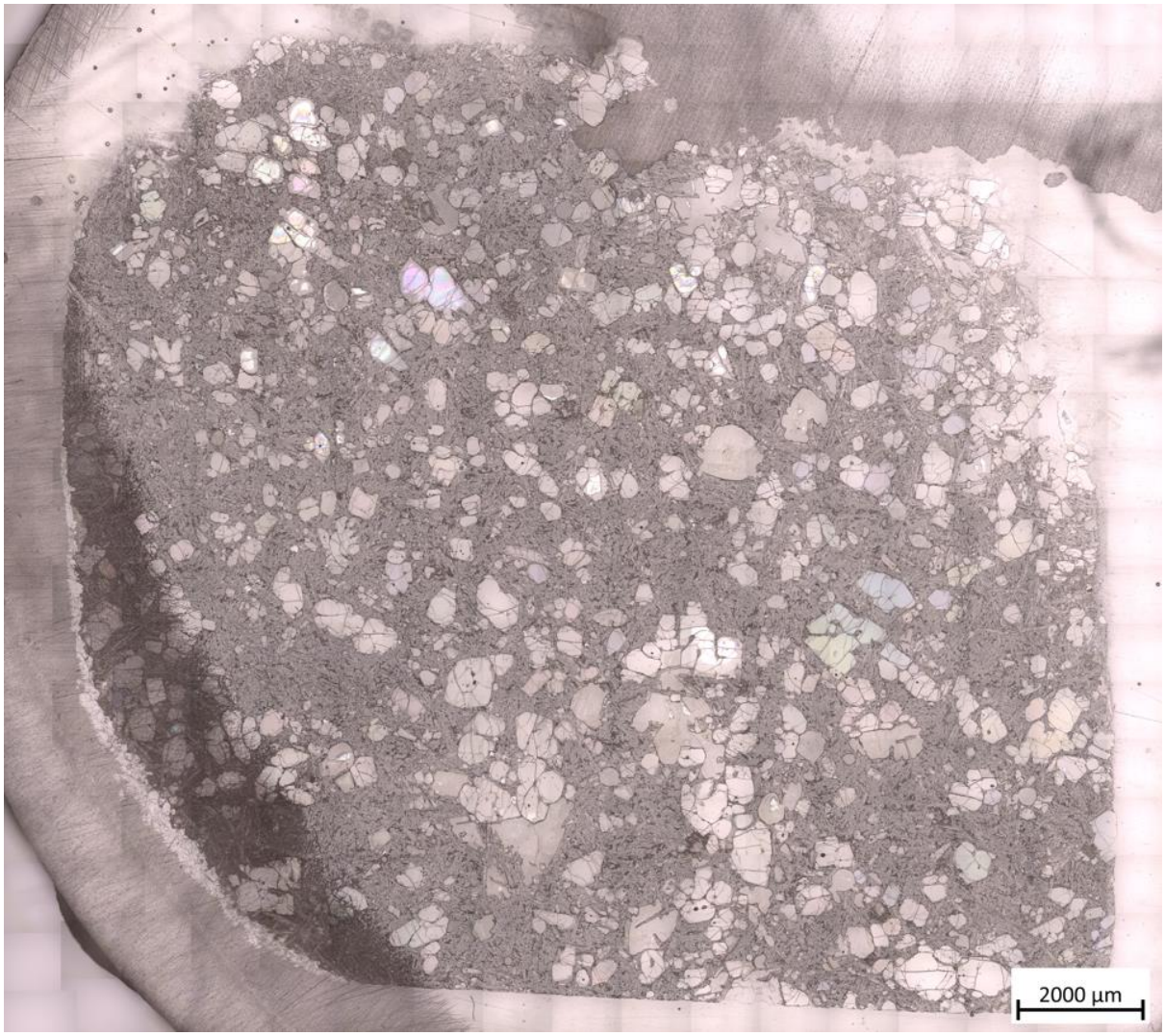

Figure A7.13: Reflected Light Image of Sample 13.

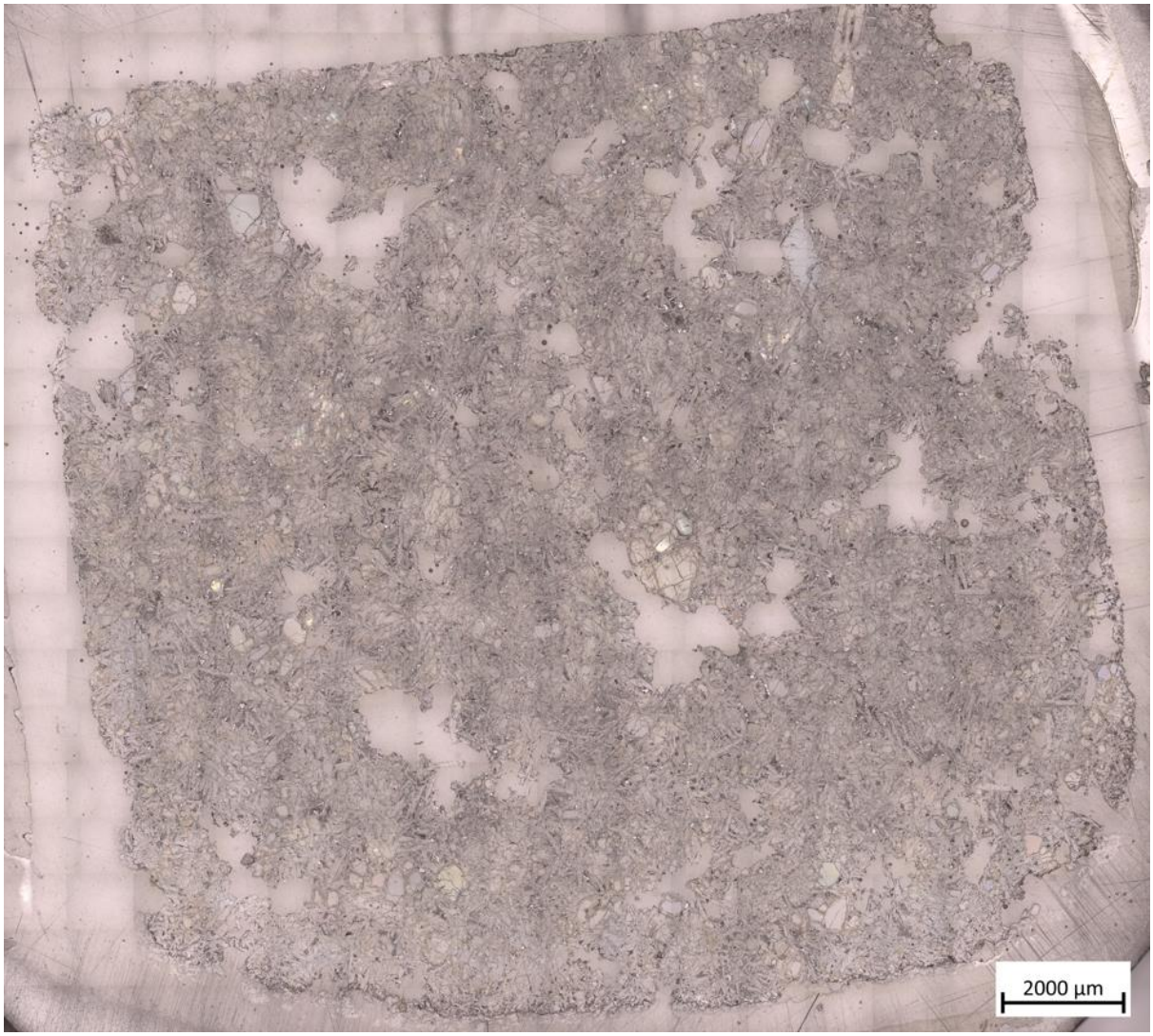

Figure A7.14: Reflected Light Image of Sample 14.

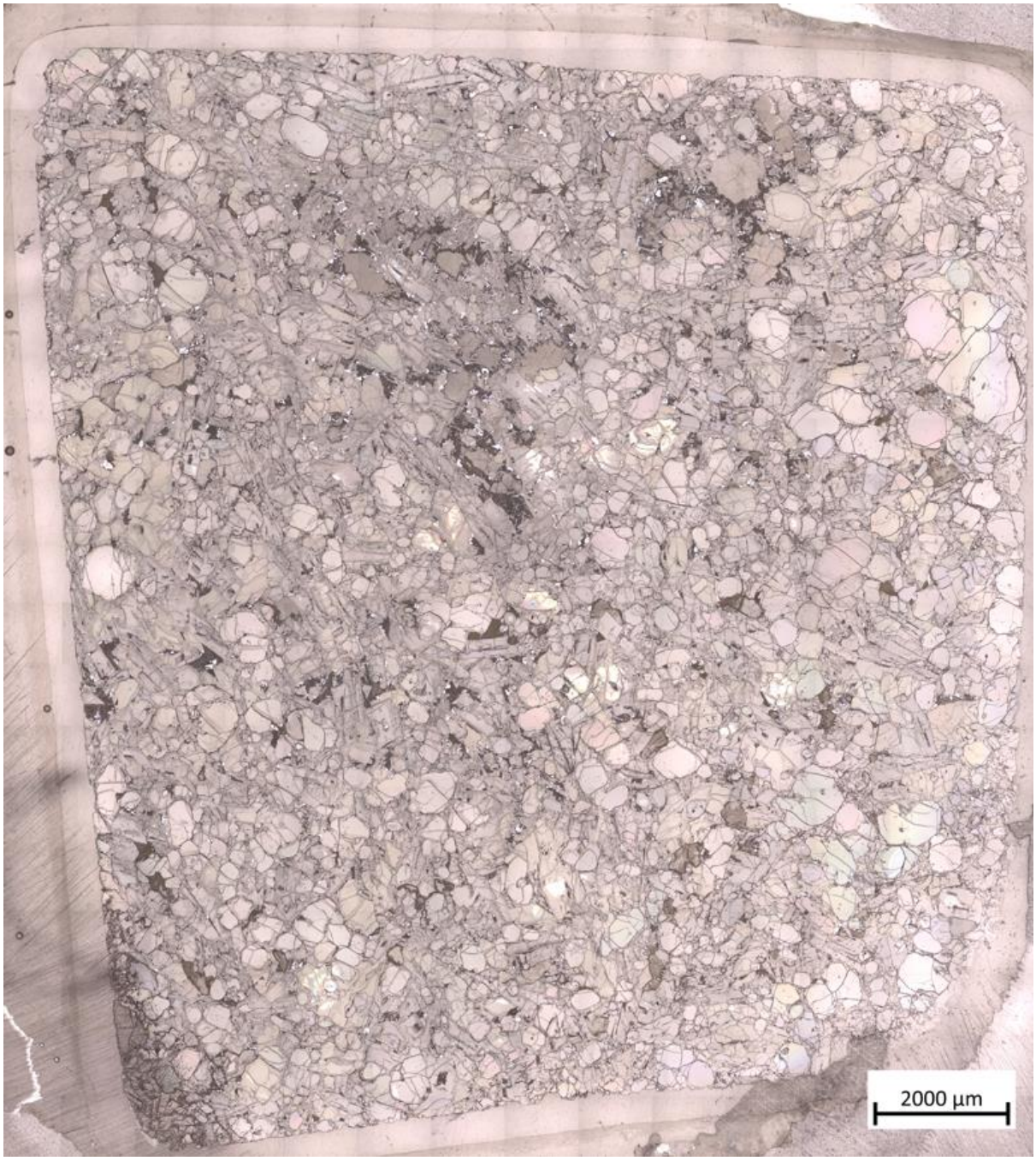

Figure A7.15: Reflected Light Image of Sample 15.

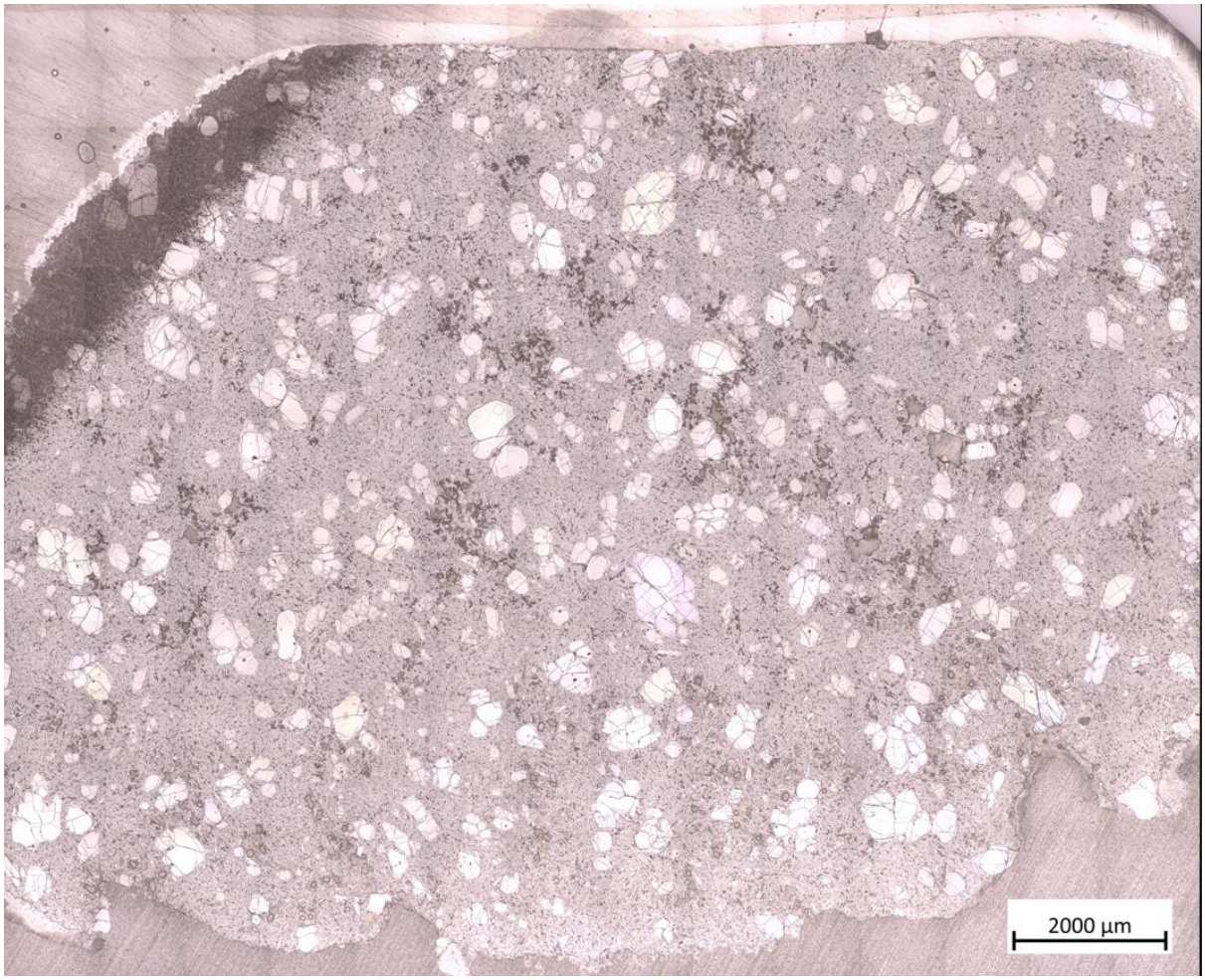

Figure A7.16: Reflected Light Image of Sample 16.

Figure A7.17: Reflected Light Image of Sample 17.

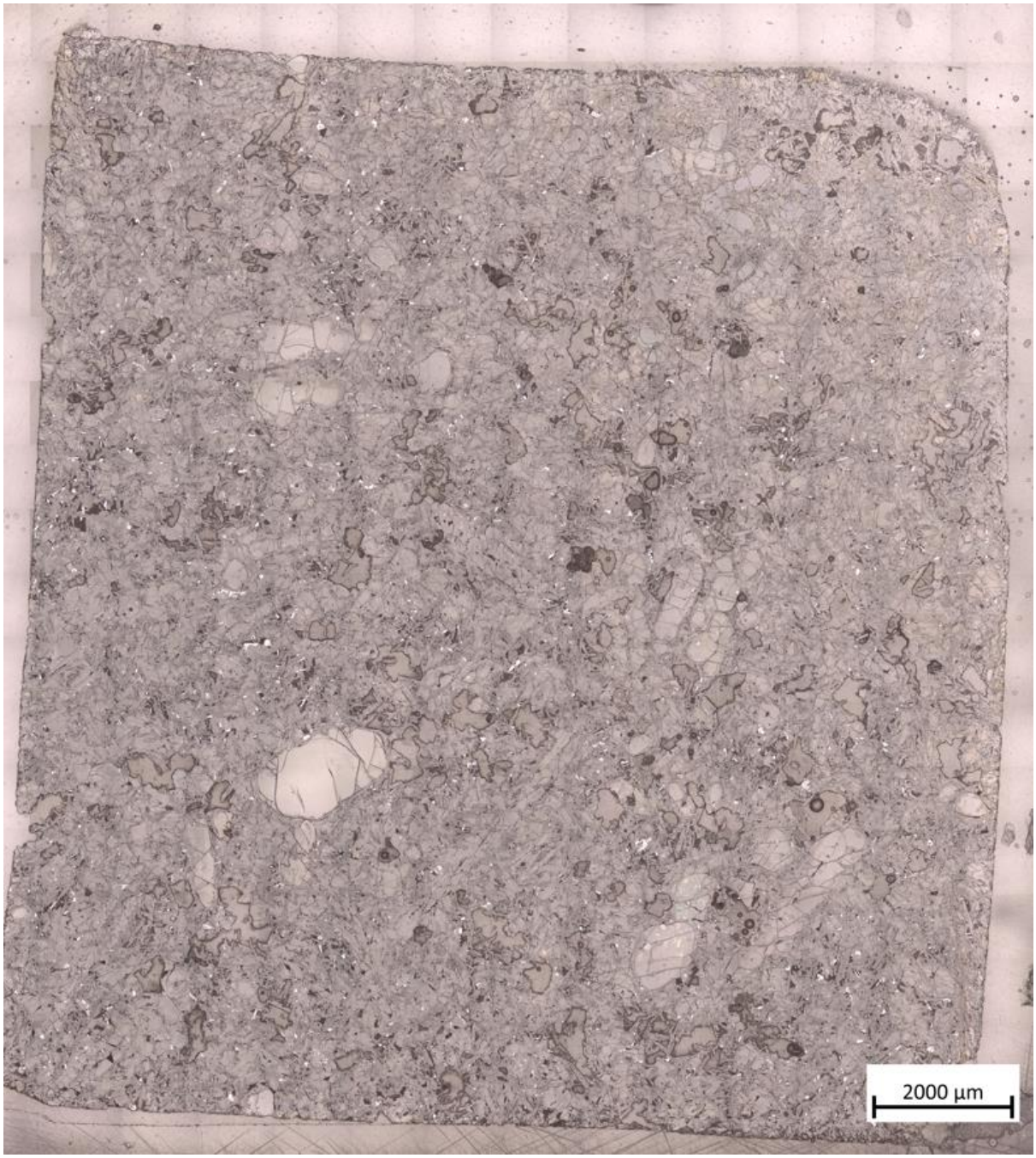

Figure A7.18: Reflected Light Image of Sample 18.

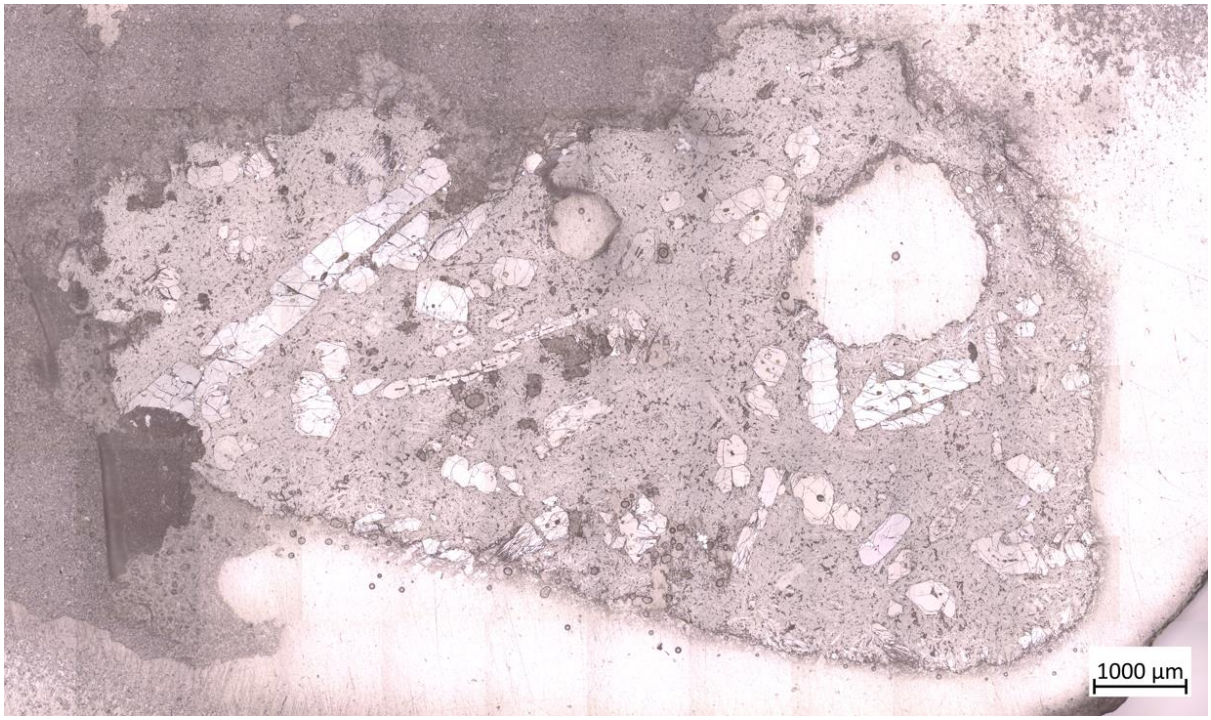

Figure A7.19: Reflected Light Image of Sample 19.

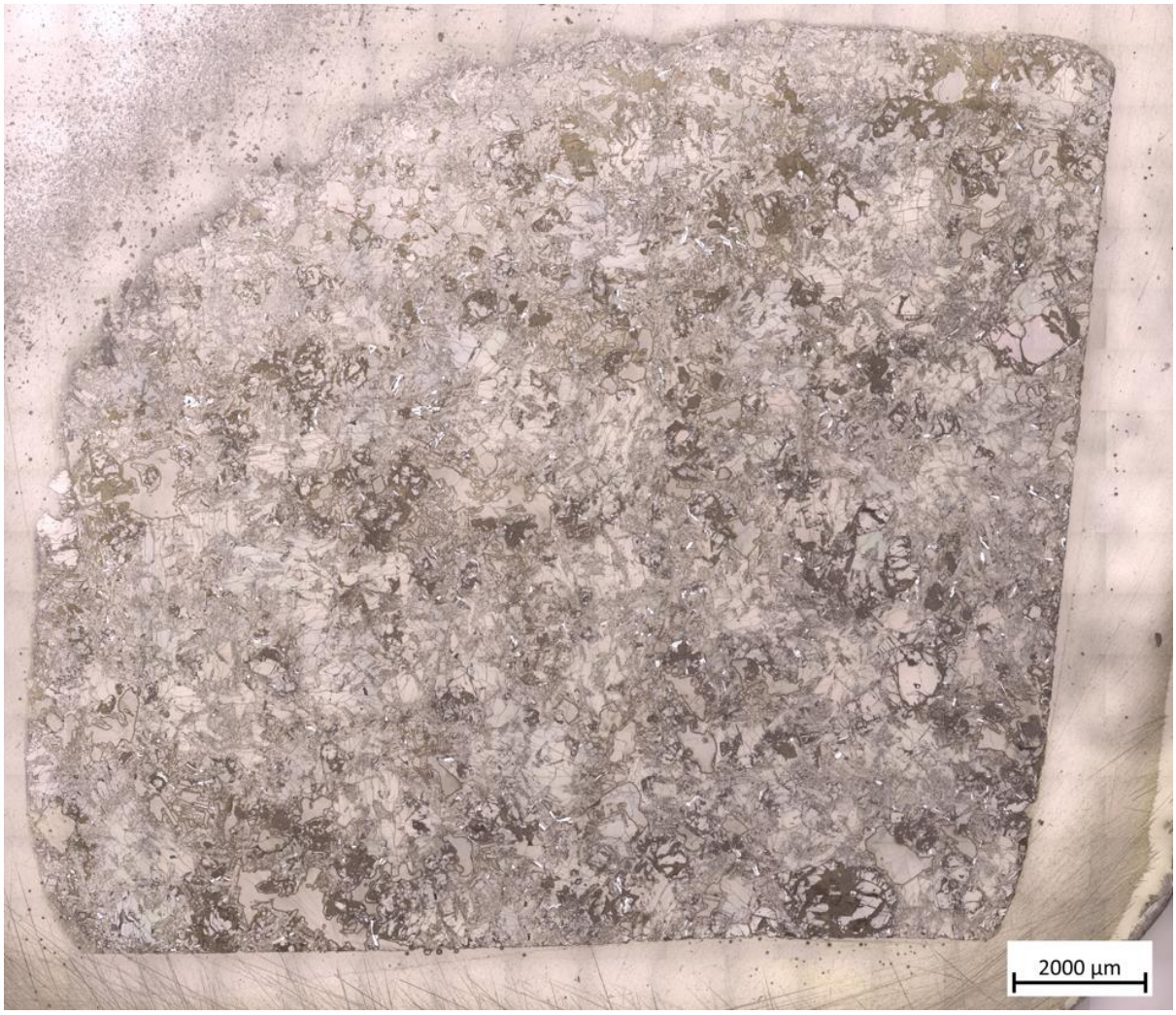

Figure A7.20: Reflected Light Image of Sample 20.

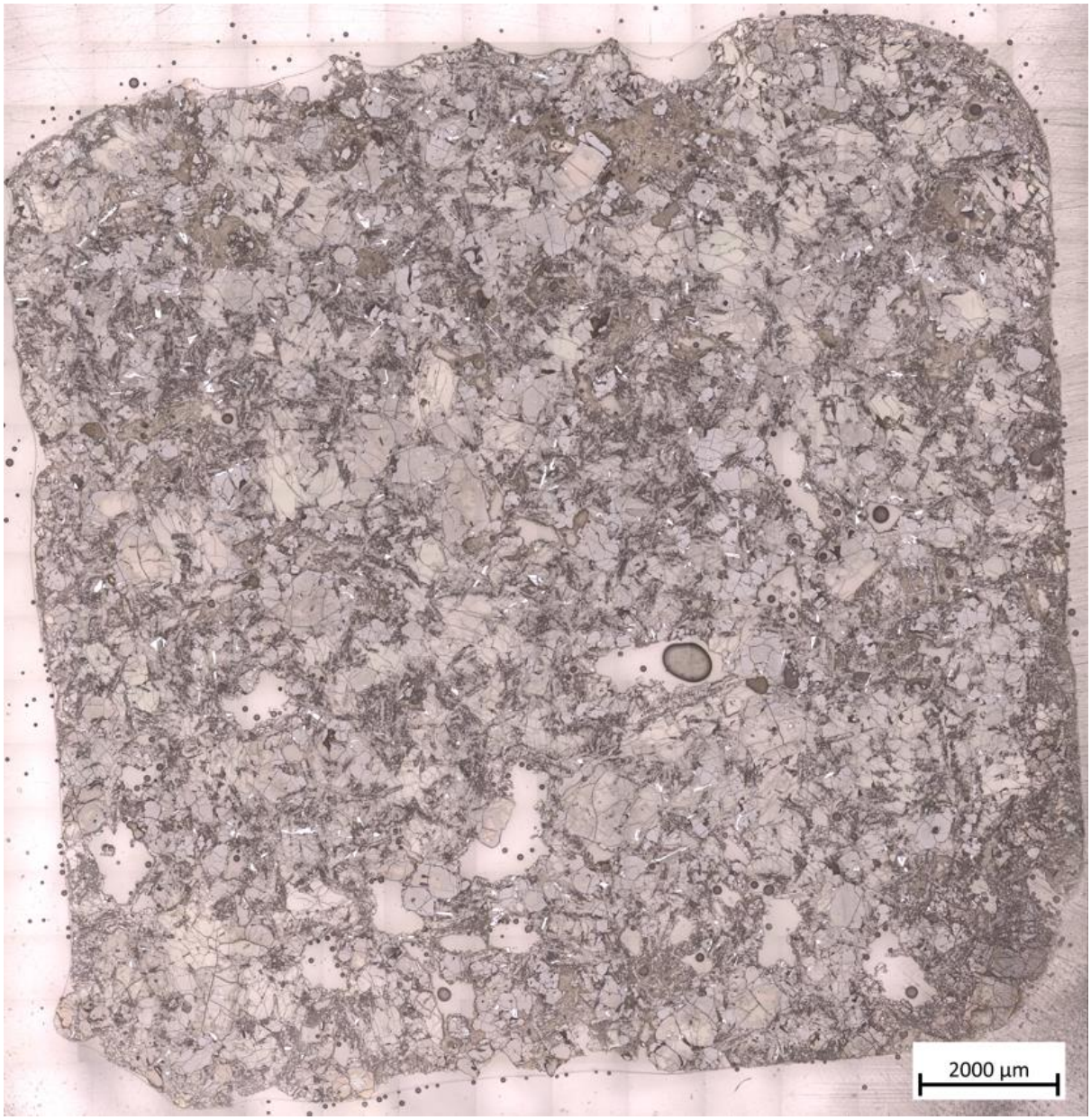

Figure A7.21: Reflected Light Image of Sample 21.

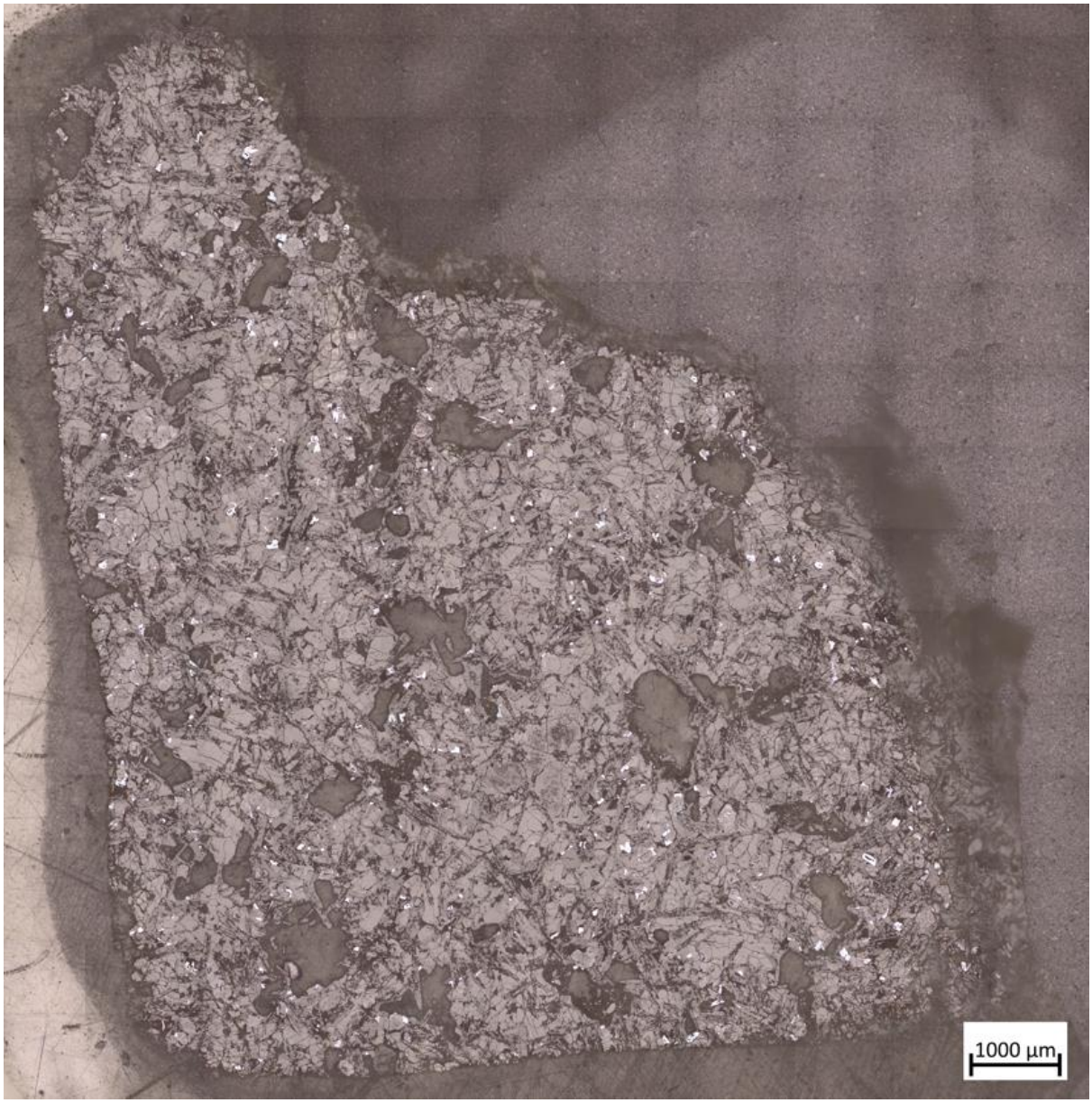

Figure A7.22: Reflected Light Image of Sample 22.

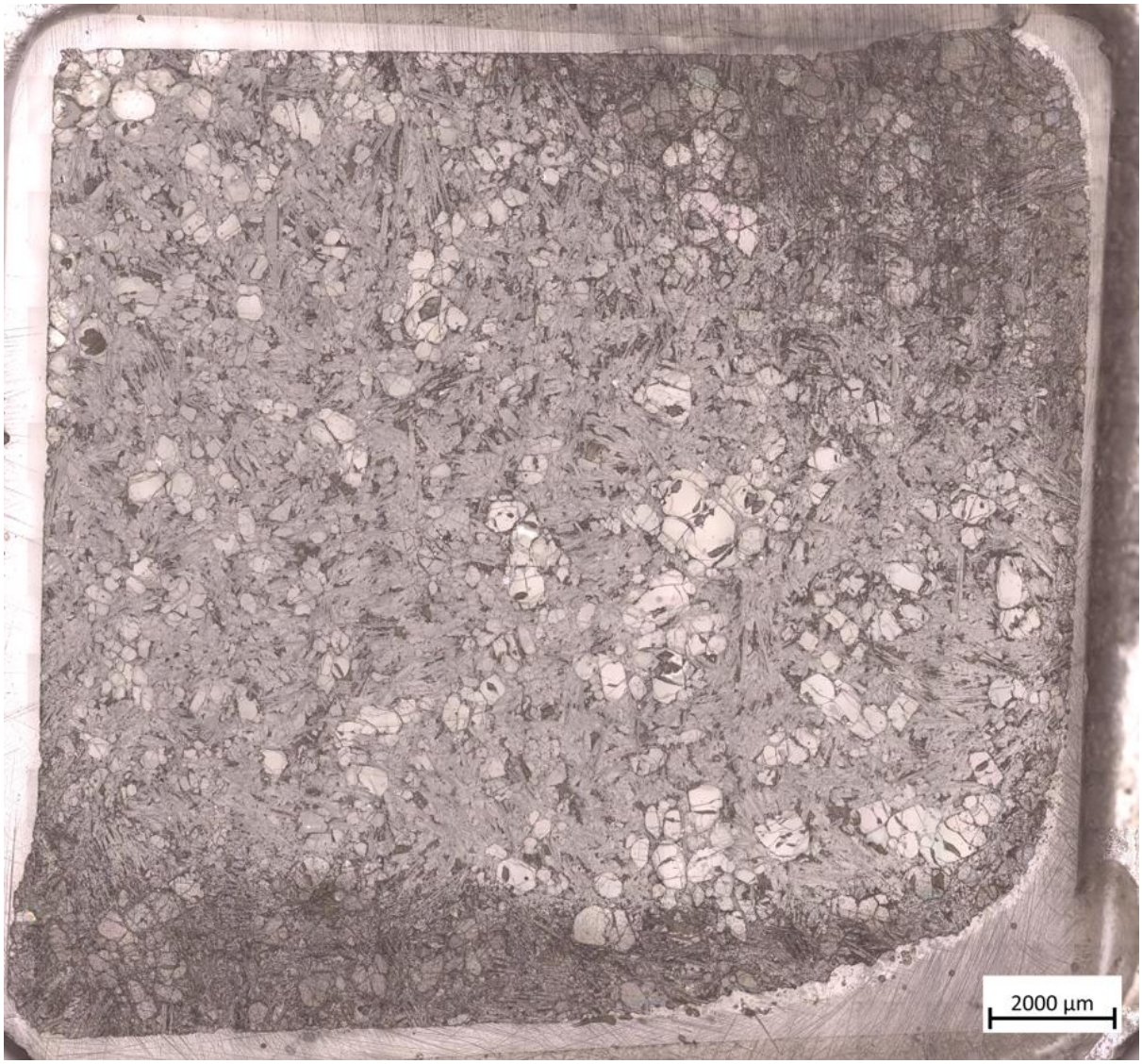

Figure A7.23: Reflected Light Image of Sample 23.

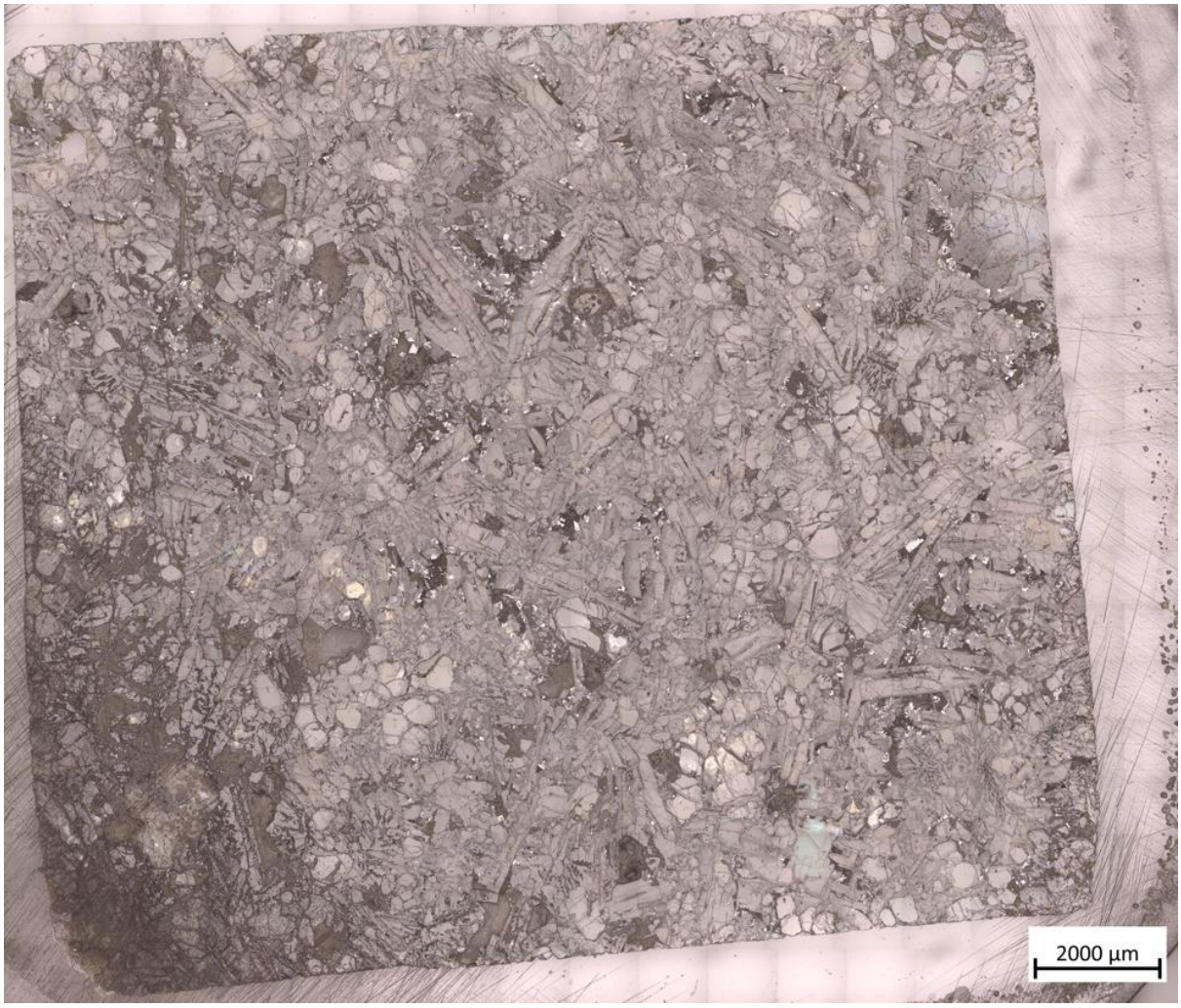

Figure A7.24: Reflected Light Image of Sample 24.

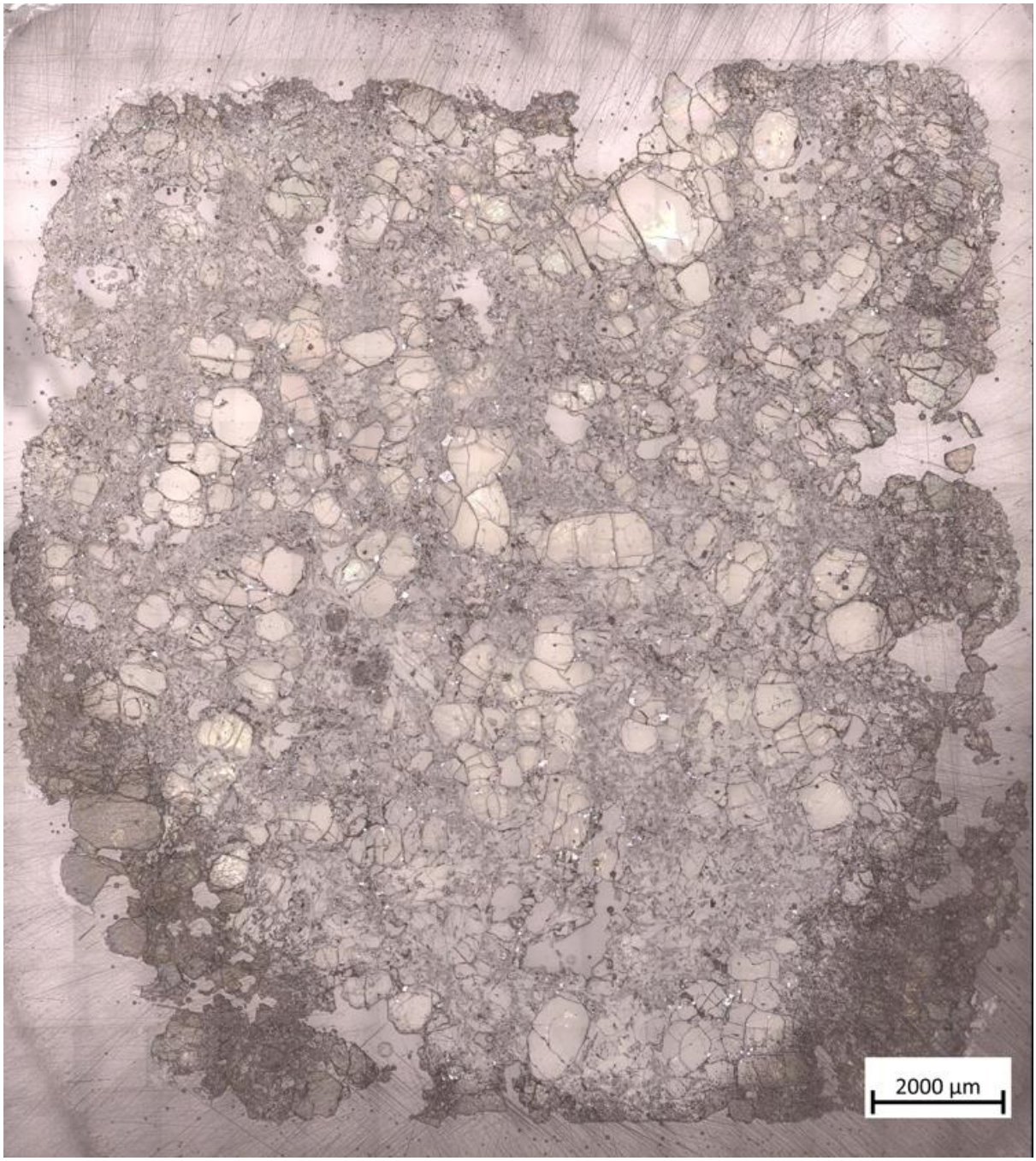

Figure A7.25: Reflected Light Image of Sample 25.

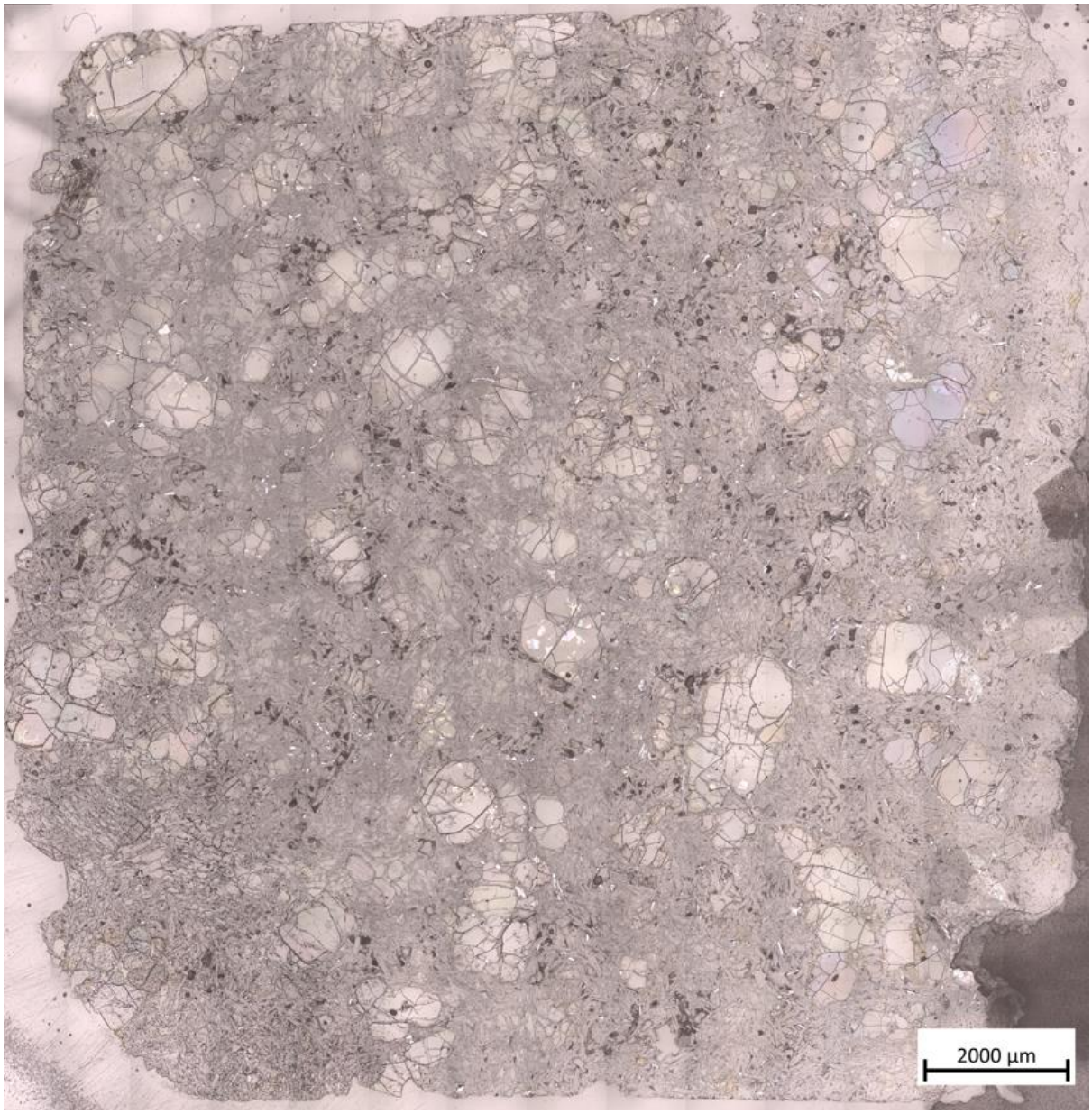

Figure A7.26: Reflected Light Image of Sample 26.

Figure A7.27: Reflected Light Image of Sample 27.